UNIVERSITY OF KENT

DOCTORAL THESIS

# Developing Opto-acoustic Microscopy instruments for Biomedical imaging Applications


*Author:*

Gianni NTEROLI

*Supervisor:*

Dr. Adrian BRADU


*A thesis submitted in fulfilment of the requirements*

*for the degree of Doctor of Philosophy*

*in the*

Applied Optics Group

School of Physics and Astronomy


External Examiner: Prof. Adrien Desjardins

Inernal Examiner: Dr. George Dobre

Viva-voce examination: 4 December 2023

# Declaration of Authorship

I, Gianni NTEROLI, declare that this thesis titled, "Developing Opto-acoustic Microscopy instruments for Biomedical imaging Applications" and the work presented in it are my own. I confirm that:

- This work was done wholly or mainly while in candidature for a research degree at this University.
- Where any part of this thesis has previously been submitted for a degree or any other qualification at this University or any other institution, this has been clearly stated.
- Where I have consulted the published work of others, this is always clearly attributed.
- Where I have quoted from the work of others, the source is always given. With the exception of such quotations, this thesis is entirely my own work.
- I have acknowledged all main sources of help.
- Where the thesis is based on work done by myself jointly with others, I have made clear exactly what was done by others and what I have contributed myself.

Signed:

_____

Date:

_____

"*Biomedical optics is a window into the human body, where light is used to uncover the hidden structures and functions of living tissues. It is a powerful tool that enables non-invasive diagnosis, imaging, and therapy, opening up new horizons for personalized medicine and precision healthcare.*"

ChatGPT (AI)

UNIVERSITY OF KENT

# *Abstract*

Faculty of Sciences

School of Physics and Astronomy

Doctor of Philosophy

**Developing Opto-acoustic Microscopy instruments for Biomedical imaging Applications**

by Gianni NTEROLI

Opto-acoustic Microscopy is an emerging technique for cross-sectional imaging that provides structural and functional volumetric information with micrometer resolution. This allows for non-invasive detection of endogenous contrast agents and chromophores without using ionizing radiation. The objective of this thesis is to investigate the potential of opto-acoustic microscopy combined with optical coherence tomography in developing advanced diagnostic tools for biomedical applications, in particular for cancer diagnosis.

To achieve this objective, the thesis focuses on *in-vivo* multi-spectral opto-acoustic microscopy imaging of multiple endogenous contrast agents in *Xenopus laevis*. The study used a high-resolution opto-acoustic microscopy instrument capable of multi-spectral imaging covering two octaves of the spectrum, and a novel technique to distinguish between different chromophores in the sample. An optical coherence tomography instrument was integrated in the opto-acoustic microscopy system to guide imaging and provide reliable structural information. Additionally, visible light optical coherence tomography system was developed as an ultra-high resolution alternative.

Prior to this study, mapping of lipids in *Xenopus laevis* was achieved using an in-house all-fibre supercontinuum optical source developed in DTU, Denmark operating in the extended near-infrared region. Both opto-acoustic microscopy and optical coherence tomography instruments are capable of acquiring cross-sectional and volumetric images in real-time.

Finally, a high-resolution opto-acoustic microscopy set-up to explore the impact of picosecond pulse duration excitation on the axial resolution of the imaging system. The study compared a picosecond pulse duration laser-based opto-acoustic microscopy instrument to a nanosecond laser-based one in terms of axial resolution and obtained unprecedented *in-vivo* images of the brain in *Xenopus laevis* tadpoles.

# *Acknowledgements*

IT is clear that the successful completion of this thesis and the work presented in it would not have been possible without the guidance and influence of some truly exceptional individuals whom I have had the privilege of interacting with over the past years.

I am grateful to my supervisor **Adrian Bradu** and my second supervisor **Adrian Podoleanu**, for their invaluable assistance and mentorship throughout my PhD journey, as well as for the opportunity to pursue this degree. I owe a debt of gratitude to Adrian Bradu for his unwavering faith in the potential success of my experiments and his continual encouragement to strive for better results. Likewise, I extend my appreciation to Adrian Podoleanu for his exceptional management abilities and his guidance on how to interact effectively with others. Moreover, I would like to extend my gratitude to **Ilias Kapareliotis** for acting as a positive influence in my professional endeavours. His guidance and encouragement have been instrumental in my decision to pursue this particular career path, and I am thankful for his unwavering support and companionship, akin to that of a brother.

I wish to express my gratitude to the outstanding individuals with whom I had the privilege of collaborating. Firstly, I extend my thanks to Manoj Kumar Dasa from DTU, Denmark for his remarkable professionalism, unwavering dedication, and for initiating a highly productive collaboration that resulted in several publications. I would also like to acknowledge the invaluable contributions of Stella Koutsikou and Giulia Messa from the School of Pharmacy, University of Kent, UK. Their insightful discussions, exceptional training, and immense support throughout the experimentation and article writing process were truly remarkable. Furthermore, I wish to recognize the contributions and support of Mireca Guina and Antti Pettinen from Tampere University, Finland.

I would like to express my sincere appreciation to the remarkable individuals with whom I had the pleasure of working with in the Applied Optics Group. Beginning with my fellow students, many of whom have moved on, I would like to thank Adrian Fernandez Uceda, the huggy Spaniard; Andrew Thrapp, the

tech-savvy American; Mike Everson, who would stay late to indulge in a game of DOOM; Hal Dorrington, the compassionate environmentalist who likely misplaced his keys again; Julien Camard, the exceptional president of our student chapter; Alejandro Martinez Jimenez, the joyful enthusiastic foodie; René Říha, who fervently believes in the resurrection of David Attenborough; Gopika Venugopal, the most kind-hearted and courteous student in the AOG; Sacha Grelet, the laser expert from France; Marie Klufts, the smiley face; Irene Rodriguez Lamoso, the Greek-speaking Spaniard; and Lucy Abbott, for her infectious positivity and optimistic outlook. I am grateful for the many stimulating discussions, movie nights, and occasional extended lunch breaks, where we delved into a diverse range of fascinating topics. I also extend my appreciation to the remaining AOG researchers, Manuel Marques for embodying the spirit of helpfulness and collegiality and Ramona Cernat for being a calming and supportive presence. I would also like to acknowledge the other AOG members, including Yong Hu, Radu Stancu, Mike Hughes, George Dobre, and Prof David Jackson. Furthermore, many exchange students, external researchers, and collaborators came and went during my tenure. Therefore, I would like to recognize the contributions of James Davis, Vlastimil Kropac, Matej Spacek, Melanie Wacker, Veronika Tsatourian, Victor Rico, Yuwei Qin, and Rasmus Hansen.

I express my gratitude to the University of Kent for affording me the studentship that has enabled me to pursue my academic goals. In addition, I am appreciative of the opportunity to engage in teaching as a graduate teaching assistant, which has enriched my experience and deepened my understanding of the academic process.

On a more personal level, I would like to express my sincere gratitude to my beloved spouse, Aikaterini Charla, whose unwavering support and understanding have been a source of strength and comfort throughout my academic journey. Despite the challenges and pressures that come with pursuing a thesis, she has remained steadfast and accommodating, making the most demanding period of the past year remarkably enjoyable.

I would like to convey my profound appreciation to my parents, Stavri Nteroli

and Kyriakoula Nteroli, for their extraordinary devotion and steadfast encouragement during my personal and academic odyssey. Furthermore, I extend my gratitude to my sisters, Angelliki and Chrysoula, as well as my cherished nieces, Melina and Lidia, and my nephew Thomas, whose presence in my life has been essential, providing me with continuous affection and motivation.

Finally, and of utmost significance, I would like to convey my heartfelt appreciation to my spiritual fathers, Fr. Apostolos Theologou and Fr. Vissarion Kokkliotis, for standing by my side throughout my journey of discovering the one true GOD, Jesus Christ. Words cannot express the depth of my gratitude to Fr. Apostolos Theologou for his nurturing care, unwavering support, guidance, and mentorship, which have contributed significantly to shaping me into the person I am today. I am forever indebted to him for his role in my life. Similarly, I am grateful to Fr. Vissarion Kokkliotis for being the sole source of light and solace in a foreign land. Through his subtle yet effective teaching methods, he has instilled in me the importance of loving others and all of creation - a fundamental aspect of being human.

# Contents

# List of Figures

# List of Abbreviations

| | |
|---|---|
| **OAM** | **O**pto- **A**coustic **M**icroscopy |
| **MS-OAM** | **M**ulti- **S**pectral **O**pto-**A**coustic **M**icroscopy |
| **sp-OAM** | **S**pectroscopic **O**pto-**A**coustic **M**icroscopy |
| **AR-OAM** | **A**coustic **R**esolution **O**pto-**A**coustic **M**icroscopy |
| **OR-OAM** | **O**ptical **R**esolution **O**pto- **A**coustic **M**icroscopy |
| **OCT** | **O**ptical **C**oherence **T**omography |
| **FD-OCT** | **F**ourier-**D**omain **O**ptical **C**oherence **T**omography |
| **TD-OCT** | **T**ime-**D**omain **O**ptical **C**oherence **T**omography |
| **PS-OCT** | **P**olarisation-**S**ensitive **O**ptical **C**oherence **T**omography |
| **SD-OCT** | **S**pectral-**D**omain **O**ptical **C**oherence **T**omography |
| **SB-OCT** | **S**ectrometer-**B**ased **O**ptical **C**oherence **T**omography |
| **SS-OCT** | **S**wept **S**ource **O**ptical **C**oherence **T**omography |
| **OPD** | **O**ptical **P**ath **D**ifference |
| **EPP** | **E**nergy **P**er **P**ulse |
| **PRR** | **P**ulse **R**epetition **R**ate |
| **MAP** | **M**aximum **A**mplitude **P**rojection |
| **MPE** | **M**aximum **P**ermissible **E**xposure |
| **FWHM** | **F**ull **W**idth at **H**alf **M**aximum |
| **FFT** | **F**ast **F**ourier **T**ransform |
| **FOV** | **F**ield **O**f **V**iew |
| **CMS** | **C**omplex **M**aster **S**lave |
| **SC** | **S**upercontinuum |
| **SNR** | **S**ignal-to-**N**oise Ratio |
| **LSF** | **L**ine **S**pread Function |
| **ESF** | **E**dge **S**pread Function |
| **LVF** | **L**inear **V**ariable Filter |
| **PLD** | **P**ulsed **L**aser Diode |
| **OPO** | **O**ptical **P**arametric Oscillator |

# Chapter 1

# Introduction

The aim of this thesis is to explore and utilise the boundaries and capabilities of the two aforementioned modalities in order to develop imaging instruments that would revolutionize clinical diagnosis. Part of the results were published in [1–8].

In 1901, Wilhelm Conrad Rontgen, was awarded the Nobel Prize in Physics for the discovery of x-rays. This point in history can be marked as the birth of biomedical imaging [9, 10]. Both opto-acoustic imaging and Optical Coherence Tomography, are rapidly emerging biomedical imaging techniques.

Earlier in the 1880's, Alexander Graham Bell discovered the opto-acoustic effect [11], by observing that sound waves were generated by materials exposed to sunlight. Although the first results were poor, in the 1940's the opto-acoustic effect was used for gas detection by Tyndall and Rontgen using infrared rays [12, 13]. And then, in 1964, the opto-acoustic effect was used for a biomedical application on a living rabbit eye, using a ruby laser [14, 15]. Olsen et al. acquired 2-D images for the first time in 1982 [16, 17]. And only later, in 1994, Oraevsky et al. [18] and Kruger et al.[19] presented opto-acoustic images using pulsed lasers. According to the laser-based opto-acoustic technique used by Oraevsky and Kruger, a modulated optical source excites the sample and the emitted acoustic waves are detected to generate a three-dimensional image.

Optical Coherence Tomography (OCT) was invented in the 1990's, with the first *in-vivo* cross-sectional image of a human eye reported by Huang et al. (Prof.

Fujimoto's group) in 1991. [20].


FIGURE 1.1: Engraved brick marking a milestone in the history of the Applied Optics Group, University of Kent (https://research.kent.ac.uk/applied-optics/en-face-oct/first-en-face-oct-of-the-retina/). The brick can be found in the historic Crab and Winkle Path at University of Kent, commemorating one of the first British train lines.

OCT is based on scattering allowing for non-invasive imaging in depth. The first en-face OCT of the retina, was reported by Prof. Adrian Podoleanu (Applied Optics Group, University of Kent) in 1996 [21].

## 1.1 Project Motivation

The work presented in this thesis was motivated by the rapidly emerging interest in biomedical imaging throughout the past decades, especially regarding the advancements in medical diagnosis [22–26]. Multi-modal imaging instruments have been sought after as it imparts supplementary contrast from both tissue scattering (OCT) and absorption (Opto-acoustic imaging).

Both opto-acoustic imaging and optical coherence tomography offer volumetric images of tissue, with a field of view in the range off $mm^2$ and a depth of several $mm$. Dual-modality instruments, comprising of OCT and opto-acoustic imaging, have demonstrated results [27–35]. Often, a different optical source was employed for each modality, to accommodate the contrasting requirements of each technique. For example, opto-acoustic imaging requires a narrow spectral bandwidth to accurately target specific absorbers and short (<10 ns) pulses to achieve high signal to noise ratio (SNR) signals. To ensure effective differentiation of sequential acoustic waves due to the limitation of acoustic wave travel speed, it is imperative that the sources do not surpass a pulse repetition rate (PRR) of 2-3 MHz [36, 37]. Optical coherence tomography on the other hand, requires broadband or swept sources to achieve high axial resolution. Utilizing supercontinuum (SC) optical sources necessitates a pulse repetition rate (PRR) within the range of hundreds of megahertz to attain heightened detection sensitivity [38, 39]. This is essential due to the inherent relative intensity fluctuations found in supercontinuum sources. Increasing the repetition rate helps alleviate these fluctuations, leading to a smoother spectrum through averaging. Loewenstein demonstrated this phenomenon, showcasing that elevating the PRR by a factor N results in a reduction of relative intensity noise (RIN) by a factor of $\sqrt{N}$ [40].

Optical coherence tomography, a well-established diagnostic technique, is widely used to evaluate various retinal pathologies. Furthermore, its application is expanding towards the monitoring of skin lesions. This has increased the interest of clinicians for higher resolution, faster, cost effective and more versatile OCT systems.

Opto-acoustic imaging on the other hand, is now making its first steps in preclinical studies introducing a better resolution than ultrasound (by order of magnitudes), which is well established as an essential diagnostic instrument for various conditions. Moreover, opto-acoustic imaging introduces functional imaging

by exploiting the wavelength dependent absorption properties of common endogenous contrast agents such as haemoglobin, melanin, gelatin/collagen, glucose, lipids and more [31, 41–50]. Allowing for blood oxygen saturation measurements, melanin, gelatin/collagen, glucose and lipids spatial distribution [2].

A significant factor in reducing the cost of both instruments is the optical source. Supercontinuum sources for OCT, provide high PRR with a few ns pulse duration while delivering a very broad spectrum varying from 450 nm up to 2400 nm. The spectrum can be filtered using band-pass filters (BPF) for spectroscopic opto-acoustic microscopy (sp-OAM). The only commercially available SC source is the SuperK COMPACT which is seven times cheaper than other SC sources. This source was employed to perform multi-spectral opto-acoustic microscopy over the entire SC spectrum (from 475 nm up to 2000 nm) [2]. However, the COMPACT provides low energy per pulse (EPP) in the visible region (< 30 nJ below 550 nm) making OAM below 550 nm quite challenging. Opto-acoustic imaging requires over 50 nJ per pulse in order to acquire high SNR images [28, 51]. Furthermore, although 20 kHz PRR is sufficient for real-time *in-vivo* imaging, compensating the low SNR due to low EPP by averaging [38, 39] limits the imaging speed to the point where real-time imaging is not possible.

The work presented in this thesis is the endeavour to address these challenges and develop imaging instruments for biomedical applications.

## 1.2 Project Overview

This project was funded by the University of Kent via the Vice Chancellors Scholarships program. The experimental setup was based in the Canterbury campus of University of Kent, UK. All experiments were conducted in the University of Kent from September 2018 to November 2022. Part of the results were published in [1–8].

### 1.2.1 List of Journal Publications

1. **G. Nteroli** et al., “Enhanced resolution optoacoustic microscopy using a picosecond high repetition rate Q-switched microchip laser,” en, Journal of Biomedical Optics, vol. 27, no. 11, Nov. 2022, Accepted: 2022-11-04 Number: 11 Publisher: SPIE, ISSN: 1083-3668. [Online].
   Available: https://doi.org/10.1117/1.JBO.27.11.110501.

2. **G. Nteroli** et al., “Two octaves spanning photoacoustic microscopy,” en, Scientific Reports, vol. 12, Jun. 2022, Accepted: 2022-06-14 Publisher: Nature Research, ISSN: 2045-2322. [Online].
   Available: https://doi.org/10. 1038/s41598-022-14869-5.

3. **M. K. Dasa** and **G. Nteroli** et al., “All-fibre supercontinuum laser for in vivo multispectral photoacoustic microscopy of lipids in the extended near-infrared region,” en, Photoacoustics, vol. 18, p. 100 163, Jun. 2020, ISSN: 2213-5979. DOI: 10. 1016/j.pacs.2020.100163.

### 1.2.2 List of Peer review conference publications

1. **G. Nteroli**, Adrian Podoleanu, Adrian Bradu, "Combining photoacoustic and optical coherence tomography imaging for nondestructive testing applications," Proc. SPIE 12170, Advances in 3OM: Opto-Mechatronics, Opto-Mechanics, and Optical Metrology, 121700P (5 May 2022); doi: 10.1117/12.2626041.

2. Christa Serban, **Gianni Nteroli**, Emanuela L. Craciunescu, Meda L. Negrutiu, Helmine Serban, Virgil F. Duma, Adrian Bradu, Adrian Podoleanu, Cosmin Sinescu, "Methods of dental shade determination," Proc. SPIE 11942, Lasers in Dentistry XXVIII, 1194206 (4 March 2022); doi: 10.1117/12.2606721.

3. **G. Nteroli**, A. Bradu, and A. Podoleanu, "Chasing sub-micrometer axial resolution in Visible Optical Coherence Tomography," in European Conferences on Biomedical Optics 2021 (ECBO), OSA Technical Digest (Optica Publishing Group, 2021), paper EW4A.32.

4. Manoj Kumar Dasa, Kyei Kwarkye, **G. Nteroli**, Benjamin O. Efunbajo, Magalie Bondu, Getinet Woyessa, Niels M. Israelsen, Adrian Bradu, Christian R. Petersen, Peter M. Moselund, Patrick Bowen, Christos Markos, Ole Bang, "High-pulse energy supercontinuum sources for multi-spectral photoacoustic imaging in the near-infrared wavelength region (Conference Presentation)," Proc. SPIE 11234, Optical Biopsy XVIII: Toward Real-Time Spectroscopic Imaging and Diagnosis, 112340B (9 March 2020); https://doi.org/10.1117/12.2549947.

5. **G. Nteroli**, S. Koutsikou, P. Moselund, A. Podoleanu, and A. Bradu, "Real-time multimodal high resolution biomedical imaging instrument using supercontinuum optical sources," in Frontiers in Optics + Laser Science APS/DLS, OSA Technical Digest (Optica Publishing Group, 2019), paper JTu3A.99.

6. **G. Nteroli**, M. Bondu, P. M. Moselund, A. Podoleanu, and A. Bradu, "Developments on using supercontinuum sources for high resolution multi-imaging instruments for biomedical applications," in Clinical and Preclinical Optical Diagnostics II, Vol. EB101 of SPIE Proceedings (Optica Publishing Group, 2019), paper 11077 22.

## 1.3 Organization of the thesis

This thesis is structured in four parts. First, in Part 1, an introduction to the theoretical background required to understand the experimental work presented in Part 2. Finally, the publications in the scope of the thesis are listed in Part 3 as well as, appendices of external media used.

# References

[1] G. Nteroli *et al.*, "Enhanced resolution optoacoustic microscopy using a picosecond high repetition rate Q-switched microchip laser," en, *Journal of Biomedical Optics*, vol. 27, no. 11, Nov. 2022, Accepted: 2022-11-04 Number: 11 Publisher: SPIE, ISSN: 1083-3668. [Online]. Available: https://doi.org/10.1117/1.JBO.27.11.110501 (visited on 02/10/2023).

[2] G. Nteroli *et al.*, "Two octaves spanning photoacoustic microscopy," en, *Scientific Reports*, vol. 12, Jun. 2022, Accepted: 2022-06-14 Publisher: Nature Research, ISSN: 2045-2322. [Online]. Available: https://doi.org/10.1038/s41598-022-14869-5 (visited on 02/10/2023).

[3] M. K. Dasa *et al.*, "All-fibre supercontinuum laser for in vivo multispectral photoacoustic microscopy of lipids in the extended near-infrared region," en, *Photoacoustics*, vol. 18, p. 100 163, Jun. 2020, ISSN: 2213-5979. DOI: 10.1016/j.pacs.2020.100163. (visited on 03/09/2020).

[4] G. Nteroli, A. Podoleanu, and A. Bradu, "Combining photoacoustic and optical coherence tomography imaging for nondestructive testing applications," in *Advances in 3OM: Opto-Mechatronics, Opto-Mechanics, and Optical Metrology*, vol. 12170, SPIE, May 2022, pp. 212–217. DOI: 10.1117/12.2626041. [Online]. Available: https://www.spiedigitallibrary.org/conference-proceedings-of-spie/12170/121700P/Combining-photoacoustic-and-optical-coherence-tomography-imaging-for-nondestructive-testing/10.1117/12.2626041.full (visited on 02/15/2023).

[5] C. Serban *et al.*, "Methods of dental shade determination," in *Lasers in Dentistry XXVIII*, vol. 11942, SPIE, Mar. 2022, pp. 28–33. DOI: 10.1117/12.2606721. [Online]. Available: https://www.spiedigitallibrary.org/conference-proceedings-of-spie/11942/1194206/Methods-

of-dental-shade-determination/10.1117/12.2606721.full (visited on 02/15/2023).

[6] M. K. Dasa *et al.*, "High-pulse energy supercontinuum sources for multi-spectral photoacoustic imaging in the near-infrared wavelength region (Conference Presentation)," in *Optical Biopsy XVIII: Toward Real-Time Spectroscopic Imaging and Diagnosis*, vol. 11234, SPIE, Mar. 2020, 112340B. DOI: 10.1117/12.2549947. [Online]. Available: https://www.spiedigitallibrary.org/conference-proceedings-of-spie/11234/112340B/High-pulse-energy-supercontinuum-sources-for-multi-spectral-photoacoustic-imaging/10.1117/12.2549947.full (visited on 02/15/2023).

[7] G. Nteroli, S. Koutsikou, P. Moselund, A. Podoleanu, and A. Bradu, "Real-time multimodal high resolution biomedical imaging instrument using supercontinuum optical sources," EN, in *Frontiers in Optics + Laser Science APS/DLS (2019), paper JTu3A.99*, Optica Publishing Group, Sep. 2019, JTu3A.99. DOI: 10.1364/FIO.2019.JTu3A.99. [Online]. Available: https://opg.optica.org/abstract.cfm?uri=FiO-2019-JTu3A.99 (visited on 02/15/2023).

[8] G. Nteroli, M. Bondu, P. M. Moselund, A. Podoleanu, and A. Bradu, "Developments on using supercontinuum sources for high resolution multi-imaging instruments for biomedical applications," EN, in *Clinical and Preclinical Optical Diagnostics II (2019), paper 11077_22*, Optica Publishing Group, Jun. 2019, 11077_22. DOI: 10.1117/12.2527111. [Online]. Available: https://opg.optica.org/abstract.cfm?uri=ECBO-2019-11077_22 (visited on 02/15/2023).

[9] "On a New Kind of Rays," en, *Nature*, vol. 53, no. 1369, pp. 274–276, Jan. 1896, Number: 1369 Publisher: Nature Publishing Group, ISSN: 1476-4687.

DOI: 10.1038/053274b0. [Online]. Available: https://www.nature.com/articles/053274b0 (visited on 03/13/2023).

[10] *The Nobel Prize in Physics 1901*, en-US. [Online]. Available: https://www.nobelprize.org/prizes/physics/1901/summary/ (visited on 02/14/2023).

[11] A. G. Bell, "On the production and reproduction of sound by light," en, *American Journal of Science*, vol. s3-20, no. 118, pp. 305–324, Oct. 1880, Publisher: American Journal of Science Section: General geophysics, ISSN: 0002-9599, 1945-452X. DOI: 10.2475/ajs.s3-20.118.305. [Online]. Available: https://www.ajsonline.org/content/s3-20/118/305 (visited on 02/14/2023).

[12] A. H. Pfund, "Atmospheric Contamination," *Science*, vol. 90, no. 2336, pp. 326–327, Oct. 1939, Publisher: American Association for the Advancement of Science. DOI: 10.1126/science.90.2336.326. [Online]. Available: https://www.science.org/doi/10.1126/science.90.2336.326 (visited on 02/14/2023).

[13] M. Vengerov, "An Optical-Acoustic Method of Gas Analysis," en, *Nature*, vol. 158, no. 4001, pp. 28–29, Jul. 1946, Number: 4001 Publisher: Nature Publishing Group, ISSN: 1476-4687. DOI: 10.1038/158028c0. [Online]. Available: https://www.nature.com/articles/158028c0 (visited on 02/14/2023).

[14] L. Amar, M. Bruma, M. Velghe, and P. Desvignes, "On the detection of laser induced ultrasonic waves in the human eye and the elaboration of a theory on the fundamental mechanism of vision," en, *Journal of Applied Mathematics and Physics (ZAMP)*, vol. 16, no. 1, pp. 182–183, Jan. 1965, ISSN: 1420-9039. DOI: 10.1007/BF01589092. [Online]. Available: https://doi.org/10.1007/BF01589092 (visited on 02/14/2023).

[15] S. Manohar and D. Razansky, "Photoacoustics: A historical review," EN, *Adv. Opt. Photon., AOP*, vol. 8, no. 4, pp. 586–617, Dec. 2016, Publisher: Optica Publishing Group, ISSN: 1943-8206. DOI: 10.1364/AOP.8.000586. [Online]. Available: https://opg.optica.org/aop/abstract.cfm?uri=aop-8-4-586 (visited on 02/14/2023).

[16] R. G. Olsen, "Generation of Acoustical Images from the Absorption of Pulsed Microwave Energy," en, in *Acoustical Imaging*, ser. Acoustical Imaging, J. P. Powers, Ed., Boston, MA: Springer US, 1982, pp. 53–59, ISBN: 978-1-4684-1137-9. DOI: 10.1007/978-1-4684-1137-9_4. [Online]. Available: https://doi.org/10.1007/978-1-4684-1137-9_4 (visited on 02/09/2023).

[17] R. G. Olsen and J. C. Lin, "Acoustical imaging of a model of a human hand using pulsed microwave irradiation," en, *Bioelectromagnetics*, vol. 4, no. 4, pp. 397–400, 1983, _eprint: https://onlinelibrary.wiley.com/doi/pdf/10.1002/bem.225 ISSN: 1521-186X. DOI: 10.1002/bem.2250040410. [Online]. Available: https://onlinelibrary.wiley.com/doi/abs/10.1002/bem.2250040410 (visited on 02/14/2023).

[18] A. A. Oraevsky, S. L. Jacques, R. O. Esenaliev, and F. K. Tittel, "Laser-based optoacoustic imaging in biological tissues: Laser-Tissue Interaction V; and Ultraviolet Radiation Hazards 1994," *Proceedings of SPIE - The International Society for Optical Engineering*, vol. 2134, no. 1, pp. 122–128, Aug. 1994, ISSN: 0277-786X. DOI: 10.1117/12.182927. [Online]. Available: http://www.scopus.com/inward/record.url?scp=33744687561&partnerID=8YFLogxK (visited on 02/14/2023).

[19] R. A. Kruger, "Photoacoustic ultrasound," eng, *Med Phys*, vol. 21, no. 1, pp. 127–131, Jan. 1994, ISSN: 0094-2405. DOI: 10.1118/1.597367.

[20] D. Huang *et al.*, "Optical coherence tomography," *Science*, vol. 254, no. 5035, pp. 1178–1181, 1991, ISSN: 0036-8075. DOI: 10.1126/science.1957169.

[Online]. Available: http://www.scopus.com/inward/record.url?scp=0026254046&partnerID=8YFLogxK (visited on 02/10/2023).

[21] A. G. Podoleanu, G. M. Dobre, D. J. Webb, and D. A. Jackson, "Coherence imaging by use of a Newton rings sampling function," eng, *Optics Letters*, vol. 21, no. 21, pp. 1789–1791, Nov. 1996, ISSN: 0146-9592. DOI: 10.1364/ol.21.001789.

[22] R. Weissleder and M. Nahrendorf, "Advancing biomedical imaging," *Proceedings of the National Academy of Sciences*, vol. 112, no. 47, pp. 14 424–14 428, Nov. 2015, Publisher: Proceedings of the National Academy of Sciences. DOI: 10.1073/pnas.1508524112. [Online]. Available: https://www.pnas.org/doi/full/10.1073/pnas.1508524112 (visited on 03/14/2023).

[23] D. Das, A. Sharma, P. Rajendran, and M. Pramanik, "Another decade of photoacoustic imaging," en, *Phys. Med. Biol.*, vol. 66, no. 5, 05TR01, Oct. 2021, Publisher: IOP Publishing, ISSN: 0031-9155. DOI: 10.1088/1361-6560/abd669. [Online]. Available: https://dx.doi.org/10.1088/1361-6560/abd669 (visited on 03/14/2023).

[24] A. B. E. Attia *et al.*, "A review of clinical photoacoustic imaging: Current and future trends," en, *Photoacoustics*, vol. 16, p. 100 144, Dec. 2019, ISSN: 2213-5979. DOI: 10.1016/j.pacs.2019.100144. [Online]. Available: https://www.sciencedirect.com/science/article/pii/S2213597919300679 (visited on 03/14/2023).

[25] T. Zhao, A. E. Desjardins, S. Ourselin, T. Vercauteren, and W. Xia, "Minimally invasive photoacoustic imaging: Current status and future perspectives," en, *Photoacoustics*, vol. 16, p. 100 146, Dec. 2019, ISSN: 2213-5979. DOI: 10.1016/j.pacs.2019.100146. [Online]. Available: https://www.sciencedirect.com/science/article/pii/S2213597919300692 (visited on 03/14/2023).

[26] L. V. Wang, "Multiscale photoacoustic microscopy and computed tomography," *Nature photonics*, vol. 3, no. 9, pp. 503–509, Aug. 2009, ISSN: 1749-4885. DOI: 10.1038/nphoton.2009.157. [Online]. Available: https://www.ncbi.nlm.nih.gov/pmc/articles/PMC2802217/ (visited on 02/10/2023).

[27] L. Li, K. Maslov, G. Ku, and L. V. Wang, "Three-dimensional combined photoacoustic and optical coherence microscopy for in vivo microcirculation studies," EN, *Optics Express*, vol. 17, no. 19, pp. 16 450–16 455, Sep. 2009, Publisher: Optica Publishing Group, ISSN: 1094-4087. DOI: 10.1364/OE.17.016450. [Online]. Available: https://opg.optica.org/oe/abstract.cfm?uri=oe-17-19-16450 (visited on 02/09/2023).

[28] B. Rao, L. Li, K. Maslov, and L. V. Wang, "In vivo, dual-modality imaging of mouse eyes: Optical coherence tomography and photoacoustic microscopy within a single instrument," en, in F. Manns, P. G. Söderberg, and A. Ho, Eds., Issue: 7550 Number: 7550, Bellingham, WA: Society of Photo-Optical Instrumentation Engineers, Mar. 2010, Art. No. 75501Q, ISBN: 978-0-8194-7946-4. [Online]. Available: https://resolver.caltech.edu/CaltechAUTHORS:20180925-104554174 (visited on 02/10/2023).

[29] E. Z. Zhang *et al.*, "Multimodal photoacoustic and optical coherence tomography scanner using an all optical detection scheme for 3D morphological skin imaging," eng, *Biomedical Optics Express*, vol. 2, no. 8, pp. 2202–2215, Aug. 2011, ISSN: 2156-7085. DOI: 10.1364/BOE.2.002202.

[30] L. Xi, C. Duan, H. Xie, and H. Jiang, "Miniature probe combining optical-resolution photoacoustic microscopy and optical coherence tomography for in vivo microcirculation study," eng, *Applied Optics*, vol. 52, no. 9, pp. 1928–1931, Mar. 2013, ISSN: 1539-4522. DOI: 10.1364/AO.52.001928.

[31] S.-L. Chen, L. J. Guo, and X. Wang, "All-optical photoacoustic microscopy," en, *Photoacoustics*, vol. 3, no. 4, pp. 143–150, Dec. 2015, ISSN: 2213-5979. DOI:

10.1016/j.pacs.2015.11.001. [Online]. Available: https://www.sciencedirect.com/science/article/pii/S2213597915300069 (visited on 02/10/2023).

[32] R. Haindl *et al.*, "Dual modality reflection mode optical coherence and photoacoustic microscopy using an akinetic sensor," EN, *Optics Letters*, vol. 42, no. 21, pp. 4319–4322, Nov. 2017, Publisher: Optica Publishing Group, ISSN: 1539-4794. DOI: 10.1364/OL.42.004319. [Online]. Available: https://opg.optica.org/ol/abstract.cfm?uri=ol-42-21-4319 (visited on 02/09/2023).

[33] C. Lee *et al.*, "Combined photoacoustic and optical coherence tomography using a single near-infrared supercontinuum laser source," EN, *Appl. Opt., AO*, vol. 52, no. 9, pp. 1824–1828, Mar. 2013, Publisher: Optica Publishing Group, ISSN: 2155-3165. DOI: 10.1364/AO.52.001824. [Online]. Available: https://opg.optica.org/ao/abstract.cfm?uri=ao-52-9-1824 (visited on 02/14/2023).

[34] S. Jiao, Z. Xie, H. F. Zhang, and C. A. Puliafito, "Simultaneous multimodal imaging with integrated photoacoustic microscopy and optical coherence tomography," EN, *Opt. Lett., OL*, vol. 34, no. 19, pp. 2961–2963, Oct. 2009, Publisher: Optica Publishing Group, ISSN: 1539-4794. DOI: 10.1364/OL.34.002961. [Online]. Available: https://opg.optica.org/ol/abstract.cfm?uri=ol-34-19-2961 (visited on 02/14/2023).

[35] W. Song *et al.*, "A combined method to quantify the retinal metabolic rate of oxygen using photoacoustic ophthalmoscopy and optical coherence tomography," en, *Sci Rep*, vol. 4, no. 1, p. 6525, Oct. 2014, Number: 1 Publisher: Nature Publishing Group, ISSN: 2045-2322. DOI: 10.1038/srep06525. [Online]. Available: https://www.nature.com/articles/srep06525 (visited on 02/14/2023).

[36] C.-W. Wei *et al.*, "Real-time integrated photoacoustic and ultrasound (PAUS) imaging system to guide interventional procedures: Ex vivo study," eng, *IEEE Trans Ultrason Ferroelectr Freq Control*, vol. 62, no. 2, pp. 319–328, Feb. 2015, ISSN: 1525-8955. DOI: 10.1109/TUFFC.2014.006728.

[37] S.-W. Cho *et al.*, "High-speed photoacoustic microscopy: A review dedicated on light sources," en, *Photoacoustics*, vol. 24, p. 100 291, Dec. 2021, ISSN: 2213-5979. DOI: 10.1016/j.pacs.2021.100291. [Online]. Available: https://www.sciencedirect.com/science/article/pii/S2213597921000513 (visited on 02/15/2023).

[38] W. J. Brown, S. Kim, and A. Wax, "Noise Characterization of Supercontinuum Sources for Low Coherence Interferometry Applications," *J Opt Soc Am A Opt Image Sci Vis*, vol. 31, no. 12, pp. 2703–2710, Dec. 2014, ISSN: 1084-7529. [Online]. Available: https://www.ncbi.nlm.nih.gov/pmc/articles/PMC4457326/ (visited on 03/14/2023).

[39] M. Maria *et al.*, "Q-switch-pumped supercontinuum for ultra-high resolution optical coherence tomography," en, *Optics Letters*, vol. 42, no. 22, p. 4744, Nov. 2017, ISSN: 0146-9592, 1539-4794. DOI: 10.1364/OL.42.004744. (visited on 03/09/2020).

[40] E. B. Loewenstein, "Reducing the Effects of Noise in a Data Acquisition System by Averaging," en,

[41] J. Koo *et al.*, "In vivo non-ionizing photoacoustic mapping of sentinel lymph nodes and bladders with ICG-enhanced carbon nanotubes," en, *Phys. Med. Biol.*, vol. 57, no. 23, p. 7853, Aug. 2012, Publisher: IOP Publishing, ISSN: 0031-9155. DOI: 10.1088/0031-9155/57/23/7853. [Online]. Available: https://dx.doi.org/10.1088/0031-9155/57/23/7853 (visited on 02/14/2023).

[42] S. Zanganeh *et al.*, "Photoacoustic imaging enhanced by indocyanine green-conjugated single-wall carbon nanotubes," eng, *J Biomed Opt*, vol. 18, no. 9,

p. 096 006, Sep. 2013, ISSN: 1560-2281. DOI: 10.1117/1.JBO.18.9.096006.

[43] Z. Chen, S. Yang, Y. Wang, and D. Xing, "All-optically integrated photoacoustic microscopy and optical coherence tomography based on a single Michelson detector," EN, *Optics Letters*, vol. 40, no. 12, pp. 2838–2841, Jun. 2015, Publisher: Optica Publishing Group, ISSN: 1539-4794. DOI: 10.1364/OL.40.002838. [Online]. Available: https://opg.optica.org/ol/abstract.cfm?uri=ol-40-12-2838 (visited on 02/10/2023).

[44] K. Maslov, G. Stoica, and L. V. Wang, "In vivo dark-field reflection-mode photoacoustic microscopy," EN, *Optics Letters*, vol. 30, no. 6, pp. 625–627, Mar. 2005, Publisher: Optica Publishing Group, ISSN: 1539-4794. DOI: 10.1364/OL.30.000625. [Online]. Available: https://opg.optica.org/ol/abstract.cfm?uri=ol-30-6-625 (visited on 02/10/2023).

[45] Z. Xie, S. Jiao, H. F. Zhang, and C. A. Puliafito, "Laser-scanning optical-resolution photoacoustic microscopy," EN, *Optics Letters*, vol. 34, no. 12, pp. 1771–1773, Jun. 2009, Publisher: Optica Publishing Group, ISSN: 1539-4794. DOI: 10.1364/OL.34.001771. [Online]. Available: https://opg.optica.org/ol/abstract.cfm?uri=ol-34-12-1771 (visited on 02/10/2023).

[46] J. Yao, K. I. Maslov, E. R. Puckett, K. J. Rowland, B. W. Warner, and L. V. Wang, "Double-illumination photoacoustic microscopy," EN, *Optics Letters*, vol. 37, no. 4, pp. 659–661, Feb. 2012, Publisher: Optica Publishing Group, ISSN: 1539-4794. DOI: 10.1364/OL.37.000659. [Online]. Available: https://opg.optica.org/ol/abstract.cfm?uri=ol-37-4-659 (visited on 02/10/2023).

[47] W. Liu *et al.*, "In vivo corneal neovascularization imaging by optical-resolution photoacoustic microscopy," *Photoacoustics*, vol. 2, no. 2, pp. 81–86, Apr. 2014,

ISSN: 2213-5979. DOI: 10.1016/j.pacs.2014.04.003. [Online]. Available: https://www.ncbi.nlm.nih.gov/pmc/articles/PMC4083229/ (visited on 02/09/2023).

[48] R. Cao, J. P. Kilroy, B. Ning, T. Wang, J. A. Hossack, and S. Hu, "Multispectral photoacoustic microscopy based on an optical–acoustic objective," en, *Photoacoustics*, vol. 3, no. 2, pp. 55–59, Jun. 2015, ISSN: 2213-5979. DOI: 10.1016/j.pacs.2014.12.004. (visited on 03/09/2020).

[49] B. Dong *et al.*, "Isometric multimodal photoacoustic microscopy based on optically transparent micro-ring ultrasonic detection," EN, *Optica*, vol. 2, no. 2, pp. 169–176, Feb. 2015, Publisher: Optica Publishing Group, ISSN: 2334-2536. DOI: 10.1364/OPTICA.2.000169. [Online]. Available: https://opg.optica.org/optica/abstract.cfm?uri=optica-2-2-169 (visited on 02/10/2023).

[50] P. Hajireza, W. Shi, K. Bell, R. J. Paproski, and R. J. Zemp, "Non-interferometric photoacoustic remote sensing microscopy," en, *Light: Science & Applications*, vol. 6, no. 6, e16278–e16278, Jun. 2017, Number: 6 Publisher: Nature Publishing Group, ISSN: 2047-7538. DOI: 10.1038/lsa.2016.278. [Online]. Available: https://www.nature.com/articles/lsa2016278 (visited on 02/10/2023).

[51] T. Liu, Q. Wei, W. Song, J. M. Burke, S. Jiao, and H. F. Zhang, "Near-infrared light photoacoustic ophthalmoscopy," EN, *Biomedical Optics Express*, vol. 3, no. 4, pp. 792–799, Apr. 2012, Publisher: Optica Publishing Group, ISSN: 2156-7085. DOI: 10.1364/BOE.3.000792. [Online]. Available: https://opg.optica.org/boe/abstract.cfm?uri=boe-3-4-792 (visited on 02/10/2023).

# Part I

# Theory

# Chapter 2

# Theory and Methodology

Opto-acoustic microscopy and optical coherence tomography provide supplementary information about the sample. The opto-acoustic signal depends on the optical absorption properties of the sample whereas, OCT signal is dependent on the reflective profile of the sample. Both OAM and OCT enable non-invasive, volumetric (3-D) imaging with micrometer resolution at a depth range up to several millimetres and a field of view (FOV) of a few $mm^2$. In the following sections (2.2, 2.3), OAM and OCT working principles and supplementary theoretical background and methodologies are provided to aid in understanding the experimental work presented in chapters 3, 4, 5, and 6. Since the optical source is the most crucial sub-system for both modalities, the desired parameters of optical sources are presented for each modality.

## 2.1 Light-matter Interaction

Imaging contrast, particularly in optical techniques, is shaped by various factors, each contributing to the richness of visual information. Consider the scattering coefficient – a fundamental property dictating how light scatters in tissues. Tissues with a higher scattering coefficient, like certain cancerous tissues, exhibit increased light scattering, affecting the contrast between healthy and diseased areas. The wavelength of light is another crucial factor; for instance, near-infrared light penetrates deeper into tissues, providing enhanced contrast for imaging

structures below the surface. The microarchitecture of tissues, such as variations in cell density or the presence of blood vessels, introduces contrasts seen in imaging modalities like confocal microscopy or optical coherence tomography. Contrast agents, like fluorescent dyes targeting specific cellular components, can highlight structures for better visibility. Additionally, polarization-sensitive imaging can reveal details based on the orientation of tissue structures. Examples such as these showcase the nuanced interplay of factors influencing contrast in optical imaging, allowing researchers to tailor imaging systems for diverse applications, from cancer detection to studying cellular processes. Light directed to a sample can either be reflected, absorbed (and emitted), transmitted, or scattered. Fig. 2.1 depicts these processes.

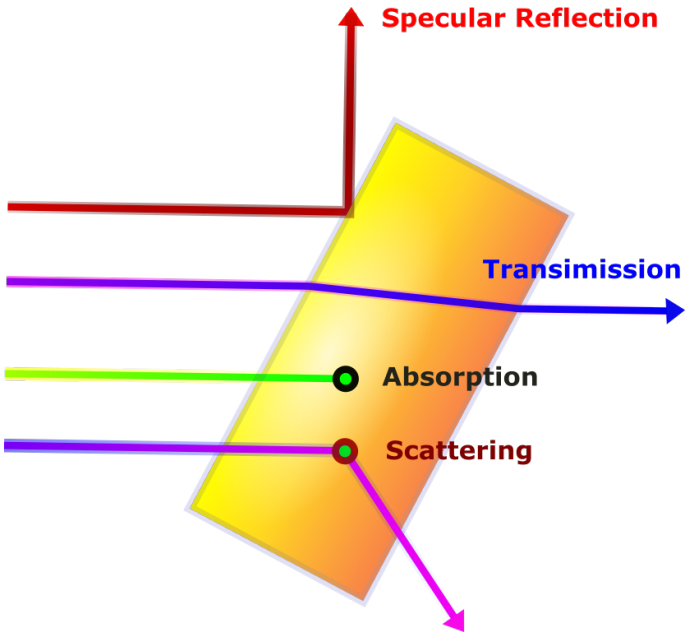


FIGURE 2.1: Main light-matter interactions.

Photoacoustic imaging is a powerful hybrid modality that integrates optical and ultrasound imaging, providing comprehensive insights into tissue composition, structure, and function. Contrast in this imaging technique originates from diverse sources, such as absorption differences in various tissue components like hemoglobin and melanin. The use of exogenous contrast agents, engineered for targeted applications, enhances molecular-level imaging, facilitating studies in

areas like drug delivery. Additionally, variations in tissue density and composition contribute to contrast, enabling visualization of tissue boundaries and interfaces. Temperature-dependent contrast, influenced by temperature variations in tissues, holds promise for applications in thermal therapies and hyperthermia treatment. The conversion of optical energy to acoustic waves, a fundamental process in photoacoustic imaging, is influenced by factors like the absorption coefficient, laser pulse duration, optical absorption wavelength, fluence level, acoustic detection sensitivity, tissue optical properties, spatial resolution, and repetition rate of laser pulses. These factors collectively contribute to the efficiency and sensitivity of photoacoustic imaging, allowing for detailed visualization of biological tissues at different depths and resolutions.

When light (visible - infrared) is absorbed by the sample, the photon's energy can be absorbed by atoms or by molecules resulting in molecular vibrations, rotations, and torsion. This causes lower energy photon emission (spontaneous emission) and thermal energy to dissipate in the sample. For OAM, the thermal energy created during absorption, results in the thermal expansion of the molecules. During the relaxation of which, acoustic waves are generated and propagate as spherical sound waves. The acoustic waves are detected to map the structural morphology of the sample.

The transmission ($T$) of light through a medium of thickness $d$ and absorption coefficient $a$ ($1$ / $cm$) is expressed as:

$$T = e^{-ad} \tag{2.1}$$

When light is scattered by a medium, its trajectory changes. There are three scattering models for low energy (< $2\ eV$) photons [1]. When the size of the particles is much greater than the light wavelength ($\lambda$), geometric scattering occurs and the phenomena are described by geometric optics laws. When particles are much smaller than the light wavelength, the losses introduced by the scattered

light follow a $1/\lambda^4$ trend and it's defined as Rayleigh scattering. Finally, when the size of the particles is comparable to the light wavelength, it's defined as Mie scattering. In organic tissues, the predominant light scattering mechanism is often characterized by anisotropic scattering. Anisotropic scattering occurs when incident light encounters variations in refractive index within tissues, such as cellular structures and organelles, leading to directional changes in the light path. This mechanism is particularly relevant due to the complex and heterogeneous nature of biological tissues, where the sizes and shapes of cellular components influence the scattering behaviour. While anisotropic scattering is a key component, it coexists with other scattering mechanisms such as Rayleigh scattering and Mie scattering. Rayleigh scattering dominates when the size of scattering particles is much smaller than the wavelength of light, whereas Mie scattering becomes more relevant when the size of the scattering structures is comparable to or larger than the wavelength of light. Although, Mie scattering exhibits strong forward propagation, the remaining percentage of light back-scattered by tissue is enough to be detected with OCT. Both OAM and OCT utilise minimally scattered ballistic photons for optical microscopy. Ballistic photons are photons that travel through media in straight trajectories. The range of the trajectory of such photons is limited by the optical diffusion limit ($\approx mm$).

## 2.2 Opto-acoustic Microscopy

The working principle behind opto-acoustic microscopy is presented in this section to help understand the experimental work reported in chapters 3, 4, and 5. The definitions of lateral and axial resolution for OAM are presented in section 2.2.2. Section 2.2.3 explores other detection system technologies reported so far, followed by the description of the ultrasound wave detection system and signal processing developed for the experimental work in this thesis. Supplementary information on the detection system modifications to facilitate each experiment

is provided in each respective chapter. In section 2.2.5, the parameters of the optical source required for OAM are discussed. Section 2.2.6, provides an overview of the noise properties of OAM. Finally, the functional capabilities of OAM systems are presented in section 2.2.7.

### 2.2.1 OAM working Principle

Opto-acoustic imaging (also found in the literature as Photoacoustic imaging) is an emerging Biomedical imaging modality based on a laser-excited ultrasound. Opto-acoustic imaging incorporates both the high contrast and spectroscopic-based specificity of optical imaging and the high spatial resolution of ultrasound imaging. An opto-acoustic image is essentially an ultrasound image, the contrast of which is proportional to the optical properties of the tissue and not the mechanical and elastic properties of the tissue. Thus, opto-acoustic imaging provides higher specificity than ultrasound imaging while enabling the detection of haemoglobin, melanin, gelatin/collagen, glucose, lipids, and other light-absorbing chromophores. Although opto-acoustic imaging has a lower range of depth than ultrasound imaging, opto-acoustic imaging has a higher depth penetration than purely optical imaging modalities (e.g. OCT) that rely on ballistic photons. Besides structural information, opto-acoustic imaging enables the acquisition of functional information in the form of blood oxygen saturation, blood flow, and temperature measurements [2].

By irradiating the tissue with low-energy ($\approx$ 50 to 500 nJ per pulse) modulated electromagnetic radiation, usually pulsed on a nanosecond time scale, acoustic waves (ultrasound) are emitted [2–4]. The absorption of the optical energy by specific endogenous tissue chromophores is followed by rapid conversion to heat with a temperature rise of approximately 0.1 K and a pressure increase of about 10 kPa. The relaxation of the pressure results in the emission of MHz low amplitude acoustic waves. These waves propagate through the tissue and are detected by an ultrasound transducer or an array of transducers to acquire the acoustic

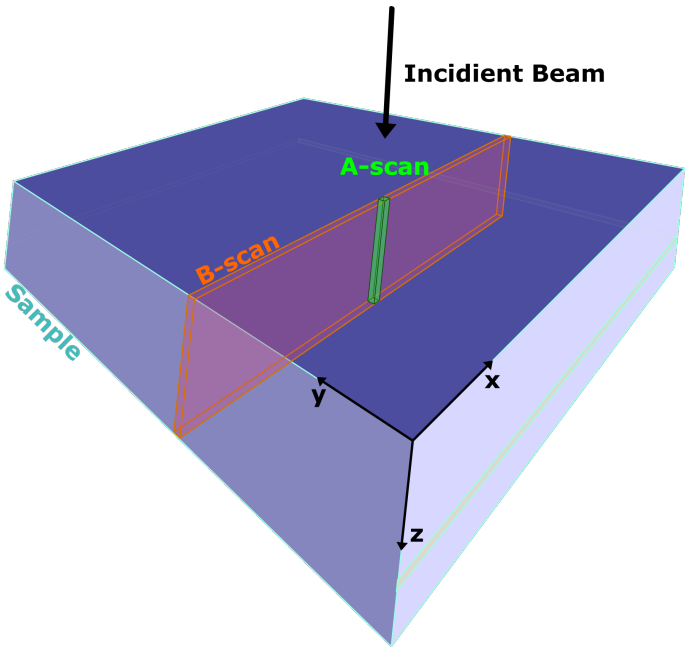


FIGURE 2.2: Schematic representation of the definition of an *A-scan* and a *B-scan*

signals. These signals give information on the amplitude of the acoustic waves as a function of time. The envelope of these signals is calculated by a Hilbert transform to form an *A-scan*. As the speed of sound is well known, the position of the initial pressure can be calculated to form an image of amplitude versus axial distance (*A-scan* definition) [2].

The studies conducted for the compilation of this thesis, are based on optical resolution opto-acoustic microscopy (OR-OAM), where the optical excitation is tightly focused on a small region of the sample. The optical spot is scanned through the area of interest (with a pair of galvanometric mirrors), acquiring *A-scans*. Another method is to have the beam fixed in a specific point and move the sample instead. *A-scans* are generated from the acoustic waves detected at each scanning point and contain the depth (z) resolved absorption profile of the sample at a specific point. The collection of *A-scans* in one direction forms a two-dimensional image named *B-scan* and represents a cross-sectional image of the sample (x,z). By also scanning the focal point perpendicularly (y) to the x-axis, a three-dimensional (x,y,z) image can be formed.

### 2.2.2 Resolution in Opto-acoustic Microscopy

Opto-acoustic Microscopy can be distinguished between two categories, depending on whether the optical beam or the acoustic detection is focused (Fig. 2.3). In the context of acoustic resolution opto-acoustic microscopy (AR-OAM), a focused ultrasound transducer is employed while the optical components are not subjected to tight focusing. Therefore, the lateral resolution for AR-OAM is defined by the focal size and the central frequency of the detection system. AR-OAM can achieve a lateral resolution of tens of micrometers and has the advantage of a higher range of depth since ultrasonic acoustic waves can propagate deeper in the tissue than ballistic photons.

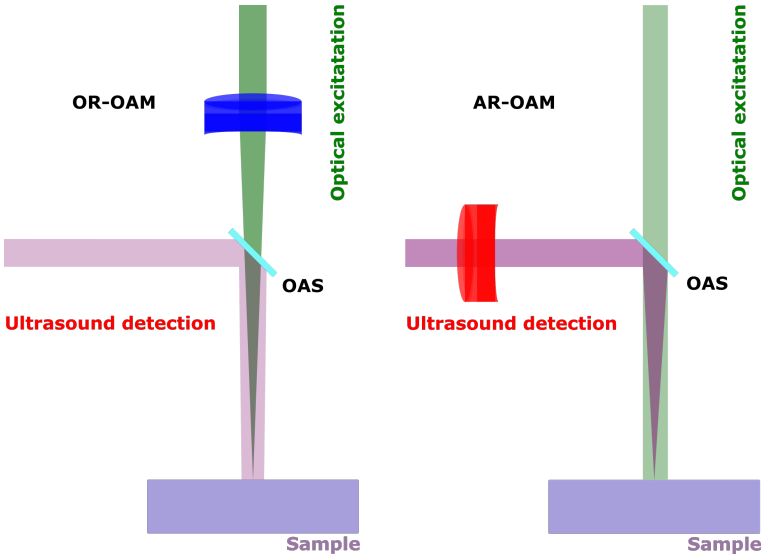


FIGURE 2.3: Explanatory schematic diagram illustrating OR-OAM and AR-OAM configurations. In OR-OAM the Optical excitation beam (green) is focused on the sample, while the ultrasound waves are reflected towards an unfocused ultrasound traducer through a opto-acoustic splitter (OAS). Whereas in AR-OAM a focused ultrasound transducer is employed while the optical beam is not focused.

Optical resolution opto-acoustic microscopy can achieve sub-micron lateral resolution with the expense of depth penetration limited to a few millimetres. The axial resolution for both AR-OAM and OR-OAM is defined mainly by the detection bandwidth of the transducer and is described by [5, 6]:

$$\delta z = 0.88\frac{u_s}{\delta f} \tag{2.2}$$

where $u_s$ is the speed of sound in the medium and $\delta f$ is the frequency bandwidth of the detected acoustic signal.

For AR-OAM, the lateral resolution is defined by the acoustic focal spot and the central frequency of the ultrasound transducer and is expressed by [5, 6]:

$$\delta x_{AR-OAM} = 0.71\frac{u_s}{f_0 NA_0} \tag{2.3}$$

where $f_0$ is the central frequency of the detected opto-acoustic wave, $NA_0$ the numerical aperture of the ultrasound transducer and $u_s$ is the speed of sound ( $1480\ m/s$ in biological tissue). These parameters are defined by the design of the ultrasound transducer and can achieve a lateral resolution of about 50 $\mu m$. Although 50 $\mu m$ is much better than the resolution of ultrasound imaging, such resolution is not sufficient to describe cellular structures that can vary from submicron to 10 $\mu m$ in size. A higher detection frequency can be used to enhance the lateral resolution of AR-OAM, however with the expense of depth penetration. This trade-off makes OR-OAM more desirable, since OR-OAM can achieve high lateral resolution without sacrificing the imaging depth.

For OR-OAM, the lateral resolution is defined by the central wavelength of the optical source and the numerical aperture of the objective lens and is given by [5, 6]:

$$\delta x_{OR-OAM} = 0.51\frac{\lambda_0}{NA} \tag{2.4}$$

where $\lambda_0$ is the optical excitation central wavelength and NA is the numerical aperture of the objective lens used to focus the beam on the sample. OR-OAM has the potential to achieve sub-micron lateral resolution with a range of depth of a few millimetres, which is why OR-OAM was chosen for the studies presented in this thesis. Opto-acoustic microscopy's limitations in terms of spatial resolution

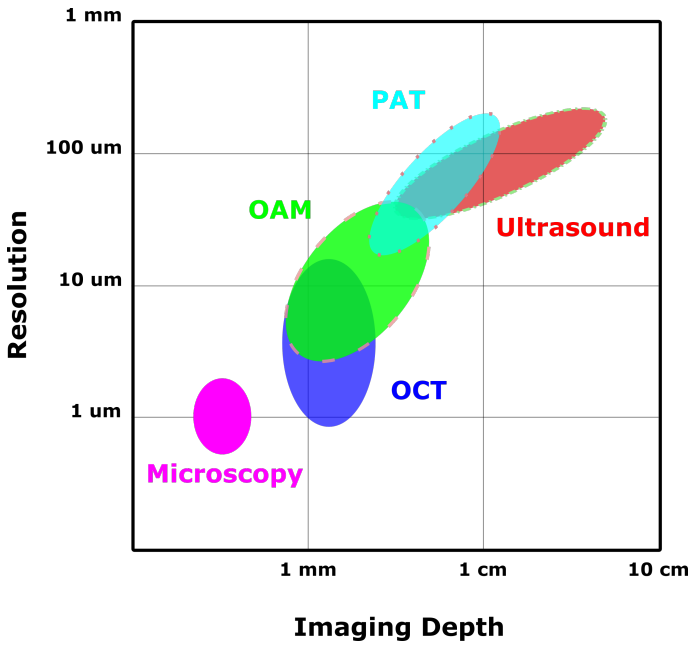


FIGURE 2.4: A Comparison of relevant imaging techniques in terms of resolution and imaging depth. Adapted from [7]

and range of depth are determined by the ultrasound detection system and the optical source.

To improve the axial resolution, a high frequency ultrasound transducer can be employed. However, higher frequency acoustic waves exhibit higher attenuation by the medium, limiting the penetration depth. For example, according to Eq. 2.2, using a 100 MHz ultrasound transducer, an axial resolution of 13 $\mu m$ with a depth range below 1 mm can be obtained. Using more power on the sample can enhance slightly the penetration depth as long as the power limitations dictated by the ANSI standards for each type of tissue are maintained.

### 2.2.3 OAM Detection System

The central frequency and bandwidth of the ultrasound transducer are the most important parameters of an OAM detection system. To minimize the losses, a

medium between the sample and the ultrasound transducer is necessary to compensate for the impedance mismatch in the boundaries and maximize wave propagation instead of reflection. Therefore, coupling the acoustic waves to the ultrasound transducer requires a specific configuration.

The most popular ultrasound transducers are piezoelectric transducers such as polyvinylidene fluoride transducers (PVDF) with central frequencies of tens of MHz [8–16]. The bandwidth of the transducer defines the axial resolution of the OAM system (Eq. 2.2) and is typically in the tens of MHz. Both ultrasonic gel and water can be used to couple the acoustic waves to the detector as their acoustic impedance is very similar to the impedance of biological tissues. Ultrasound transducers are either unfocused or focused with a specific focal length (typically a few millimetres). As the numerical aperture of the transducer depends on the lateral size of the transducer and its focal length, these parameters define the lateral resolution AR-OAM.

In this thesis, both unfocused and focused ultrasound transducers were employed, as unfocused transducers are easier to implement whereas focused transducers sacrifice the field of view to achieve higher detection sensitivity. All experiments were conducted in transmission mode for easier implementation and to avoid the effects of light travelling through the coupling medium (water, ultrasound gel).

Transmission mode is convenient when imaging very thin samples, thus more suitable for proof of concept studies. However, for imaging thick and large samples, reflection mode is mandatory. The technical data of the ultrasound transducers used in this thesis are presented in the appendix.

Fabry Perot interferometers allow for larger detection bandwidth and a larger field of view. Fabry Perot interferometers are made of thick parylene polymer film ultrasound sensors in contact with the sample [17–21]. As the polymer film is transparent from 590 - 1200 nm, the excitation beam propagates through the sensor to the sample. The ultrasound waves emitted by the sample reach the

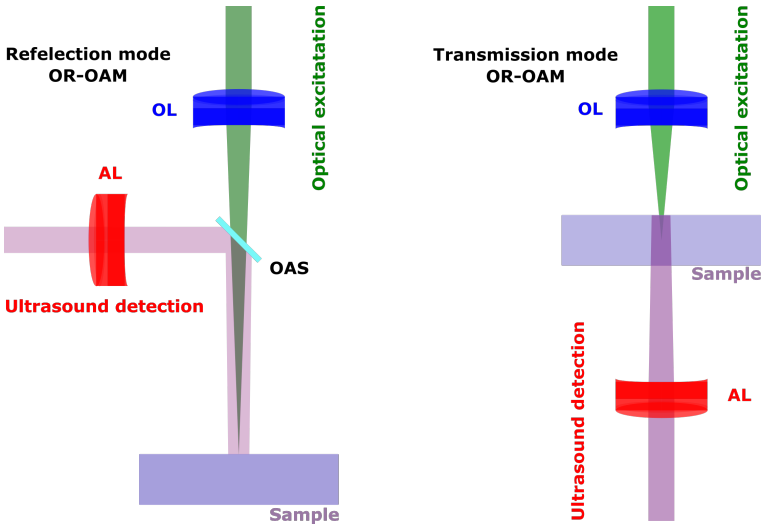


FIGURE 2.5: Explanatory schematic diagram illustrating Reflection mode and Transmission mode OR-OAM configurations. In reflection mode OR-OAM, the incident laser beam (green) is in the same plane with emitted acoustic wave (magenta). The same plane configuration can be implemented either by using a opto-acoustic splitter (OAS) or by placing the ultrasound transducer at an angle. In transmission mode OR-OAM, The incident excitation beam is in the opposite plane of the emitted acoustic wave. AL: acoustic lens; OL: Optic lens.

sensor, modulating the optical thickness of the Fabry Perot interferometer. Using a reference beam at 1550 nm for example, the optical thickness changes can be detected to measure the strength of the acoustic waves. Using a Fabry Perot ultrasound detection system, a better axial and lateral resolution can be achieved when compared to piezoelectric ultrasound transducers.

Another promising OAM detection system comprises the use of micro-ring resonator-based ultrasound detectors [22–25]. These ultrasound detectors are composed of tightly spaced bus and ring wave-guides. The acoustic waves excite the ring wave-guides affecting the refractive index of the wave-guide medium, as well as the ring size. This process affects the resonant frequency of the micro-ring resonator-based ultrasonic detector and is detected by the modulated optical signal propagating through the bus wave-guide. Broader bandwidth can be achieved with this method enhancing both the axial and the lateral resolution of the OAM system.

Acoustic waves can also be detected indirectly with low-coherence interferometers, having the advantage of being non-contact. This facilitates the integration within an OCT system with either a Michelson interferometer [26, 27] or a Mach Zehnder interferometer [28]. All-optical ultrasound detection systems have been developed based on polarization-dependent optical reflection sensing [29] and on opto-acoustic remote sensing [30].

The challenging configuration and integration of the ultrasound transducer into a microscope set-up as well as the increasing attenuation of the acoustic waves at higher frequencies constitute the main detection limitations in OAM. In order to tackle this limitation, a higher energy per pulse (EPP) optical source can be employed, as long as the AS/NZS standards regarding the radiation limits for each sample are maintained. Another method, developed during the studies reported in this thesis (chapter 5), is to exploit the properties of shorter pulse (picosecond) optical sources. With shorter pulses of similar energy per pulse, the same energy is delivered over a shorter period of time, resulting in broader and higher amplitude acoustic waves [31–33], improving the axial resolution (by up to 50%) for both OR-OAM and AR-OAM and the lateral resolution of AR-OAM.

### 2.2.4 OAM Signal Processing

For OAM, piezoelectric ultrasound transducers are used to acquire acoustic signals as a function of time. By calculating the envelope of a temporal signal (the detected acoustic signal) and multiplying it with the speed of sound ($u_s$), the corresponding *A-scan* can be generated. The envelope of the acquired signal can be obtained by performing a Hilbert transform on the acoustic signal. Scanning the optical beam laterally (in the x-direction) a *B-scan* can be formed as a collection of consecutive *A-scan*. A *B-scan* is the equivalent of a cross-sectional (x,z) image. The representation of an *A-scan* and a *B-scan* is depicted in Fig. 2.6. Volumetric (x,y,z) images can be formed by also scanning in the y-direction. *En-face* z-projected images can be presented by z-projecting a collection of *en-face* images either with a

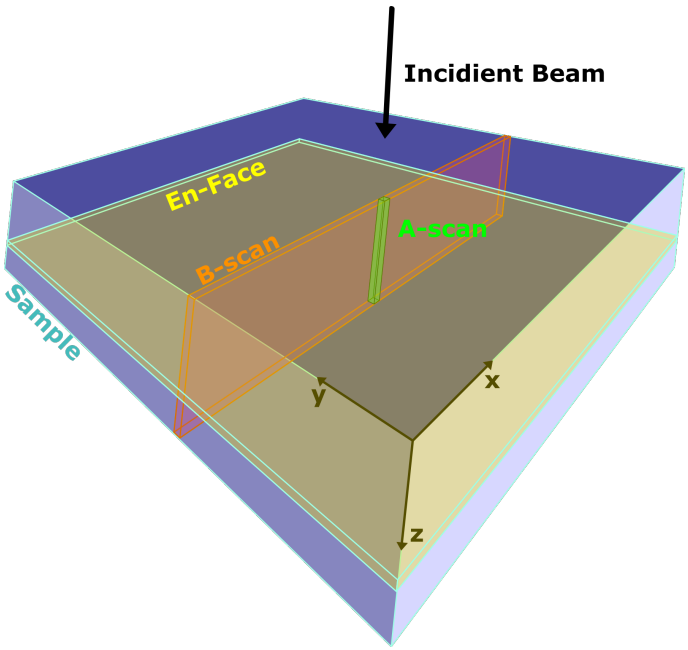


FIGURE 2.6: Slicing of an acquired volume and the representations of *A-scan*, *B-scan*, and MAP images. The projection of several images in the z direction forming 2D (x,y) images (*En-face* images) form a maximum amplitude projection (MAP) image. In this thesis, average amplitude projections are referred to as MAPs for simplicity.

maximum amplitude projection (MAP) or with an average amplitude projection. Both methods are referred to as MAPs for simplicity of abbreviations, besides the fact that in this thesis, the average amplitude projection is preferred. A maximum amplitude projection is a summation of the signal's amplitudes which can easily result in the saturation of an 8-bit image, whereas an average amplitude projection image is an average of the signal's amplitude, thus the SNR of the image is improved without exceeding the amplitude saturation limits of the image.

The following example is presented for a deeper understanding of how an *A-scan* can be obtained. A virtual OAM signal of a sample is presented in Fig. 2.7. By performing a Hilbert transform on the signal, an *A-scan* can be obtained. The acquisition of the OAM signal is synchronized with the trigger of the optical source. An *A-scan* is acquired for each pulse, thus the time interval between two consecutive *A-scans* is the pulse repetition rate (PRR) of the optical source. Although the initial pressure is generated in synchronization with the trigger, a time delay ($z/u_s$) can be observed (Fig. 2.7). This time delay corresponds to the

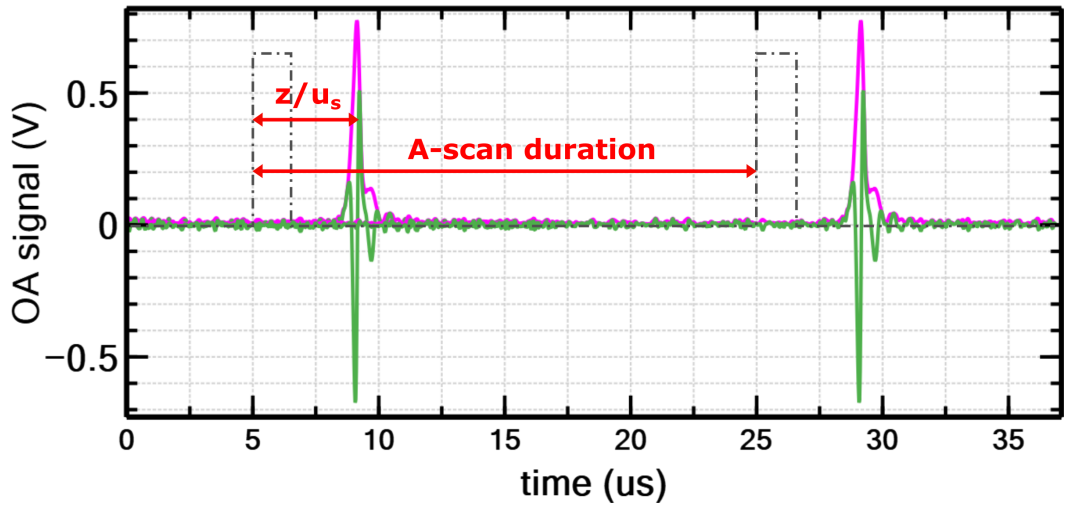


FIGURE 2.7: Typical OAM signals (Green) and the Hilbert transform of the signals (Magenta) forming consecutive *A-scans*. The rising edge of the TTL trigger signal (grey) dictates the time the initial pressure is generated. The acoustic pulse then travels through the sample and the coupling medium to reach the ultrasound transducer. Since the transducer is positioned about 8 mm from the sample, the time delay between the trigger and the acoustic pulse is about 5.5 $\mu s$.

propagation (at speed of sound $u_S$) time of the acoustic wave from the position of the initial pressure to the detector. This specific characteristic limits the OAM speed to a few MHZ of PRR; after that limit, two consecutive *A-scans* start overlapping. As the time scale in depth is measured, multiplying the time values with the speed of sound ($u_S$), the distance between two consecutive *A-scans* can be determined.

### 2.2.5 Optical Source parameters for OAM

The desired parameters of the optical source for OAM will be examined in this section. The most important parameters of the optical source regarding OAM, are the following:

1. the central wavelength,
2. the spectral bandwidth,
3. the duration of the excitation pulse,

4. the PRR of the optical source,

5. and the energy per pulse.

#### 2.2.5.1 Spectral properties of Optical Sources for OAM

The contrast of OAM is based on the absorption of the optical energy by endogenous tissue chromophores. The absorption coefficient of such chromophores is presented in Fig. 2.9 as a function of wavelengths. Hence, the central wavelength of the optical source is of paramount importance to target specific chromophores. One method to distinguish chromophores in the same sample, includes the extraction of the absorption coefficient of each chromophore, by performing spectroscopic OAM (sp-OAM). More precisely, OAM is performed in a very narrow spectral window ($< 5\ nm$) over multiple steps (in wavelength). This is however very challenging, as the energy density of broadband sources limits the available energy when narrow spectral windows are introduced. It is impossible to perform sp-OAM with single-wavelength optical sources since sp-OAM requires fine steps over a certain spectral range. Several groups have demonstrated the mapping of one or two chromophores at the same time using a limited spectral bandwidth [8, 34–37]. In this thesis (chapter 4), a novel technique to map five endogenous chromophores was developed by performing OAM over a very broad spectral range, spanning from 475 nm up to 2000 nm [38]. The theoretical background of which is presented in section 2.2.7.

#### 2.2.5.2 Pulse duration of Optical Sources for OAM

Thermal and stress confinement are essential for the occurrence of the opto-acoustic effect when a modulated laser beam is focused on the region of interest of the sample. Thermal and stress confinement ensures that thermal diffusion and the volume expansion of the absorber are negligible, respectively. This can be achieved

by selecting a pulse duration much shorter than the time scale of the heat dissipation of the absorbed optical energy by thermal conduction ($\tau_{th}$) and much shorter than the time for the generated acoustic wave to cross the heated region ($\tau_s$). Thermal and stress confinement margins can be expressed as [39, 40]:

$$\tau_{th} \approx \frac{L_d^2}{4D_{th}} \quad \text{and} \quad \tau_s \approx \frac{L_d}{u_s} \tag{2.5}$$

where $L_d$ is the spatial resolution, $D_{th}$ the thermal diffusivity of the tissue ( $\approx 0,15mm^2/s$ for soft tissues) and $u_s$ the speed of sound in the sample. According to the latest reports, OAM can achieve an axial resolution varying from 10 to 50 $\mu m$. A pulse duration below 10 ns should be selected to achieve such a resolution. In fact, by selecting a much shorter (picosecond) pulse duration, the axial resolution of OAM can be enhanced by 50 $\%$ [31], in comparison to the achievable axial resolution when employing the commonly used nanosecond pulse duration optical sources.

#### 2.2.5.3 Pulse repetition rate of Optical Sources for OAM

The piezoelectric ultrasound transducer converts the pressure from the acoustic waves into electrical signals. The acquisition is in a fixed delay synchronization with the source trigger. This delay corresponds to the moment the acoustic wave is generated, to the moment the acoustic wave arrives (at speed of sound) at the ultrasound transducer, plus the time the electrical signal travels through the coaxial cables to the low-noise amplifiers, and finally to the data acquisition card. Thus, to avoid the overlapping of two consecutive acoustic pulses, the time between two consecutive pulses has to be below the fraction of the maximum imaging depth ($\Delta z_{max}$) over the speed of sound ($u_s$). Thus,

$$PRR_{max} = \frac{u_s}{\Delta z_{max}} \tag{2.6}$$

where $PRR_{max}$ is the highest pulse repetition rate of the optical sources for a total imaging depth of $\Delta z_{max}$, and $u_s$ is the speed of sound in tissue (1480 m/s). The most commonly used ultrasound transducers for OAM have a central frequency varying from 20 to 100 MHz. Due to the attenuation of the propagating acoustic wave at these frequencies, the range of depth is limited to 1 mm. Thus, a total imaging depth of 1 mm limits the selection of the optical source to PRR below 1.5 MHz. This limits the imaging speed, especially in OAM, since averaging from tens to hundreds of times is necessary to achieve a sufficient signal-to-noise ratio (SNR). As a consequence, *in-vivo* OAM imagining is very challenging. The fastest OAM was recently reported by Allen et al. with an OR-OAM system, using a master oscillator power amplifier (MOPA) fiber laser with a PRR of 2 MHz.

#### 2.2.5.4 Energy per pulse of Optical Sources for OAM and maximum permissible exposure

All experiments have been in-line with the maximum permissible exposure (MPE) limits for human skin, according to **IEC 60825-1 Ed. 3.0 (2014)**. These standards are used as safety guidelines for laser products in Europe and various other countries.

The MPE of all samples used during the experiments in this thesis is considered the MPE of human skin. The broadband sources employed for the imaging systems reported in this thesis, exhibit very low EPP, Thus, the energy of the optical sources was well below the MPE for human skin. The MPE for human skin, for a single, nanosecond pulse is a function of pulse duration and wavelength:

$$MPE_{single,skin} = 200 \times C_4 \quad \frac{J}{m^2} \tag{2.7}$$

where $MPE_{single,skin}$ is the MPE for a single pulse and:

- $C_4$ = 1 for t = $10^{-9}$ to $10^{-7}$ and $\lambda$ = 400 to 700 nm,
- $C_4$ = $10^{0.002(\lambda-700)}$ for t = $10^{-9}$ to $10^{-7}$ and $\lambda$ = 700 to 1400 nm,

- $C_4$ = 5 for t = $10^{-9}$ to $10^{-7}$ and $\lambda$ = 1400 to 1500 nm,
- $C_4$ = 50 for t = $10^{-9}$ to $10^{-7}$ and $\lambda$ = 1500 to 1800 nm,
- $C_4$ = 5 for t = $10^{-9}$ to $10^{-7}$ and $\lambda$ = 1800 to 2600 nm,

For multiple pulses, the MPE values are given by:

$$MPE_{train} = MPE_{single,skin} \times C_5 \tag{2.8}$$

where $MPE_{train}$ is the total MPE of the pulse train, $MPE_{single,skin}$ is the MPE for a single pulse, and $C_5$ = 1, for a maximum exposure duration larger than 0.25 s and N $\leq$ 600. Where $N$ is the total number of pulses. During the experiments conducted for the compilation of this thesis, the sample was scanned laterally for imaging averaging up to 32 times. Thus, $N$ was always $\leq$ 600 and $C_5$ = 1. As such:

$$MPE_{train} = MPE_{single,skin} \tag{2.9}$$

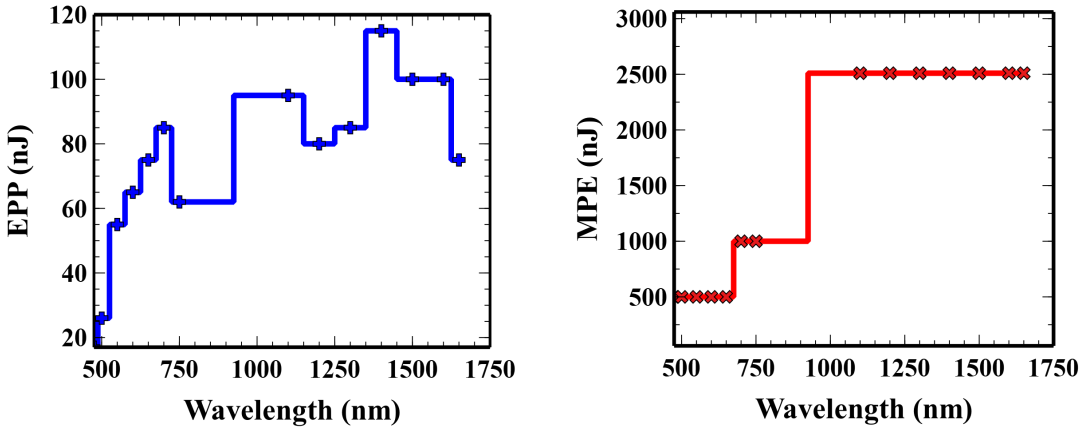


FIGURE 2.8: EPP on the sample measured over the entire emission range of the SC optical source using 25 nm bandwidth hard-coated bandpass filters, and the respective MPE according to **IEC 60825-1, Ed. 3.0 (2014)**.

To conclude, the MPE for imaging human skin depends on the central wavelength of the optical source, the duration, the number of pulses, and the beam size. The typical lateral resolution for OAM is about 5 $\mu m$. As the confocal plane

is placed in a depth of 200 to 400 $\mu m$ below the skin surface, the beam diameter at the surface of the skin is larger than 20 $\mu m$. The MPE values presented in Fig. 2.8 have been calculated for a beam diameter of 20 $\mu m$ at the surface of the skin according to **IEC 60825-1, Ed. 3.0 (2014)**, Safety of laser products (Appendix). The optical sources employed had a PRR of at least 20 kHz and nanosecond pulse duration sources, apart from the picosecond pulse duration case study presented in chapter 5. The EPP of the sources used are also presented in Fig. 2.8 to provide an overview in comparison to the MPE for human skin.

### 2.2.6 Sensitivity in OAM

In OAM, optical energy is absorbed by tissue and converted to thermal energy by molecular vibration, rotation, and torsion. Sequentially, thermal energy is converted to mechanical energy via thermoelastic expansion, and then the mechanical energy is converted to electrical energy via the piezoelectric effect by the ultrasound transducer [41, 42]. For each energy conversion phase, the conversion efficiency is limited whereas noise is present. As such, the main sources of noise in OAM are [43]:

- the noise of the optical source,
- the thermal acoustic noise of the medium,
- the thermal noise of the ultrasound transducer,
- the electronic noise of the signal amplification system

The aforementioned sources of noise affect the signal quality of the OAM by reducing the signal-to-noise ratio (SNR). By definition, SNR can be calculated using:

$$SNR = 20log_{10}\frac{S_{max}}{N_{std}} \tag{2.10}$$

where $S_{max}$ is the highest value of signal amplitude and $N_{std}$ is the standard deviation of the signal's noise floor. The contributions to the noise of the optical source arise mainly from the power amplitude fluctuations. This noise is defined as the relative intensity noise (RIN), expressed by:

$$RIN = \frac{P_{std}}{P_{average}} \tag{2.11}$$

where $P_{std}$ is the standard deviation of the power of the optical source and $P_{average}$ is the average power. A popular technique to improve the SNR is to average several *A-scans*. This commonly used method, however, reduces significantly the imaging speed.

### 2.2.7 Multi-spectral Opto-acoustic Microscopy (MS-OAM)

At first, Nd:YAG Q-switched optical sources were employed for Opto-acoustic imaging, either with a central wavelength at 1064 nm [13] or a frequency-doubled at 532 nm [44–48]. To perform OAM at other wavelengths, dye lasers were used [15, 49]. Although, single-wavelength optical sources have the required properties for OAM, such as nanosecond pulse duration, kHz PRR, and hundreds of nJ per pulse, the lack of wavelength tunability makes them not suitable for performing Multi-spectral Opto-acoustic Microscopy (MS-OAM). Due to the diverse range of endogenous contrast agents present in biological tissue, each exhibiting a distinct absorption response, it becomes necessary to employ an optical source with a tunable central wavelength to effectively target these contrast agents. The absorption behaviour of the most common endogenous contrast agents is presented in Fig. 2.9. The concept of MS-OAM involves conducting OAM at multiple sequential central wavelengths, ideally with a narrow spectral bandwidth to achieve enhanced spectral resolution. Consequently, MS-OAM facilitates the discrimination and visualization of multiple endogenous contrast agents through differentiation and mapping.

The strength of the OAM signal when the sample is illuminated by an optical source operating at a wavelength $\lambda_i$ is proportional to the opto-acoustic initial pressure amplitude, which can quantitatively be determined using [50]:

$$p(\lambda_i) = \Gamma \times \mu_j \times \Phi(\lambda_i) \tag{2.12}$$

Here, $\Gamma$ represents the Grüneisen coefficient, $\mu_j$ the optical absorption coefficient of a specific contrast agent, and $\Phi$ is the laser's irradiance. As, $\Gamma$ exhibits only low variations within the biological media [51], it is reasonable to consider it as a constant. If a total number of $N$ contrast agents are present in the sample, the optical energy is absorbed by all of them, and Eq. (2.12) can be re-written as,

$$p(\lambda_i) = \Gamma \times \sum_{j=1}^{N} \mu_j \times \Phi(\lambda_i) \tag{2.13}$$

As it can be observed (Fig. 2.9), for any wavelength across the spectral range, typically only 2-3 chromophores contribute significantly towards the opto-acoustic signal: melanin and haemoglobin in the visible, water, collagen, lipids in the 1200 nm spectral region, glucose, lipids and water in the 1550-2000 nm region.

For simplicity, let us consider that the sample is first illuminated with a wavelength $\lambda_1$ then by a wavelength $\lambda_2$ and that only two chromophores $a$ and $b$ of absorption coefficients, $\mu_a$ and $\mu_b$ respectively, contribute towards the final opto-acoustic signal. If we calculate the difference between the initial pressures created by the two chromophores at $\lambda_1$ and $\lambda_2$ ($\delta p$), by using Eq. (2.13), the initial pressures created by the radiation at each wavelength can be calculated as,

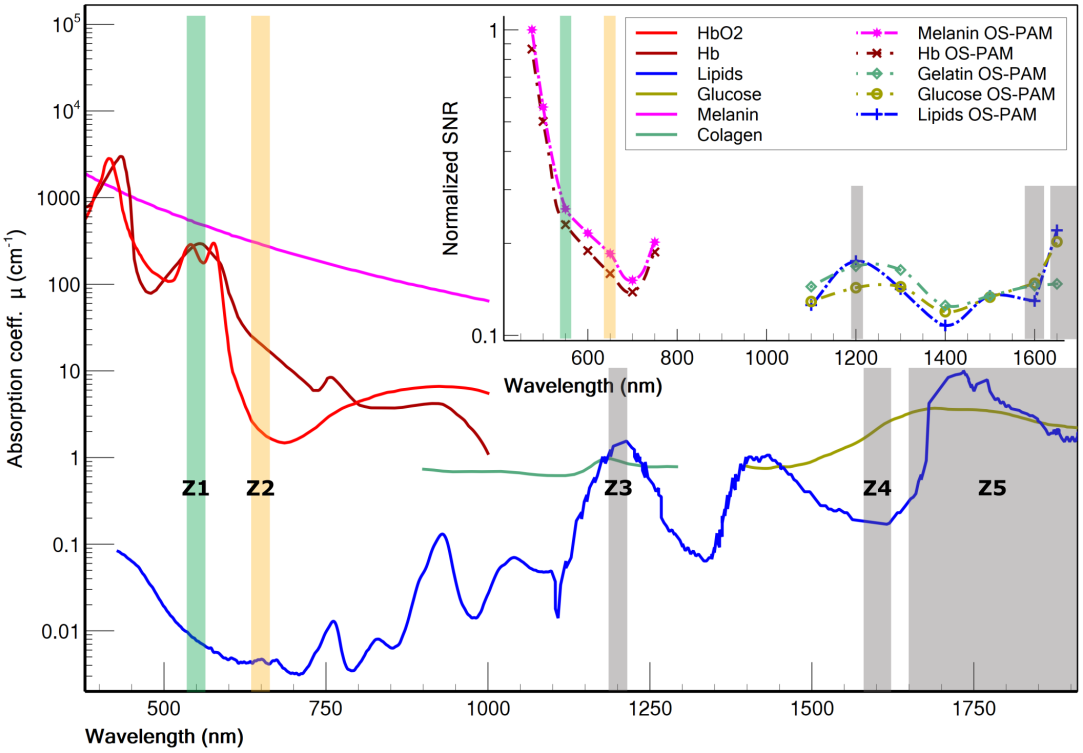


FIGURE 2.9: Graphs of the absorption coefficient for the most common endogenous contrast agents in tissue. Data for HBO2, Hb and Melanin were compiled from [52], data for Collagen from [53], data for Glucose from [54], whereas data for lipids from [55]. The spectral windows used for octave spanning opto-acoustic microscopy (OS-OAM) imaging in chapter 4 are highlighted in colours. Z1-Z5 represent the spectral zones used for mapping the contrast agents. Inset data is obtained performing *in-vitro* OS-OAM imaging.

$$\begin{cases} p(\lambda_1, a) &= \dfrac{\delta p}{\zeta} \\ p(\lambda_1, b) &= m_1 \dfrac{\delta p}{\zeta} \\ p(\lambda_2, a) &= \alpha_a \dfrac{\delta p}{\zeta} \\ p(\lambda_2, b) &= m_2 \alpha_a \dfrac{\delta p}{\zeta} \end{cases} \tag{2.14}$$

In equation 2.14,

$$\begin{cases} m_1 = \dfrac{\mu_b(\lambda_1)}{\mu_a(\lambda_1)}, \quad m_2 = \dfrac{\mu_b(\lambda_2)}{\mu_a(\lambda_2)} \\ \\ \alpha_a = \dfrac{\mu_a(\lambda_2)\Phi(\lambda_2)}{\mu_a(\lambda_1)\Phi(\lambda_1)}, \quad \alpha_b = \dfrac{\mu_b(\lambda_2)\Phi(\lambda_2)}{\mu_b(\lambda_1)\Phi(\lambda_1)} \\ \\ \zeta = 1 + m_1 - \alpha_a - \alpha_a m_2 \end{cases}$$

The wavelengths $\lambda_1$ and $\lambda_2$ can be selected in such a way that the initial pressure due to chromophore *a* is higher at $\lambda_1$, than at $\lambda_2$ and the initial pressure due to chromophore *b* is lower at $\lambda_1$ than at $\lambda_2$. Supposing that only one chromophore contributes to the brightness of a pixel in the image, we compute the difference between images generated at different wavelengths to figure out which of the chromophores is present at each location in the image. If for a given pixel, the difference is positive, the chromophore contributing to the signal is *a*. On the contrary, if the difference is negative, the contributing chromophore is b. Chromophore *a* can for example be Hb and chromophore *b* melanin, $\lambda_1 = 550$ nm (zone Z1 in Fig. 2.9) and $\lambda_2 = 650$ nm (zone Z2 in Fig. 2.9). Using the absorption coefficients of the two chromophores at their respective wavelengths, and the values of the optical powers on the sample experimentally measured (0.36 mW at 550 nm and 1.1 mW at 650 nm), we have $m_1 = 1.83$, $m_2 = 14.14$, $\alpha_a = 0.22$ and $\alpha_b = 1.72$. If we take for example $\dfrac{\delta p}{\zeta} = 1$ arbitrary unit, we obtain,

$$\begin{cases} p(\lambda_1, a) &= 1 \\ p(\lambda_1, b) &= 1.83 \\ p(\lambda_2, a) &= 0.22 \\ p(\lambda_2, b) &= 3.17 \end{cases}$$

So, if in a point of the OAM image we have contributions from both, melanin, and Hb, when switching from 550 nm to 650 nm we do expect an increase of the initial pressure due to the melanin and a decrease of the initial pressure due to the Hb. Now, if we suppose that from a single point, we have either signal from Hb or melanin then, $\delta p > 0$ indicates the presence of the Hb whereas $\delta p < 0$ that of the melanin.

By carefully selecting the operation wavelength of the instrument, various chromophores can be mapped in the *en-face* (transverse) OAM image. To map Hb and melanin, we used the spectral windows Z1 and Z2, around 550 and 650 nm, respectively. To map glucose, collagen and lipids, three zones were selected (Z3 around 1200 nm, Z4 around 1600 and Z5 above 1700 nm, respectively). Because water is a major absorber at long wavelengths, zones Z3-Z5 were selected in such a way that, when performing the difference between images, one of the targeted chromophores increase (or decrease) its initial pressure from one zone to the other, whereas water and the other chromophore decrease (or increase) their initial pressure.

## Conclusion

In this section, the working principle of OAM was presented to aid the understanding of the experimental chapters 3, 4, and 5. OAM is a biomedical imaging modality based on the optical absorption of endogenous chromophores. MS-OAM provides functional information (in addition to structural information) such as blood oxygen saturation and the mapping of several endogenous chromophores *in-vivo*. Volumetric images can be acquired in real-time with high spatial resolution. OAM requires a pulse duration below 10 ns with a PRR ranging from several kHz up to 2 MHz and an EPP of 70-100 nJ. The employment of SC optical sources is being considered in the studies presented in this thesis due to the ultra-wide spectrum SC sources provide.

## 2.3 Optical Coherence Tomography

In this section, Optical Coherence Tomography (OCT) is presented to help the understanding of the experimental work carried out in chapter 4. The working principle of an OCT system is introduced in section 2.3.1. The detection system is described in section 2.3.5. Signal processing and signal requirements in order to obtain an OCT image are shown in section 2.3.7. The requirements in terms of optical sources for OCT are presented in section 2.3.8.

### 2.3.1 OCT working principle

Optical coherence tomography is a non-invasive, high spatial resolution imaging technique with the ability to detect back-scattered light based on low-coherence interferometry allowing for depth-resolved tissue imaging. OCT has the capability to provide cross-sectional (*B-scan*, *En-Face*) and volumetric (3D) images in real-time. Mie scattering is the predominant scattering phenomenon for biological tissues. In Mie scattering, most scattered photons follow a forward trajectory while the rest are back-scattered. This back-scattered light, however, is enough to be detected and form the depth-resolved reflection profile named *A-scan*. By scanning beam laterally (x-direction), over the sample, a *B-scan* can be obtained. A *B-scan* is essentially a collection of *A-scans* and forms a cross-sectional (x,z) image of the sample. Therefore, by scanning also in the perpendicular direction (y), a volumetric (x,y,z) image can be obtained. A volumetric image is a collection of *B-scans* and forms a three-dimensional image of the sample. A representation of the *A-scan*, *B-scan*, and the *en-face* image is depicted in Fig. 2.6.

The lateral directions are expressed as $x$ and $y$ with the convention that $x$ is the fast scanning direction and $y$ is the slow scanning direction. The z-direction represents the longitudinal direction. A slice at a single depth ($z_i$) forms a two-dimensional image (x,y) named *en-face* image. A common practice to produce

richer x,y images is to make a composite of *en-face* images from different depths. Such images are z-projected *en-face* images and are equivalent to confocal images.

Optical coherence tomography falls into two categories, Fourier Domain OCT (FD-OCT) and Time Domain OCT (TD-OCT), depending on the detection type and the optical source employed.

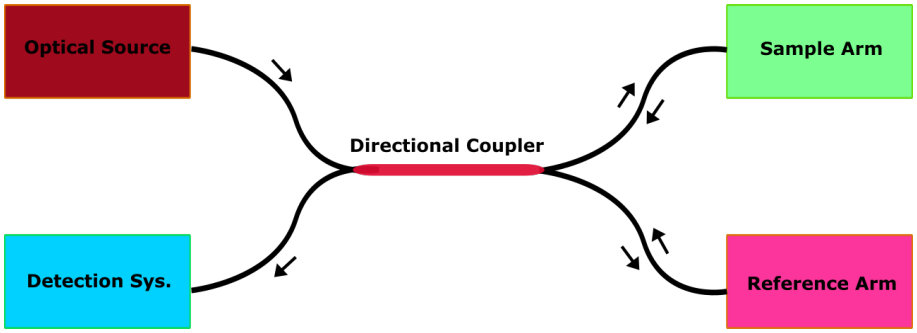


FIGURE 2.10: Schematic diagram of a typical FD-OCT system.

The schematic diagram of a common OCT system based on a Michelson interferometer is depicted in Fig. 2.10. The interferometer can be built either using a fibre directional coupler or using a beam splitter. Fibre directional couplers are more favourable as they are easier to implement and require no alignment. The coupler splits the light coming from the optical source and directs a percentage of the light toward the sample and the rest toward the reference arm. Light from the reference and sample arm is reflected by a mirror and the sample, respectively. The beam in the sample arm is scanned laterally by a pair of galvo-scanners. The back-reflected light is then recombined in the coupler and a percentage of the recombined light is directed toward the detection system.

For a single scattering point, the total electric Field $E$ and the total irradiance $I$ are given by [56]:

$$E = E_R \cdot exp(-i(2kz - \omega t)) + E_S \cdot exp(-i(2kz - \omega t)), \tag{2.15}$$

$$I \propto 0.5 < E \cdot E^* >= I_R + I_S + 2\sqrt{I_R I_S} cos(\Delta\phi), \tag{2.16}$$

Where,

$$\Delta\phi = k \cdot OPD, \tag{2.17}$$

$$k = \frac{2\pi}{\lambda}, \tag{2.18}$$

$$I_R = 0.5|E_R|^2 \; and \; I_S = 0.5|E_S|^2, \tag{2.19}$$

$I_R$ is the intensity of the beam back-scattered from the reference arm, whereas $I_S$ is the intensity of the back-scattered light from the sample arm. OPD stands for optical path difference (between the sample arm and the reference arm) and is defined as $OPD = 2n(z_S - z_R)$, where $z_S$ and $z_R$ refer to the optical lengths of the sample arm and reference arm, respectively. These optical lengths ($z_S$ and $z_R$) can be measured from the coupler to the mirror and back for $z_R$ and from the coupler to the sample and back for $z_S$. $\omega$ is the optical frequency, $\lambda$ is the wavelength end $k$ the wavenumber.

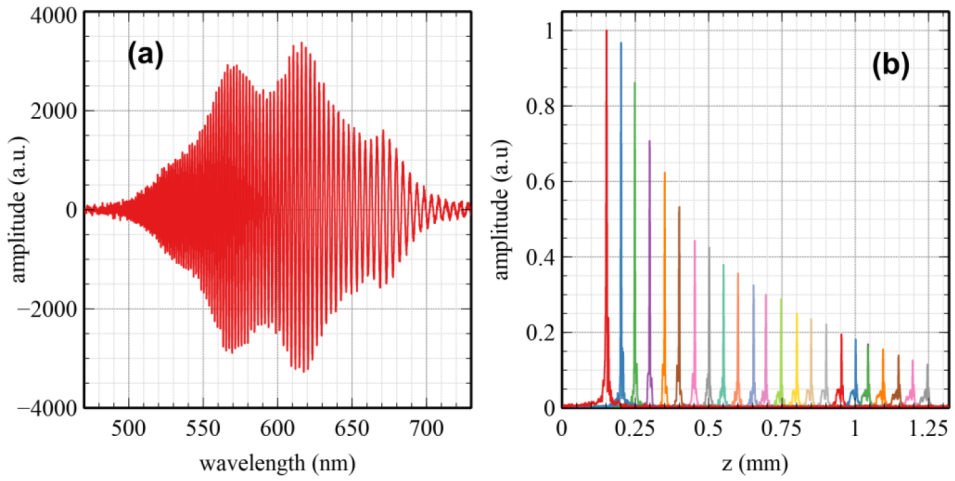


FIGURE 2.11: (a): Channelled spectrum of an SC-based OCT system with a mirror in the sampling arm. and (b): *A-scans* obtained at different OPDs, presenting the signal drop-off characterization of an SB-OCT instrument. The axial position $z$ is effectively the absolute value of the measured OPD.

The electric field of a single scattering point is given by:

$$E_A = \frac{s(k)}{\sqrt{2}}, A \in [R, S] \tag{2.20}$$

Where,

$$S(k) =< |s(k)|^2 >, \tag{2.21}$$

contains the spectral properties of the optical source, i.e. power density, spectral shape, etc. $r_A$ refers to the reflection coefficient of the scattering point, where $|r_A| = R_A$ is the reflectivity. Therefore, the irradiance can be rewritten as:

$$I(k) = 0.25S(k) \cdot [R_R + R_S + 2\sqrt{R_R R_S} cos(2k(z_S - z_R))], \tag{2.22}$$

Interference takes place as long as $|OPD| < \lambda_c$, The coherence length of the optical source. This is called the coherence condition. For $cos(\Delta\phi) = 1 \Rightarrow OPD = n\lambda/2$, where $n$ is an integer number. This is the condition for constructive interference. OCT relies on the properties of low coherent optical sources to decode the depth information of the sample with an uncertainty defined by the coherent length of the optical source.

### 2.3.2 Fourier-Domain Optical Coherence Tomography

The first optical coherence tomography system was employed in the 1990s using a time-domain detection configuration [57]. In time-domain OCT (TD-OCT), the interferometric signal is detected by a photodetector, with the sample positioned at $OPD = 0$, where constructive interference can be observed. Therefore, the signal of a single depth in the sample $z_S$ can be detected with an axial resolution $\lambda_c$ when $z_R = z_S$ ($OPD = 0$). in addition, if the beam in the sample arm is scanned laterally, an en-face image corresponding to a depth $z_S$ can be formed [58]. To obtain an *en-face* image at another depth $z_{S_i}$, the reference arm can be displaced at the corresponding $z_{R_i}$ position, where $z_{S_i} = z_{S_i}$ ($OPD = 0$). The

requirement for mechanical movement of the reference arm makes TD-OCT very slow to acquire a three-dimensional image.

In 1999 Mitsui and later in 2003 Leitgeb et al. and Choma et al. demonstrated the sensitivity superiority of Fourier-domain optical coherence tomography (FD-OCT) over TD-OCT [59–61]. Fourier-Domain Optical Coherence Tomography does not require mechanical axial scanning in the reference arm, and all depths are acquired at once. This makes FD-OCT imaging much faster [56, 62]. Although TD-OCT is a more preferable technique for high numerical aperture microscopy for its dynamic focus capabilities, FD-OCT is the dominant imaging technique for retinal imaging. FD-OCT can be implemented via two different systems, namely spectrometer-based OCT (SB-OCT) and swept-source OCT (SS-OCT). In SS-OCT, a spectral window is swept over time with *A-scan* rates ranging from kHz up to MHz [62–69]. The detection of the interferometric signal is performed via a photodetector. SS-OCT has only been briefly introduced in this thesis. The primary focus of this thesis is OAM and SB-OCT. For SB-OCT, wide-band optical sources are utilized to illuminate the sample, and a camera-based spectrometer to collect the channelled spectra. SB-OCT can reach imaging speeds up to hundreds of kHz [70, 71].

### 2.3.3 Resolution of Optical Coherence Tomography

While the absorption and scattering properties of tissues impose limitations on the depth penetration of light, it is important to note that the depth penetration is further constrained by the optics interface (confocal gate) and the length of the *A-scan*. In this section, the definition of the resolution, the depth of field, and the *A-scan* length are introduced.

The axial resolution of OCT is defined as the coherence length ($\lambda_c$) of the optical source. Assuming a Gaussian-shaped spectrum the axial resolution can be expressed as [56, 62]:

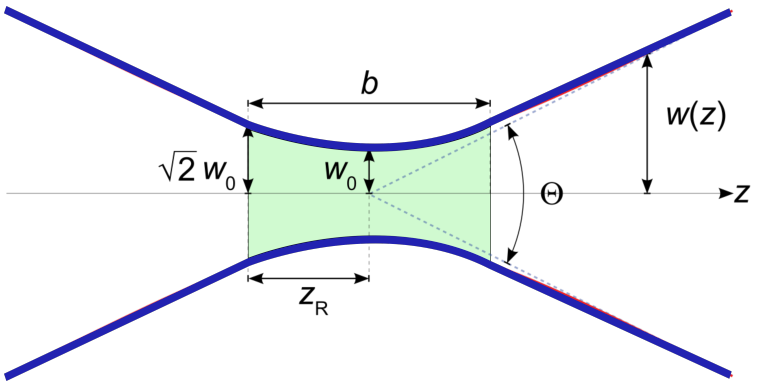


FIGURE 2.12: The Rayleigh length $z_R$, represents the axial distance from the beam waist $w_0$ to the point where the cross-sectional area is doubled. $z_R$ is also referred to as the confocal gate since it defines the imaging axial range. $w_0$ defines the lateral resolution.

$$\delta z = \lambda_c = \frac{2ln(2)}{\pi}\frac{\lambda_0^2}{\Delta\lambda}, \tag{2.23}$$

where $\lambda_0$ is the central wavelength end $\Delta\lambda$ the full-width half maximum (FWHM) of the spectrum. Typical OCT systems are centred at 850 nm, 1050 nm, and 1300 nm. Although $\Delta\lambda$ is usually presented as the FWHM over the spectrum of the optical source, in reality, detection bandwidth (the FWHM of the spectrum reaching the spectrometer) determines the axial resolution. To measure the axial resolution experimentally, an *A-scan* from a mirror as a sample must be acquired. Therefore, the FWHM of the *A-scan* peak can be considered a valid estimation of the axial resolution.

Sub-micron axial resolution can be achieved by using shorter wavelengths and wide spectrum optical sources. This, however, comes with a trade-off with the imaging depth. The absorption coefficient of melanin and haemoglobin increases at shorter (450 nm to 750 nm) wavelengths limiting the amount of reflected light, thus reducing the imaging depth. The typical axial resolution of conventional OCT systems is a few microns (<15 $\mu m$). A combination of SC optical sources and wide bandwidth spectrometers can be employed to enable OCT instruments obtain sub-micron axial resolution.

Considering a spatial power distribution of a Gaussian beam with a Gaussian

shape, the lateral resolution $\delta x$, defined as the spot size of the focus beam can be written as [56, 62]:

$$\delta x = 0.37 \frac{\lambda_0}{NA}, \tag{2.24}$$

where $NA$ Is the numerical aperture of the objective lens. The lateral resolution and the depth of field are linked via the confocal parameter expressed as [62]:

$$b = 2 \cdot z_R = 2 \cdot \frac{\pi \omega_0^2}{\lambda_0} = 2 \cdot \frac{\lambda_0}{\pi NA^2} \approx 4.5 \frac{\delta x^2}{\lambda_0}, \tag{2.25}$$

where $z_R$ is the Rayleigh length and $\omega_0$ is the beam diameter. The Rayleigh length is defined by the distance, longitudinally, between the focus and the axial position where the beam diameter has doubled in comparison to the diameter at the focal position. The FWHM of the beam determines the lateral resolution. In order to achieve high lateral resolution (< 3 $\mu m$), high $NA$ objectives are employed.

### 2.3.4 Detection System of SB-OCT

SB-OCT employs camera-based spectrometers for its detection system. Therefore, in this section, spectrometers for OCT are introduced. Spectrometers can be built either in transmission or reflection mode (in regard to the diffraction grating DG Fig. 2.13). In this thesis, all spectrometers employed were designed and built in transmission mode. A transmission mode spectrometer comprises a collimator, a transmission diffraction grating, and a lens to focus the diffracted light on the line camera (Fig. 2.13).

The central wavelength, the bandwidth, and the shape of the spectrum emitted by the optical source dictate the properties of the components and the detection bandwidth of the spectrometer. Line cameras come with fixed parameters such as the number of pixels, and the size and configuration of the pixels. The

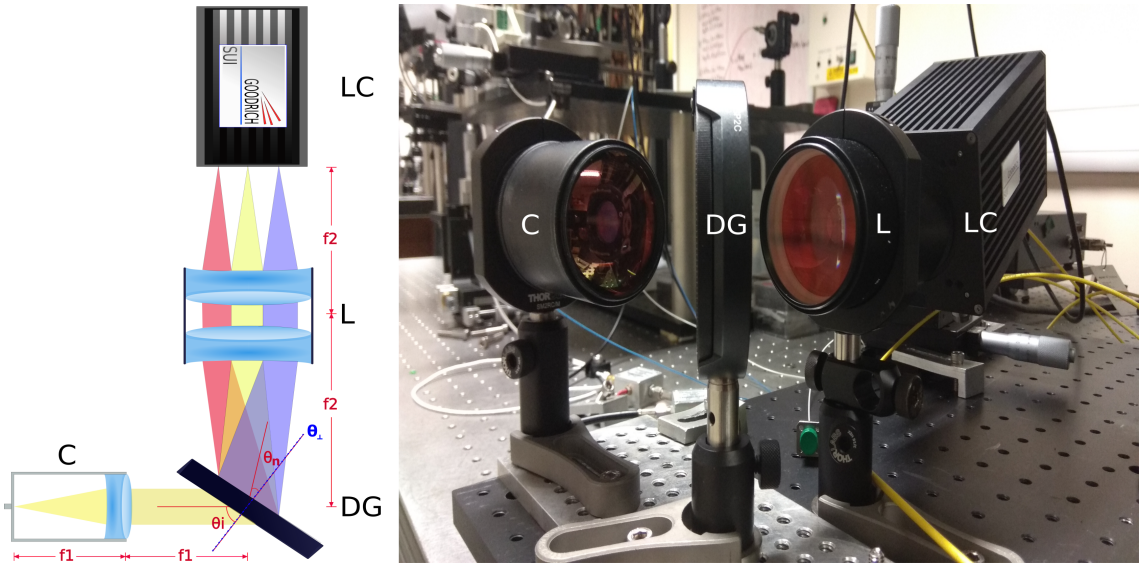


FIGURE 2.13: Schematic diagram of a transmission mode spectrometer and a picture of one of the spectrometers developed for this thesis. C: Collimator; DG: Diffraction Grating; L: Lens; LC: Line Camera.

focal length ($F_2$ Fig. 2.13) of the lens $L$ is selected to match the camera chip size, and the spot size to be similar to the pixel size of the line camera. The choice of the diffraction grating is of paramount importance, to have high diffraction efficiency, high resolution (l/mm), and low transmission losses to ensure high sensitivity detection. Achieving a bandwidth projection exceeding 200 nm on a line camera poses a significant challenge. This difficulty arises from the non-linear, wavelength-dependent focal shift inherent in any lens, leading to a curved focal plane as the wavelengths separate in space. To overcome this limitation, the use of custom optics is necessary, which, however, can entail considerable expenses. According to the diffraction grating formula:

$$n\lambda = a \cdot [sin(\theta_i) - sin(\theta_n)], \tag{2.26}$$

Where $n$ is the order of diffraction, $a$ is the grating pitch, $\theta_i$ is the angle of incidence, and $\theta_n$ is the maximum angle (Fig. 2.13). Diffraction gratings designed for OCT spectrometers are usually optimized for use at the first order of diffraction ($n = 1$). The size of the beam can be calculated by:

$$d = F_2 \cdot tan(\theta_n - \theta_\perp), \tag{2.27}$$

The depth of field of an OCT system is defined as the length of an *A-scan* and can be expressed as:

$$z_{max} = 0.25 \cdot \frac{N \cdot \lambda_0^2}{\Delta\lambda}, \tag{2.28}$$

where $N$ is the number of pixels.

In the context of the studies outlined in this thesis, custom-designed spectrometers were constructed with central wavelengths of 1300 nm, 670 nm, and 570 nm. The 1300 nm spectrometer employed an InGaAs line camera comprising 1024 pixels ($N = 1000$) and a bandwidth of 200 nm. On the other hand, for the OCT system operating in the visible range, a 4096-pixel camera was utilized, with the bandwidth ranging from 100 to 240 nm. It is evident from the equation 2.28, the depth of field is proportional to the number of pixels $N$ and inversely proportional to the detection bandwidth $\Delta\lambda$. This is a trade-off between the axial resolution and the imaging depth. Moreover, eq. 2.28 shows the strong dependency of the imaging depth range with the central wavelength.

### 2.3.5 Fourier-Domain OCT

In contrast to TD-OCT, FD-OCT enables the acquisition of all depths simultaneously. An *A-scan* represents the axial (z-direction) reflectivity of $n$ scattering points in the sample, where $n$ refers to different positions in the z-direction. The electric field $E$ and the incident irradiance $I$ can be written as:

$$E = E_R \cdot exp(-i(2kz_R - \omega t)) + \sum_n E_{S_n} \cdot exp(-i(2kz_{S_n} - \omega t)), \tag{2.29}$$

where $E_R$ is the electric field in the reference arm, whereas $E_{S_n}$ is the electric field in the sample arm for each axial position ($n$).

$$\begin{aligned} I(k) = 0.5S(k) \cdot (R_R + \sum_n R_{S_n}) \\ + 0.5S(k) \cdot \sum_n \sqrt{R_R R_{S_n}} \cos\left[2k(z_{S_n} - z_R)\right] \\ + 0.25S(k) \cdot \sum_{n,m,n\neq m} \sqrt{R_{S_n} R_{S_m}} \cos\left[2k(z_{S_m} - z_{S_n})\right] \end{aligned} \tag{2.30}$$

The term channelled spectrum refers to the modulation of the spectrum (emitted by the optical source) in an interferometer. This modulation is attributed to the interference which takes place when the waves from both arms are recombined (from the directional coupler, to the detection system (Fig. 2.10)), and when all four conditions of interference are met.

1. The polarization condition ($A \cdot B \neq 0$),
2. The monchromaticity condition ($\omega_1 = \omega_2$),
3. The phase stability condition ($\Delta\Phi \approx$ **constant**),
4. The coherence condition ($|\text{OPD}| <$ coherence length of the optical source).

The amplitude of the channelled spectrum is proportional to the incident irradiance $I$. In SS-OCT, the wavelength components of the channelled spectrum are separated in time by the temporal sweeping of the optical source, whereas in SB-OCT the wavelengths are separated spatially by diffraction and/or dispersion. The first term in eq. 2.30 describes the DC term. The shape of the spectrum emitted by the optical source is described by $S(k)$. The reflectivity of the reference arm is described by $R_R$, whereas the $R_{S_n}$ pertains to the reflectivity in the sample arm for each axial position ($n$). The second term represents the interference between the scattering points in the sample arm and the back-scattered signal from the

mirror in the reference arm. The modulation frequency increases proportionally to $|z_{S_n} - z_R|$ (Fig. 2.11). The third term is the auto-correlation term and describes the modulation generated in the sample arm only.

### 2.3.6 Signal Processing in Fourier-Domain OCT

The signal processing method used in this thesis to generate images is called complex master-slave interferometry (CMS), developed at the University of Kent [72–74]. CMS enables *en-face* images to be produced directly, similar to TD-OCT, utilizing FD-OCT principles. CMS reduces significantly the number of processing steps required to produce an *en-face* image. Thus, the production of an *en-face* image is much faster for CMS-OCT than the traditional FFT processing method. This, however, is not the case when a whole three-dimensional image is produced. And yet, CMS is more favourable since no dispersion compensation (in software or hardware) and no data re-sampling is required [75]. An *A-scan* is generated by a correlation operator instead of an FFT algorithm.

The two main sequential steps of a CMS algorithm to produce an *A-scan* can be identified as Master and Slave. In the first stage (Master), several channelled spectra are collected with a mirror in the sample arm. These channelled spectra (calibration data) are collected at different OPDs to produce theoretically inferred masks. The number of the generated masks depends on the axial range and the axial resolution of the OCT system. In essence, the set of theoretical masks is a calibration multiplication matrix ($M$). A CMS *A-scan* ($A^*$) is the product of an acquired *A-scan* ($A$) (Slave) multiplied by the calibration matrix $M$.

$$A^* = MA \tag{2.31}$$

The calibration matrix $M$ contains both the correction of the modulation chirp and the correction of the unmatched dispersion between the sample arm and the reference arm. The use of complex values during the calculations enables the

acquisition of phase information. Hence, dispersion and re-sampling are not necessary. As long as the system is not modified, the calibration data files (acquired during the Master stage) can be used for multiple sessions. Meaning, a CMS-OCT system requires only pre-calibration.

### 2.3.7 Optical Sources For OCT

The optical sources of choice for SB-OCT are Superluminescent diodes (SLDs) and SC optical sources. SLDs provide a bandwidth below 150 nm with very low noise, and a low cost. SC sources on the other hand, provide an ultra-wide spectrum varying from 450 nm up to 2400 nm with higher noise levels and a higher acquisition costs. The axial resolution of an OCT instrument is usually limited by the spectral bandwidth of the optical source. In the case of an SC-based OCT system, the axial resolution is ultimately limited by the detection bandwidth of the spectrometer. SC sources enable very high resolution with a wide selection of wavelengths, from the visible to the NIR. In contrast, only SLDs with a very narrow bandwidth are available in the visible. This makes SC optical sources the only available option for OCT in the visible region, especially if high resolution is required.

In terms of PRR, both SLDs and SC optical sources provide properties that exceed the requirements of an SB-OCT system. SLDs provide continuous emission, whereas SC sources provide PRR ranging from kHz up to hundreds of MHz. Thus, the imaging speed of an SB-OCT instrument is limited by the speed of the line camera (line period) in the spectrometer. During the exposure time of the camera, channelled spectra are averaged. CMS is applied to the averaged signal to produce an *A-scan*. By increasing the exposure time of the camera, lower noise signals can be acquired at the expense of imaging speed.

To conclude, for SB-OCT, the choice between SLDs and SC optical sources involves trade-offs. SLDs offer narrow bandwidth below 150 nm with low noise and cost, suitable for the visible region. SC sources provide a wide spectrum

from 450 nm to 2400 nm, enabling high resolution in the visible to NIR, but come with higher noise levels and acquisition costs. SC sources are crucial for high-resolution imaging in the visible region, where only SLDs with narrow bandwidth are available. Both sources meet PRR requirements, with SLDs offering continuous emission and SC sources providing varying PRR. The imaging speed is limited by the line camera's speed, and adjustments in exposure time trade off imaging speed for lower noise signals. In conclusion, optical sources for SB-OCT demand milliwatts of power, wide bandwidth, and a PRR ranging from kHz to hundreds of MHz.

### 2.3.8 Sensitivity in OCT

Shot noise, excess photon noise and thermal noise all contribute to noise in SB-OCT. For a SC-based OCT system, however, the main source of noise is RIN. Usually, to characterize an OCT instrument, sensitivity and SNR must be measured. These quantities represent an estimation of the minimum detectable signal and image quality of an OCT system. The predominant method to reduce the RIN in an SC-based OCT instrument is to greatly increase the PRR of the SC source. An increase of the PRR by a factor $N$ results in a RIN reduction by a factor of $\sqrt{N}$ [76]. Another method to reduce noise and subtract the DC term (eq. 2.30) is balanced detection [77].

## Conclusion

In this section, the working principle of OCT was presented to aid the readers comprehension of the work carried out in the experimental chapter 4. OCT is a non-invasive, depth-resolved, high-resolution imaging modality. OCT enables the acquisition of three-dimensional images with a typical resolution of a few

$\mu m$. Wide bandwidth optical sources are favourable for the development of high-resolution OCT instruments. To significantly improve the sensitivity of SC-based OCT systems, a PRR of several hundred MHz is required.

In the pursuit of integrating OCT with OAM, the challenge extends to the selection and synchronization of optical sources tailored for each modality. OCT typically utilizes sources like SLDs or SC optical sources, each with specific bandwidth and resolution characteristics. In contrast, OAM relies on pulsed laser sources, which are essential for inducing the photoacoustic effect in tissues. The integration of these diverse optical sources introduces complexities in harmonizing their temporal and spectral properties for simultaneous imaging. Achieving optimal integration while addressing the cost-effectiveness of these sources poses an open problem in the development of dual-modality OCT/OAM systems. The challenges lie in selecting sources that provide sufficient power, bandwidth, and penetration depth for both imaging modalities, all while ensuring compatibility and cost efficiency in the integrated setup. Addressing these issues is critical for advancing the capabilities of dual-modality imaging systems and broadening their applicability in clinical and research domains.

The combination of different modalities presents an opportunity of great interest to clinicians for *in-vivo*, non-invasive assessment of tissues. The fact that OCT and OAM provide supplementary contrast mechanisms has driven several groups to develop various multi-modal imaging instruments for biomedical applications [11, 17, 18, 22, 44–46, 78, 79]. This supplementary contrast is attributed to their respective reflection, and absorption dependency. A flying spot scanning configuration can be implemented on both OAM and OCT, making the implementation of a dual-modality OAM/OCT instrument feasible. Moreover, the resolution and imaging depth for OAM and OCT are very similar (Fig. 2.4).

Dual-modality OAM/OCT usually employ two different optical sources to facilitate their different requirements [11, 17, 18, 22, 44, 45]. Therefore, such systems can be rather expensive and very complex to implement.

# References

[1] E. J. McCartney and F. F. Hall, "Optics of the Atmosphere: Scattering by Molecules and Particles," *Physics Today*, vol. 30, no. 5, pp. 76–77, May 1977, Publisher: American Institute of Physics, ISSN: 0031-9228. DOI: 10.1063/1.3037551. [Online]. Available: https://physicstoday.scitation.org/doi/10.1063/1.3037551 (visited on 02/09/2023).

[2] P. Beard, "Biomedical photoacoustic imaging," *Interface Focus*, vol. 1, no. 4, pp. 602–631, Aug. 2011, ISSN: 2042-8898. DOI: 10.1098/rsfs.2011.0028. [Online]. Available: https://www.ncbi.nlm.nih.gov/pmc/articles/PMC3262268/ (visited on 02/09/2023).

[3] T. H. Maiman, "Stimulated Optical Radiation in Ruby," en, *Nature*, vol. 187, no. 4736, pp. 493–494, Aug. 1960, Number: 4736 Publisher: Nature Publishing Group, ISSN: 1476-4687. DOI: 10.1038/187493a0. [Online]. Available: https://www.nature.com/articles/187493a0 (visited on 02/09/2023).

[4] R. G. Olsen, "Generation of Acoustical Images from the Absorption of Pulsed Microwave Energy," en, in *Acoustical Imaging*, ser. Acoustical Imaging, J. P. Powers, Ed., Boston, MA: Springer US, 1982, pp. 53–59, ISBN: 978-1-4684-1137-9. DOI: 10.1007/978-1-4684-1137-9_4. [Online]. Available: https://doi.org/10.1007/978-1-4684-1137-9_4 (visited on 02/09/2023).

[5] L. V. Wang and S. Hu, "Photoacoustic Tomography: In Vivo Imaging from Organelles to Organs," *Science*, vol. 335, no. 6075, pp. 1458–1462, Mar. 2012, Publisher: American Association for the Advancement of Science. DOI: 10.1126/science.1216210. [Online]. Available: https://www.science.org/doi/10.1126/science.1216210 (visited on 02/09/2023).

[6] J. Yao and L. V. Wang, "Photoacoustic microscopy," *Laser & Photonics Reviews*, vol. 7, no. 5, pp. 758–778, 2013, _eprint: https://onlinelibrary.wiley.com/doi/pd ISSN: 1863-8899. DOI: 10.1002/lpor.201200060. [Online]. Available: https://onlinelibrary.wiley.com/doi/abs/10.1002/lpor.201200060 (visited on 02/09/2023).

[7] J. G. F. Wolfgang Drexler, *Optical Coherence Tomography*, vol. 24, ISBN: 978-3-319-06418-5. DOI: 10.1007/978-3-319-06419-2. [Online]. Available: https://link.springer.com/referencework/10.1007/978-3-319-06419-2.

[8] X. Shu, M. Bondu, B. Dong, A. Podoleanu, L. Leick, and H. F. Zhang, "Single all-fiber-based nanosecond-pulsed supercontinuum source for multispectral photoacoustic microscopy and optical coherence tomography," EN, *Optics Letters*, vol. 41, no. 12, pp. 2743–2746, Jun. 2016, Publisher: Optical Society of America, ISSN: 1539-4794. DOI: 10.1364/OL.41.002743. (visited on 05/22/2020).

[9] M. Bondu, M. Denninger, P. M. Moselund, and A. Podoleanu, "Using a single supercontinuum source for visible multispectral photoacoustic microscopy and 1300 nm optical coherence tomography," EN, in *Opto-Acoustic Methods and Applications in Biophotonics III (2017), paper 1041507*, Optica Publishing Group, Jun. 2017, p. 1 041 507. DOI: 10.1117/12.2286119. [Online]. Available: https://opg.optica.org/abstract.cfm?uri=ECBO-2017-1041507 (visited on 02/09/2023).

[10] M. Bondu, M. J. Marques, P. M. Moselund, G. Lall, A. Bradu, and A. Podoleanu, "Multispectral photoacoustic microscopy and optical coherence tomography using a single supercontinuum source," en, *Photoacoustics*, vol. 9, pp. 21–30, Mar. 2018, ISSN: 2213-5979. DOI: 10.1016/j.pacs.2017.11.002. (visited on 03/09/2020).

[11] L. Li, K. Maslov, G. Ku, and L. V. Wang, "Three-dimensional combined photoacoustic and optical coherence microscopy for in vivo microcirculation studies," EN, *Optics Express*, vol. 17, no. 19, pp. 16 450–16 455, Sep. 2009, Publisher: Optica Publishing Group, ISSN: 1094-4087. DOI: 10.1364/OE.17.016450. [Online]. Available: https://opg.optica.org/oe/abstract.cfm?uri=oe-17-19-16450 (visited on 02/09/2023).

[12] S. S, C. Z, Z. Y, Y. S, and X. D, "Simultaneous imaging of atherosclerotic plaque composition and structure with dual-mode photoacoustic and optical coherence tomography," en, *Optics express*, vol. 25, no. 2, Jan. 2017, Publisher: Opt Express, ISSN: 1094-4087. DOI: 10.1364/OE.25.000530. [Online]. Available: https://pubmed.ncbi.nlm.nih.gov/28157944/ (visited on 02/09/2023).

[13] W. Liu *et al.*, "In vivo corneal neovascularization imaging by optical-resolution photoacoustic microscopy," *Photoacoustics*, vol. 2, no. 2, pp. 81–86, Apr. 2014, ISSN: 2213-5979. DOI: 10.1016/j.pacs.2014.04.003. [Online]. Available: https://www.ncbi.nlm.nih.gov/pmc/articles/PMC4083229/ (visited on 02/09/2023).

[14] Y. N. Billeh, M. Liu, and T. Buma, "Spectroscopic photoacoustic microscopy using a photonic crystal fiber supercontinuum source," EN, *Optics Express*, vol. 18, no. 18, pp. 18 519–18 524, Aug. 2010, Publisher: Optica Publishing Group, ISSN: 1094-4087. DOI: 10.1364/OE.18.018519. [Online]. Available: https://opg.optica.org/oe/abstract.cfm?uri=oe-18-18-18519 (visited on 02/09/2023).

[15] S. Hu, K. Maslov, and L. V. Wang, "Three-Dimensional Optical-Resolution Photoacoustic Microscopy," in R. Liang, Ed., Heidelberg: Springer-Verlag, Aug. 2012, pp. 55–77, ISBN: 978-3-642-28390-1. [Online]. Available: https://resolver.caltech.edu/CaltechAUTHORS:20160617-124136158 (visited on 02/09/2023).

[16] C. Lee, M. Jeon, M. Y. Jeon, J. Kim, and C. Kim, "In vitro photoacoustic measurement of hemoglobin oxygen saturation using a single pulsed broadband supercontinuum laser source," EN, *Applied Optics*, vol. 53, no. 18, pp. 3884–3889, Jun. 2014, Publisher: Optica Publishing Group, ISSN: 2155-3165. DOI: 10.1364/AO.53.003884. [Online]. Available: https://opg.optica.org/ao/abstract.cfm?uri=ao-53-18-3884 (visited on 02/09/2023).

[17] E. Z. Zhang *et al.*, "Multimodal photoacoustic and optical coherence tomography scanner using an all optical detection scheme for 3D morphological skin imaging," eng, *Biomedical Optics Express*, vol. 2, no. 8, pp. 2202–2215, Aug. 2011, ISSN: 2156-7085. DOI: 10.1364/BOE.2.002202.

[18] R. Haindl *et al.*, "Dual modality reflection mode optical coherence and photoacoustic microscopy using an akinetic sensor," EN, *Optics Letters*, vol. 42, no. 21, pp. 4319–4322, Nov. 2017, Publisher: Optica Publishing Group, ISSN: 1539-4794. DOI: 10.1364/OL.42.004319. [Online]. Available: https://opg.optica.org/ol/abstract.cfm?uri=ol-42-21-4319 (visited on 02/09/2023).

[19] R. Nuster *et al.*, "Downstream Fabry–Perot interferometer for acoustic wave monitoring in photoacoustic tomography," EN, *Optics Letters*, vol. 36, no. 6, pp. 981–983, Mar. 2011, Publisher: Optica Publishing Group, ISSN: 1539-4794. DOI: 10.1364/OL.36.000981. [Online]. Available: https://opg.optica.org/ol/abstract.cfm?uri=ol-36-6-981 (visited on 02/09/2023).

[20] P. Hajireza, J. Sorge, M. Brett, and R. Zemp, "In vivo optical resolution photoacoustic microscopy using glancing angle-deposited nanostructured Fabry–Perot etalons," EN, *Optics Letters*, vol. 40, no. 7, pp. 1350–1353, Apr. 2015, Publisher: Optica Publishing Group, ISSN: 1539-4794. DOI: 10.1364/

OL.40.001350. [Online]. Available: https://opg.optica.org/ol/abstract.cfm?uri=ol-40-7-1350 (visited on 02/09/2023).

[21] S. J. Mathews, E. Z. Zhang, A. E. Desjardins, and P. C. Beard, "Miniature fibre optic probe for minimally invasive photoacoustic sensing," vol. 9708, 97082R, Mar. 2016, Conference Name: Photons Plus Ultrasound: Imaging and Sensing 2016 ADS Bibcode: 2016SPIE.9708E..2RM. DOI: 10.1117/12.2211661. [Online]. Available: https://ui.adsabs.harvard.edu/abs/2016SPIE.9708E..2RM (visited on 02/09/2023).

[22] S.-L. Chen, L. J. Guo, and X. Wang, "All-optical photoacoustic microscopy," en, *Photoacoustics*, vol. 3, no. 4, pp. 143–150, Dec. 2015, ISSN: 2213-5979. DOI: 10.1016/j.pacs.2015.11.001. [Online]. Available: https://www.sciencedirect.com/science/article/pii/S2213597915300069 (visited on 02/10/2023).

[23] B. Dong *et al.*, "Isometric multimodal photoacoustic microscopy based on optically transparent micro-ring ultrasonic detection," EN, *Optica*, vol. 2, no. 2, pp. 169–176, Feb. 2015, Publisher: Optica Publishing Group, ISSN: 2334-2536. DOI: 10.1364/OPTICA.2.000169. [Online]. Available: https://opg.optica.org/optica/abstract.cfm?uri=optica-2-2-169 (visited on 02/10/2023).

[24] H. Li, B. Dong, Z. Zhang, H. F. Zhang, and C. Sun, "A transparent broadband ultrasonic detector based on an optical micro-ring resonator for photoacoustic microscopy," en, *Scientific Reports*, vol. 4, no. 1, p. 4496, Mar. 2014, Number: 1 Publisher: Nature Publishing Group, ISSN: 2045-2322. DOI: 10.1038/srep04496. [Online]. Available: https://www.nature.com/articles/srep04496 (visited on 02/10/2023).

[25] Z. Zhang, B. Dong, H. Li, F. Zhou, H. F. Zhang, and C. Sun, "Theoretical and experimental studies of distance dependent response of micro-ring resonator-based ultrasonic detectors for photoacoustic microscopy," *Journal*

*of Applied Physics*, vol. 116, no. 14, p. 144 501, Oct. 2014, Publisher: American Institute of Physics, ISSN: 0021-8979. DOI: 10.1063/1.4897455. [Online]. Available: https://aip.scitation.org/doi/10.1063/1.4897455 (visited on 02/10/2023).

[26] Z. Chen, S. Yang, Y. Wang, and D. Xing, "All-optically integrated photoacoustic microscopy and optical coherence tomography based on a single Michelson detector," EN, *Optics Letters*, vol. 40, no. 12, pp. 2838–2841, Jun. 2015, Publisher: Optica Publishing Group, ISSN: 1539-4794. DOI: 10.1364/OL.40.002838. [Online]. Available: https://opg.optica.org/ol/abstract.cfm?uri=ol-40-12-2838 (visited on 02/10/2023).

[27] Y. Wang, C. Li, and R. K. Wang, "Noncontact photoacoustic imaging achieved by using a low-coherence interferometer as the acoustic detector," EN, *Optics Letters*, vol. 36, no. 20, pp. 3975–3977, Oct. 2011, Publisher: Optica Publishing Group, ISSN: 1539-4794. DOI: 10.1364/OL.36.003975. [Online]. Available: https://opg.optica.org/ol/abstract.cfm?uri=ol-36-20-3975 (visited on 02/10/2023).

[28] T. Berer, E. Leiss-Holzinger, A. Hochreiner, J. Bauer-Marschallinger, and A. Buchsbaum, "Multimodal noncontact photoacoustic and optical coherence tomography imaging using wavelength-division multiplexing," eng, *Journal of Biomedical Optics*, vol. 20, no. 4, p. 46 013, Apr. 2015, ISSN: 1560-2281. DOI: 10.1117/1.JBO.20.4.046013.

[29] X. Zhu, Z. Huang, G. Wang, W. Li, D. Zou, and C. Li, "Ultrasonic detection based on polarization-dependent optical reflection," EN, *Optics Letters*, vol. 42, no. 3, pp. 439–441, Feb. 2017, Publisher: Optica Publishing Group, ISSN: 1539-4794. DOI: 10.1364/OL.42.000439. [Online]. Available: https://opg.optica.org/ol/abstract.cfm?uri=ol-42-3-439 (visited on 02/10/2023).

[30] P. Hajireza, W. Shi, K. Bell, R. J. Paproski, and R. J. Zemp, "Non-interferometric photoacoustic remote sensing microscopy," en, *Light: Science & Applications*, vol. 6, no. 6, e16278–e16278, Jun. 2017, Number: 6 Publisher: Nature Publishing Group, ISSN: 2047-7538. DOI: 10.1038/lsa.2016.278. [Online]. Available: https://www.nature.com/articles/lsa2016278 (visited on 02/10/2023).

[31] G. Nteroli *et al.*, "Enhanced resolution optoacoustic microscopy using a picosecond high repetition rate Q-switched microchip laser," en, *Journal of Biomedical Optics*, vol. 27, no. 11, Nov. 2022, Accepted: 2022-11-04 Number: 11 Publisher: SPIE, ISSN: 1083-3668. [Online]. Available: https://doi.org/10.1117/1.JBO.27.11.110501 (visited on 02/10/2023).

[32] K. Irisawa, T. Hirasawa, K. Hirota, K. Tsujita, and M. Ishihara, "Influence of laser pulse width to the photoacoustic temporal waveform and the image resolution with a solid-state excitation laser," in *Photons Plus Ultrasound: Imaging and Sensing 2012*, vol. 8223, SPIE, Feb. 2012, pp. 544–551. DOI: 10.1117/12.907714. [Online]. Available: https://www.spiedigitallibrary.org/conference-proceedings-of-spie/8223/82232W/Influence-of-laser-pulse-width-to-the-photoacoustic-temporal-waveform/10.1117/12.907714.full (visited on 11/15/2021).

[33] T. Agano, M. K. A. Singh, R. Nagaoka, and K. Awazu, "Effect of light pulse width on frequency characteristics of photoacoustic signal – an experimental study using a pulse-width tunable LED-based photoacoustic imaging system," en-US, *International Journal of Engineering & Technology*, vol. 7, no. 4, pp. 4300–4303, Dec. 2018, Number: 4, ISSN: 2227-524X. DOI: 10.14419/ijet.v7i4.19907. [Online]. Available: https://www.sciencepubco.com/index.php/ijet/article/view/19907 (visited on 11/01/2021).

[34] M. K. Dasa *et al.*, "All-fibre supercontinuum laser for in vivo multispectral photoacoustic microscopy of lipids in the extended near-infrared region,"

en, *Photoacoustics*, vol. 18, p. 100 163, Jun. 2020, ISSN: 2213-5979. DOI: 10.1016/j.pacs.2020.100163. (visited on 03/09/2020).

[35] T. Buma, N. C. Conley, and S. W. Choi, "Multispectral photoacoustic microscopy of lipids using a pulsed supercontinuum laser," en, *Biomedical Optics Express*, vol. 9, no. 1, p. 276, Jan. 2018, ISSN: 2156-7085, 2156-7085. DOI: 10.1364/BOE.9.000276. (visited on 03/09/2020).

[36] T. Allen *et al.*, "Ultrafast laser-scanning optical resolution photoacoustic microscopy at up to 2 million A-lines per second," *To add*, 2018. DOI: 10.1117/1.JBO.23.12.126502.

[37] R. Cao, J. P. Kilroy, B. Ning, T. Wang, J. A. Hossack, and S. Hu, "Multispectral photoacoustic microscopy based on an optical–acoustic objective," en, *Photoacoustics*, vol. 3, no. 2, pp. 55–59, Jun. 2015, ISSN: 2213-5979. DOI: 10.1016/j.pacs.2014.12.004. (visited on 03/09/2020).

[38] G. Nteroli *et al.*, "Two octaves spanning photoacoustic microscopy," en, *Scientific Reports*, vol. 12, Jun. 2022, Accepted: 2022-06-14 Publisher: Nature Research, ISSN: 2045-2322. [Online]. Available: https://doi.org/10.1038/s41598-022-14869-5 (visited on 02/10/2023).

[39] M. Xu and L. V. Wang, "Photoacoustic imaging in biomedicine," *Review of Scientific Instruments*, vol. 77, no. 4, p. 041 101, Apr. 2006, Publisher: American Institute of Physics, ISSN: 0034-6748. DOI: 10.1063/1.2195024. [Online]. Available: https://aip.scitation.org/doi/10.1063/1.2195024 (visited on 02/10/2023).

[40] J. Xia, J. Yao, and L. V. Wang, "Photoacoustic tomography: Principles and advances," eng, *Electromagnetic Waves (Cambridge, Mass.)*, vol. 147, pp. 1–22, 2014, ISSN: 1070-4698. DOI: 10.2528/pier14032303.

[41] Y. Zhou, J. Yao, and L. V. Wang, "Tutorial on photoacoustic tomography," *Journal of Biomedical Optics*, vol. 21, no. 6, p. 061 007, Apr. 2016, Publisher: SPIE, ISSN: 1083-3668, 1560-2281. DOI: 10.1117/1.JBO.21.6.061007.

[Online]. Available: https://www.spiedigitallibrary.org/journals/journal-of-biomedical-optics/volume-21/issue-6/061007/Tutorial-on-photoacoustic-tomography/10.1117/1.JBO.21.6.061007.full (visited on 02/10/2023).

[42] L. V. Wang, "Multiscale photoacoustic microscopy and computed tomography," *Nature photonics*, vol. 3, no. 9, pp. 503–509, Aug. 2009, ISSN: 1749-4885. DOI: 10.1038/nphoton.2009.157. [Online]. Available: https://www.ncbi.nlm.nih.gov/pmc/articles/PMC2802217/ (visited on 02/10/2023).

[43] J. Yao and L. V. Wang, "Sensitivity of photoacoustic microscopy," eng, *Photoacoustics*, vol. 2, no. 2, pp. 87–101, Jun. 2014, ISSN: 2213-5979. DOI: 10.1016/j.pacs.2014.04.002.

[44] B. Rao, L. Li, K. Maslov, and L. V. Wang, "In vivo, dual-modality imaging of mouse eyes: Optical coherence tomography and photoacoustic microscopy within a single instrument," en, in F. Manns, P. G. Söderberg, and A. Ho, Eds., Issue: 7550 Number: 7550, Bellingham, WA: Society of Photo-Optical Instrumentation Engineers, Mar. 2010, Art. No. 75501Q, ISBN: 978-0-8194-7946-4. [Online]. Available: https://resolver.caltech.edu/CaltechAUTHORS:20180925-104554174 (visited on 02/10/2023).

[45] L. Xi, C. Duan, H. Xie, and H. Jiang, "Miniature probe combining optical-resolution photoacoustic microscopy and optical coherence tomography for in vivo microcirculation study," eng, *Applied Optics*, vol. 52, no. 9, pp. 1928–1931, Mar. 2013, ISSN: 1539-4522. DOI: 10.1364/AO.52.001928.

[46] X. Zhang, S. Jiao, and H. Zhang, "Optical coherence photoacoustic microscopy: Accomplishing optical coherence tomography and photoacoustic microscopy with a single light source," *Journal of Biomedical Optics*, vol. 17, no. 3, p. 030 502, Mar. 2012, Publisher: SPIE, ISSN: 1083-3668, 1560-2281. DOI: 10.1117/1.JBO.17.3.030502. [Online]. Available: https://www.spiedigitallibrary.

org/journals/journal-of-biomedical-optics/volume-17/issue-3/030502/Optical-coherence-photoacoustic-microscopy--accomplishing-optical-coherence-tomography-and/10.1117/1.JBO.17.3.030502.full (visited on 02/10/2023).

[47] K. Maslov, G. Stoica, and L. V. Wang, "In vivo dark-field reflection-mode photoacoustic microscopy," EN, *Optics Letters*, vol. 30, no. 6, pp. 625–627, Mar. 2005, Publisher: Optica Publishing Group, ISSN: 1539-4794. DOI: 10.1364/OL.30.000625. [Online]. Available: https://opg.optica.org/ol/abstract.cfm?uri=ol-30-6-625 (visited on 02/10/2023).

[48] T. Liu, Q. Wei, W. Song, J. M. Burke, S. Jiao, and H. F. Zhang, "Near-infrared light photoacoustic ophthalmoscopy," EN, *Biomedical Optics Express*, vol. 3, no. 4, pp. 792–799, Apr. 2012, Publisher: Optica Publishing Group, ISSN: 2156-7085. DOI: 10.1364/BOE.3.000792. [Online]. Available: https://opg.optica.org/boe/abstract.cfm?uri=boe-3-4-792 (visited on 02/10/2023).

[49] Z. Xie, S. Jiao, H. F. Zhang, and C. A. Puliafito, "Laser-scanning optical-resolution photoacoustic microscopy," EN, *Optics Letters*, vol. 34, no. 12, pp. 1771–1773, Jun. 2009, Publisher: Optica Publishing Group, ISSN: 1539-4794. DOI: 10.1364/OL.34.001771. [Online]. Available: https://opg.optica.org/ol/abstract.cfm?uri=ol-34-12-1771 (visited on 02/10/2023).

[50] V. P. Nguyen, J. Kim, K.-l. Ha, J. Oh, and H. W. Kang, "Feasibility study on photoacoustic guidance for high-intensity focused ultrasound-induced hemostasis," *Journal of Biomedical Optics*, vol. 19, no. 10, p. 105 010, Oct. 2014, Publisher: International Society for Optics and Photonics, ISSN: 1083-3668, 1560-2281. DOI: 10.1117/1.JBO.19.10.105010. (visited on 03/25/2020).

[51] D.-K. Yao, C. Zhang, K. Maslov, and L. V. Wang, "Photoacoustic measurement of the Grüneisen parameter of tissue," *Journal of Biomedical Optics*, vol. 19, no. 1, Jan. 2014, ISSN: 1083-3668. DOI: 10.1117/1.JBO.19.1.017007. (visited on 04/16/2020).

[52] *Assorted Spectra, https://omlc.org/spectra/*. [Online]. Available: https://omlc.org/spectra/ (visited on 03/31/2020).

[53] C.-L. Tsai and J.-C. C. W.-J. Wang, "Near-infrared Absorption Property of Biological Soft Tissue Constituents," en, *J. Med. Biol. Eng.*, vol. 21, p. 7, 2001.

[54] M. K. Dasa, C. Markos, J. Janting, and O. Bang, "Multispectral photoacoustic sensing for accurate glucose monitoring using a supercontinuum laser," EN, *JOSA B*, vol. 36, no. 2, A61–A65, Feb. 2019, Publisher: Optical Society of America, ISSN: 1520-8540. DOI: 10.1364/JOSAB.36.000A61. (visited on 03/31/2020).

[55] J. Hui, R. Li, E. H. Phillips, C. J. Goergen, M. Sturek, and J. X. Cheng, "Bond-selective photoacoustic imaging by converting molecular vibration into acoustic waves," English (US), *Photoacoustics*, vol. 4, no. 1, pp. 11–21, Mar. 2016, Publisher: Elsevier GmbH, ISSN: 2213-5979. DOI: 10.1016/j.pacs.2016.01.002. (visited on 03/31/2020).

[56] *Optical Coherence Tomography*, en. [Online]. Available: https://link.springer.com/book/10.1007/978-3-319-06419-2 (visited on 02/10/2023).

[57] D. Huang *et al.*, "Optical coherence tomography," *Science*, vol. 254, no. 5035, pp. 1178–1181, 1991, ISSN: 0036-8075. DOI: 10.1126/science.1957169. [Online]. Available: http://www.scopus.com/inward/record.url?scp=0026254046&partnerID=8YFLogxK (visited on 02/10/2023).

[58] A. G. Podoleanu, G. M. Dobre, D. J. Webb, and D. A. Jackson, "Coherence imaging by use of a Newton rings sampling function," eng, *Optics Letters*,

vol. 21, no. 21, pp. 1789–1791, Nov. 1996, ISSN: 0146-9592. DOI: 10.1364/ol.21.001789.

[59] T. Mitsui, "Dynamic Range of Optical Reflectometry with Spectral Interferometry," en, *Japanese Journal of Applied Physics*, vol. 38, no. 10R, p. 6133, Oct. 1999, Publisher: IOP Publishing, ISSN: 1347-4065. DOI: 10.1143/JJAP.38.6133. [Online]. Available: https://iopscience.iop.org/article/10.1143/JJAP.38.6133/meta (visited on 02/10/2023).

[60] R. Leitgeb, C. K. Hitzenberger, and A. F. Fercher, "Performance of fourier domain vs. time domain optical coherence tomography," EN, *Optics Express*, vol. 11, no. 8, pp. 889–894, Apr. 2003, Publisher: Optica Publishing Group, ISSN: 1094-4087. DOI: 10.1364/OE.11.000889. [Online]. Available: https://opg.optica.org/oe/abstract.cfm?uri=oe-11-8-889 (visited on 02/10/2023).

[61] M. A. Choma, M. V. Sarunic, C. Yang, and J. A. Izatt, "Sensitivity advantage of swept source and Fourier domain optical coherence tomography," EN, *Optics Express*, vol. 11, no. 18, pp. 2183–2189, Sep. 2003, Publisher: Optica Publishing Group, ISSN: 1094-4087. DOI: 10.1364/OE.11.002183. [Online]. Available: https://opg.optica.org/oe/abstract.cfm?uri=oe-11-18-2183 (visited on 02/10/2023).

[62] W. Drexler, M. Liu, A. Kumar, T. Kamali, A. Unterhuber, and R. A. Leitgeb, "Optical coherence tomography today: Speed, contrast, and multimodality," eng, *Journal of Biomedical Optics*, vol. 19, no. 7, 2014, ISSN: 1560-2281. DOI: 10.1117/1.JBO.19.7.071412.

[63] S. Moon and D. Y. Kim, "Ultra-high-speed optical coherence tomography with a stretched pulse supercontinuum source," eng, *Optics Express*, vol. 14, no. 24, pp. 11 575–11 584, Nov. 2006, ISSN: 1094-4087. DOI: 10.1364/oe.14.011575.

[64] B. Potsaid *et al.*, "Ultrahigh speed 1050nm swept source / Fourier domain OCT retinal and anterior segment imaging at 100,000 to 400,000 axial scans per second," EN, *Optics Express*, vol. 18, no. 19, Sep. 2010, Publisher: Optica Publishing Group, ISSN: 1094-4087. DOI: 10.1364/OE.18.020029. [Online]. Available: https://opg.optica.org/oe/abstract.cfm?uri=oe-18-19-20029 (visited on 02/10/2023).

[65] J. Xu *et al.*, "High-performance multi-megahertz optical coherence tomography based on amplified optical time-stretch," eng, *Biomedical Optics Express*, vol. 6, no. 4, pp. 1340–1350, Apr. 2015, ISSN: 2156-7085. DOI: 10.1364/BOE.6.001340.

[66] C. Kong, X. Wei, K. K. M. Tsia, and K. K. Y. Wong, "Ultrafast Green-Light Swept-Source Imaging Through Advanced Fiber-Optic Technologies," *IEEE Journal of Selected Topics in Quantum Electronics*, vol. 24, no. 3, May 2018, Number: 3 Publisher: IEEE, ISSN: 1077-260X. [Online]. Available: https://resolver.caltech.edu/CaltechAUTHORS:20171116-111405260 (visited on 02/10/2023).

[67] T. Klein and R. Huber, "High-speed oct light sources and systems," eng, *Biomedical Optics Express*, vol. 8, no. 2, Feb. 2017, ISSN: 2156-7085. DOI: 10.1364/BOE.8.000828.

[68] S. Tan *et al.*, "High-speed wavelength-swept source at 2.0um and its application in imaging through a scattering medium," *Optics Letters*, vol. 42, no. 8, Apr. 2017, ISSN: 1539-4794. DOI: 10.1364/OL.42.001540.

[69] J. P. Kolb, T. Pfeiffer, M. Eibl, H. Hakert, and R. Huber, "High-resolution retinal swept source optical coherence tomography with an ultra-wideband fourier-domain mode-locked laser at mhz a-scan rates," eng, *Biomedical Optics Express*, vol. 9, no. 1, Jan. 2018, ISSN: 2156-7085. DOI: 10.1364/BOE.9.000120.

[70] L. An, P. Li, T. T. Shen, and R. Wang, "High speed spectral domain optical coherence tomography for retinal imaging at 500,000 a-lines per second," eng, *Biomedical Optics Express*, vol. 2, no. 10, Oct. 2011, ISSN: 2156-7085. DOI: 10.1364/BOE.2.002770.

[71] B. Potsaid *et al.*, "Ultrahigh speed spectral domain oct ophthalmic imaging at 70,000 to 312,500 axial scans per second," eng, *Optics Express*, vol. 16, no. 19, Sep. 2008, ISSN: 1094-4087. DOI: 10.1364/oe.16.015149.

[72] A. G. Podoleanu and A. Bradu, "Master–slave interferometry for parallel spectral domain interferometry sensing and versatile 3D optical coherence tomography," EN, *Opt. Express, OE*, vol. 21, no. 16, pp. 19 324–19 338, Aug. 2013, Publisher: Optica Publishing Group, ISSN: 1094-4087. DOI: 10.1364/OE.21.019324. [Online]. Available: https://opg.optica.org/oe/abstract.cfm?uri=oe-21-16-19324 (visited on 02/14/2023).

[73] S. Rivet, M. Maria, A. Bradu, T. Feuchter, L. Leick, and A. Podoleanu, "Complex master slave interferometry," EN, *Opt. Express, OE*, vol. 24, no. 3, pp. 2885–2904, Feb. 2016, Publisher: Optica Publishing Group, ISSN: 1094-4087. DOI: 10.1364/OE.24.002885. [Online]. Available: https://opg.optica.org/oe/abstract.cfm?uri=oe-24-3-2885 (visited on 02/14/2023).

[74] A. Bradu, S. Rivet, and A. Podoleanu, "Master/slave interferometry – ideal tool for coherence revival swept source optical coherence tomography," EN, *Biomed. Opt. Express, BOE*, vol. 7, no. 7, pp. 2453–2468, Jul. 2016, Publisher: Optica Publishing Group, ISSN: 2156-7085. DOI: 10.1364/BOE.7.002453. [Online]. Available: https://opg.optica.org/boe/abstract.cfm?uri=boe-7-7-2453 (visited on 02/14/2023).

[75] A. Bradu, M. Maria, and A. G. Podoleanu, "Demonstration of tolerance to dispersion of master/slave interferometry," en, *Optics Express*, vol. 23, no. 11, p. 14 148, Jun. 2015, ISSN: 1094-4087. DOI: 10.1364/OE.23.014148. (visited on 03/09/2020).

[76] E. B. Loewenstein, "Reducing the Effects of Noise in a Data Acquisition System by Averaging," en,

[77] G. Abbas, V. Chan, and T. Yee, "A dual-detector optical heterodyne receiver for local oscillator noise suppression," *Journal of Lightwave Technology*, vol. 3, no. 5, pp. 1110–1122, Oct. 1985, Conference Name: Journal of Lightwave Technology, ISSN: 1558-2213. DOI: 10.1109/JLT.1985.1074301.

[78] C. Lee *et al.*, "Combined photoacoustic and optical coherence tomography using a single near-infrared supercontinuum laser source," EN, *Appl. Opt., AO*, vol. 52, no. 9, pp. 1824–1828, Mar. 2013, Publisher: Optica Publishing Group, ISSN: 2155-3165. DOI: 10.1364/AO.52.001824. [Online]. Available: https://opg.optica.org/ao/abstract.cfm?uri=ao-52-9-1824 (visited on 02/14/2023).

[79] X. Liu *et al.*, "Optical coherence photoacoustic microscopy for in vivo multimodal retinal imaging," EN, *Opt. Lett., OL*, vol. 40, no. 7, pp. 1370–1373, Apr. 2015, Publisher: Optica Publishing Group, ISSN: 1539-4794. DOI: 10.1364/OL.40.001370. [Online]. Available: https://opg.optica.org/ol/abstract.cfm?uri=ol-40-7-1370 (visited on 02/14/2023).

# Part II

# Experimental Work

# Chapter 3

# *In-vivo* multi-spectral opto-acoustic microscopy of lipids in the extended near-infrared region

AUTHOR'S NOTE: Part of the experimental work presented in this chapter is based on work which has been reported in a peer-reviewed publication [1] and has been presented at an international conference (Photonics West 2020). The work described in this chapter is a collaboration with Dr. Manoj K. Dasa from Technical University of Denmark (DTU). The laser was built by Manoj in DTU, whereas the imaging system, the imaging procedure and the analysis was designed and built entirely by myself.

## 3.1 Introduction

Having the ability to visualize endogenous biological molecules *in-vivo* without the use of perturbative labels is critical to understanding their physiological impact and subsequent regulatory mechanisms. Opto-acoustic microscopy is a powerful tool for visualizing endogenous agents such as haemoglobin and melanin in real-time. This technique uses the inherent wavelength-dependent absorption of these agents to enable extended penetration depths. Label-free optical imaging techniques have shown great promise in the detection, diagnosis,

and monitoring of various diseases. Among these techniques, OAM stands out for its ability to provide accurate and reliable results without the need for labelling agents [2–5].

Lipids are vital for cellular physiology. They serve as structural components of biological membranes, act as biosynthetic precursors, and store energy. It is crucial to understand the significance of lipids in order to maintain proper cellular function [6]. Contrast agents play a crucial role in identifying fatal chronic diseases such as atherosclerosis and myocardial infarction. They are used to enhance the contrast between different tissues and organs in medical imaging, making it easier for doctors to detect abnormalities [7]. It is imperative that high-resolution label-free imaging of lipids be made available in medical imaging. This is due to the growing demand for accurate and efficient diagnostic tools [6, 8–14]. However, based on early studies focused on OAM, it has been found that the absorption features of other endogenous agents, such as haemoglobin and melanin, hinder the successful imaging of lipids within the traditional optical imaging window of 400 – 700 nm [7, 15].

It is recommended to shift focus towards optical imaging windows in the longer near-infrared wavelength regions of 1100-1300 nm and 1650-1850 nm. This is due to the presence of C-H molecular overtone transitions in these regions, which make them ideal for imaging purposes. [16–18]. The absorption spectrum of lipids exhibits distinct peaks in the 1100-1300 nm (second overtone of C-H bonds) and 1650-1850 nm (first overtone of C-H bonds) ranges, with significantly higher absorption coefficients than other major biological tissue components like water and haemoglobin [19–28]. The absorption of lipids in the first overtone region is stronger than in the second overtone region ($\approx 6.3$ times). This makes the first overtone region the recommended band for detecting developmental changes in biological bodies non-invasively through intravascular opto-acoustic imaging. Water absorption in this spectral region, although exhibits lower absorption than lipids, its presence manifests as increased background noise. The

use of this band however, allows for accurate and precise imaging without the need for invasive procedures [26]. OAM in the first overtone region has been reported on white matter in a rat spinal cord [19], intramuscular fat and Drosophila Melanogaster larva [28] using optical resolution (OR)-OAM mode, and on lipid-laden atherosclerotic plaques and human femoral arteries using IVPAI mode [21, 24–26].

So far, most of the aforementioned reports have used nanosecond optical parametric oscillators (OPOs) as the excitation source for opto-acoustic generation. Despite their broadband tunability with high enough pulse energy density to excite an opto-acoustic signal, OPOs are expensive, with a large footprint and low pulse repetition rate, making them unsuitable for small size and efficient OAM systems [28]. A necessary source that could circumvent the use of an OPO is predicated on supercontinuum( SC) generation [28–38], which can have spectral bandwidths spanning several octaves [28] and provide a brightness order of magnitude higher than a synchrotron [38].

The use of SC laser sources for the practice of MS-OAM applications [34, 39] and OAM based multimodal applications have been already reported [40, 41]. Still, the reported SC spotlights are moreover limited by the emission wavelength or by the pulse energy density needed for MS-OAM of lipids in the first undertone region of C- H bonds. Lately, a SC source pumped at 1047 nm, below the zero-dispersion wavelength of a photonic crystal fibre, has been used for the monitoring of lipids [28]. However, due to the low pulse energy density in the first overtone zone of C-H bonds, multi-spectral opto-acoustic microscopy (MS-OAM) could not be proven. A feasible method for making a suitable SC based source on a simple single-stage erbium-doped fibre amplifier and a few metres of standard single-mode optical fibre (SMF-28), producing enough pulse energy density to perform *ex-vivo* MS-OAM of lipids in the first overtone zone was demonstrated by Dasa et al. [34].

In this chapter, for the first time to my knowledge, *in-vivo* MS-OAM in the

first C-H overtone region is demonstrated by further increasing the pulse energy density of the SC laser. When compared to previously reported SC laser [33], the current source exhibits not only higher power spectral density but also a significantly higher pulse repetition rate, thus increasing the image acquisition speed. Furthermore, the potential of MS-OAM is shown by imaging of lipids on *ex-vivo* adipose tissue and *in-vivo* imaging on *Xenopus laevis* tadpoles over the entire first overtone region. This method can clearly visualise lipid spatial distribution inside both samples with high contrast, paving the way for efficient, and cost-effective label-free lipid imaging in both developmental biology and medicinal applications.

## 3.2 Methods and Materials

### 3.2.1 Ethical Approval

*In-vivo* experiments were performed on the *Xenopus laevis* tadpole at developmental stage 37/38, based on Nieuwkoop and Faber 1956 [42]. Embryos were supplied by the European Xenopus Resource Centre (EXRC, Portsmouth UK) and kept at $\approx 20^0\ C$ in tap water. During the MS-OAM experiments, animals were anaesthetised in $0.1\%$ MS-222 solution (ethyl 3-aminobenzoate methanesulfonate, Sigma-Aldrich). All experimental procedures on stage 37/38 tadpoles are unregulated but were nevertheless approved by the University of Kent's animal welfare ethics committee.

### 3.2.2 MS-OAM system

The schematic diagram of the MS-OAM set up together with a photo of the all-fibre SC laser used in the experiments is presented in Fig. 3.1(a). The MS-OAM system is based on a custom in-house built (in DTU, Denmark) fibre-coupled SC

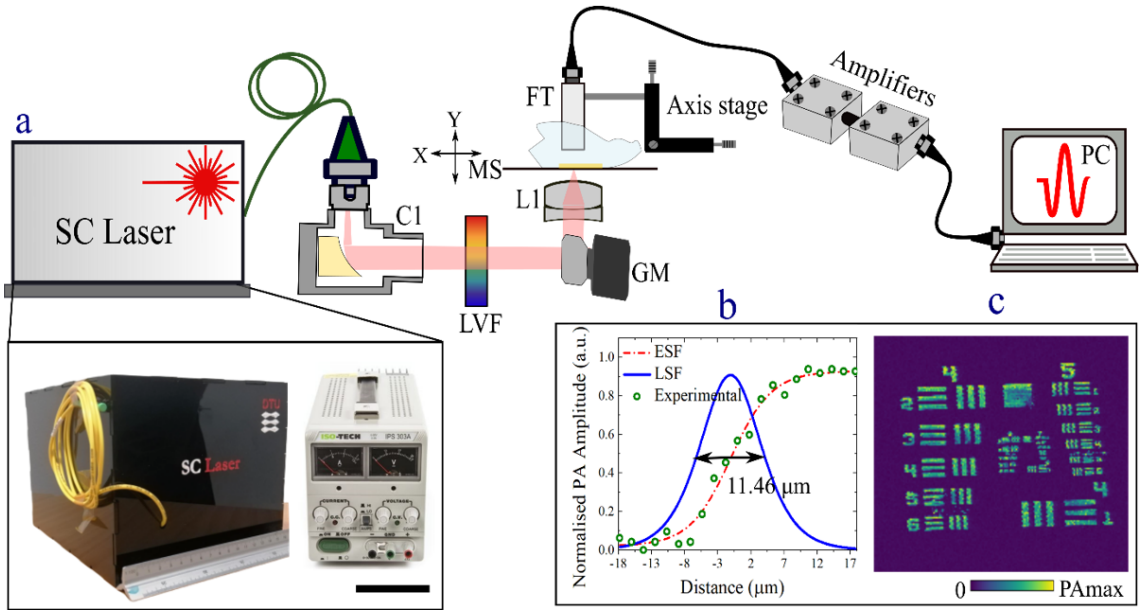


FIGURE 3.1: (a) Schematic of the MS-OAM system. C1: reflective collimator, LVF: linear variable filter, GM: galvo-mirrors, L1: achromatic lens, MS: microscopy slide, FT: flat transducer, PC: the personal computer. The photograph in the bottom left shows the all-fibre SC laser and the power supply unit with a scale bar of 10 cm. (b): Lateral resolution of the MS-OAM system estimated by using the edge and line spread functions. (c): OAM image of the USAF resolution target at 1720 nm.

optical source as the excitation source. A linear variable filter (LVF) (LVF 1.2-2.5-3.5-15-0.5, Vortex Optical Coatings) was utilised to spectrally filter the spectrum of the optical source for MS-OAM. A pair of orthogonal galvanometer-based $X, Y$ scanners (6220H, Cambridge Technology Ltd) was employed for the lateral scanning of the filtered excitation beam over the sample. The excitation beam was then focused onto the sample through an achromatic doublet lens (AC254-040-C-ML, Thorlabs). The acoustic signal generated by the focused optical excitation beam was detected and converted to electrical signal by a custom-made ultrasonic transducer (COPAC) with a centre frequency of 10 MHz.

Two low-noise wide-band amplifiers were used to amplify the detected opto-acoustic signal (ZFL-500LN, Mini-Circuits). The amplified signal was then conveyed towards the input of a fast digitizer (PCI-5124, National Instruments) for data processing. The digitizer, hosted in a PC, operates at 200 MS/second, allowing signal up to a maximum bandwidth of 125 MHz. The digitizer's inbuilt

hardware filter was configured as a low pass filter up to 40 MHz. Each pulse was digitised into 2,000 sampling points within an interval of 10 $\mu s$, while the optical beam was scanned over the sample. However, the data is cropped into 410 points around the area of interest to improve the signal-to-noise ratio (SNR) and maintain an isometrically resolved image. A triangle signal drives the rapid galvo-scanner at 122 Hz; the rising part of the triangular signal is used for acquisition, while the descending component is employed for data processing. This ensures that each B-scan image can be displayed in real time. As a result of the optical source being set to a repetition rate of 100 kHz, each resulting *B-scan* image is made up of $410$ lateral pixels. As a consequence, a complete 3D volumetric image of size $410 \times 410 \times 410$ pixels is acquired in 3.2 s.

Following each lateral scan of the optical beam over the sample, the signal is processed by a Hilbert transform to obtain the envelope of the sample's opto-acoustic signal in order to deliver the acoustic depth profile (*A-scan*) for each lateral pixel, and then the depth profiles are assembled to obtain a *B-scan*. To ensure real-time display of *B-scan* images at a frame rate of 122 Hz, it was necessary for the fast galvo-scanner to complete its return to the initial position within 8.2 ms after processing 410 *A-scans*.

To enable acoustic coupling, all samples used in the studies were placed in Petri dishes and immersed in either clear ultrasonic gel for *ex-vivo* tests or a water-based solution for *in-vivo* research. Due to the limited transparency of the available petri dish within the desired spectral window, a custom imaging window was constructed at the bottom of the dish. This window was then sealed using a microscope slide with a thickness of 0.2 mm. To support and align the sample holder and transducer to the optical excitation beam, two separate 3D translation stages were employed.

The MS-OAM system's lateral resolution was measured experimentally by imaging the edge of an element on a positive 1951 United States Air Force test target (R1DS1P, Thorlabs). As shown in Fig. 3.1(b), the edge spread function (ESF)

was calculated by fitting the raw opto-acoustic signal collected from scanning the edge in steps of 1.6 $\mu m$. The line spread function (LSF) was then calculated by taking the derivative of the ESF. The system's lateral resolution is defined as the full width at half maximum (FWHM) of the LSF and was found to be $\approx 11.46$ $\mu m$. The theoretical lateral resolution of the MS-OAM system at the beam focus was calculated to be $\approx 10.79$ $\mu m$ at a 1720 nm excitation wavelength, indicating that the system is close to the diffraction limit. The opto-acoustic maximum amplitude projection of the test target is shown in Fig. 3.1(c).

## 3.3 Results and Discussion

### 3.3.1 *Ex-vivo* MS-OAM imaging of Adipose tissue

MS-OAM imaging in the 1600-1800 nm wavelength range was performed on a thin slice (approximately 3 mm) of sheep adipose tissue. The LVF was used to filter six excitation bands from the SC laser in 40 nm increments (Fig. 3.1). The raw data is acquired and analysed using in-house software written in LabVIEW. The program instructs a fast digitizer to transform the analogue signal gathered by the transducer to digital in synchronism with the optical pulses (generated by the source), and the start and stop of lateral scanning (by the galvo-scanners).

The opto-acoustic signal is digitised for each position of the beam on the sample, and an *A-scan* is generated using a Hilbert transform. An intensity graph is created by displaying the opto-acoustic amplitudes recovered from each acquired *A-scan* as a function of $X$ and $Y$ position to build an OAM image. As mentioned earlier, a complete 3D volumetric image of size $410 \times 410 \times 410$ pixels is acquired in 3.2 s. In order to enhance the signal-to-noise ratio, a commonly employed practice in OAM, the data acquisition process is repeated 16 times, and the acquired signals are averaged (taking the average over 16 *A-scans*) prior to generating a

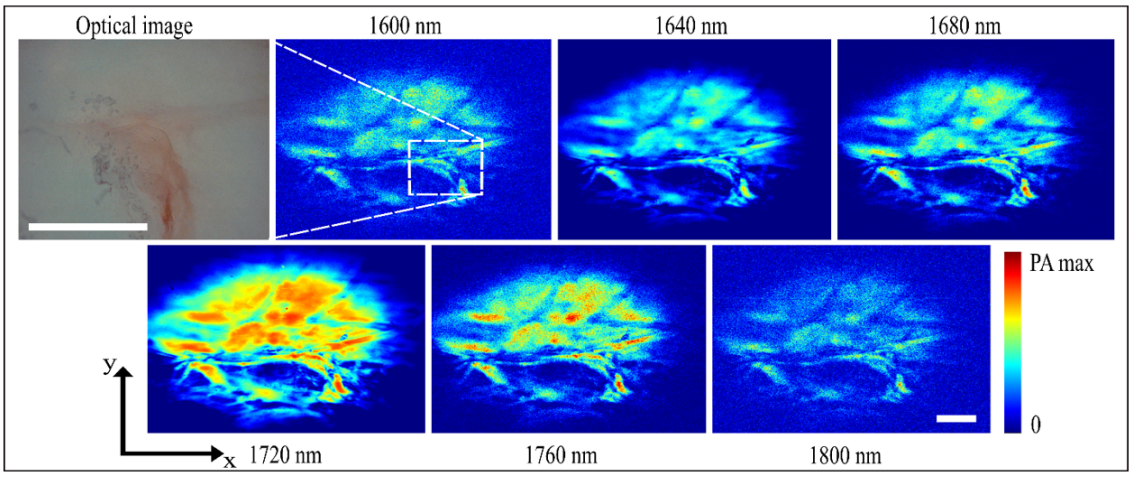


FIGURE 3.2: Optical image and MS-OAM images of *ex-vivo* adipose tissue. Six z-projected *en-face* MS-OAM images are acquired from 1600 nm to 1800 nm in steps of 40 nm. The white bar in the optical image and the last MS-OAM image at 1800 nm represents the scale bar of 1 mm.

*B-scan*. Therefore, the OAM images demonstrated in Fig. 3.2, require 51.2 s. This technique improves the image contrast.

Figure 3.2 shows an optical image and MS-OAM images of *ex-vivo* adipose tissue that are z-projected *en-face* images at six different excitation bands. The images are normalised to their respective pulse energy ([1], page 4) in the excitation band used. The *ex-vivo* adipose tissue pictures show an opto-acoustic amplitude peak at 1720 nm, which is comparable with the opto-acoustic spectrum observations described in our prior report [34]. Figure 3.3(a) shows the opto-acoustic spectra of tissue obtained from two separate areas; locations revealed higher opto-acoustic absorption at 1720 nm, which may be due to higher lipid absorption at 1720 nm attributable to the first overtone transition of C-H bonds [21, 25, 28, 34]. The opto-acoustic spectra are normalized considering the EPP variations at each wavelength.

The SNR (ratio of the detected opto-acoustic signal to the total noise at each *A-scan*) of MS-OAM images at all six excitation bands is computed and displayed in Fig. 3.3(b). As expected, the SNR is greater at 1720 nm (18.1 dB) when compared to other excitation bands because lipid absorption is stronger at 1720 nm. It is worth mentioning that the LVF bands have a bandwidth of 30 - 50 nm. This

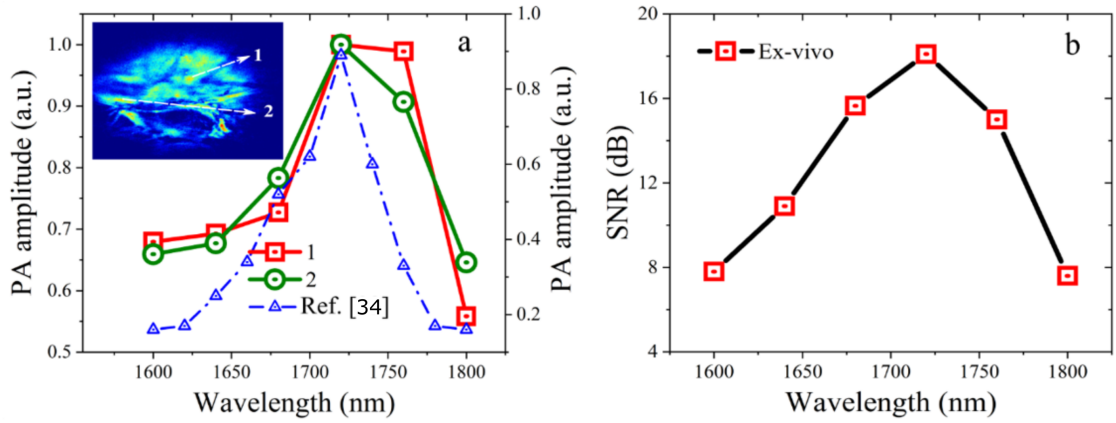


FIGURE 3.3: (a) Normalized opto-acoustic amplitudes at two different regions (labelled 1 and 2 in the inset) for the six excitation bands with corresponding opto-acoustic amplitudes for adipose tissue measurements reported in our previous study [34]. The area of each region is 0.087 $mm^2$. (b) Measured spectral variation of the SNR of *ex-vivo* adipose tissue measured in MS-OAM images.

introduces uncertainty as more wavelengths are absorbed and contribute to the opto-acoustic signal amplitude.

### 3.3.2 *In-vivo* MS-OAM imaging of the *Xenopus laevis* tadpole

*Xenopus laevis* tadpoles were raised in water to stage 37-38, about 53 hrs post-fertilisation. Tadpoles were chosen for MS-OAM imaging at this early stage of development because they offer simple access to the yolk sac, which is a well-defined location (Fig. 3.4) with a high concentration of lipids [39].

Furthermore, the epidermis surrounding the yolk sac is pigment-free, allowing for unhindered laser penetration through the entire sample. Throughout the experiment, laser radiation in the excitation bands is well within the maximum permissible exposure (MPE) threshold. The MPE for tissue is 1 $J/cm^2$ for ns pulses and for the SC excitation band with maximum pulse energy density (914 nJ in the 1600 nm excitation band), the exposure level is about 0.88 $J/cm^2$.

Figure 3.4 shows a microscope image of the tadpole along with z-projected *en-face* MS-OAM images of the whole body at the six different excitation bands. The MS-OAM images are averaged over 16 *A-scans* and normalised to the respective pulse energies in the excitation bands. Due to the high concentration of lipids,

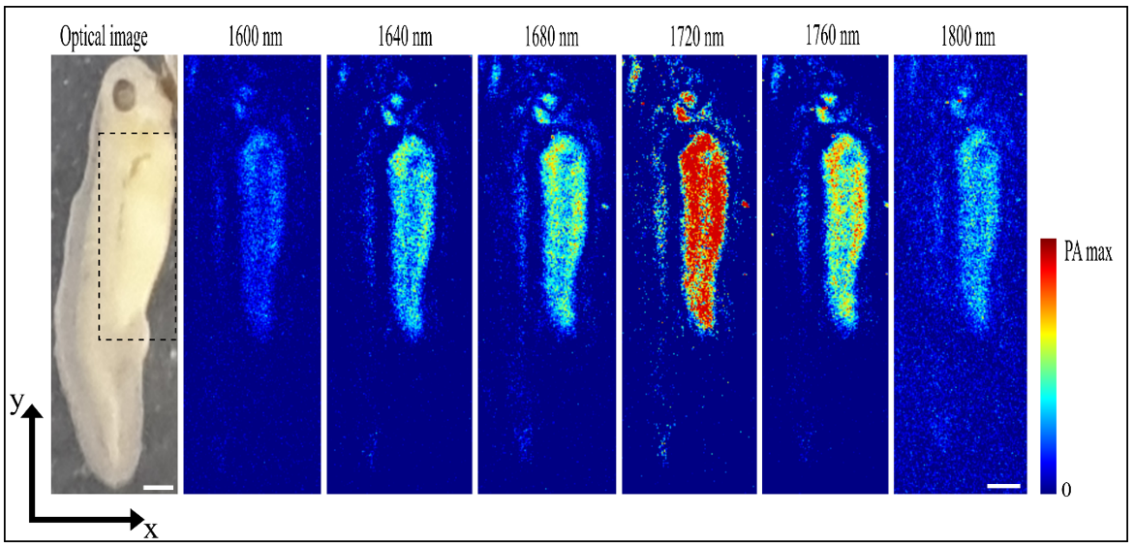


FIGURE 3.4: Optical image and 6 *in-vivo* z-projected *en-face* MS-OAM images of a *Xenopus laevis* tadpole acquired from 1600 nm to 1800 nm in steps of 40 nm. The highlighted region in the optical image shows the yolk sac. The scale bar represents 1 mm.

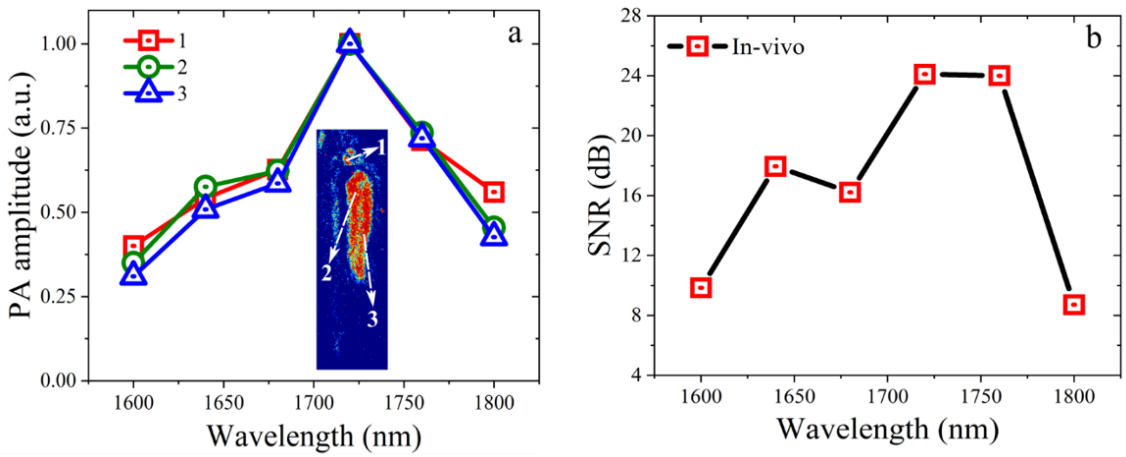


FIGURE 3.5: (a) Normalized opto-acoustic amplitudes of a small region in the MS-OAM images of a tadpole at three different places (labelled 1, 2, and 3) for the six excitation bands. (b) Measured SNR of tadpole MS-OAM images at all the six excitation bands.

a significant signal is obtained at 1720 nm excitation, and the contrast decreases at all other excitation wavelengths. As observed in the tadpole's MS-OAM images, the yolk sack section exhibits opto-acoustic signals that are dispersed across the section along its anterior-posterior and ventral-dorsal axes. The existence of large amounts of lipid molecules, which exhibit substantial optical absorption in response to the first overtone transition of the C-H bond, can be linked to strong

opto-acoustic signals from the yolk sac [43]. This is consistent with the known presence of the lipoprotein Vitellogenin in the yolk sac of *Xenopus laevis* tadpoles [43].

Figure 3.5(a) depicts the opto-acoustic spectra of three distinct areas (each with a size of 0.087 $mm^2$) in the tadpole MS-OAM images obtained at the six excitation bands mentioned above. The opto-acoustic signals exhibit consistent results with the predicted maxima at 1720 nm. The SNR of the *in-vivo* images at the six excitation bands is calculated and displayed in Fig. 3.5(b). Again, the SNR is higher at 1720 nm when compared to other excitation bands. SNR for *in-vivo* MS-OAM images is higher when in comparison to the SNR for *ex-vivo* MS-OAM images as the image scan area used for *in-vivo* experiments is smaller than the scan area used for the *ex-vivo* experiments.

### 3.3.3 Exploring the MS-OAM capabilities (Megahertz MS-OAM Imaging)

The all-fibre SC laser has the capability to tune the pulse repetition rate from a few kHz up to 1 MHz. In addition, the imaging system devised for the experiments conducted during this study can also achieve very fast imaging rates. These capabilities where further exploited aiming to push for another breakthrough in MHz MS-OAM imaging using SC optical sources.

Four images at different imaging speeds were acquired and the results are presented in Fig. 3.6. A carbon-fibre tape sample was used. A drop in SNR towards higher imaging speeds is evident as expected. The SC laser could be tuned up to 2 MHz by additional optimization and updating the software. This however required the laser to be shipped back to DTU.

The fastest single wavelength OAM imaging instrument was reported by Allen et al. (P. Beard's group) using a master oscillator power amplifier configuration,

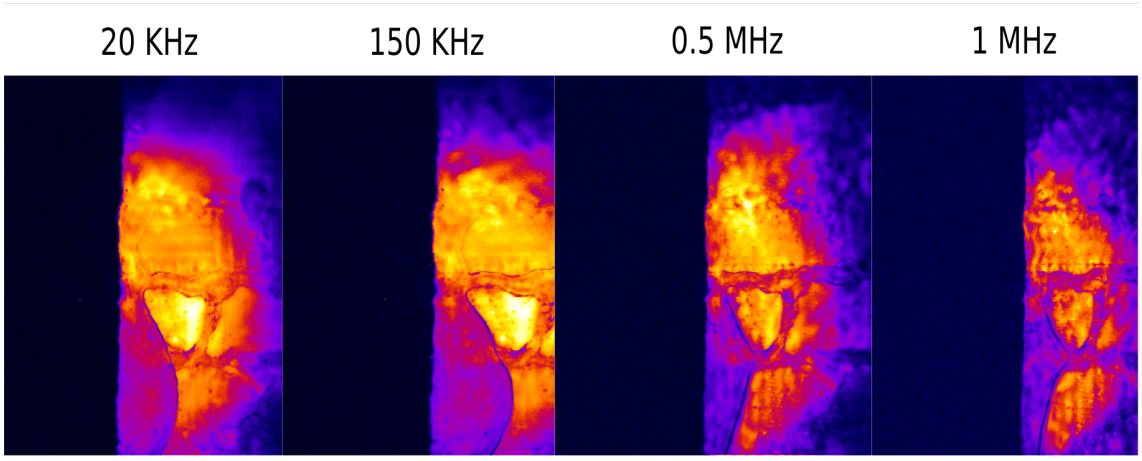


FIGURE 3.6: MS-OAM images acquired at different pulse repetition rates (20 kHz, 150 kHz, 500 kHz and 1 MHz). The frame rate was adjusted to maintain a similar field of view. This however, was not done to perfection due to the scanning speed limitation of the fast galvo-scanner.

operating at an emission wavelength of 1064 nm, which was then frequency doubled to 532 nm [44]. The fastest broadband source however was reported by Dasa et al. devising a custom made SC source with a 100 kHz pulse repetition rate [1].

The motivation behind these preliminary results presented in this section, is to achieve Mega Hertz MS-OAM imaging. The estimated achievable pulse repetition rate for the in-house built SC source is 2 MHz. If four *A-scans* are averaged at a time, a *B-scan* can be acquired every 1 ms. A frame rate of 1000 kHz however, can only be achieved using advanced scanning methods such as the scanning method presented by Allen et al., or by employing resonant scanning mirrors [45]. As such, a three-dimensional image can be obtained within 500 ms. An image acquired within a few hundred milliseconds does not require tracking when performing *in-vivo* MS-OAM imaging, since it is as fast, or faster than involuntary movement. The aforementioned aspect and the low cost of the in-house SC source can drastically improve the adaptability of OAM instruments in pre-clinical and ultimately clinical applications.

## 3.4 Conclusion

In this chapter, MS-OAM imaging of lipids is demonstrated by employing a high-pulse energy all-fibre SC source based on standard telecom range optical components. The pulse energy density of the filtered optical pulses from the SC source is sufficient for MS-OAM research on lipids through the first overtone transition of C-H vibration bonds (1650-1850 nm). The utility of such an optical source is demonstrated by conducting MS-OAM imaging of lipids in *ex-vivo* adipose tissue and *in-vivo Xenopus laevis* tadpole by utilising the SC laser in combination with a linear variable filter.

This work demonstrated that the MS-OAM system is capable of monitoring lipids in both *ex-vivo* and *in-vivo* tissues, making it suitable for a wide range of applications. The proposed high pulse energy SC laser opens the door to more compact sources for label-free imaging of lipids in both developmental biology and medical imaging.

Scaling the pulse energy density of the SC optical source will enable MS-OAM imaging without any signal averaging. Furthermore, the higher pulse energy density of the laser makes possible the use of narrow band pass filters, allowing for high-resolution MS-OAM of multiple endogenous biological molecules (lipids, glucose, water, and collagen) that exhibit dominant absorption features in the developed source's emission wavelength (1540-1840 nm).

In order to avoid the tadpoles movement, which is unpredictable, the tadpoles were submerged in anesthetic solution instead of coupling water or ultrasound gel. As such, the tadpoles were efficiently immobilized without the need of pinning them down with needles as usually performed in such cases, avoiding harming the tadpole.

# References

[1] M. K. Dasa *et al.*, "All-fibre supercontinuum laser for in vivo multispectral photoacoustic microscopy of lipids in the extended near-infrared region," en, *Photoacoustics*, vol. 18, p. 100 163, Jun. 2020, ISSN: 2213-5979. DOI: 10.1016/j.pacs.2020.100163. (visited on 03/09/2020).

[2] J. Yao and L. V. Wang, "Photoacoustic microscopy," *Laser & Photonics Reviews*, vol. 7, no. 5, pp. 758–778, 2013, _eprint: https://onlinelibrary.wiley.com/doi/pd ISSN: 1863-8899. DOI: 10.1002/lpor.201200060. [Online]. Available: https://onlinelibrary.wiley.com/doi/abs/10.1002/lpor.201200060 (visited on 02/09/2023).

[3] E. M. Strohm, M. J. Moore, and M. C. Kolios, "Single Cell Photoacoustic Microscopy: A Review," *IEEE Journal of Selected Topics in Quantum Electronics*, vol. 22, no. 3, pp. 137–151, Feb. 2016, Conference Name: IEEE Journal of Selected Topics in Quantum Electronics, ISSN: 1558-4542. DOI: 10.1109/JSTQE.2015.2497323.

[4] H. F. Zhang, K. Maslov, M. Sivaramakrishnan, G. Stoica, and L. V. Wang, "Imaging of hemoglobin oxygen saturation variations in single vessels in vivo using photoacoustic microscopy," *Appl. Phys. Lett.*, vol. 90, no. 5, p. 053 901, Jan. 2007, Publisher: American Institute of Physics, ISSN: 0003-6951. DOI: 10.1063/1.2435697. [Online]. Available: https://aip.scitation.org/doi/full/10.1063/1.2435697 (visited on 02/14/2023).

[5] J.-T. Oh, M.-L. Li, H. F. Zhang, K. Maslov, and L. V. Wang, "Three-dimensional imaging of skin melanoma in vivo by dual-wavelength photoacoustic microscopy," *JBO*, vol. 11, no. 3, p. 034 032, May 2006, Publisher: SPIE, ISSN: 1083-3668, 1560-2281. DOI: 10.1117/1.2210907. [Online]. Available: https://www.spiedigitallibrary.org/journals/journal-of-biomedical-optics/volume-11/issue-3/034032/Three-

dimensional-imaging-of-skin-melanoma-in-vivo-by-dual/10.1117/1.2210907.full (visited on 02/14/2023).

[6] R. V. Farese and T. C. Walther, "Lipid Droplets Finally Get a Little R-E-S-P-E-C-T," English, *Cell*, vol. 139, no. 5, pp. 855–860, Nov. 2009, Publisher: Elsevier, ISSN: 0092-8674, 1097-4172. DOI: 10.1016/j.cell.2009.11.005. [Online]. Available: https://www.cell.com/cell/abstract/S0092-8674(09)01417-2 (visited on 02/14/2023).

[7] P. C. Beard and T. N. Mills, "Characterization of post mortem arterial tissue using time-resolved photoacoustic spectroscopy at 436, 461 and 532 nm," en, *Phys. Med. Biol.*, vol. 42, no. 1, p. 177, Jan. 1997, ISSN: 0031-9155. DOI: 10.1088/0031-9155/42/1/012. [Online]. Available: https://dx.doi.org/10.1088/0031-9155/42/1/012 (visited on 02/14/2023).

[8] S. O. Zhang, R. Trimble, F. Guo, and H. Y. Mak, "Lipid droplets as ubiquitous fat storage organelles in C. elegans," *BMC Cell Biology*, vol. 11, no. 1, p. 96, Dec. 2010, ISSN: 1471-2121. DOI: 10.1186/1471-2121-11-96. [Online]. Available: https://doi.org/10.1186/1471-2121-11-96 (visited on 02/14/2023).

[9] A. Folick, W. Min, and M. C. Wang, "Label-free imaging of lipid dynamics using Coherent Anti-stokes Raman Scattering (CARS) and Stimulated Raman Scattering (SRS) microscopy," en, *Current Opinion in Genetics & Development*, Developmental mechanisms, patterning and evolution, vol. 21, no. 5, pp. 585–590, Oct. 2011, ISSN: 0959-437X. DOI: 10.1016/j.gde.2011.09.003. [Online]. Available: https://www.sciencedirect.com/science/article/pii/S0959437X11001389 (visited on 02/14/2023).

[10] J. Chi *et al.*, "Three-Dimensional Adipose Tissue Imaging Reveals Regional Variation in Beige Fat Biogenesis and PRDM16-Dependent Sympathetic Neurite Density," en, *Cell Metabolism*, vol. 27, no. 1, 226–236.e3, Jan. 2018,

ISSN: 1550-4131. DOI: 10.1016/j.cmet.2017.12.011. [Online]. Available: https://www.sciencedirect.com/science/article/pii/S1550413117307246 (visited on 02/14/2023).

[11] T. Huff and J.-X. Cheng, "In vivo coherent anti-Stokes Raman scattering imaging of sciatic nerve tissue," en, *Journal of Microscopy*, vol. 225, no. 2, pp. 175–182, 2007, _eprint: https://onlinelibrary.wiley.com/doi/pdf/10.1111/j.1365-2818.2007.01729.x, ISSN: 1365-2818. DOI: 10.1111/j.1365-2818.2007.01729.x. [Online]. Available: https://onlinelibrary.wiley.com/doi/abs/10.1111/j.1365-2818.2007.01729.x (visited on 02/14/2023).

[12] C.-R. Hu, D. Zhang, M. N. Slipchenko, J.-X. Cheng, and B. Hu, "Label-free real-time imaging of myelination in the Xenopus laevis tadpole by in vivo stimulated Raman scattering microscopy," *JBO*, vol. 19, no. 8, p. 086 005, Aug. 2014, Publisher: SPIE, ISSN: 1083-3668, 1560-2281. DOI: 10.1117/1.JBO.19.8.086005. [Online]. Available: https://www.spiedigitallibrary.org/journals/journal-of-biomedical-optics/volume-19/issue-8/086005/Label-free-real-time-imaging-of-myelination-in-the-Xenopus/10.1117/1.JBO.19.8.086005.full (visited on 02/14/2023).

[13] M. J. Den Broeder *et al.*, "Altered Adipogenesis in Zebrafish Larvae Following High Fat Diet and Chemical Exposure Is Visualised by Stimulated Raman Scattering Microscopy," en, *International Journal of Molecular Sciences*, vol. 18, no. 4, p. 894, Apr. 2017, Number: 4 Publisher: Multidisciplinary Digital Publishing Institute, ISSN: 1422-0067. DOI: 10.3390/ijms18040894. [Online]. Available: https://www.mdpi.com/1422-0067/18/4/894 (visited on 02/14/2023).

[14] C.-H. Chien, W.-W. Chen, J.-T. Wu, and T.-C. Chang, "Label-free imaging of Drosophila in vivo by coherent anti-Stokes Raman scattering and two-photon excitation autofluorescence microscopy," *JBO*, vol. 16, no. 1, p. 016 012, Jan. 2011, Publisher: SPIE, ISSN: 1083-3668, 1560-2281. DOI: 10.1117/1.3528642. [Online]. Available: https://www.spiedigitallibrary.org/journals/journal-of-biomedical-optics/volume-16/issue-1/016012/Label-free-imaging-of-Drosophila-in-vivo-by-coherent-anti/10.1117/1.3528642.full (visited on 02/14/2023).

[15] S. Sethuraman, J. H. Amirian, S. H. Litovsky, R. W. Smalling, and S. Y. Emelianov, "Spectroscopic intravascular photoacoustic imaging to differentiate atherosclerotic plaques," EN, *Opt. Express, OE*, vol. 16, no. 5, pp. 3362–3367, Mar. 2008, Publisher: Optica Publishing Group, ISSN: 1094-4087. DOI: 10.1364/OE.16.003362. [Online]. Available: https://opg.optica.org/oe/abstract.cfm?uri=oe-16-5-3362 (visited on 02/14/2023).

[16] H.-W. Wang *et al.*, "Label-Free Bond-Selective Imaging by Listening to Vibrationally Excited Molecules," *Phys. Rev. Lett.*, vol. 106, no. 23, p. 238 106, Jun. 2011, Publisher: American Physical Society. DOI: 10.1103/PhysRevLett.106.238106. [Online]. Available: https://link.aps.org/doi/10.1103/PhysRevLett.106.238106 (visited on 02/14/2023).

[17] T. J. Allen, P. C. Beard, A. Hall, A. P. Dhillon, and J. S. Owen, "Spectroscopic photoacoustic imaging of lipid-rich plaques in the human aorta in the 740 to 1400 nm wavelength range," *JBO*, vol. 17, no. 6, p. 061 209, May 2012, Publisher: SPIE, ISSN: 1083-3668, 1560-2281. DOI: 10.1117/1.JBO.17.6.061209. [Online]. Available: https://www.spiedigitallibrary.org/journals/journal-of-biomedical-optics/volume-17/issue-6/061209/Spectroscopic-photoacoustic-imaging-of-

lipid-rich-plaques-in-the-human/10.1117/1.JBO.17.6.061209.full (visited on 02/14/2023).

[18] P. Wang, P. Wang, H.-W. Wang, and J.-X. Cheng, "Mapping lipid and collagen by multispectral photoacoustic imaging of chemical bond vibration," *JBO*, vol. 17, no. 9, p. 096 010, Sep. 2012, Publisher: SPIE, ISSN: 1083-3668, 1560-2281. DOI: 10.1117/1.JBO.17.9.096010. [Online]. Available: https://www.spiedigitallibrary.org/journals/journal-of-biomedical-optics/volume-17/issue-9/096010/Mapping-lipid-and-collagen-by-multispectral-photoacoustic-imaging-of-chemical/10.1117/1.JBO.17.9.096010.full (visited on 02/14/2023).

[19] K. Jansen *et al.*, "Spectroscopic intravascular photoacoustic imaging of lipids in atherosclerosis," *JBO*, vol. 19, no. 2, p. 026 006, Feb. 2014, Publisher: SPIE, ISSN: 1083-3668, 1560-2281. DOI: 10.1117/1.JBO.19.2.026006. [Online]. Available: https://www.spiedigitallibrary.org/journals/journal-of-biomedical-optics/volume-19/issue-2/026006/Spectroscopic-intravascular-photoacoustic-imaging-of-lipids-in-atherosclerosis/10.1117/1.JBO.19.2.026006.full (visited on 02/14/2023).

[20] W. Wu, P. Wang, J.-X. Cheng, and X.-M. Xu, "Assessment of White Matter Loss Using Bond-Selective Photoacoustic Imaging in a Rat Model of Contusive Spinal Cord Injury," *Journal of Neurotrauma*, vol. 31, no. 24, pp. 1998–2002, Dec. 2014, Publisher: Mary Ann Liebert, Inc., publishers, ISSN: 0897-7151. DOI: 10.1089/neu.2014.3349. [Online]. Available: https://www.liebertpub.com/doi/abs/10.1089/neu.2014.3349 (visited on 02/14/2023).

[21] K. Jansen, M. Wu, A. F. W. van der Steen, and G. van Soest, "Photoacoustic imaging of human coronary atherosclerosis in two spectral bands," en,

*Photoacoustics*, vol. 2, no. 1, pp. 12–20, Mar. 2014, ISSN: 2213-5979. DOI: 10.1016/j.pacs.2013.11.003. [Online]. Available: https://www.sciencedirect.com/science/article/pii/S2213597913000372 (visited on 02/14/2023).

[22] T. Buma, B. C. Wilkinson, and T. C. Sheehan, "Near-infrared spectroscopic photoacoustic microscopy using a multi-color fiber laser source," EN, *Biomed. Opt. Express, BOE*, vol. 6, no. 8, pp. 2819–2829, Aug. 2015, Publisher: Optica Publishing Group, ISSN: 2156-7085. DOI: 10.1364/BOE.6.002819. [Online]. Available: https://opg.optica.org/boe/abstract.cfm?uri=boe-6-8-2819 (visited on 02/14/2023).

[23] J. Hui *et al.*, "High-speed intravascular photoacoustic imaging at 1.7 m with a KTP-based OPO," EN, *Biomed. Opt. Express, BOE*, vol. 6, no. 11, pp. 4557–4566, Nov. 2015, Publisher: Optica Publishing Group, ISSN: 2156-7085. DOI: 10.1364/BOE.6.004557. [Online]. Available: https://opg.optica.org/boe/abstract.cfm?uri=boe-6-11-4557 (visited on 02/14/2023).

[24] Z. Piao *et al.*, "High speed intravascular photoacoustic imaging with fast optical parametric oscillator laser at 1.7m," *Appl. Phys. Lett.*, vol. 107, no. 8, p. 083 701, Aug. 2015, Publisher: American Institute of Physics, ISSN: 0003-6951. DOI: 10.1063/1.4929584. [Online]. Available: https://aip.scitation.org/doi/full/10.1063/1.4929584 (visited on 02/14/2023).

[25] M. Wu, K. Jansen, A. F. W. v. d. Steen, and G. v. Soest, "Specific imaging of atherosclerotic plaque lipids with two-wavelength intravascular photoacoustics," EN, *Biomed. Opt. Express, BOE*, vol. 6, no. 9, pp. 3276–3286, Sep. 2015, Publisher: Optica Publishing Group, ISSN: 2156-7085. DOI: 10.1364/BOE.6.003276. [Online]. Available: https://opg.optica.org/boe/abstract.cfm?uri=boe-6-9-3276 (visited on 02/14/2023).

[26] J. Hui, R. Li, E. H. Phillips, C. J. Goergen, M. Sturek, and J. X. Cheng, "Bond-selective photoacoustic imaging by converting molecular vibration into acoustic waves," English (US), *Photoacoustics*, vol. 4, no. 1, pp. 11–21, Mar. 2016, Publisher: Elsevier GmbH, ISSN: 2213-5979. DOI: 10.1016/j.pacs.2016.01.002. (visited on 03/31/2020).

[27] T. Buma, J. L. Farland, and M. R. Ferrari, "Near-infrared multispectral photoacoustic microscopy using a graded-index fiber amplifier," en, *Photoacoustics*, Special Issue: Photoacoustic Microscopy, vol. 4, no. 3, pp. 83–90, Sep. 2016, ISSN: 2213-5979. DOI: 10.1016/j.pacs.2016.08.002. [Online]. Available: https://www.sciencedirect.com/science/article/pii/S221359791630026X (visited on 02/14/2023).

[28] T. Buma, N. C. Conley, and S. W. Choi, "Multispectral photoacoustic microscopy of lipids using a pulsed supercontinuum laser," en, *Biomedical Optics Express*, vol. 9, no. 1, p. 276, Jan. 2018, ISSN: 2156-7085, 2156-7085. DOI: 10.1364/BOE.9.000276. (visited on 03/09/2020).

[29] J. M. Dudley, G. Genty, and S. Coen, "Supercontinuum generation in photonic crystal fiber," *Rev. Mod. Phys.*, vol. 78, no. 4, pp. 1135–1184, Oct. 2006, Publisher: American Physical Society. DOI: 10.1103/RevModPhys.78.1135. [Online]. Available: https://link.aps.org/doi/10.1103/RevModPhys.78.1135 (visited on 02/14/2023).

[30] C. Markos, J. C. Travers, A. Abdolvand, B. J. Eggleton, and O. Bang, "Hybrid photonic-crystal fiber," *Rev. Mod. Phys.*, vol. 89, no. 4, p. 045 003, Nov. 2017, Publisher: American Physical Society. DOI: 10.1103/RevModPhys.89.045003. [Online]. Available: https://link.aps.org/doi/10.1103/RevModPhys.89.045003 (visited on 02/14/2023).

[31] A. Boucon, A. Fotiadi, P. Mégret, H. Maillotte, and T. Sylvestre, "Low-threshold all-fiber 1000nm supercontinuum source based on highly non-linear fiber," en, *Optics Communications*, vol. 281, no. 15, pp. 4095–4098, Aug. 2008, ISSN:

0030-4018. DOI: 10.1016/j.optcom.2008.04.024. [Online]. Available: https://www.sciencedirect.com/science/article/pii/S0030401808003763 (visited on 02/14/2023).

[32] M. M. Bondu *et al.*, "High energy supercontinuum sources using tapered photonic crystal fibers for multispectral photoacoustic microscopy," *JBO*, vol. 21, no. 6, p. 061 005, Feb. 2016, Publisher: SPIE, ISSN: 1083-3668, 1560-2281. DOI: 10.1117/1.JBO.21.6.061005. [Online]. Available: https://www.spiedigitallibrary.org/journals/journal-of-biomedical-optics/volume-21/issue-6/061005/High-energy-supercontinuum-sources-using-tapered-photonic-crystal-fibers-for/10.1117/1.JBO.21.6.061005.full (visited on 02/14/2023).

[33] E. Aytac-Kipergil *et al.*, "Development of a Fiber Laser with Independently Adjustable Properties for Optical Resolution Photoacoustic Microscopy," en, *Sci Rep*, vol. 6, no. 1, p. 38 674, Dec. 2016, ISSN: 2045-2322. DOI: 10.1038/srep38674. [Online]. Available: https://www.nature.com/articles/srep38674 (visited on 02/14/2023).

[34] M. K. Dasa, C. Markos, M. Maria, C. R. Petersen, P. M. Moselund, and O. Bang, "High-pulse energy supercontinuum laser for high-resolution spectroscopic photoacoustic imaging of lipids in the 1650-1850 nm region," EN, *Biomed. Opt. Express, BOE*, vol. 9, no. 4, pp. 1762–1770, Apr. 2018, Publisher: Optica Publishing Group, ISSN: 2156-7085. DOI: 10.1364/BOE.9.001762. [Online]. Available: https://opg.optica.org/boe/abstract.cfm?uri=boe-9-4-1762 (visited on 02/14/2023).

[35] M. K. Dasa, C. Markos, J. Janting, and O. Bang, "Multispectral photoacoustic sensing for accurate glucose monitoring using a supercontinuum laser," EN, *JOSA B*, vol. 36, no. 2, A61–A65, Feb. 2019, Publisher: Optical Society of America, ISSN: 1520-8540. DOI: 10.1364/JOSAB.36.000A61. (visited on 03/31/2020).

[36] N. M. Israelsen *et al.*, "Real-time high-resolution mid-infrared optical coherence tomography," en, *Light Sci Appl*, vol. 8, no. 1, p. 11, Jan. 2019, Number: 1 Publisher: Nature Publishing Group, ISSN: 2047-7538. DOI: 10.1038/s41377-019-0122-5. [Online]. Available: https://www.nature.com/articles/s41377-019-0122-5 (visited on 02/14/2023).

[37] C. R. Petersen, P. M. Moselund, L. Huot, L. Hooper, and O. Bang, "Towards a table-top synchrotron based on supercontinuum generation," en, *Infrared Physics & Technology*, vol. 91, pp. 182–186, Jun. 2018, ISSN: 1350-4495. DOI: 10.1016/j.infrared.2018.04.008. [Online]. Available: https://www.sciencedirect.com/science/article/pii/S1350449518301129 (visited on 02/14/2023).

[38] C. R. Petersen *et al.*, "Mid-infrared multispectral tissue imaging using a chalcogenide fiber supercontinuum source," EN, *Opt. Lett., OL*, vol. 43, no. 5, pp. 999–1002, Mar. 2018, Publisher: Optica Publishing Group, ISSN: 1539-4794. DOI: 10.1364/OL.43.000999. [Online]. Available: https://opg.optica.org/ol/abstract.cfm?uri=ol-43-5-999 (visited on 02/14/2023).

[39] Y. N. Billeh, M. Liu, and T. Buma, "Spectroscopic photoacoustic microscopy using a photonic crystal fiber supercontinuum source," EN, *Optics Express*, vol. 18, no. 18, pp. 18 519–18 524, Aug. 2010, Publisher: Optica Publishing Group, ISSN: 1094-4087. DOI: 10.1364/OE.18.018519. [Online]. Available: https://opg.optica.org/oe/abstract.cfm?uri=oe-18-18-18519 (visited on 02/09/2023).

[40] C. Lee *et al.*, "Combined photoacoustic and optical coherence tomography using a single near-infrared supercontinuum laser source," EN, *Appl. Opt., AO*, vol. 52, no. 9, pp. 1824–1828, Mar. 2013, Publisher: Optica Publishing

Group, ISSN: 2155-3165. DOI: 10.1364/AO.52.001824. [Online]. Available: https://opg.optica.org/ao/abstract.cfm?uri=ao-52-9-1824 (visited on 02/14/2023).

[41] X. Shu, M. Bondu, B. Dong, A. Podoleanu, L. Leick, and H. F. Zhang, "Single all-fiber-based nanosecond-pulsed supercontinuum source for multispectral photoacoustic microscopy and optical coherence tomography," EN, *Optics Letters*, vol. 41, no. 12, pp. 2743–2746, Jun. 2016, Publisher: Optical Society of America, ISSN: 1539-4794. DOI: 10.1364/OL.41.002743. (visited on 05/22/2020).

[42] E. Pshennikova and A. Voronina, "Expression of the transcription factor xvent-2 in xenopus laevis embryogenesis," EN, *American Journal of Molecular Biology*, vol. 2, 2016. DOI: 10.4236/ajmb.2012.22014. (visited on 2012).

[43] P. Jorgensen, J. A. J. Steen, H. Steen, and M. W. Kirschner, "The mechanism and pattern of yolk consumption provide insight into embryonic nutrition in Xenopus," en, *Development*, vol. 136, no. 9, pp. 1539–1548, May 2009, Publisher: The Company of Biologists Ltd Section: Research Article, ISSN: 0950-1991, 1477-9129. DOI: 10.1242/dev.032425. (visited on 03/30/2020).

[44] T. Allen *et al.*, "Ultrafast laser-scanning optical resolution photoacoustic microscopy at up to 2 million A-lines per second," *To add*, 2018. DOI: 10.1117/1.JBO.23.12.126502.

[45] J. Chen *et al.*, "Dual-foci fast-scanning photoacoustic microscopy with 3.2-MHz A-line rate," *Photoacoustics*, vol. 23, p. 100 292, Aug. 2021, ISSN: 2213-5979. DOI: 10.1016/j.pacs.2021.100292. [Online]. Available: https://www.ncbi.nlm.nih.gov/pmc/articles/PMC8367837/ (visited on 04/07/2023).

# Chapter 4

# Two Octaves Spanning Opto-acoustic Microscopy

AUTHOR'S NOTE: Part of the experimental work presented in this chapter is based on work which has been reported in a peer-reviewed publication [1] and has been presented at an international conference (Photonics West 2020). The work described in this chapter has been done in collaboration with Dr. Manoj K. Dasa from Technical University of Denmark (DTU). The initial idea of performing MS-OAM over the entire supercontinuum spectrum and preliminary experiments were developed by myself and Dr. Manoj K. Dasa, whereas the method described in section 2.2.7, the experiments, the imaging system, the imaging procedure and the analysis was designed and built entirely by myself.

## 4.1 Introduction

Opto-acoustic microscopy is presumably the most rapidly expanding biomedical imaging technique due to its capacity to detect high-resolution optical contrast *in-vivo* at depths beyond the optical transport mean free path. Opto-acoustic microscopy enables non-invasive detection of chromophores, paving the way for applications in medical diagnostics, cancer, biology, and neurology [2–9].

At the moment, OAM devices work in narrow spectrum regions where only a few chromophores may be detected, resulting in limited spectral capabilities.

Such OAM instruments were developed for example either in the 532 nm [10, 11], 900 nm spectral bands [12, 13], or above 1440 nm [14].

Producing OAM maps for multiple biological chromophores at the same time, such as Hb, melanin, collagen, glucose, and lipids, is a difficult undertaking given the current technology. Several research teams have previously shown that OAM can generate oxygen saturation maps. For instance, Liu *et al.* measured simultaneously Hb concentration, oxygen saturation and blood flow speed via OAM, using 3 laser lines[11]. This was achieved thanks to a single nanosecond pulsed laser operating at 532 nm and two stimulated Raman shifted pulses at 545 and 558 nm. By using a high numerical aperture acoustic lens, Li *et al.* [15] performed *in-vivo* oxygen saturation imaging with only 10 nJ per pulse, at 532 nm without the need of data averaging. Galanzha *et al.* [16] employed *in-vivo* OAM flow cytometry for label-free detection of melanin-bearing circulating tumor cells in patients with melanoma, using a pulsed laser operating at 1060 nm. On the other hand, supercontinuum (SC) optical sources provide a wide spectral range (typically 500 nm - 2400 nm), enabling multi-spectral opto-acoustic imaging and spectroscopic opto-acoustic sensing, despite exhibiting challenging low pulse energies.

Shu *et al.* [17] demonstrated a single SC source powered OCT/OAM instrument capable of multi-spectral microscopy (MS-OAM) in the visible (500 - 800 nm). Also, Buma *et al.* [18] and Dasa *et al.* [14] developed in-house SC sources to map lipids in the near infra-red (NIR). Table 4.1, presents a review of the instrumentation of OAM systems employed to target absorbers in biological tissues. This shows that, currently, the imaging instrument needs to be tailored to match the spectral characteristics of the chromophore of interest.

A concerning factor limiting OAM to non-clinical or preclinical applications is the cost of an OAM system, where the cost of the source is a major contributor. Several research groups have attempted to develop low-cost OAM imaging instruments. Pulsed laser diodes (PLD) operating in the visible and near-infrared (NIR) ranges were used to achieve this purpose. PLD-based OAM devices, on

| Reference | OS Tech. | CWL (nm) | PRR | Cost | Target | EPP ($\mu$J) |
|---|---|---|---|---|---|---|
| [19] | PLD | 405 | 1 kHz | low | A | 0.052 |
| [12] | PLD | 905 | 1 kHz | low | A | 3 |
| [10] | YFL | 532 | 2 MHz | high | A | 0.1 - 5 |
| [11] | YFL | 532 | 4 kHz | high | A | 0.8 |
| [20] | Dye Laser | 532 | 10 kHz | high | A | 5 |
| [21] | PLD | 780, 1560 | 5 - 20 kHz | N/A | C | 2 - 4 |
| [22] | CW | 488, 808 | N/A | low | A,B | N/A |
| [16] | N/A | 1060 | 10 kHz | N/A | B | 240 |
| [23] | OPO | 270 - 1400 | 1 kHz | high | A, E | N/A |
| [24] | SC | 450 - 840 | 20 kHz | low | A, B | N/A |
| [17] | custom SC | 500 - 900 | 5 kHz | low | A, B | N/A |
| [18] | custom SC | 1210 - 1720 | 2 kHz | high | E | 1 - 6 |
| [14] | custom SC | 1440 - 1870 | 100 kHz | low | E | 0.197 |
| [25] | custom SC | 1500 - 1900 | 30 kHz | low | D | 1 |
| OS-OAM | SC | 475 - 2400 | 20 kHz | low | A, B, C, D, E | 0.017 - 0.11 |

TABLE 4.1: Review of the instrumentation used for OAM imaging of haemoglobin (A), melanin (B), collagen (C), glucose (D) and lipids (E). OS: optical source employed; CWL: central wavelength of OS; PRR: pulse repetition rate; PLD: pulsed laser diode; OPO: optical parametric oscillator; SC: supercontinuum source; YFL: Ytterbium fibre laser; EPP: Energy per pulse;

the other hand, have a low pulse repetition rate. Low PRR results in poor imaging rate, and low pulse energies lead to hundreds of times heavier averaging of observed signals [12–14, 19, 26–28].

Other approaches include frequency-domain (FD) systems. For example Kellnberger *et al*. [22] used a CW laser emitting at 488 and 808 nm, whilst Tserevelakis *et al*. [29] employed a CW laser (at 488 nm) with an acousto-optic modulator at 10 MHz. In contrast to PLD based OAM and FD-CW laser based systems, a more costly instrument, was reported by Allen *et al*. [10]. They set up an ultra-fast OAM system with a PRR of 2 MHz using a master oscillator power amplifier configuration, frequency-doubled to 532 nm.

So far, optical parametric oscillators (OPO) are popular optical sources employed for OAM. Although they are widely tunable in wavelength, they are characterized by a low PRR [23]. Recently, mapping of lipids using a low cost customised SC source to deliver sufficiently high energy per pulse (EPP) in the NIR was reported by Dasa *et al*.

To my knowledge, an optical source which,

1. has the ability to cover both VIS and NIR ranges (450 nm - 2000 nm)
2. can deliver sufficient EPP to enable OAM imaging (50 - 500 nJ)
3. provides sufficiently high PRR for fast imaging (100 kHz - 2 MHz)
4. is cost effective (below £10k)

does not exist. In this investigation, a commercially available low-cost supercontinuum (SC) source was utilized, which exhibited some of the desired characteristics mentioned earlier. Its broad emission spectrum provided the flexibility to target various endogenous chromophores, as their absorption peaks were dispersed across a wide spectral range of approximately 2000 nm (ranging from 475 to 2400 nm).

Using such a SC source, for the first time, a two Octaves Spanning Opto-acoustic Microscopy (OS-OAM) instrument is demonstrated. The device can identify chromophores throughout a spectral range of roughly 2000 nm across the electromagnetic spectrum and can generate real-time 3D OAM maps of diverse chromophores (melanin, haemoglobin (Hb), collagen, glucose, and lipids). In addition, we developed an enhanced multimodal imaging system (OS-OAM/OCT) by introducing a high-resolution Optical Coherence Tomography imaging channel. Because of the vast bandwidth covered and the multimodality presented, such devices may be employed in future studies of early-stage cancer detection.

## 4.2 Methods and Materials

### 4.2.1 Ethical Approval

Animals and Ethical Approval *In-vivo* imaging was performed on four *Xenopus laevis* tadpoles at developmental stage 37/38, based on Nieuwkoop and Faber 1956. All experimental procedures were approved by the University of Kent Animal Welfare and Ethical Review Body (AWERB; Institutional Ethics Reference Number: 0037-SK-17). Reporting of all *in-vivo* experimental work conforms with the ARRIVE guidelines.

*Xenopus laevis* embryos were supplied by the European Xenopus Resource Center (EXRC; Portsmouth UK). The Xenopus embryos were kept in water at 20 C until they reached the developmental stage 37/38 [30]. Prior to OS-OAM imaging, animals were anaesthetized in $0.1\%$ MS-222 solution (ethyl 3-aminobenzoate methane sulfonate, Sigma-Aldrich UK, [31]. Animals remained anaesthetised in MS-222 solution for the entire duration of the imaging procedure (4.2 min). All methods employed were performed in accordance with guidelines and regulations as described in the research protocol approved by the University of Kent Animal Welfare and Ethical Review Body.

### 4.2.2 OS-OAM / OCT System

The schematic diagram of the multi-modal OS-OAM/OCT imaging instrument is presented in Fig. 4.1. In the OS-OAM channel, a SC source (SuperK COMPACT, NKT Photonics) delivering pulses of 2 ns duration at 20 kHz pulse repetition rate (maximum) is employed (OS1). The size of the beam diameter was doubled to increase imaging lateral resolution by employing a reflecting beam expander BE (BEO2R/M, Thorlabs), as the spot size is proportional to the focal length and inversely proportional to the beam diameter. Sequentially, a smaller spot size

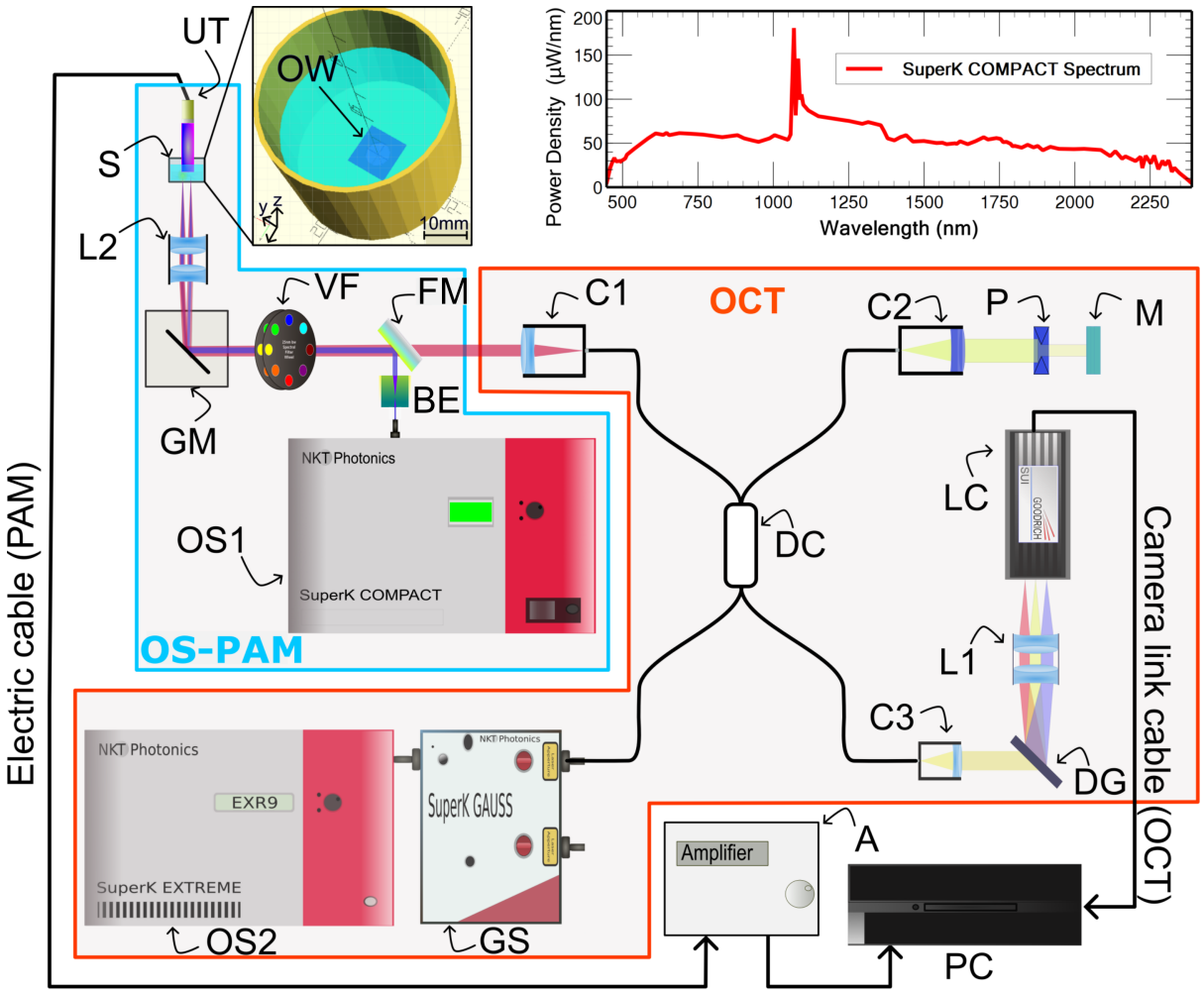


FIGURE 4.1: Schematic diagram of the OS-OAM/OCT system. OS1: OS-OAM excitation optical source (SuperK COMPACT, NKT Photonics); OS2: OCT optical source (SuperK EXTREME EXR9, NKT Photonics); GS: Variable filter (SuperK GAUSS, NKT Photonics); VF: Bandpass filter wheel; BE: Beam expander; FM: Flipping mirror; GM: X-Y galvanometer mirrors; LC: Line camera; DG: Diffraction grating; DC: 50/50 directional coupler; UT: Ultrasound transducer; S: Sample; C1-C3: Collimators; L1-L2: Lenses; M: Flat mirror; P: Pinhole; A: Amplifier; OW: Optical window of the 3D printed sample-holder; Drawing produced using Incscape 1.0.1 (https://inkscape.org/)

means higher fluence according to eq. 2.12 (same energy over a smaller area), resulting in an improvement of SNR.

Figure 4.2c shows the measured variation of lateral resolution with the wavelength. This is especially relevant at shorter wavelengths, as the output beam width of the COMPACT source ranges from 1 mm in the visible to 3 mm in the near-infrared. Since the numerical aperture is determined by the diameter of

the beam, which is dictated by the wavelength used, measurements of the OS-OAM system's lateral resolution are presented for each operating wavelength (Fig. 4.2c). Increasing the beam diameter by a factor of two, results into a smaller spot size (after focusing). Therefore, the optical energy is directed in a smaller region, which is critical for obtaining high-quality OAM images when utilising a laser with a low energy per pulse. (Fig. 4.2) such as the COMPACT.

To optimise the optical power on the sample, optical components were carefully chosen so that chromatic aberrations did not significantly disrupt the beam wave-front. The only optical components in the beam's path for this purpose are a reflective beam expander, a flipping silver coated mirror (FM, used to switch between the OAM and OCT imaging modes), 25 nm bandwidth hard coated band-pass filters (87-776, Edmund Optics), a pair of orthogonal galvo-scanners (6220H, Cambridge Technology), and a 19 mm focal length achromatic doublet (AC127-019-AB, Thorlabs) as objective lens.

Losses can be high when utilising achromatic doublets since the anti-reflection coating is effective only across a restricted spectral range. However, the EPP presented in Fig. 4.2a was measured on the sample which includes the losses coming from the lens. Furthermore, because the experimental lateral resolution assessed did not change significantly across the spectral range, no or very little aberrations were noticed, as shown by the pictures in Fig 4.4. All optical components in the sample arm attenuate the optical power by 13 %. Switching between filters takes about 2-5 s, however this procedure can be faster by using PC controlled filters.

To improve acoustic coupling, the sample is immersed in water. A high frequency customized unfocused polyvinylidene fluoride (PVDF) needle ultrasonic transducer (40.3 MHz center frequency, 90 % bandwidth at 6 dB, 0.4 mm diameter active element, University of Southern California) detects acoustic waves with an axial resolution of 50 $\mu$m (Fig. 4.2d). This is placed in contact with water. At the bottom of the 3D printed sample (S in Fig. 4.1) a circular optical window (OW)

of 0.22 mm thickness is placed. The sample is sitting on the optical window, being illuminated from below. The OW does not absorb optical energy, therefore is invisible in all OS-OAM images. The electrical signal generated is then amplified by two low noise wide-band amplifiers (ZFL-500LN+, Mini Circuits) and then digitized using a 12-bit fast acquisition board operating at a sampling rate of 200 MS/s (PCI-5124, National Instruments).

The OCT channel can also potentially be powered by the COMPACT according to the work reported by [24, 32]. The studies presented in this chapter however, aim to demonstrate the functional imaging capabilities of the OS-OAM instrument. The OCT subsystem was only integrated in the OS-OAM system to provide structural information and to guide the imaging process. Thus, for the OCT channel, a second low noise supercontinuum laser (SuperK EXTREME EXR9, NKT Photonics) (OS2) was employed. Here hides a conflict point between OCT and OAM. Supercontinuum based OCT requires high PRR (300 MHz) in order to achieve acceptable SNR whereas OAM cannot be performed over 2 MHz as described in section 2.2.5.3.

The optical source powering the OCT is coupled into a commercial tunable filter (SuperK Gauss, NKT Photonics). The tunable filter is capable of splitting the spectrum in two, separating the visible to near-infrared (600 nm to 900 nm) light from the infrared (900 - 2400 nm) light. A low-pass filter with a cut-on wavelength at 1100 nm is introduced in the infrared channel to remove the pump peak of the source at 1064 nm. Therefore, the OCT is powered from the infrared channel with a central wavelength at 1310 nm and spectral bandwidth of 180 nm.

The state-of-the-art ultra-high resolution OCT instrument is used sequentially with the OS-OAM. A collimated beam from OS2 is directed towards the galvanometer scanner (GM), which is then conveyed through the objective lens to the sample. Light back-scattered by the sample returns into the 50/50 directional coupler (DC) being directed towards the spectrometer. The spectrometer consists

of a custom made collimator, a transmission diffraction grating (Wasatch Photonics), a doublet pair as a focusing lens and a line camera (LC, SU1014-LDHI, Goodrich,) with 1024 pixels and 25 $\mu$m pitch, 47 kHz max reading rate. Here the line period of the camera is set to operate at 20 kHz to be in synchronization with the OS-OAM. Data is digitized using a camera link board (National Instruments, model IMAQ 1429).

*B-scans* from both OCT and OS-OAM are displayed in real-time. The generation of the OAM *A-scans* does not involve complex mathematical operations. A Hilbert transform is applied to each acquired temporal signal, making the real-time display of the images straightforward. The OCT *A-scans* are produced by the complex master-slave procedure described in section 2.3.6., which allows for generation of direct *en-face* views and of *A-scans*, with no need for resampling/-linearisation of data [33, 34].

An in-house LabVIEW software was developed to drive the acquisition and analysis procedure. A PCI 5124 digitizer was employed to digitize the electrical signal generated by the ultrasound transducer in synchronism with the pulses generated by OS1. *A-scans* from the signals generated by both OAM and the OCT channels are produced for each position of the scanned beam during the lateral scanning of the sample.

### 4.2.3 System Characterization and OS-OAM/OCT imaging

The OS-OAM system was rigorously characterized and the results are presented in Fig. 4.2. The EPP was measured on the sample for each wavelength and was found to range from 20 to 110 $nJ$ (Fig. 4.2a). The FOV was estimated imaging a carbon fibre tape demonstrating high opto-acoustic signal amplitude over 8 mm (Fig. 4.2b).

As the lateral resolution varies with the wavelength and the beam diameter, it is necessary to measure the lateral resolution for each wavelength. Thus, for each

wavelength, a sharp edge of a USAF target (a letter on the USAF target) was imaged. Images of $500 \times 400\ pixels^2$ were produced, of size $500 \times 400\ \mu m^2$ therefore, each pixel in the image spans over 1 $\mu m$. The edge spread function (ESF) and the line spread function (LSF) were measured and the FWHM of the Gaussian fit to the LSF determined the lateral resolution. The measured lateral resolution, presented in Fig. 4.2c, was found to vary from 4.9 to 7.1 $\mu m$ over a spectral range spanning from 475 to 1650 nm. This range of variation in the lateral resolution is expected due to the combination of variation of the beam diameter at the collimated output of the optical source as a function of wavelength (intrinsic SC source characteristics), and the wavelength dependency of the lateral resolution (eq. 2.24). Therefore, if we define the lateral resolution of the instrument as given by 1/2 of the size of the Airy disk [35, 36] and consider the 2x magnification of the beam expander BE, theoretical lateral resolutions of 5.8 $\mu m$ at 500 nm (beam diameter 2 mm) and of 6.95 $\mu m$ at 1500 nm (beam diameter 5 mm) are obtained. These values match the experimental values and ensure that the achromatic lens employed did not introduce significant optical aberrations.

The theoretical axial resolution of the OS-OAM system is 38 $\mu m$. However, outside the acoustic focal point, the SNR is weaker, and the axial resolution degrades. Furthermore, the transducer has a maximum detectable bandwidth when it is oriented orthogonal to the direction of propagation of the incident acoustic waves. Any small deviation of the incidence angle from 90 degrees, due to the angle directivity dependence, determines a reduction in the detectable signal bandwidth [37]. Hence, the measured axial resolution using the carbon fibre tubes (Fig. 4.2d) was found to be 50 $\mu m$. The ratio between the max signal amplitude (Fig. 4.2) and the standard deviation of the noise determines the SNR of the OS-OAM system, found to be 43.8 dB.

The method presented in section 2.2.7 was experimentally confirmed by producing OAM images showing the spatial distribution of the melanin, haemoglobin,

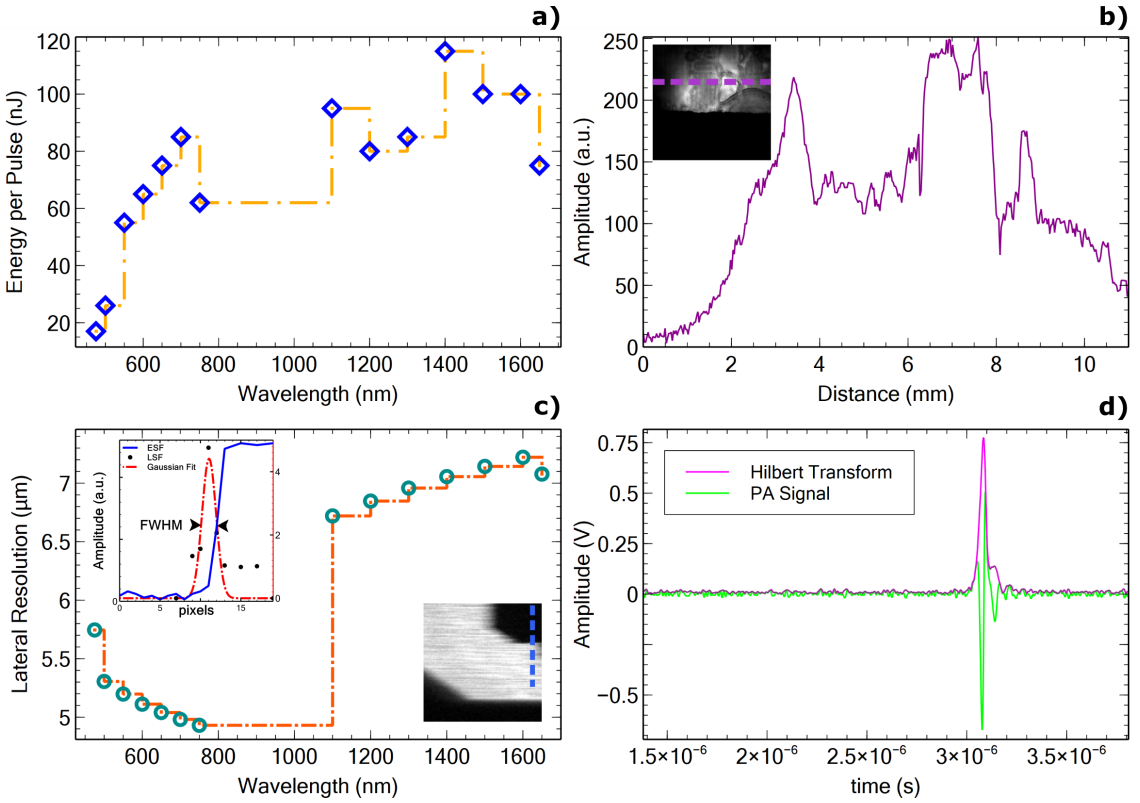


FIGURE 4.2: OS-OAM System characterization; a: EPP graph over the whole imaging spectral range measured on the sample; b: Characterisation of the lateral field of view (FOV) of the instrument. OAM signal collected whilst imaging a carbon fibre tape is plotted for each lateral position in the image. The plot corresponds to the amplitudes of the signal at the positions showed by the purple dashed line in the inset image. The size of the image $10 \times 10$ mm; c: Lateral resolution per wavelength measured by imaging a sharp edge (letter) on a USAF target, extracting the ESF and calculating the LSF. The size of the image is $0.5 \times 0.5$ mm; d: Axial resolution measured imaging carbon fibre tubes. The Axial resolution is defined by the FWHM of the Hilbert transform (Signal envelope).

gelatine, glucose, and lipids present in various samples. To map the spatial distribution of melanin, three human hairs were placed in the 3D sample holder S (Fig. 4.3), on the optical window, and illuminated from below using the instrument presented in Section 4.2.2.

To guide the imaging operation, and hold the hairs in place, a carbon fibre tape partially covered the hairs, as shown in the 2D schematic diagram of the sample presented in Fig. 4.3a. The three hairs are labelled as 1, 2 and 3, whereas the carbon fibre tape as 4.

Optical source OS1 is used to sequentially illuminate the sample with light

at 550 nm and then at 650 nm to generate OAM maps of the chromophores producing acoustic waves when excited by light at these two wavelengths. Subsequently, by using the procedure introduced in Section 2.2.7., OAM spatial distribution maps of the melanin were produced. Finally, after producing the maps of melanin, the optical source OS2, operating at a central wavelength of 1300 nm, was used to illuminate the sample to generate OCT images.

Optical coherence tomography and OAM images obtained are presented in Figs. 4.3b-4.3e. Figures 4.3b and 4.3d represent *en-face* OCT and OAM images, whereas in Figs. 4.3c and 4.3e, represent respective *B-scan* images.

The images are presented in 8-bit format, therefore, as illustrated in their corresponding colour map bars, the brightness 0 of a pixel in the image corresponds to an OCT or OAM signal equal to zero, whereas a brightness of 255 to its maximum value. The *en-face* images were produced by using the average intensity projection algorithm. As expected, the carbon fibre tape is visible in both OCT and OAM images (areas 4) and most importantly, all three hairs are clearly identifiable in both images, which proves that the procedure suggested here to map the melanin is effective. The *B-scan* views show, as expected, that the axial resolution in the OCT image is better than in the OAM one.

To validate the potential of the method proposed to be used to generate spatial distribution maps of haemoglobin, gelatine, glucose, and lipids, mixtures of these chromophores with water were created. The mixtures were placed in the sample holders S, and illuminated with light of various wavelengths, from below, as explained in Section 2.2.7. For imaging guidance purposes, carbon fibre tapes have been placed in the holder, on the optical window (the liquid mixtures would cover the carbon tape). In Figs. 4.4a1, 4.4b1, 4.4c1, and 4.4d1, 2D schematic diagrams of the four samples so created are presented showing the position of the carbon fibre tapes in each of the four cases.

1. To validate the potential of the technique to map the spatial distribution of haemoglobin, a mixture of dry haemoglobin and water (concentration 150

g/l) was placed in the sample holder, and sequentially illuminated with light from OS1, first at 550 nm and then at 650 nm. The two OAM images so created were subsequently used to generate distribution maps of haemoglobin. An *en-face* OAM distribution map of haemoglobin is presented in Fig. 4.4a2 whereas an example of a *B-scan* map in Fig. 4.4a3.

2. To map the spatial distribution of gelatine, a mixture of cooking gelatine and water (concentration 150 g/l) was created, placed in the sample holder, and sequentially illuminated with light from OS1 at 1200 nm and then at 1700 nm. The two OAM images so created were subsequently used to generate gelatine distribution maps. An *en-face* OAM distribution map of the gelatine is presented in Fig. 4.4b2 whereas an example of a *B-scan* in Fig. 4.4b3.

3. To produce glucose spatial distribution maps, a mixture of glucose and water (concentration 150 g/l) was created, placed in the sample holder, and sequentially illuminated with light from OS1 operating at 1600 nm and then at 1700 nm. The two OAM images so created were subsequently used to generate OAM glucose distribution maps. An *en-face* OAM map of the glucose is presented in Fig. 4.4c2 whereas an example of a *B-scan* map in Fig. 4.4c3.

4. To generate OAM spatial distribution maps of the lipids, a mixture of water and chicken adipose fat has been created, placed in the sample holder, and sequentially illuminated with light from OS1 at 1600 nm and then at 1700 nm. The two OAM images hence created were subsequently used to generate OAM lipids distribution maps. A OAM *en-face* distribution map of the lipids is presented in Fig. 4.4d2 whereas an example of a *B-scan* map in Fig. 4.4d3.

In all cases, *en-face* OAM images are created via an average projection algorithm. MAP, MAP-ing stands for maximum amplitude projection. As mentioned

in the theory, we use the average amplitude projection instead. A summary of the content of the samples created and the wavelengths used in each case to produce OAM spatial distribution maps of the five chromophores targeted is presented in Table 4.2. For all imaged chromophores, the values of the signal-to-noise ratio (SNR), normalized over the optical fluence, presented in the inset of Fig. 2.9 are consistent with the values of their absorption coefficients reported in the literature. To compute the SNR, we used a standard procedure [14, 18] consisting in calculating the SNR as,

$$SNR = 20\log_{10}\left[\frac{\text{MAX(area 5)}}{\text{STD(area 6)}}\right] \tag{4.1}$$

| Chromophore | Content sample | $\lambda_1$ (nm) | $\lambda_2$ (nm) |
|---|---|---|---|
| Melanin | Human hair | 550 | 650 |
| Haemoglobin | Water and dry haemoglobin (150g/l) | 550 | 650 |
| Gelatine | Water and gelatine (150 g/l) | 1200 | 1700 |
| Glucose | Water and glucose (150 g/l) | 1600 | 1700 |
| Lipids | Water and chicken adipose fat | 1200 | 1600 |

TABLE 4.2: Samples created to validate the proposed technique and the wavelengths at which they were sequentially illuminated using OS1 to generate OAM images and subsequently map the chromophores.

In eq. 4.1, MAX(area 5) and STD(area 6) are the maximum value of the OAM signal computed in area 5 and the standard deviation of the signals calculated over region 6 respectively. Regions 5 and 6 are all depicted using dotted yellow circles on the *en-face* OAM images shown in Figs.4.3 and 4.4.

### 4.2.4 *In-vivo* whole SC range OS-OAM imaging of Tadpoles

During the OS-OAM imaging, animals were anaesthetized (n=4, as described in the Methods section) and positioned on a 3D printed sample holder. The sample

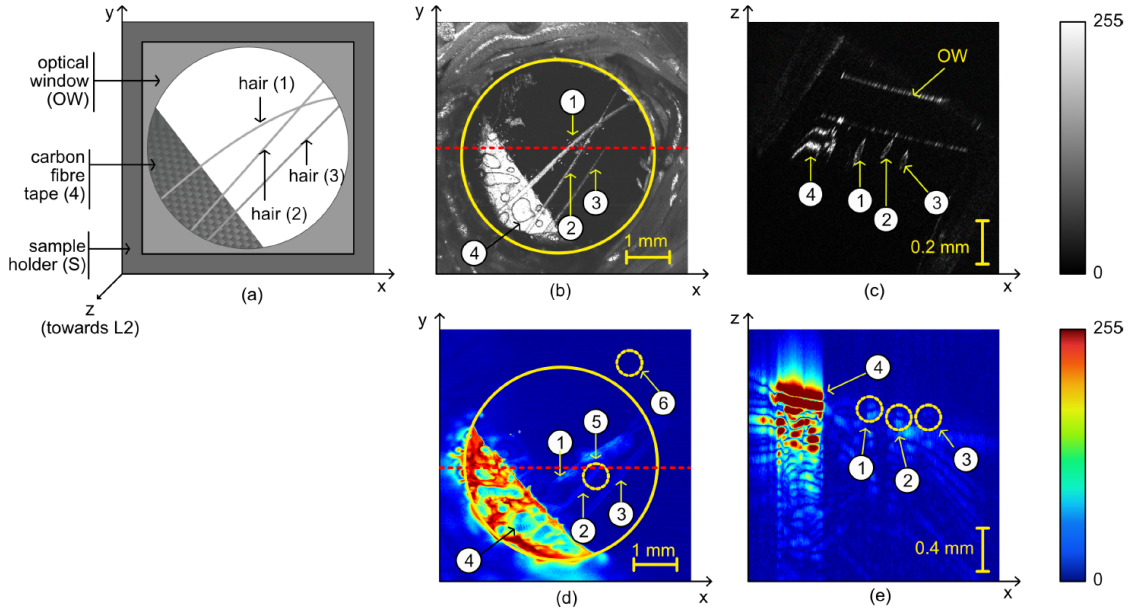


FIGURE 4.3: (a) Schematic diagram of the sample designed to produce images of the human hair: 1, 2, 3 are the three imaged hairs, placed on an optical window (OW); the ends of the hairs are covered by a carbon fibre tape (4); incident light from OS1 and OS2 travels towards the sample in the z-direction. (b) *En-face* OCT image of the sample showing both the carbon fibre tape (4) and the three hairs. (c) Example of a *B-scan* OCT image showing the carbon fibre tape, the hairs as well as the optical window. The hairs look elongated as they are not placed orthogonal to the xz-plane. (d) *En-face* OAM image showing the carbon fibre tape and the hairs. Regions 5 and 6 are used to calculate the signal-to-noise ratio using the procedure described within the manuscript. (e) Example of a *B-scan* OAM image. The optical window is not visible in the OAM image. The red horizontal dashed lines shown on the *en-face* images indicate the y-position where the *B-scans* are originating from.

holder was designed to keep the animal submerged in MS-222 solution, while the laser beam scanned the animal through a thin (0.22 mm) glass optical window from below (inset in Fig. 4.1). For OS-OAM imaging at different spectral bands, 12 hard coated band-pass filters, each of them of 25 nm bandwidth, were employed, enabling imaging from 475 nm up to 1600 nm. At 1600 nm the only commercially available filter to us had 50 nm bandwidth, whereas a long-pass filter with a cut-on at 1650 nm was employed for imaging at longer wavelengths.

In both OCT and OAM channels, *B-scan* images of 500×400 pixels were acquired and displayed in real-time at a frame rate of 20 Hz, hence a 500×400×400 3D volume was generated in 20 s (10 s to capture data and 10 s to process). To

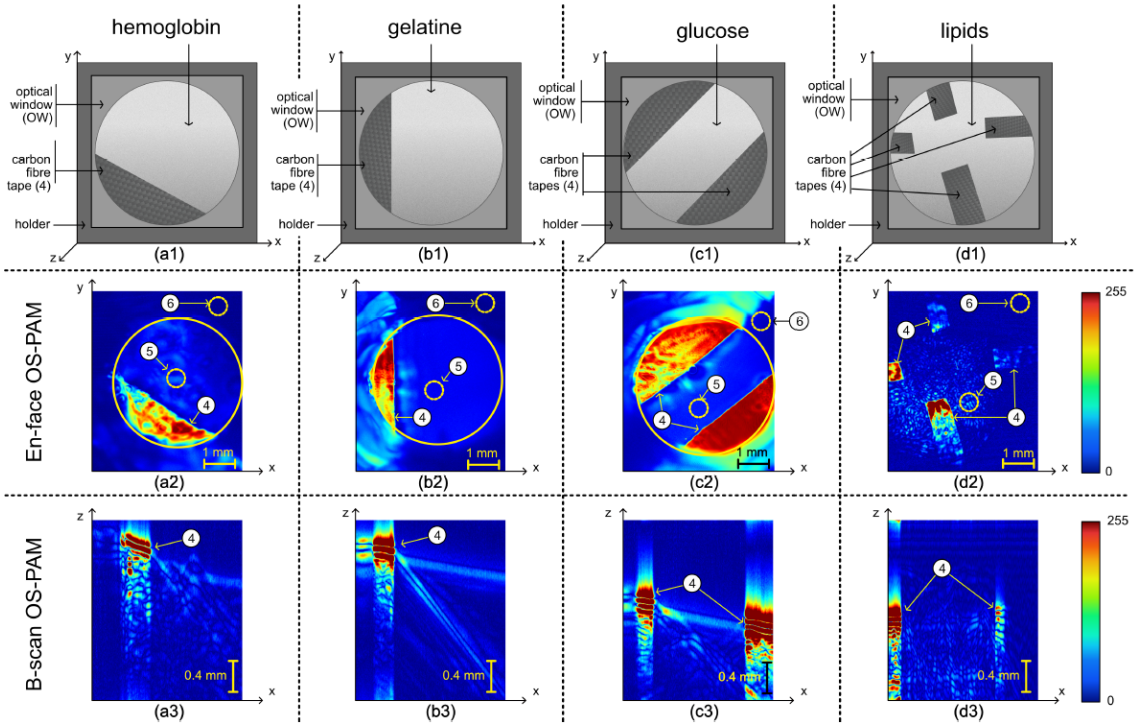


FIGURE 4.4: (a1), (b1), (c1) and (d1): schematic diagrams of the samples designed to produce OAM spatial distribution maps of: haemoglobin, gelatine, glucose, and lipids respectively. In all cases, carbon fibre tapes (4) are placed on the optical window (OW) and covered by the liquid mixture created. (a2), (b2), (c2) and (d2): *En-face* OAM maps showing the presence of haemoglobin, gelatine, glucose, and lipids respectively. Regions 5 and 6 are used to calculate the signal-to-noise ratio using the procedure described within the manuscript. (a3), (b3), (c3) and (d3): examples of *B-scan* OAM images of haemoglobin, gelatine, glucose, and lipids respectively. All images show the carbon fibre tapes (4).

enhance the Signal to Noise Ratio (SNR) in the OAM images, 32 *A-scans* were averaged, increasing the acquisition time to 10.7 minutes. In Fig. 4.5, *en-face* z-projected OS-OAM images over the whole SC range are presented, along with a structural *en-face* OCT image clearly showing the tadpole's anatomy.

Due to the unavailability of commercial band-pass filters of 25 nm bandwidth at wavelengths over 1650 nm, a long-pass filter with a cut-on at 1650 nm was employed, hence the notation $> 1650$ nm. This means that the spectral range used here is from 1650 to 2400 nm, allowing for absorption of chromophores with absorption over a much wider spectral range. Thus, brighter images at the Z5 zone were obtained. The lateral resolution of 5-7 $\mu m$ refers to the capabilities of the

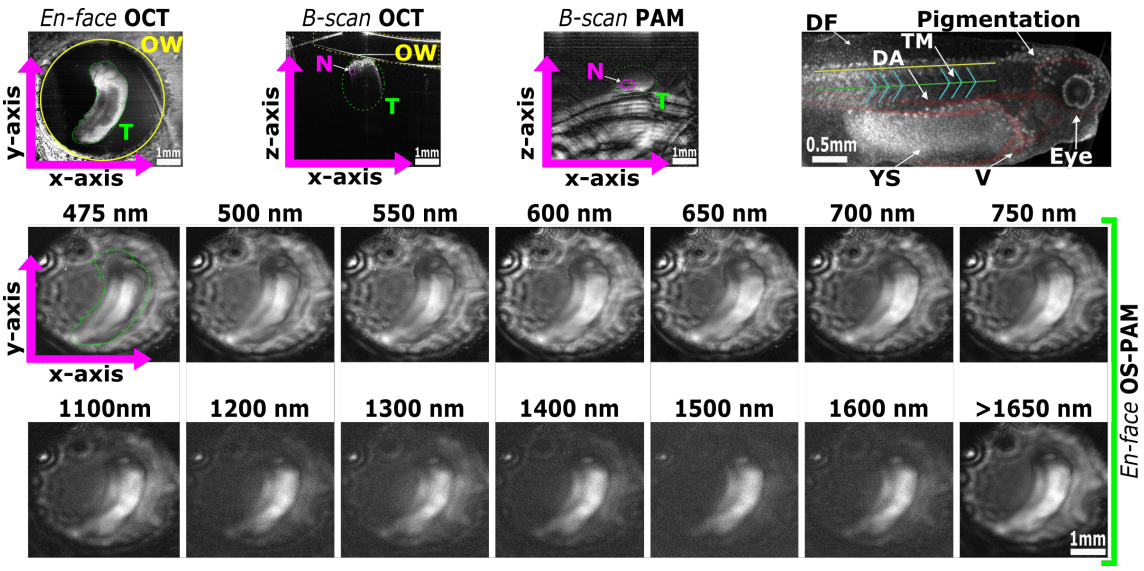


FIGURE 4.5: Representative *in-vivo* OS-OAM *en-face* images of one tadpole (T) generated at various wavelengths across the whole emission spectrum of the OS1. High noise levels can be observed above 1200 nm as water absorption increases. The OCT image has a wider field of view providing an overview of the optical window (OW) and the positioning of the tadpole; Top right: Structural *en-face* OCT image displaying tadpole anatomy with highlighted main veins and aortas (red) as well as, the trunk muscles (blue). The green line indicates the position of the notochord (N) while the yellow line the position of the spinal cord. DF: dorsal fin; YS: yolk sack; V: ventricle. This procedure was repeated on four animals (n=4).

system when the distance between two consecutive points (pixels) in the image is smaller than the lateral resolution of the system. However, in Figs. 4.3 to 4.5 we show very large size areas (5 to 8 mm) while keeping a fairly low number of lateral points (500 pixels). Therefore, the lateral resolution was digitally degraded in these images to 10 to 16 $\mu$m respectively.

### 4.2.5 Mapping of five endogenous contrast agents with OS-OAM/OCT

Utilising the capabilities of the OS-OAM/OCT instrument in combination with the technique described in section 2.2.7., five endogenous contrast agents: melanin, Hb, collagen, glucose and lipids were mapped on four tadpoles at developmental stage 37/38 [30].

The tadpole OS-OAM images were overlaid on the corresponding structural OCT images and presented in Fig. 4.6. Maps of melanin are produced using filters operating at 550 and 650 nm. The images obtained were subtracted as described in section 2.2.7. On the tadpole, at developmental stage 37/38, pigmentation (due to pigment cells) is present in the eye, on the head and on the dorsal side of the yolk sac (Fig. 4.6). Moreover, melanophores appear on the tail which is shown by the less intense melanin signal in Fig. 4.6.

Maps of Hb are produced using filters operating at 550 and 650 nm. Hb appears at the level of the cardiac ventricle, as well as, along the developing vascular system which spans the yolk sac and travels along the side of the tail (Figs. 4.5 and 4.6).

Maps of collagen are obtained by changing to filters operating at 1200 and 1700 nm. Collagen has been detected on several areas of the tadpole's body and can be detected on the developing cranial structures and at the levels of the yolk sac and trunk muscles (4.5).

To map glucose, images were produced at 1600 and 1700 nm. High levels of glucose are present within the yolk sac area (Fig. 4.6) overlapping with the high concentration of lipoproteins in this region [38].

Finally, we used filters at 1200 and 1600 nm to map lipids. Our results show that lipids are highly concentrated in the yolk sac (Fig. 4.6), which is consistent with previous studies performing multi-spectral OAM imaging on zebrafish and tadpoles [14, 18].

Water absorption is present at longer wavelengths and manifests as higher background noise since water is everywhere. This is evident in Fig. 4.5.

### 4.2.6 Visible Light Optical Coherence Tomography

A visible light OCT system was considered to exploit the superior resolution OCT provides when operating in shorter wavelengths (eq. 2.23 and eq. 2.24). The

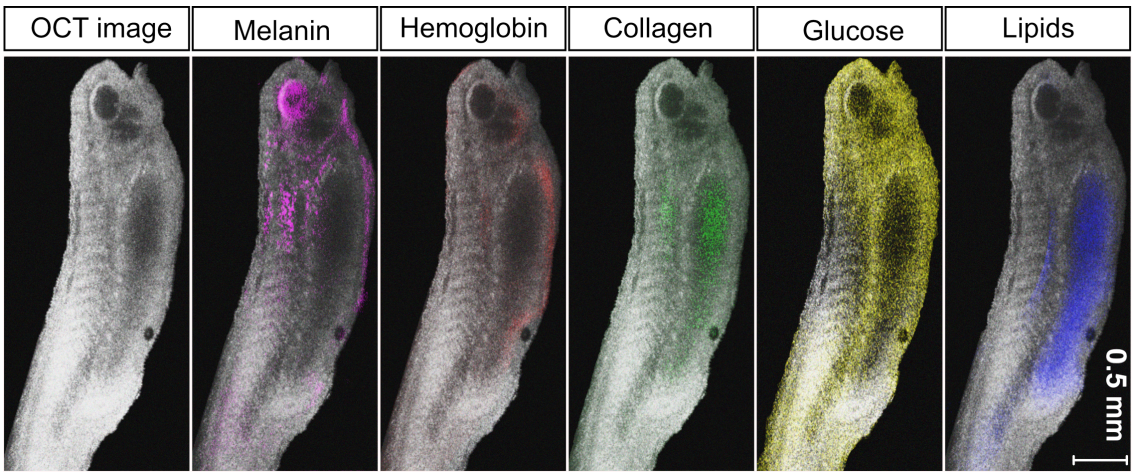


FIGURE 4.6: Qualitative illustrations of the superposition of the spatial mapping distribution of melanin (in pink), haemoglobin (magenta), collagen (green), glucose (yellow) and lipids (blue) within a tadpole obtained using the technique proposed, over a structural OCT image of the same tadpole. Similar *in-vivo* images were obtained when imaging other four tadpoles. The image on the left shows the bare OCT image of the tadpole over which the maps of the chromophores were overlaid.

visible OCT instrument was designed and built to either be integrated in the OS-OAM system or to be used for other biomedical applications such as high resolution retinal imaging. Due to power limitations and technical issues with the SC source the visible OCT was not utilized for the OS-OAM system.

Figure. 4.7 depicts the schematic diagram of the visible optical coherence tomography (OCT) system. The interferometer comprises of a directional coupler (DC) that splits and guides the beam towards the reference arm and the sample arm. Light from the fibre tip of the coupler is launched through a collimator to the 2D galvo-scanners mirrors head (GM) scanning the collimated beam on the sample through a telescope. In order to minimise chromatic aberrations, parabolic reflective collimators (RC) were chosen to launch the light from the coupler to both arms. In addition, reflective optical components such as the RC do not contribute to dispersion mismatch between the sample and the reference arm.

The telescope is implemented in a lens tube system mounted directly onto the GM Mount forming a robust and compact design. A pair of 75 mm focal length achromatic doublet lenses (L) were used for the telescope. The lens on the end

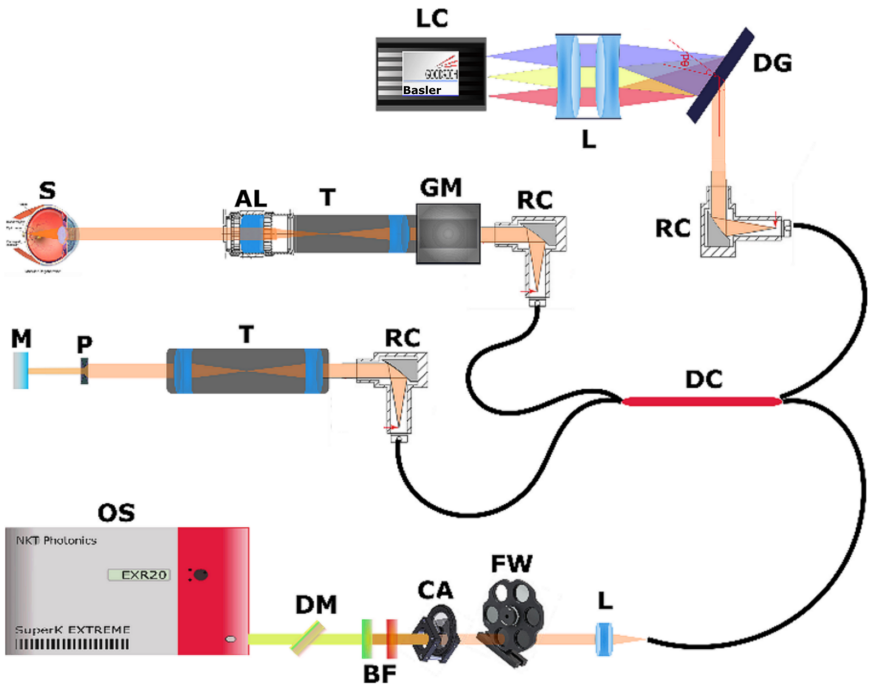


FIGURE 4.7: Schematic diagram of the Visible OCT system. LC: Line Camera; DG: Diffraction Grating; RC: Reflective Collimator; L: Lens; GM: 2D Galvo-scanner mirrors head; T: Telescope; S: Sample; P: Pinhole; M: Mirror; DC: Directional Coupler; OS: Optical Source; DM: Dichroic Mirror; BF: Bandpass Filters; CA: Continuous reflective Attenuator; FW: Filter Wheel; AL: Adjustable Lense.

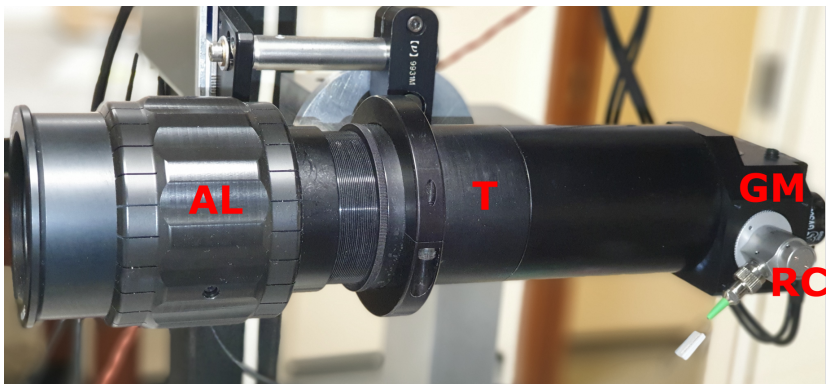


FIGURE 4.8: Picture of the compact design sample arm featuring the adjustable (axially) lens (AL), the custom telescope (T), the galvo-scanner mount (GM) and the reflective parabolic collimator (RC).

of the sample arm was mounted on an adjustable lens (AL) tube to compensate for myopia and adjust the focal plane inside the sample. A $4f$ design was implemented to provide a pivot at the pupil's aperture plane. The total losses due to the optical components in the sample arm was measured to be 12 % one way. The sample arm can be easily be modified for imaging biomedical samples by adding

a lens at the position of the pupil.

The SC optical source (SuperK EXTREME EXR20, NKT photonics) powers the visible OCT system by launching the beam in free space (Fig. 4.7). The EXR20 provides a pulse repetition rate (PRR) of 78 MHz with a pulse duration of a few picoseconds over a spectral range from 500 to 2400 nm.

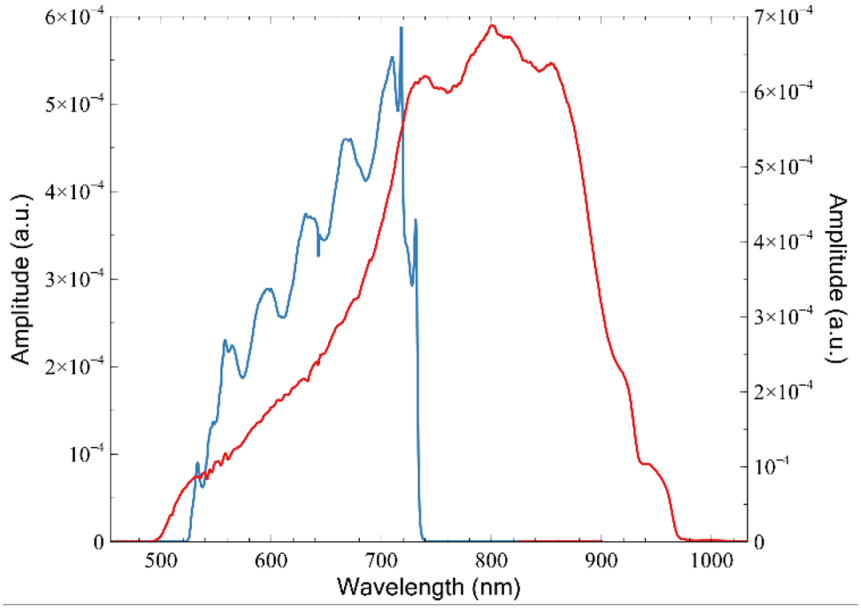


FIGURE 4.9: Spectrum of the EXR20 SC source. Red line: Full visible spectrum; Blue line: Filtered spectrum.

A dichroic mirror is used to split the visible spectrum from the infrared spectrum at 900 nm. A long pass filter with a cut-on at 550 nm and a short pass filter at 750 nm restrict the spectrum to 200 nm. A continuous reflective attenuator (CA) is introduced in the beam path enabling fine power adjustments. An additional filter wheel (FW) loaded with 25 nm bandwidth hard coded bandpass filters assists in the spectrometer characterization and alignment. Finally, the beam is coupled directly into the DC fibre input via an achromatic triplet lens (L) with a 40 mm focal length. The spectrum of the source before and after filtering presented in Fig. 4.9 was measured with a spectrum analyser.

The spectrometer was designed based on a 1800 l/mm Wasatch Photonics transmission diffraction grating (DG) with maximum diffraction efficiency at 532 nm. A 2×4096 pixels CMOS line camera (SLP 140KM, Basler) with a 10 $\mu m$ pitch

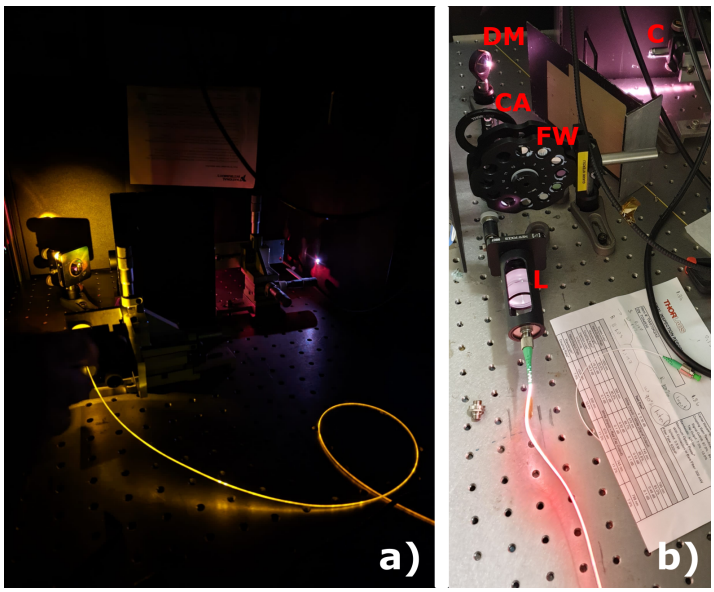


FIGURE 4.10: (b): Free space coupling of the SC optical source (OS). L: Lens; C: Collimator; DM: Dichroic Mirror; CA: Continuous reflective Attenuator; FW: Filter Wheel; (a): Impressive images created by leaking light through the fibre directing the coupled light towards the DC coupler. Picture taken by Lucy Abbott.

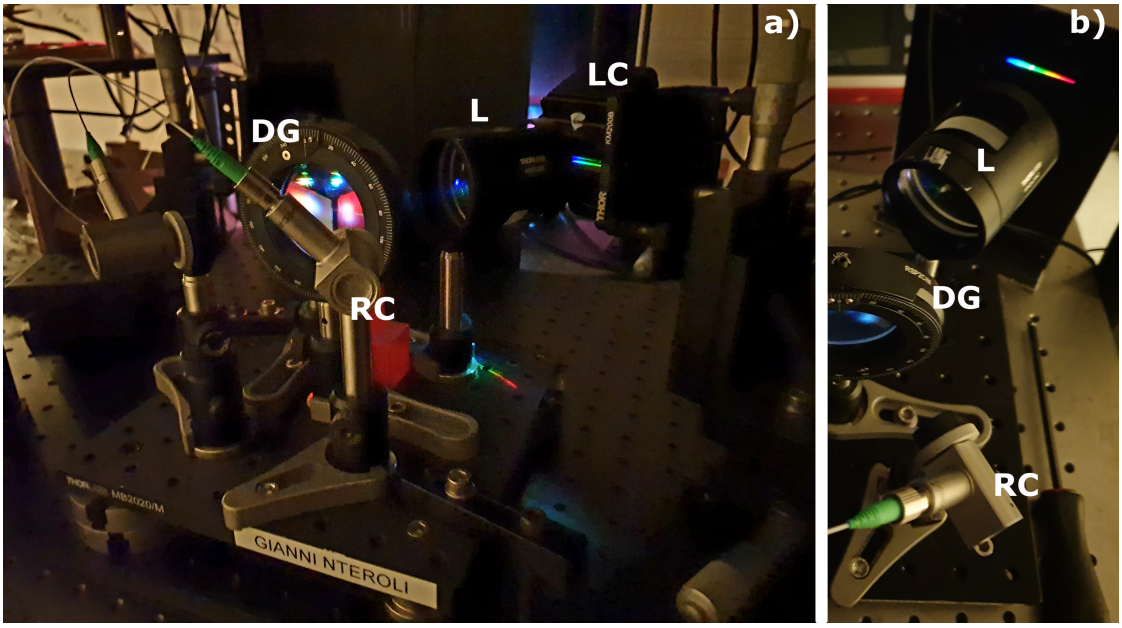


FIGURE 4.11: (a): Picture of the visible OCT spectrometer. LC: Line Camera; DG: Diffraction Grating; RC: Reflective Collimator; L: Lens; (b) Picture showing the aliment of the visible OCT spectrometer.

was used to acquire spectra with speeds up to 140 kHz. The diffracted light was focused on the camera with an achromatic doublet pair of lenses optimised for minimum chromatic and spherical aberrations.

The visible OCT was characterized to evaluate the capabilities of the instrument. The results of the characterization of the vis-OCT system are presented in Fig. 4.12. The maximum sensitivity at zero OPD was measured to be 85 dB with a sensitivity drop-off of 5 dB over one mm in air. *In-vivo* images of the retina and the optical nerve were obtained and are presented in Figs. 4.12 and 4.13. On the images presented, several retinal structures can be observed such as the

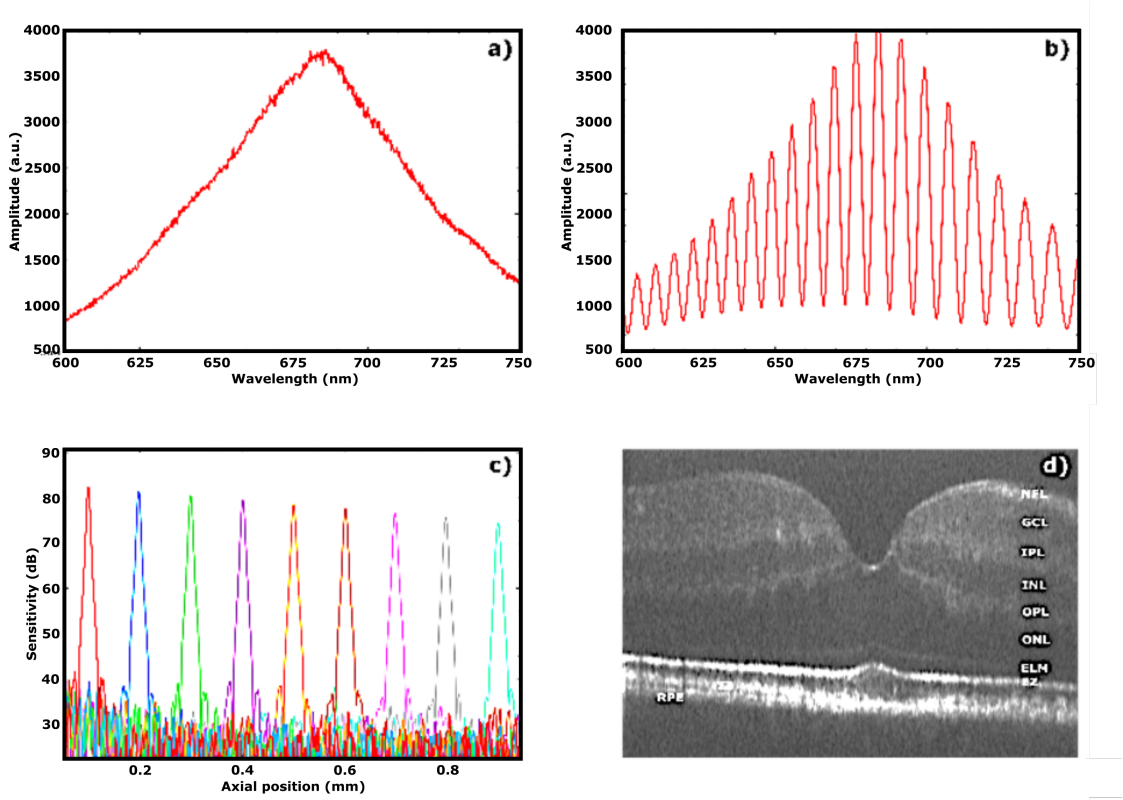


FIGURE 4.12: Characterization of the visible OCT instrument. (a): Spectrum acquired using the visible OCT system's spectrometer; (b): Channelled spectra; (c): Sensitivity drop-off characterization; (d): Vis-OCT images of the human retina.

nerve fibre layer (NFL), ganglion cell layer (GCL), inner plexiform layer (EPL), inner nuclear layer (INL), outer plexiform layer (OPL), author nuclear layer (ONL), external limiting membrane (ELM), ellipsoid zone (EZ), Interdigitation digitalization zone (IZ), and retinal pigment epithelium (RPE) thanks to the high spatial resolution.

At this point, the system requires averaging in order to obtain high quality images oh the human retina. In Fig. 4.13 on the left single *B-scans* are presented

whereas on the right, *B-scans* resulting from 10 averages.

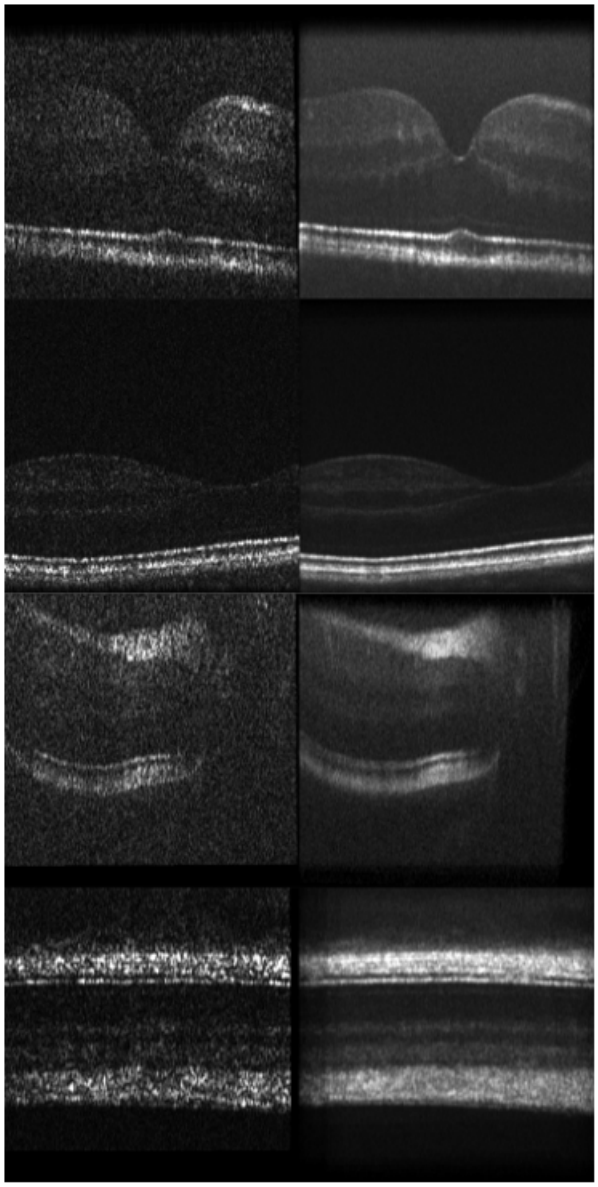

FIGURE 4.13: . Vis-OCT images of the retina and the optical nerve area. On the left: single *B-scan*; On the right: 10 times averaged *B-scan*.

To conclude, these studies demonstrate the capabilities of visible OCT to obtain high resolution *in-vivo* images. Further work is required to enhance the sensitivity over 90 dB with a drop-off sensitivity off less than 5 dB over one mm in air. The system is fundamentally limited by the noise of the SC source. This obstacle can be overcome by employing lower noise SC sources such as the SuperK EXTREME EXU6.

## 4.3 Discussion and Conclusion

An OAM imaging instrument operating at wavelengths over the entire spectral range of a commercial SC source, from 475 to 2400 nm, is demonstrated. This is employed on mapping five endogenous contrast agents in living tadpoles, namely melanin, haemoglobin, collagen, glucose, and lipids. Based on the supposition that only one chromophore contributes to the opto-acoustic signal of each individual voxel in the 3D OAM image, a novel technique of mapping absorbers is demonstrated. A sequentially operating ultra-high resolution OCT imaging channel aids the investigation.

To compensate for the limited optical power delivered by the SC source employed here, losses and optical aberrations were minimized by a careful selection of the optical components used to convey light from the source to the sample. As a result, the experimentally measured EPP on the sample ranged from 17 to 110 nJ, over the whole spectral range, hence sufficiently strong opto-acoustic signal could be generated. The main advantage of the OAM imaging method demonstrated here is its versatility in performing spectral measurements in the range of interest without resorting to multiple optical sources or changes in its optical design.

The OS-OAM instrument, in its current stage of development, is not capable of performing spectroscopic OAM, therefore the results obtained are not directly comparable to conventional spectral unmixing techniques. By using the suggested procedure, the concentration of the targeted chromophores cannot be extracted quantitatively but only their spatial mapping distribution evaluated. Adequate experimental assessments require quantitative concentration measurements. Therefore, this was not the goal of the research presented here. Instead, the focus was on using a unique approach for the spatial distribution of the chromophore. In doing so, two milestones were targeted:

1. Opto-acoustic microscopy imaging over an unprecedented spectral range using an ultra-broadband source,

2. utilizing OAM imaging to map chromophores of bio-medical interest *in-vivo*, in several spectral regions.

These two milestones were targeted despite facing the issues of low energy per pulse and intrinsic high noise challenges of a SC source. However, such sources are commercially available and utilisation of a single source for OCT and OAM as illustrated may represent a cost-effective solution.

While the current inability of the proposed method to generate quantitative absorption coefficient data is acknowledged, it displays significant potential in identifying the spatial distribution of numerous chromophores. Notably, it overcomes the limitations caused by the limited operational spectral range of conventional sources utilized in OAM.

The presented technique has been effectively utilized to identify chromophores through the use of a specific SC optical source and an optical setup with a particular design. However, for this method to be successful, a meticulous selection of two interrogation wavelengths is necessary. This selection process must consider the fluence, spectral density variation of the source, and the absorption coefficient of the targeted chromophore.

The spectral region from 700 to 1100 nm, although of interest for biomedical applications, is not targetable by OAM due to the very low absorption of the chromophores, for which reason we did not perform any measurements over this range. By avoiding this, we also kept the project cost effective.

As the diameter of the optical beam is a function of wavelength (an intrinsic characteristic of the optical source), the lateral resolution of the system does not increase linearly with the wavelength. Although, the lateral resolution should deteriorate as we move to longer wavelengths, the size of the beam diameter

expands, increasing the numerical aperture and therefore improving the lateral resolution (Fig. 4.2c).

Although more sophisticated systems are capable of obtaining accurate absorption coefficient data, they are either limited to two chromophores due to lack of spectral coverage, or they cannot perform *in-vivo* imaging due to lack of imaging speed (Table 4.1). I acknowledge that the rate at which images are produced in this study is comparable to that of the OPOs instrument. However, as this implementation is based on fast acquisition of cross-sectional slices, it is better suited for *in-vivo* imaging. To enable *in-vivo* imaging, rather than anesthetizing tadpoles and then placing them in water for acoustical coupling, we submerged the tadpoles directly in the anesthetic solution. This method eliminated the need to pin down the tadpoles, preventing any trauma or discomfort while ensuring complete immobilization, unlike conventional pinning techniques. Consequently, positioning the tadpole and capturing multiple images within the same field of view became straightforward.

A low-cost OAM imaging instrument could be devised with potential in various medical screening programs. Future work includes:

1. Increasing the acquisition sensitivity of the OS-OAM instrument for faster acquisition by replacing the ultrasound transducer (UT) with a higher sensitivity focused transducer,

2. Applying lower noise amplification methods,

3. Implementing software noise reduction techniques,

4. Replacing the band-pass filter wheel with and automated one, synced with the acquisition.

For this proof of concept study, a transmission mode OAM was considered in order to minimize imaging artefacts and provide maximum achievable SNR. As the next step of these studies is to image BCC and melanoma *in-vitro*, with the

ultimate goal to monitor these notorious skin lesions in patients (clinical applications), the probe would require to be redesigned for reflection mode.

I am confident that our system has the potential to tackle several challenges of skin cancer diagnosis. In melanoma for instance, the progression of melanocytes to subsequent pathological growth phases [2] can be monitored by mapping melanin in the epidermis. D'Alessandro *et al*. [3] demonstrated that multi-spectral imaging can be used to quantify saturated Haemoglobin ($HbO_2$), which is a major indicator for the early detection of melanomas whereas Fang *et al*. [4] showed how collagen can inhibit and promote tumour progression. Long *et al*. [5] showed that energy metabolism, especially lipid metabolism, is significantly elevated during carcinogenesis. Furthermore, various studies also demonstrated that cell metabolism is highly dysregulated in cancer, as lipids and glucose become sources for tumor progression via multiple signalling pathways [6–9].

Although the localization in real-time of multiple endogenous chromophores in tissue seems to be of paramount importance, the available technology does not allow simultaneous detection of all the physiological changes listed above.

## References

[1] G. Nteroli *et al.*, "Two octaves spanning photoacoustic microscopy," en, *Scientific Reports*, vol. 12, Jun. 2022, Accepted: 2022-06-14 Publisher: Nature Research, ISSN: 2045-2322. [Online]. Available: https://doi.org/10.1038/s41598-022-14869-5 (visited on 02/10/2023).

[2] V. Gray-Schopfer, C. Wellbrock, and R. Marais, "Melanoma biology and new targeted therapy," en, *Nature*, vol. 445, no. 7130, pp. 851–857, Feb. 2007, Number: 7130 Publisher: Nature Publishing Group, ISSN: 1476-4687. DOI: 10.1038/nature05661. (visited on 03/09/2020).

[3] B. D'Alessandro and A. P. Dhawan, "Transillumination Imaging for Blood Oxygen Saturation Estimation of Skin Lesions," *IEEE Transactions on Biomedical Engineering*, vol. 59, no. 9, pp. 2660–2667, Sep. 2012, Conference Name: IEEE Transactions on Biomedical Engineering, ISSN: 1558-2531. DOI: 10.1109/TBME.2012.2209647.

[4] M. Fang, J. Yuan, C. Peng, and Y. Li, "Collagen as a double-edged sword in tumor progression," *Tumour Biology*, vol. 35, no. 4, pp. 2871–2882, Apr. 2014, ISSN: 1010-4283. DOI: 10.1007/s13277-013-1511-7. (visited on 03/09/2020).

[5] J. Long *et al.*, "Lipid metabolism and carcinogenesis, cancer development," *American Journal of Cancer Research*, vol. 8, no. 5, pp. 778–791, May 2018, ISSN: 2156-6976. (visited on 03/09/2020).

[6] F. V. Filipp, B. Ratnikov, J. De Ingeniis, J. W. Smith, A. L. Osterman, and D. A. Scott, "Glutamine-fueled mitochondrial metabolism is decoupled from glycolysis in melanoma," *Pigment Cell & Melanoma Research*, vol. 25, no. 6, pp. 732–739, 2000. DOI: 10.1111/pcmr.12000.

[7] J. Kluza *et al.*, "Inactivation of the hif-1$\alpha$/pdk3 signaling axis drives melanoma toward mitochondrial oxidative metabolism and potentiates the therapeutic activity of pro-oxidants," *Cancer Research*, vol. 72, no. 19, pp. 5035–5047, 2012, ISSN: 0008-5472. DOI: 10.1158/0008-5472.CAN-12-0979.

[8] T. J. Parmenter *et al.*, "Response of braf-mutant melanoma to braf inhibition is mediated by a network of transcriptional regulators of glycolysis," *Cancer Discovery*, vol. 4, no. 4, pp. 423–433, 2014, ISSN: 2159-8274. DOI: 10.1158/2159-8290.CD-13-0440.

[9] D. Scott *et al.*, "Comparative metabolic flux profiling of melanoma cell lines: Beyond the warburg effect," *The Journal of biological chemistry*, vol. 286, pp. 42 626–34, Dec. 2011. DOI: 10.1074/jbc.M111.282046.

[10] T. Allen *et al.*, "Ultrafast laser-scanning optical resolution photoacoustic microscopy at up to 2 million A-lines per second," *To add*, 2018. DOI: 10.1117/1.JBO.23.12.126502.

[11] C. Liu, Y. Liang, and L. Wang, "Single-shot photoacoustic microscopy of hemoglobin concentration, oxygen saturation, and blood flow in sub-microseconds," en, *Photoacoustics*, vol. 17, p. 100 156, Mar. 2020, ISSN: 2213-5979. DOI: 10.1016/j.pacs.2019.100156. (visited on 03/09/2020).

[12] T. Wang, S. Nandy, H. S. Salehi, P. D. Kumavor, and Q. Zhu, "A low-cost photoacoustic microscopy system with a laser diode excitation," EN, *Biomedical Optics Express*, vol. 5, no. 9, pp. 3053–3058, Sep. 2014, Publisher: Optical Society of America, ISSN: 2156-7085. DOI: 10.1364/BOE.5.003053. (visited on 03/10/2020).

[13] M. Erfanzadeh, H. S. Salehi, P. Kumavor, and Q. Zhu, "Improvement and evaluation of a low-cost laser diode photoacoustic microscopy system for ovarian tissue imaging," in *Photons Plus Ultrasound: Imaging and Sensing 2016*, vol. 9708, International Society for Optics and Photonics, Mar. 2016, p. 97083I. DOI: 10.1117/12.2208943. (visited on 03/10/2020).

[14] M. K. Dasa *et al.*, "All-fibre supercontinuum laser for in vivo multispectral photoacoustic microscopy of lipids in the extended near-infrared region," en, *Photoacoustics*, vol. 18, p. 100 163, Jun. 2020, ISSN: 2213-5979. DOI: 10.1016/j.pacs.2020.100163. (visited on 03/09/2020).

[15] M. Li, J. Chen, and L. Wang, "High acoustic numerical aperture photoacoustic microscopy with improved sensitivity," EN, *Optics Letters*, vol. 45, no. 3, pp. 628–631, Feb. 2020, Publisher: Optical Society of America, ISSN: 1539-4794. DOI: 10.1364/OL.384691. (visited on 03/10/2020).

[16] E. I. Galanzha *et al.*, "In vivo liquid biopsy using Cytophone platform for photoacoustic detection of circulating tumor cells in patients with melanoma,"

en, *Science Translational Medicine*, vol. 11, no. 496, Jun. 2019, Publisher: American Association for the Advancement of Science Section: Research Article, ISSN: 1946-6234, 1946-6242. DOI: 10.1126/scitranslmed.aat5857. (visited on 03/10/2020).

[17] X. Shu, M. Bondu, B. Dong, A. Podoleanu, L. Leick, and H. F. Zhang, "Single all-fiber-based nanosecond-pulsed supercontinuum source for multispectral photoacoustic microscopy and optical coherence tomography," EN, *Optics Letters*, vol. 41, no. 12, pp. 2743–2746, Jun. 2016, Publisher: Optical Society of America, ISSN: 1539-4794. DOI: 10.1364/OL.41.002743. (visited on 05/22/2020).

[18] T. Buma, N. C. Conley, and S. W. Choi, "Multispectral photoacoustic microscopy of lipids using a pulsed supercontinuum laser," en, *Biomedical Optics Express*, vol. 9, no. 1, p. 276, Jan. 2018, ISSN: 2156-7085, 2156-7085. DOI: 10.1364/BOE.9.000276. (visited on 03/09/2020).

[19] L. Zeng, Z. Piao, S. Huang, W. Jia, and Z. Chen, "Label-free optical-resolution photoacoustic microscopy of superficial microvasculature using a compact visible laser diode excitation," *Optics Express*, vol. 23, no. 24, pp. 31 026–31 033, Nov. 2015, ISSN: 1094-4087. DOI: 10.1364/OE.23.031026. (visited on 03/10/2020).

[20] R. Haindl *et al.*, "Functional optical coherence tomography and photoacoustic microscopy imaging for zebrafish larvae," EN, *Biomedical Optics Express*, vol. 11, no. 4, pp. 2137–2151, Apr. 2020, Publisher: Optical Society of America, ISSN: 2156-7085. DOI: 10.1364/BOE.390410. [Online]. Available: https://www.osapublishing.org/boe/abstract.cfm?uri=boe-11-4-2137 (visited on 03/31/2020).

[21] H. D. Lee, J. G. Shin, H. Hyun, B.-A. Yu, and T. J. Eom, "Label-free photoacoustic microscopy for in-vivo tendon imaging using a fiber-based pulse

laser," en, *Scientific Reports*, vol. 8, no. 1, pp. 1–9, Mar. 2018, Number: 1 Publisher: Nature Publishing Group, ISSN: 2045-2322. DOI: 10.1038/s41598-018-23113-y. (visited on 04/29/2020).

[22] S. Kellnberger *et al.*, "Optoacoustic microscopy at multiple discrete frequencies," en, *Light: Science & Applications*, vol. 7, no. 1, p. 109, Dec. 2018, Number: 1 Publisher: Nature Publishing Group, ISSN: 2047-7538. DOI: 10.1038/s41377-018-0101-2. [Online]. Available: https://www.nature.com/articles/s41377-018-0101-2 (visited on 03/15/2022).

[23] R. Cao, J. P. Kilroy, B. Ning, T. Wang, J. A. Hossack, and S. Hu, "Multispectral photoacoustic microscopy based on an optical–acoustic objective," en, *Photoacoustics*, vol. 3, no. 2, pp. 55–59, Jun. 2015, ISSN: 2213-5979. DOI: 10.1016/j.pacs.2014.12.004. (visited on 03/09/2020).

[24] M. Bondu, M. J. Marques, P. M. Moselund, G. Lall, A. Bradu, and A. Podoleanu, "Multispectral photoacoustic microscopy and optical coherence tomography using a single supercontinuum source," en, *Photoacoustics*, vol. 9, pp. 21–30, Mar. 2018, ISSN: 2213-5979. DOI: 10.1016/j.pacs.2017.11.002. (visited on 03/09/2020).

[25] M. K. Dasa, C. Markos, J. Janting, and O. Bang, "Multispectral photoacoustic sensing for accurate glucose monitoring using a supercontinuum laser," EN, *JOSA B*, vol. 36, no. 2, A61–A65, Feb. 2019, Publisher: Optical Society of America, ISSN: 1520-8540. DOI: 10.1364/JOSAB.36.000A61. (visited on 03/31/2020).

[26] M.-L. Li and P.-H. Wang, "Optical resolution photoacoustic microscopy using a Blu-ray DVD pickup head," in *Photons Plus Ultrasound: Imaging and Sensing 2014*, vol. 8943, International Society for Optics and Photonics, Mar. 2014, p. 894 315. DOI: 10.1117/12.2037146. (visited on 03/10/2020).

[27] L. Zeng, G. Liu, D. Yang, and X. Ji, "3D-visual laser-diode-based photoacoustic imaging," EN, *Optics Express*, vol. 20, no. 2, pp. 1237–1246, Jan.

2012, Publisher: Optical Society of America, ISSN: 1094-4087. (visited on 03/10/2020).

[28] A. Hariri *et al.*, "Development of low-cost photoacoustic imaging systems using very low-energy pulsed laser diodes," *Journal of Biomedical Optics*, vol. 22, no. 7, p. 075 001, Jul. 2017, Publisher: International Society for Optics and Photonics, ISSN: 1083-3668, 1560-2281. DOI: 10.1117/1.JBO.22.7.075001. (visited on 03/10/2020).

[29] G. J. Tserevelakis, K. G. Mavrakis, N. Kakakios, and G. Zacharakis, "Full image reconstruction in frequency-domain photoacoustic microscopy by means of a low-cost I/Q demodulator," eng, *Optics Letters*, vol. 46, no. 19, pp. 4718–4721, Oct. 2021, ISSN: 1539-4794. DOI: 10.1364/OL.435146.

[30] E. Pshennikova and A. Voronina, "Expression of the transcription factor xvent-2 in xenopus laevis embryogenesis," EN, *American Journal of Molecular Biology*, vol. 2, 2016. DOI: 10.4236/ajmb.2012.22014. (visited on 2012).

[31] S. Koutsikou *et al.*, "A simple decision to move in response to touch reveals basic sensory memory and mechanisms for variable response times," *The Journal of Physiology*, vol. 596, no. 24, pp. 6219–6233, 2018. DOI: https://doi.org/10.1113/JP276356. eprint: https://physoc.onlinelibrary.wiley.com/doi/pdf/10.1113/JP276356. [Online]. Available: https://physoc.onlinelibrary.wiley.com/doi/abs/10.1113/JP276356.

[32] M. Maria *et al.*, "Q-switch-pumped supercontinuum for ultra-high resolution optical coherence tomography," en, *Optics Letters*, vol. 42, no. 22, p. 4744, Nov. 2017, ISSN: 0146-9592, 1539-4794. DOI: 10.1364/OL.42.004744. (visited on 03/09/2020).

[33] A. Bradu *et al.*, "Recovering distance information in spectral domain interferometry," *Scientific reports*, vol. 8, no. 1, p. 15 445, Oct. 2018, ISSN: 2045-2322. DOI: 10.1038/s41598-018-33821-0.

[34] A. G. Podoleanu and A. Bradu, "Master-slave interferometry for parallel spectral domain interferometry sensing and versatile 3D optical coherence tomography," eng, *Optics Express*, vol. 21, no. 16, pp. 19 324–19 338, Aug. 2013, ISSN: 1094-4087. DOI: 10.1364/OE.21.019324.

[35] E. Hecht., *Optics*, en. Pearson, 2002, ISBN: 0-321-18878-0.

[36] J. E. Greivenkamp, *Field Guide to Geometrical Optics*, en. 1000 20th Street, Bellingham, WA 98227-0010 USA: SPIE, Jan. 2004, ISBN: 978-0-8194-5294-8. DOI: 10.1117/3.547461. [Online]. Available: http://link.aip.org/link/doi/10.1117/3.547461 (visited on 01/20/2022).

[37] C. Zhang, K. I. Maslov, J. Yao, and L. V. Wang, "In vivo photoacoustic microscopy with 7.6-µm axial resolution using a commercial 125-MHz ultrasonic transducer," *Journal of Biomedical Optics*, vol. 17, no. 11, p. 1, Nov. 2012, Publisher: SPIE-Intl Soc Optical Eng, ISSN: 1083-3668. DOI: 10.1117/1.jbo.17.11.116016. [Online]. Available: https://www.spiedigitallibrary.org/terms-of-use.

[38] P. Jorgensen, J. A. J. Steen, H. Steen, and M. W. Kirschner, "The mechanism and pattern of yolk consumption provide insight into embryonic nutrition in Xenopus," en, *Development*, vol. 136, no. 9, pp. 1539–1548, May 2009, Publisher: The Company of Biologists Ltd Section: Research Article, ISSN: 0950-1991, 1477-9129. DOI: 10.1242/dev.032425. (visited on 03/30/2020).

# Chapter 5

# Enhanced resolution optoacoustic microscopy using a picosecond high repetition rate Q-switched microchip laser

AUTHOR'S NOTE: The experimental work presented in this chapter is based on work which has been reported in a peer-reviewed publication [1] and has been presented at an international conference (ECBO 2023). The work described in this chapter has been done in collaboration with Prof. Mircea Guina and his team from Tampere, Finland and Dr. Stella Koutsikou and Dr. Giulia Messa from the School of Pharmacy, University of Kent.

## 5.1 Introduction

Confocal, multi-photon, and light-sheet microscopy, are optical imaging techniques used in various biomedical applications [2] that require either the use of exogenous probes or genetic manipulations [3] to achieve the targeted optical contrast. Opto-acoustic microscopy (OAM) is a hybrid imaging technique that utilises the capabilities of intrinsic components of the sample to absorb the optical energy of light, to achieve the desired optical contrast. Opto-acoustic microscopy

imaging of complex biological samples has already been reported in numerous publications [4–12].

The optical sources used for OAM are lasers delivering pulses of a typical duration of several nanoseconds [13, 14]. These lasers are used in conjunction with a single-element ultrasound transducer (UT) to detect the opto-acoustic waves by transducing the mechanical pressure applied by the opto-acoustic waves on the surface of the UT to electrical signals. Parameters of the optical source, such as the energy per pulse, the duration of the pulses, and the detection bandwidth of the transducer are of paramount importance for achieving high-quality OAM images in terms of signal-to-noise ratio (SNR) and axial resolution.

The axial resolution of an OAM instrument is limited by the bandwidth of the generated acoustic waves[15], assuming a large bandwidth transducer is employed. Typically, the bandwidth of the transducers used for OAM range from a few MHz up to 100 MHz with a few exceptional reports with 400 and even 1000 MHz. The techniques reported to enhance the axial resolution so far, have involved either the use of numerical methods requiring long post-processing times or high-frequency transducers [16, 17]. The number of reports demonstrating improvement in the axial resolution by manipulating the bandwidth of the acoustic waves is limited and typically restricted to situations where the bandwidth is enhanced by reducing the duration of the pulses from hundreds to several nanoseconds [13, 14]. Using numerical simulations, it has been demonstrated that a 3 picosecond pulse duration laser is more efficient in generating high-frequency acoustic signals than a 3 nanosecond pulse duration laser, however, no improvement in axial resolution was reported [17].

To my knowledge, enhancement in axial resolution by reducing the pulse duration below several nanoseconds has not been experimentally demonstrated yet. The OAM imaging instrument described in this context incorporates a Q-switched microchip laser that emits short pulses lasting 85 ps at a wavelength of 532 nm. This configuration offers improved axial resolution when compared to

another OAM instrument equipped with a supercontinuum (SC) optical source that delivers longer excitation pulses lasting 2 ns and operates at the same wavelength as the picosecond (ps) laser. The capability of the OAM instrument equipped with the ps-based Q-switched microchip laser to produce high-resolution OAM images is presented by images of the brain of the *Xenopus laevis* tadpole.

## 5.2 Methods and Materials

### 5.2.1 Ethical Approval

*In-vivo* experiments were performed on the *Xenopus laevis* tadpole at developmental stage 37/38, based on Nieuwkoop and Faber 1956 [18]. Embryos were supplied by the European Xenopus Resource Centre (EXRC, Portsmouth UK) and kept at $\approx 20^0\ C$ in tap water. During the MS-OAM experiments, animals were anaesthetised in 0.1 $\%$ MS-222 solution (ethyl 3-aminobenzoate methanesulfonate, Sigma-Aldrich). All experimental procedures on stage 37/38 tadpoles are unregulated but were nevertheless approved by the University of Kent's animal welfare ethics committee.

### 5.2.2 OAM System

The experimental set-up used for the studies conveyed in this chapter comprises of two similar OAM imaging instruments sharing the same detection system and the same probe while employing different pulse duration optical sources. The schematic diagram of the set-up is depicted in Fig. 5.1. The optical source (OS1) is a frequency-doubled Q-switched microchip laser emitting at 532 nm (Picophotonics Ltd, Tampere, Finland) capable of generating optical pulses of typically 85 ps with a variable output power. The picosecond optical source (OS1) was operated at 60 nJ per pulse and a pulse repetition rate of 50 kHz. The average optical power measured on the sample was 3 mW. The second optical source (OS2) is a

SC optical source (SuperK Compact, NKT Photonics, Denmark) delivering pulses of 2 ns duration with a repetition rate of 20 kHz. The OS2 emits over vast spectrum, ranging from 400 nm up to 2500 nm. Here a hard coated band-pass filter is employed to restrict the bandwidth within 25 nm with a central wavelength of similar to OS1. Both OS1 and OS2 delivered the similar energy per pulse.

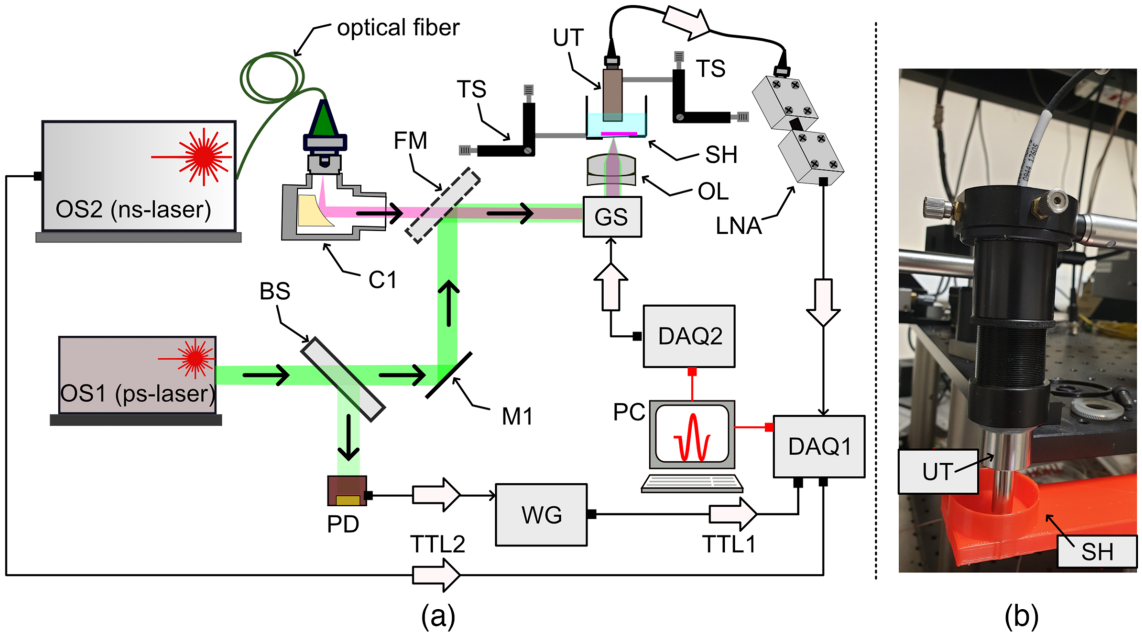


FIGURE 5.1: (a) Schematic diagram. OS1: picosecond laser; OS2: supercontinuum optical source; C1: reflective collimator; SH: sample holder; FM: flipping mirror; PD: photodetector; GS: orthogonal galvo-scanners; DAQ1,2: data acquisition cards; LNA: low noise amplifiers; UT: ultrasound transducer; OL: objective lens. TS: translation stage; TTL1,2: TTL signals synchronized with the emission of the pulses. (b) Picture showing the UT and SH.

A 12-bit data acquisition board, DAQ1 (National Instruments, Model PCI-5124) was employed for the digitization of the triggered (by TTL1/2 signals) electrical signal at the output of the low noise amplifiers, LNA (ZFL-500LN+, Mini Circuits). DAQ1 was operated at a sampling rate of 200 MS/s. DAQ2 was utilised to drive the galvo-scanners in synchronization with DAQ1. The lasers were powered sequentially by switching the position of a flipping mirror FM. The samples were submerged in water to facilitate acoustic coupling. The sample holder (SH) is mounted on a high-resolution 3D translation stage (TS) to position the sample with a defined precision.

A high-frequency Polyvinylidene Fluoride ultrasonic transducer (50 MHz central frequency, 53% bandwidth at 6 dB, Model PA1199, Precision Acoustics) was employed to detect the opto-acoustic waves. The transducer is submerged in water to facilitate acoustic coupling. The sample lies on an optical window of 0.22 mm thickness whereas the excitation beam illuminates the sample from below. The electrical signal generated by the transducer is amplified by the two LNAs, and then digitized by DAQ1.

## 5.3 Results and Discussion

### 5.3.1 Optical characterisation of the SC laser

The capabilities of the OAM instrument were rigorously explored over several experiments. The lateral resolution was evaluated by imaging a sharp edge of a positive USAF target. Using the image produced, the edge spread function (magenta curve in Fig. 5.2(a)), and the line spread function (green line in Fig. 5.2(a)) were calculated. The lateral resolution, defined as the full-width-at-half-maximum (FWHM) of the line spread function, was found to be 3.8 $\mu m$, close to the expected theoretical value (3.1 $\mu m$ using Rayleigh's criterion [19]).

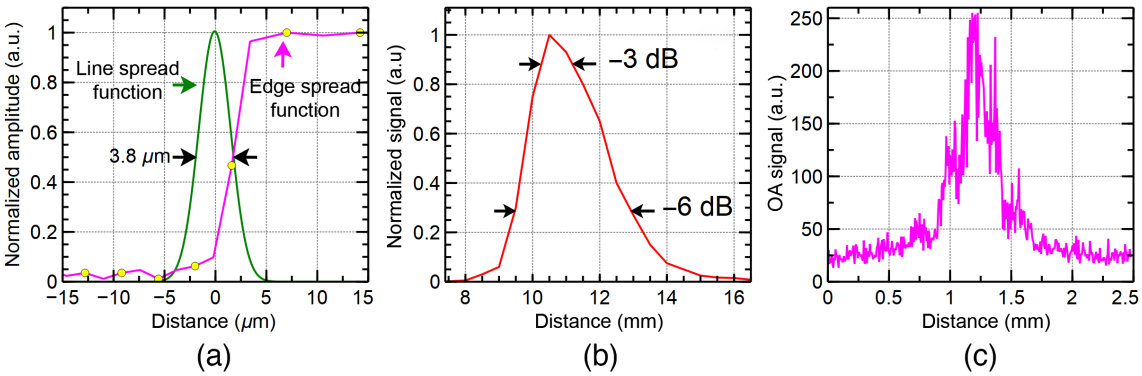


FIGURE 5.2: (a) Experimentally measured edge (magenta) and line (green) spread functions. (b) Detected acoustic signal versus axial position (data provided by the manufacturer of the transducer). (c) Lateral FOV, measured by imaging a carbon fibre tape.

In Figs. 5.2(b,c), we show the capability of the instrument in terms of the field of view (FOV), experimentally measured in both axial and lateral directions, using OS1. The axial range, measured by collecting the OAM signal generated by water, was provided by the manufacturer of the transducer. As illustrated in Fig 5.2(b), when the OAM signal drops by 3 dB, the axial range is around 1.5 mm, which represents a sufficiently long axial imaging range to cover a large variety of biological samples including the *Xenopus laevis* tadpole, which is less than 1 mm in thickness. The lateral FOV was experimentally measured by imaging a carbon fibre tape. As a focused ultrasonic transducer was employed, the opto-acoustic signal recorded at various lateral positions on the sample shows a maximum in the middle of the image. The lateral FOV, estimated from Fig. 5.2(c), was $1\times1$ $mm^2$.

The axial resolution was measured experimentally by imaging a carbon fiber tape using both the microchip ps laser (OS1) and the SC ns source (OS2). Both sources were operated at the same central wavelength of 532 nm, however over different spectral ranges. The ps laser, with an intrinsic bandwidth of a couple of nanometres, delivers sufficient energy per pulse to obtain high-quality images in terms of signal-to-noise ratio (SNR). To obtain images for similar central wavelength, the light from the SC source was filtered by a bandpass filter of 25 nm bandwidth centered at 550 nm.

As illustrated in Fig. 5.3(a), when pulses of 2 ns duration were employed, the FWHM of the acoustic signal was found to be 35 ns, which, given the speed of sound in soft tissues of $\approx$1480 m/s, corresponds to an axial resolution of 51 $\mu m$. In contrast, when utilizing an 85 ps pulse duration, it was observed that the full width at half maximum (FWHM) of the acoustic signal measured 17 ns, resulting in an axial resolution of 25 $\mu m$(Fig. 5.3(b)). These results were consistent with those obtained in subsequent measurements by imaging different regions of the sample. In Figs. 5.3(a,b) only one typical result is presented. The secondary peak observed, is consistent in all images obtained, leading to the conclusion that is

most likely generated by artifacts or by another fiber.

Both picosecond and nanosecond pulse duration optical sources allowed for similar optoacoustic SNRs of 42.9 and 43.8 dB, respectively. In terms of the axial resolution achievable with the two lasers, a 50% enhancement is obtained when using the picosecond pulses in comparison to the nanosecond pulses, when higher frequency acoustic waves are generated as illustrated in Fig. 3(c). The ps-induced optoacoustic signal shows a central frequency at around 41 MHz (Fig. 5.3(c), red curve), whereas the nanosecond-induced opto-acoustic signal shows a central frequency at around 30 MHz (Fig. 5.3(c), blue curve). To perform these measurements, the same ultrasonic transducer and sample were employed.

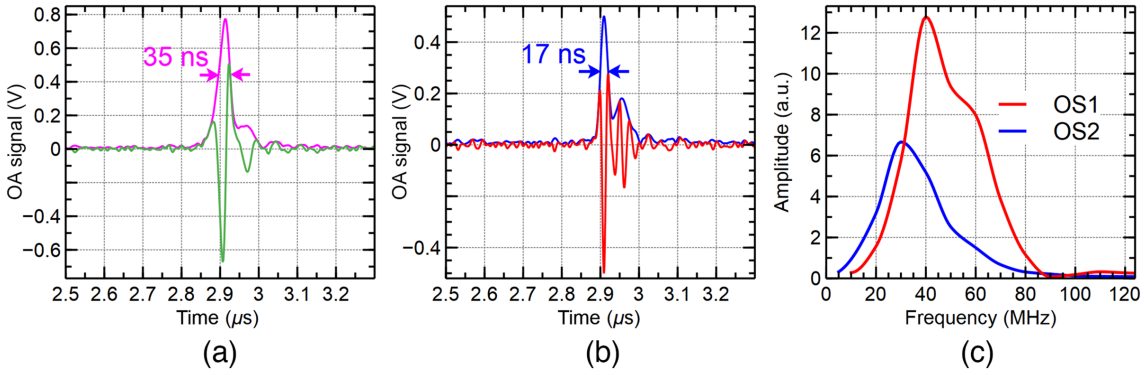


FIGURE 5.3: Typical opto-acoustic signals generated by exciting a carbon fibre with a 2-ns pulse duration [green curve in (a)] and 85-ps pulse duration laser [red curve in (b)]. The envelopes of the two signals are presented in pink and blue, respectively. From the signals presented in (a) and (b), the acoustic spectra generated by using OS1 and OS2 were calculated in (c). By measuring the FWHM of the two spectra, we could infer axial resolutions of 25 and 51 $\mu m$, respectively. The fact that the two spectra are not identical in terms of central frequency and bandwidth shows that, the axial resolution is not determined by the bandwidth of the transducer alone.

Figure 5.3(c) shows that the spectrum of the acoustic waves collected using OS1 (red) is larger than the spectrum collected using the OS2 (blue). As a further manifestation of different spectra generated, the centres of the two spectra do not coincide more acoustic energy is generated by the OS1 closer to the central frequency of the transducer of 50 MHz than when using OS2.

In Fig. 5.4, *en-face*, high-resolution opto-acoustic images at different axial positions inside the tadpole are presented, along with an optical microscopy *en-face*

image (Fig. 5.4(a)). The *en-face* OAM images were produced by using the maximum intensity projection algorithm. Images obtained at different focusing positions of the optical beam were colour-coded (i.e., colours correspond to different focusing positions) and then combined into a composite image such as that depicted in Fig. 5.4(b). In Figs. 5.4(c)–5.4(e), three *en-face* images are presented, which are spaced by 200 $\mu m$ from each other's axial position. In Fig. 5.4(c), the focus of the beam is inside the eye, therefore, sharp images of the tadpole's eye and part of the otic capsule are visible. As a high concentration of melanin is localized in the eye, a high amplitude optoacoustic signal is expected to be generated by the ocular tissue. When the focal plane of the OL is shifted inside the tadpole by 200 $\mu m$, the blurred shapes of the midbrain and the forebrain appear [Fig. 5.4(d)], whereas a sharp image of the eye is not resolved in this focal plane. Moving another 200 $\mu m$ inward, the hindbrain is displayed, as shown in Fig. 5.4(e). A flowchart illustrating the procedure employed to record the images and the post-processing steps needed to produce the overlayed images is presented at the top of Fig. 5.4 (part A).

To the best of my knowledge, this level of detail of the tadpole's brain shown in Fig. 5.4 has not been demonstrated yet by any other research group using an OAM instrument equipped with a ps pulse duration laser.

### 5.3.2 Determination of dental shade employing Opto-Acoustic Microscopy

The optoacoustic microscopy instrument was also employed to accurately determine dental colour shade. This *in-vitro* study was an attempt to aid dental clinicians to assess their restorative work in the oral cavity. This is an essential and very challenging step for dental clinicians to achieve aesthetic integration of dental restorative work and ensure patient satisfaction [20–22].

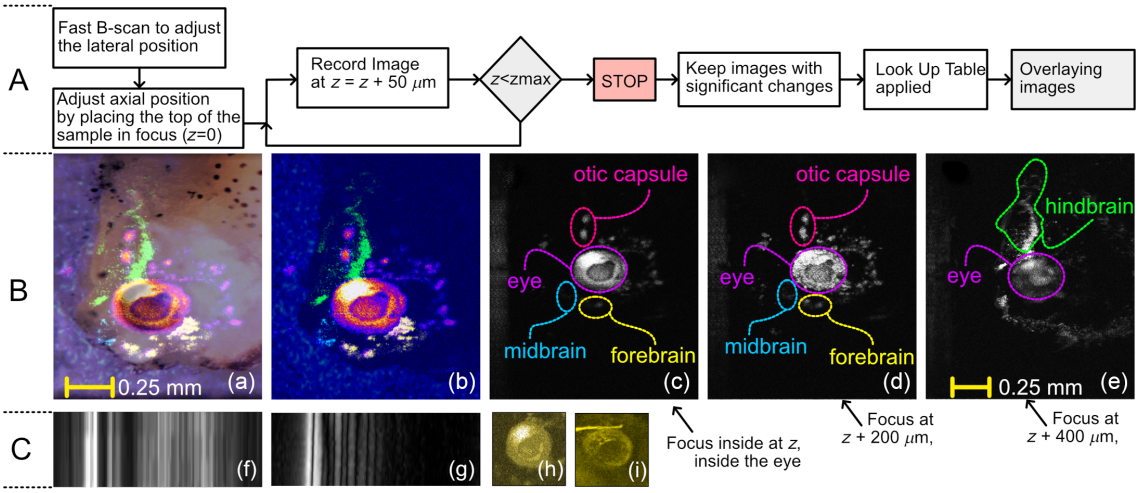


FIGURE 5.4: Part A: flowchart describing the imaging protocol and the post-processing steps. Part B: (a) microscope image of the tadpole's head over which the OAM image showed in (b) is overlapped. (b) Composite *en-face* image obtained by merging images collected at 24 axial positions separated by 50 $\mu m$. (c)–(e) Single-plane images showing significant examples of defined brain structures that appear as the focal plane is shifted deeper into the tadpole. The axial separation between (c) and (d), and (d) and (e) is 200 $\mu m$. It is noteworthy that (a) has the same lateral size as (b) and (c) has the same lateral size as (d) and (e). Part C: (f) and (g) *B-scan* images of the carbon tape produced using the ps and the ns lasers, respectively. Axial size (along the horizontal direction): 1.6 mm. Lateral size (vertical direction): 50 $\mu m$. (h) and (i), typical *en-face* images of the tadpole's eye produced using the ps and the ns lasers, respectively. In both cases, the light is focused inside the eye. The artefact in (i) is due to a structural defect of the optical window.

The sample arm of the OAM instrument was redesigned for transmission mode as depicted in Fig. 5.5. The sample (T) was positioned in the sample holder (SH) with the help of blu tack and carbon fibre tape strips (CF) were attached on the surface of the tooth. The carbon fibre tape strips were used to guide the imaging and to provide a reference signal to be compared with the signal from the tooth. Distilled water was added in the sample holder submerging the sample, the active area of the ultrasound transducer (UT), and part of the objective lens (OL).

Both the picosecond and the nanosecond source was used. Multi-spectral OAM was performed covering a spectral range from 475 nm up to 2000 nm using the SC source. The SC source was also used full power illuminating the sample with all the SC spectrum simultaneously. However, no opto-acoustic signal was

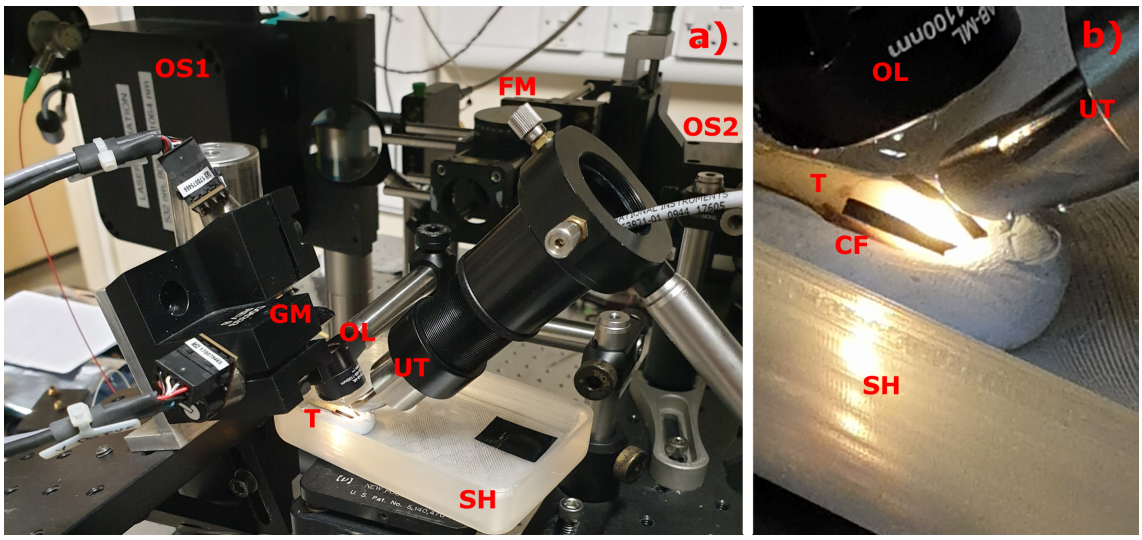


FIGURE 5.5: Images of the reflection mode OAM instrument depicting the sample positioning and illumination. (a) OS1: picosecond laser; OS2: nanosecond laser; GM: galvo-scanners; OL: objective lens; T: human tooth; UT: ultrasound transducer; SH: sample holder; CF: carbon fibre tape. FM: flipping mirror used to switch the illumination between the picosecond and the nanosecond laser. (b) close-up of the the sample positioning and illumination.

detected.

This was expected to a degree because dental materials (such as calcium and phosphorous) are rather reflective than absorptive. Calcium absorption peaks can only be observed in shorter wavelengths. Perhaps, a reflectivity based contrast mechanism such as visible OCT with multi-spectral capabilities would be a more suitable candidate for such studies.

## 5.4 Conclusion

The work presented in this chapter demonstrates that the axial resolution of any OAM instrument can be improved by narrowing the pulse duration of the excitation laser. More precisely, this study experimentally proves that by using a Q-switched microchip laser delivering 85 ps pulses, the axial resolution is 50 % better than when employing a 2 ns pulse duration laser. Agano et al. and Irasawa et al. conducted simulations revealing that shorter pulses can generate

stronger and broader bandwidth ultrasound waves. While these simulations primarily focused on longer pulse duration, we anticipate similar outcomes with much shorter pulses, such as 85 ps. This, however, can limit significantly the maximum permissible exposure of the sample.

By simulation, a 3 ps pulse duration laser has been shown [17] to generate frequencies well above 270 MHz. In principle, if the conditions to produce the opto-acoustic effect are fulfilled, extremely low pulse duration lasers can be used to develop high-axial resolution instruments. However, extreme short pulses for similar energies may exhibit such high peak pulse power that non-linear optical effects may limit further reduction of the pulse duration.

In comparison to other optical sources commonly used in OAM, such as frequency-converted nanosecond (ns) Q-switched lasers [23, 24] or supercontinuum (SC) fiber systems [25, 26], the microchip laser utilized in this study provides several additional advantageous characteristics. Although it currently operates solely at a single wavelength, it offers a higher pulse repetition rate than standard Q-switched systems and/or higher pulse energy when compared to mode-locked systems. Moreover, the laser has a small footprint ( $15 \times 15 \times 15\ cm^3$), a rather simple architecture and low cost, which makes it advantageous compared to solutions based on amplified gain-switched lasers.

Although the ps laser employed here only operates at 532 nm, we must point out that 532 nm is a very popular wavelength used for opto-acoustic imaging since light at this wavelength is absorbed by a plethora of chromophores present in biological samples.

A high repetition rate suggests that the chip laser employed here can be a highly sought-after optical source for OAM. To take full advantage of the enhancement in axial resolution, further investigations are needed as soon as faster ultrasound transducers become available, and shorter pulse duration laser technologies are developed.

As of now, we need to mention two limitations of the instrument we developed due to the repetitive nature of the experiments conducted. First, to achieve constant high lateral resolution along the axial direction, and therefore be able to differentiate the anatomical brain structures of the tadpole, repetitive imaging at 50 $\mu m$ increments was required and secondly, although the *B-scan* images were produced in real-time, the combined image shown in Fig. 5.4 required post-processing. To overcome these limitations, higher pulse repetition rates must be used in an instrument equipped with a fast-focusing capability (such as the use of a liquid lens, instead of the manual adjustment we performed) and harness the computing power of the graphics cards to improve the post-processing time.

The work presented here was inspired by a collaboration with the department of neuroscience aiming to identify the "missing" decision making neurons in tadpoles. Identifying and localizing these decision making neurons would be a significant milestone in neuroscience because the applications and the pathologies related to these neurons translate also to humans. This study demonstrates the required specificity to be able to localize these neurons. The next step would be to integrate a functional imaging channel such as calcium imaging, in synchronization with the OAM system. This way, OAM images of the sample can be obtained and differentiated to images synchronous to neuron firing (activity) and images prior/post neuron firing. According to the work reported by Dean-Ben et al. [27] the amplitude of the opto-acoustic signal changes when the neurons are firing. Taking into account that these "missing" decision making neurons fire only within a well defined time window indicates that this approach is very promising. Such an achievement will not only be a milestone in neuroscience but will also initiate a fruitful field for opto-acoustic microscopy.

# Conclusion

Opto-acoustic Microscopy (OAM) emerges as a promising technique in biomedical imaging, offering nuanced structural and functional insights with high resolution. This thesis sets out to delve into OAM's capabilities, particularly in the realm of diagnostic tools, with a specific focus on cancer diagnosis.

Drawing from the research outlined in this thesis, it becomes evident that OAM holds considerable promise in the realm of biomedical imaging. For instance, the utilization of a high-resolution opto-acoustic microscopy instrument enabled the successful in-vivo multi-spectral imaging of multiple endogenous contrast agents in Xenopus laevis tadpoles. By harnessing the capabilities of a novel supercontinuum (SC) source, lipid mapping was achieved, showcasing OAM's adaptability and efficacy in diverse biological contexts.

Moreover, the integration of optical coherence tomography (OCT) into the OAM system not only provided structural guidance but also enhanced the reliability of the imaging process. This integration exemplifies the interdisciplinary nature of biomedical research, where the synergy between different modalities yields comprehensive insights.

One notable achievement highlighted in the thesis is the successful demonstration of OAM imaging across the entire spectral range of a commercial SC source. This accomplishment opens up avenues for comprehensive mapping of endogenous contrast agents, such as melanin, haemoglobin, collagen, glucose, and lipids, in living specimens.

Despite these advancements, challenges persist, particularly in obtaining quantitative absorption coefficient data. However, collaborative efforts with neuroscience departments offer promising prospects in the exploration of neural circuitry, showcasing OAM's versatility beyond traditional biomedical applications.

Looking towards the future, advancements in ultrasound transducers and laser technologies hold the potential to further enhance OAM's capabilities. For instance, the adoption of shorter pulse duration lasers promises improved axial resolution, paving the way for more precise diagnostics. Additionally, the development of low-cost OAM instruments could democratize access to advanced diagnostic tools, revolutionizing healthcare delivery.

In conclusion, the research presented in this thesis underscores the transformative potential of opto-acoustic microscopy in biomedical imaging. By pushing the boundaries of technological innovation and fostering interdisciplinary collaboration, OAM stands poised to revolutionize diagnostic techniques, ultimately improving patient outcomes and advancing healthcare on a global scale.

# References

[1] G. Nteroli *et al.*, "Enhanced resolution optoacoustic microscopy using a picosecond high repetition rate Q-switched microchip laser," en, *Journal of Biomedical Optics*, vol. 27, no. 11, Nov. 2022, Accepted: 2022-11-04 Number: 11 Publisher: SPIE, ISSN: 1083-3668. [Online]. Available: https://doi.org/10.1117/1.JBO.27.11.110501 (visited on 02/10/2023).

[2] J. Ripoll, B. Koberstein-Schwarz, and V. Ntziachristos, "Unleashing Optics and Optoacoustics for Developmental Biology," en, *Trends in Biotechnology*, vol. 33, no. 11, pp. 679–691, Nov. 2015, ISSN: 0167-7799. DOI: 10.1016/j.tibtech.2015.08.002. [Online]. Available: https://www.sciencedirect.com/science/article/pii/S0167779915001742 (visited on 02/15/2023).

[3] T. Péresse and A. Gautier, "Next-Generation Fluorogen-Based Reporters and Biosensors for Advanced Bioimaging," en, *International Journal of Molecular Sciences*, vol. 20, no. 24, p. 6142, Jan. 2019, Number: 24 Publisher: Multidisciplinary Digital Publishing Institute, ISSN: 1422-0067. DOI: 10.3390/ijms20246142. [Online]. Available: https://www.mdpi.com/1422-0067/20/24/6142 (visited on 02/15/2023).

[4] P. Wang, P. Wang, H.-W. Wang, and J.-X. Cheng, "Mapping lipid and collagen by multispectral photoacoustic imaging of chemical bond vibration," *JBO*, vol. 17, no. 9, p. 096 010, Sep. 2012, Publisher: SPIE, ISSN: 1083-3668, 1560-2281. DOI: 10.1117/1.JBO.17.9.096010. [Online]. Available: https://www.spiedigitallibrary.org/journals/journal-of-biomedical-optics/volume-17/issue-9/096010/Mapping-lipid-and-collagen-by-multispectral-photoacoustic-imaging-of-chemical/10.1117/1.JBO.17.9.096010.full (visited on 02/14/2023).

[5] S. Jeon, J. Kim, D. Lee, J. W. Baik, and C. Kim, "Review on practical photoacoustic microscopy," en, *Photoacoustics*, vol. 15, p. 100 141, Sep. 2019, ISSN: 2213-5979. DOI: 10.1016/j.pacs.2019.100141. [Online]. Available: https://www.sciencedirect.com/science/article/pii/S2213597919300175 (visited on 02/15/2023).

[6] T. Buma, N. C. Conley, and S. W. Choi, "Multispectral photoacoustic microscopy of lipids using a pulsed supercontinuum laser," en, *Biomedical Optics Express*, vol. 9, no. 1, p. 276, Jan. 2018, ISSN: 2156-7085, 2156-7085. DOI: 10.1364/BOE.9.000276. (visited on 03/09/2020).

[7] M. K. Dasa, C. Markos, J. Janting, and O. Bang, "Multispectral photoacoustic sensing for accurate glucose monitoring using a supercontinuum laser," EN, *JOSA B*, vol. 36, no. 2, A61–A65, Feb. 2019, Publisher: Optical Society

of America, ISSN: 1520-8540. DOI: 10.1364/JOSAB.36.000A61. (visited on 03/31/2020).

[8] R. Haindl *et al.*, "Dual modality reflection mode optical coherence and photoacoustic microscopy using an akinetic sensor," EN, *Optics Letters*, vol. 42, no. 21, pp. 4319–4322, Nov. 2017, Publisher: Optica Publishing Group, ISSN: 1539-4794. DOI: 10.1364/OL.42.004319. [Online]. Available: https://opg.optica.org/ol/abstract.cfm?uri=ol-42-21-4319 (visited on 02/09/2023).

[9] T. Allen *et al.*, "Ultrafast laser-scanning optical resolution photoacoustic microscopy at up to 2 million A-lines per second," *To add*, 2018. DOI: 10.1117/1.JBO.23.12.126502.

[10] R. Ansari, E. Z. Zhang, A. E. Desjardins, and P. C. Beard, "All-optical forward-viewing photoacoustic probe for high-resolution 3D endoscopy," en, *Light Sci Appl*, vol. 7, no. 1, p. 75, Oct. 2018, Number: 1 Publisher: Nature Publishing Group, ISSN: 2047-7538. DOI: 10.1038/s41377-018-0070-5. [Online]. Available: https://www.nature.com/articles/s41377-018-0070-5 (visited on 04/28/2023).

[11] C. Liu, Y. Liang, and L. Wang, "Single-shot photoacoustic microscopy of hemoglobin concentration, oxygen saturation, and blood flow in sub-microseconds," en, *Photoacoustics*, vol. 17, p. 100 156, Mar. 2020, ISSN: 2213-5979. DOI: 10.1016/j.pacs.2019.100156. (visited on 03/09/2020).

[12] G. Nteroli *et al.*, "Two octaves spanning photoacoustic microscopy," en, *Scientific Reports*, vol. 12, Jun. 2022, Accepted: 2022-06-14 Publisher: Nature Research, ISSN: 2045-2322. [Online]. Available: https://doi.org/10.1038/s41598-022-14869-5 (visited on 02/10/2023).

[13] K. Irisawa, T. Hirasawa, K. Hirota, K. Tsujita, and M. Ishihara, "Influence of laser pulse width to the photoacoustic temporal waveform and the image resolution with a solid-state excitation laser," in *Photons Plus Ultrasound:*

*Imaging and Sensing 2012*, vol. 8223, SPIE, Feb. 2012, pp. 544–551. DOI: 10.1117/12.907714. [Online]. Available: https://www.spiedigitallibrary.org/conference-proceedings-of-spie/8223/82232W/Influence-of-laser-pulse-width-to-the-photoacoustic-temporal-waveform/10.1117/12.907714.full (visited on 11/15/2021).

[14] T. Agano, M. K. A. Singh, R. Nagaoka, and K. Awazu, "Effect of light pulse width on frequency characteristics of photoacoustic signal – an experimental study using a pulse-width tunable LED-based photoacoustic imaging system," en-US, *International Journal of Engineering & Technology*, vol. 7, no. 4, pp. 4300–4303, Dec. 2018, Number: 4, ISSN: 2227-524X. DOI: 10.14419/ijet.v7i4.19907. [Online]. Available: https://www.sciencepubco.com/index.php/ijet/article/view/19907 (visited on 11/01/2021).

[15] L. V. Wang and S. Hu, "Photoacoustic Tomography: In Vivo Imaging from Organelles to Organs," *Science*, vol. 335, no. 6075, pp. 1458–1462, Mar. 2012, Publisher: American Association for the Advancement of Science. DOI: 10.1126/science.1216210. [Online]. Available: https://www.science.org/doi/10.1126/science.1216210 (visited on 02/09/2023).

[16] E. M. Strohm, M. J. Moore, and M. C. Kolios, "Single Cell Photoacoustic Microscopy: A Review," *IEEE Journal of Selected Topics in Quantum Electronics*, vol. 22, no. 3, pp. 137–151, Feb. 2016, Conference Name: IEEE Journal of Selected Topics in Quantum Electronics, ISSN: 1558-4542. DOI: 10.1109/JSTQE.2015.2497323.

[17] J. Yao *et al.*, "High-speed label-free functional photoacoustic microscopy of mouse brain in action," en, *Nat Methods*, vol. 12, no. 5, pp. 407–410, May 2015, Number: 5 Publisher: Nature Publishing Group, ISSN: 1548-7105. DOI: 10.1038/nmeth.3336. [Online]. Available: https://www.nature.com/articles/nmeth.3336 (visited on 02/15/2023).

[18] E. Pshennikova and A. Voronina, "Expression of the transcription factor xvent-2 in xenopus laevis embryogenesis," EN, *American Journal of Molecular Biology*, vol. 2, 2016. DOI: 10.4236/ajmb.2012.22014. (visited on 2012).

[19] E. Hetch, *Optics*, EN, 4th ed. Pearson, 2002, ISBN: 0-321-18878-0.

[20] S. Hein, J. Tapia, and P. Bazos, "eLABor_aid: A new approach to digital shade management," eng, *Int J Esthet Dent*, vol. 12, no. 2, pp. 186–202, 2017, ISSN: 2198-591X.

[21] J. F. Fondriest, "Shade Matching a Single Maxillary Central Incisor," en,

[22] S. Hein, D. Modrić, S. Westland, and M. Tomeček, "Objective shade matching, communication, and reproduction by combining dental photography and numeric shade quantification," en, *Journal of Esthetic and Restorative Dentistry*, vol. 33, no. 1, pp. 107–117, 2021, _eprint: https://onlinelibrary.wiley.com/do ISSN: 1708-8240. DOI: 10.1111/jerd.12641. [Online]. Available: https://onlinelibrary.wiley.com/doi/abs/10.1111/jerd.12641 (visited on 05/03/2023).

[23] S.-W. Cho *et al.*, "High-speed photoacoustic microscopy: A review dedicated on light sources," en, *Photoacoustics*, vol. 24, p. 100 291, Dec. 2021, ISSN: 2213-5979. DOI: 10.1016/j.pacs.2021.100291. [Online]. Available: https://www.sciencedirect.com/science/article/pii/S2213597921000513 (visited on 02/15/2023).

[24] G. Hu, M. Dong, K. Chen, Z. Wang, H. Niu, and L. Zhu, "Tunable multidimensional multiplexed Q-switched pulse outputs from a linear fiber laser with a bidirectional loop," en, *Optics & Laser Technology*, vol. 141, p. 107 138, Sep. 2021, ISSN: 0030-3992. DOI: 10.1016/j.optlastec.2021.107138. [Online]. Available: https://www.sciencedirect.com/science/article/pii/S0030399221002267 (visited on 11/04/2021).

[25] M. K. Dasa *et al.*, "All-fibre supercontinuum laser for in vivo multispectral photoacoustic microscopy of lipids in the extended near-infrared region," en, *Photoacoustics*, vol. 18, p. 100 163, Jun. 2020, ISSN: 2213-5979. DOI: 10.1016/j.pacs.2020.100163. (visited on 03/09/2020).

[26] M. Bondu, M. J. Marques, P. M. Moselund, G. Lall, A. Bradu, and A. Podoleanu, "Multispectral photoacoustic microscopy and optical coherence tomography using a single supercontinuum source," en, *Photoacoustics*, vol. 9, pp. 21–30, Mar. 2018, ISSN: 2213-5979. DOI: 10.1016/j.pacs.2017.11.002. (visited on 03/09/2020).

[27] X. L. Deán-Ben *et al.*, "Functional optoacoustic neuro-tomography for scalable whole-brain monitoring of calcium indicators," en, *Light Sci Appl*, vol. 5, no. 12, e16201–e16201, Dec. 2016, ISSN: 2047-7538. DOI: 10.1038/lsa.2016.201. [Online]. Available: http://www.nature.com/articles/lsa2016201 (visited on 10/04/2020).

# Part III

# Appendix

Photoacoustics 18 (2020) 100163

Contents lists available at ScienceDirect

Photoacoustics

journal homepage: www.elsevier.com/locate/pacs

# All-fibre supercontinuum laser for *in vivo* multispectral photoacoustic microscopy of lipids in the extended near-infrared region

Manoj K. Dasa[a,*,1], Gianni Nteroli[d,1], Patrick Bowen[c], Giulia Messa[e], Yuyang Feng[f], Christian R. Petersen[a,b], Stella Koutsikou[e], Magalie Bondu[c], Peter M. Moselund[c], Adrian Podoleanu[d], Adrian Bradu[d], Christos Markos[a,b], Ole Bang[a,b,c]

[a] DTU Fotonik, Technical University of Denmark, 2800 Kgs. Lyngby, Denmark
[b] NORBLIS IVS, Virumgade 35D, 2830 Virum, Denmark
[c] NKT Photonics A/S, Blokken 84, 3460 Birkerød, Denmark
[d] Applied Optics Group, University of Kent, Canterbury, UK
[e] Medway School of Pharmacy, University of Kent, Chatham, UK
[f] COPAC A/S, Diplomvej 381, 2800 Kongens Lyngby, Denmark

ARTICLE INFO

*Keywords:*
Photoacoustic microscopy
Fibre lasers
Supercontinuum
Lipids

ABSTRACT

Among the numerous endogenous biological molecules, information on lipids is highly coveted for understanding both aspects of developmental biology and research in fatal chronic diseases. Due to the pronounced absorption features of lipids in the extended near-infrared region (1650 − 1850 nm), visualisation and identification of lipids become possible using multi-spectral photoacoustic (optoacoustic) microscopy. However, the spectroscopic studies in this spectral region require lasers that can produce high pulse energies over a broad spectral bandwidth to efficiently excite strong photoacoustic signals. The most well-known laser sources capable of satisfying the multi-spectral photoacoustic microscopy requirements (tunability and pulse energy) are tunable nanosecond optical parametric oscillators. However, these lasers have an inherently large footprint, thus preventing their use in compact microscopy systems. Besides, they exhibit low-repetition rates. Here, we demonstrate a compact all-fibre, high pulse energy supercontinuum laser that covers a spectral range from 1440 to 1870 nm with a 7 ns pulse duration and total energy of 18.3 μJ at a repetition rate of 100 kHz. Using the developed high-pulse energy source, we perform multi-spectral photoacoustic microscopy imaging of lipids, both *ex vivo* on adipose tissue and *in vivo* to study the development of *Xenopus laevis* tadpoles, using six different excitation bands over the first overtone transition of C–H vibration bonds (1650 − 1850 nm).

## 1. Introduction

The ability to visualise specific endogenous biological molecules following their spatial distribution and temporal dynamics *in vivo* without the use of perturbative labels is essential for understanding their physiological impact and subsequent regulatory mechanisms. To this end, photoacoustic microscopy (PAM) enables real-time visualisation of various endogenous agents, such as haemoglobin and melanin, using their inherent wavelength-dependent absorption at extended penetration depths. This label-free ability of PAM makes it a promising technique for the detection, diagnosis, and monitoring of various diseases [1–5].

Lipids play a crucial role in cellular physiology as structural components of biological membranes, biosynthetic precursors, and energy storage [6]. Moreover, they act as major contrast agents in the identification of fatal chronic diseases like atherosclerosis and myocardial infarction [14]. Therefore, there is a demand for high-resolution label-free imaging of lipids in medical imaging [6–13]. However, early studies based on PAM revealed that the dominant absorption features of other endogenous agents, including haemoglobin and melanin, prevent effective imaging of lipids in the classical optical imaging window (400–700 nm) [14,15].

Following these early studies, attention turned to optical imaging windows in the longer near-infrared (NIR) wavelength regions: 1100 − 1300 nm and 1650 − 1850 nm, due to the presence of C–H molecular overtone transitions in these regions [16–18]. The absorption

* Corresponding author at: DTU Fotonik, Ørstedsplads 343, Lyngby 2800, Denmark.
*E-mail address:* manda@fotonik.dtu.dk (M.K. Dasa).
[1] These authors contributed equally to this work.

https://doi.org/10.1016/j.pacs.2020.100163
Received 16 December 2019; Received in revised form 15 January 2020; Accepted 22 January 2020
Available online 27 January 2020

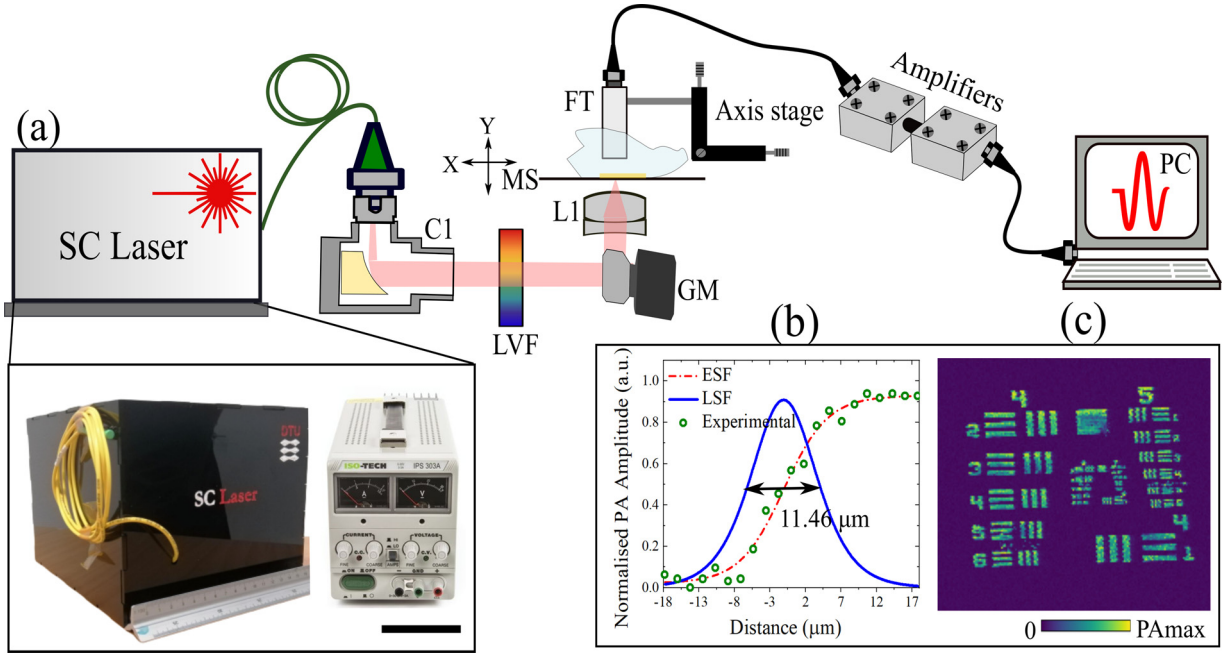


**Fig. 1.** (a) Schematic of the MS-PAM system. C1: reflective collimator, LVF: linear variable filter, GM: galvo-mirrors, L1: achromatic lens, MS: microscopy slide, FT: flat transducer, PC: the personal computer. The photograph in the bottom left shows the all-fibre SC laser and the power supply unit with a scale bar of 10 cm. (b): Lateral resolution of the MS-PAM system estimated by using the edge and line spread functions. (c): PAM image of the USAF resolution target at 1720 nm.

spectrum of lipids in both the 1100 − 1300 nm (second overtone of C–H bonds) and 1650 − 1850 nm (first overtone of C–H bonds), shows well-differentiated peaks with higher absorption coefficients compared to the other main constituents of biological tissue, such as water and haemoglobin [19–28]. Notably, the stronger absorption of lipids in the first overtone region when compared to the second overtone region (~6.3 times), recommend this band for discerning developmental changes in biological bodies non-invasively byways of intravascular photoacoustic imaging (IVPAI) [26]. PAM in the first overtone region has been reported on white matter in a rat spinal cord [20], intramuscular fat and Drosophila Melanogaster larva [28] using optical resolution (OR)-PAM mode, and on lipid-laden atherosclerotic plaques and human femoral arteries using IVPAI mode [21,24–26].

So far, in most of the reports mentioned above, nanosecond optical parametric oscillators (OPO) were employed as excitation sources for PA generation. Despite their broadband tunability with sufficiently high pulse energy density (PED) to excite a PA signal, OPOs present a high cost, a large footprint and low pulse repetition rate (PRR), making them non-ideal for compact and efficient PAM systems [28]. An alternative source that could circumvent the use of an OPO is based on supercontinuum (SC) generation [28–38], which can have spectral bandwidths spanning several octaves [28] and provide a brightness order of magnitude higher than a synchrotron [37]. The use of SC laser sources for the practice of MS−PA applications [39,40] and PAM based multimodal applications have been already reported [41,42]. However, the reported SC lasers are either limited by the emission wavelength or by the PED required for MS-PAM of lipids in the first overtone region of C–H bonds. Recently, an SC laser source pumped at 1047 nm, below the zero-dispersion wavelength (ZDW) of a photonic crystal fibre (PCF), has been used for lipid detection [28]. However, due to the limited PED in the first overtone region, multi-spectral photoacoustic microscopy (MS-PAM) could not be demonstrated in the first overtone region of C–H bonds. In a recent work, we presented a promising way of generating a suitable SC based on a commercial erbium-doped fibre amplifier and few meters of standard single-mode optical fibre (SMF-28), producing sufficient PED to perform *ex vivo* MS-PAM of lipids in the first overtone region [34].

In the current report, we demonstrate, for the first time to our knowledge, *in vivo* MS-PAM in the first C–H overtone region by further scaling up the PED of the SC laser. The high PED is achieved by increasing the output power of the pump and using a directly modulated diode (DMD) as the seed. The DMD based configuration was chosen to further exploit the flexibility in pulse duration and PRR. The SC source is based on a robust and compact design, using telecommunication range multiple-stage erbium (Er) and erbium: ytterbium (Er: Yb) co-doped fibre amplifiers and a few meters of standard dispersion-shifted fibre (DSF). When compared to the previously reported SC laser [34], the current source exhibits not only higher power spectral density (PSD) but also a significantly higher PRR, thus increasing the image acquisition speed.

In this paper, we further demonstrate the applicability of such a laser source by performing MS-PAM of lipids on *ex vivo* adipose tissue and *in vivo* on *Xenopus laevis* tadpoles over the entire first overtone region. The system can visualise lipid distribution inside both samples with high contrast, thus carving out a new direction towards compact, broadband and cost-effective sources for label-free imaging of lipids in both developmental biology and medical applications.

## 2. Materials and methods

### 2.1. Ethical approval

*In vivo* experiments were performed on the *Xenopus laevis* tadpole at developmental stage 37/38, based on Nieuwkoop and Faber 1956 [43]. Embryos were supplied by the European *Xenopus* Resource Centre (EXRC, Portsmouth UK) and kept at ~20 °C in tap water. During the MS-PAM experiments, animals were anaesthetised in 0.1 % MS-222 solution (ethyl 3-aminobenzoate methanesulfonate, Sigma-Aldrich). All experimental procedures on stage 37/38 tadpoles are unregulated but were nevertheless approved by the University of Kent's animal welfare ethics committee.

### 2.2. MS-PAM system

Fig. 1(a) shows a schematic overview of the MS-PAM set up together with a photo of the actual all-fibre SC laser used in our experiments,

including the power supply. The system is based on a custom in-house fabricated fibre-coupled SC laser as the excitation source. The laser beam from the SC is collimated using a broadband reflective collimator (RC04FC-P01, Thorlabs) and then spectrally filtered by a linear variable filter (LVF) (LVF 1.2–2.5-3.5-15-0.5, Vortex Optical Coatings). The filtered excitation beam is steered using a set of orthogonal galvanometer-based XY scanners (6220H, Cambridge Technology Ltd), allowing raster scanning of the sample in the lateral directions. A mounted achromatic lens doublet (AC254-040-C-ML, Thorlabs) was used to focus the excitation beam onto the sample. A custom-made ultrasonic transducer (COPAC) with a centre frequency of 10 MHz detects the photoacoustic (PA) signals generated by the optical excitation bands. The detected PA signal is amplified using two low-noise wideband amplifiers (ZFL-500LN, Mini-Circuits) and then conveyed towards the input of a fast digitizer (PCI-5124, National Instruments) for data processing. The digitizer, hosted in a PC, operates at 200 MS/second, allowing signal up to a maximum bandwidth of 100 MHz. An internal hardware filter of the digitizer was configured as a low pass filter up to 40 MHz. As the repetition rate of the source is 100 kHz, each temporal analogue signal of 10 μs is generated by the transducer. Each pulse is digitised into 2000 sampling points within an interval of 10 μs, while the optical beam is scanned over the sample. However, in order to improve the signal-to-noise ratio (SNR) and maintain an isometrically resolved image, the signal is cropped into 410 points around the area of interest. A triangular signal drives the fast galvo-scanner at 122 Hz, the ascending part of the triangular signal is used for the acquisition while the descending part of processing the data.

In this way, since the optical source was set at a repetition rate of 100 kHz, each generated B-scan image is assembled from 410 lateral pixels. As a consequence, a complete 3D volumetric image of size 410 × 410 × 410 pixels is acquired in 3.2 s.

After each lateral scan of the optical beam over the sample, the signal is processed by a Hilbert transform to obtain the envelope of the sample's PA signal to deliver the PA depth profile (A-scan) for each lateral pixel and then assemble the depth profiles to obtain a B-scan. As the time required to process 410 A-scans was 8.2 ms (the time required by the fast galvo-scanner to return to its initial position), B-scan images were displayed in real-time at a frame rate of 122 Hz.

All the samples used in the experiments were placed in Petri dishes and immersed in either clear ultrasound gel for *ex vivo* experiments or in a water-based solution for *in vivo* experiments, to facilitate acoustic coupling. As the Petri dish available does not exhibit sufficient transparency in the spectral window of interest, an imaging window was created at the bottom of the dish and sealed with a microscope slide (thickness of 0.2 mm). Two independent 3D translation stages were used to support and coaxially align the sample holder and transducer to the optical excitation beam.

The lateral resolution of the MS-PAM system was experimentally quantified by imaging the edge of an element on a positive 1951 United States Air Force test target (R1DS1P, Thorlabs). As shown in Fig. 1(b), the edge spread function (ESF) was calculated by fitting the raw PA signal collected from scanning the edge in steps of 1.6 μm. The line spread function (LSF) was then calculated by taking the derivative of the ESF. The lateral resolution of the system is defined as the full width at half-maximum (FWHM) of the LSF and was found to be ~11.46 μm. The theoretical lateral resolution of the MS-PAM system at the beam focus was calculated to be ~10.79 μm at a 1720 nm excitation wavelength, indicating that the system is close to the diffraction limit. The photoacoustic maximum amplitude projection (MAP) of the test target is shown in Fig. 1(c).

## 3. Results and discussion

### 3.1. Optical characterisation of the SC laser

As shown in Fig. 2(a), the seed laser (DFBITU-100, EMCORE), providing an output power of 20 μW at 1553.5 nm, is directly modulated to produce 7 ns pulses (FWHM) at a PRF of 100 kHz. Two high-gain pre-amplifier stages amplify the pulses from the directly modulated seed laser, each comprised of a 3.5 m long Er-doped optical fibre (PM-ESF-7/125, Nufern) with a core diameter of 7 μm. This optical fibre was core pumped using a single 976 nm CW laser diode (IIVI-LD976-6, II−VI) in the forward configuration. The average output power measured after the first and second preamplifiers were ~ 3 mW (17 dB optical gain) and 101 mW (15.2 dB optical gain) respectively. In the booster amplification stage, a 4.5 m co-doped Er: Yb fibre (PM-EYDF-12/130, Nufern) with a core diameter of 12 μm was cladding-pumped using two 915 nm CW multimode high-power laser diodes (MU20-915-01/02, Oclaro) in the backward configuration. A 2 nm bandpass filter after the preamplifier, is used to suppress amplified spontaneous emission (ASE) and parasitic lasing. The average output power measured after the booster amplifier is 2270 mW (with 9 W pump power, corresponding to a 25.2 % efficiency, which is equivalent to a pulse energy of 22.7 μJ per pulse at 100 kHz repetition rate.

The output from the booster amplifier is used to pump 4.5 m of a commercially available DSF (DCF 4, Thorlabs), thereby generating an SC from 1440 − 1870 nm, with an average output power of 1830 mW. SC generation is initiated by modulation instability (MI), which breaks up the long pump pulses into large numbers of solitons that undergo Raman self-frequency shifting and collisions, which further extend the spectrum towards longer wavelengths of up to 1870 nm [29–31]. To avoid back reflections from the end facet of the DSF, the output end of the DSF was angle cleaved and then connectorized (FC/APC-30126A9, Thorlabs) for ease of handling.

The PSD of the pre-amplifier (red), booster amplifier (blue) and the SC (green) are shown in Fig. 2(b). Fig. 2(c) shows the PSD of the SC from the current SC laser configuration (green) in comparison to our previous work (red). The higher PSD of the SC can be attributed to the higher pump power due to additional amplification stages. An LVF with a bandwidth of around 2 % of the centre wavelength (33 − 38 nm) is used to filter the excitation bands from the SC. Figs. 2(d) and 2(e) show the six filtered excitation bands from the SC used during the multi-spectral experiments and their respective pulse energies and the bandwidth in the individual bands. It can be noticed that all excitation bands have sufficiently high pulse energy (> 197 nJ) for performing OR-PAM [32].

### 3.2. Ex vivo MS-PAM imaging of Adipose tissue

MS-PAM imaging was performed on a thin slice (about 3 mm) of adipose tissue from sheep in the 1600 − 1800 nm wavelength range. Six excitation bands in steps of 40 nm were filtered from the SC laser using the LVF, shown in Fig. 2. The acquisition and analysis of the raw data are accomplished by using in-house software developed in LabVIEW. The programme instructs a fast digitizer to convert the analogue to digital signal collected by the transducer in synchronism with the optical pulses generated by the source and the start and stop of lateral scanning by the galvo-scanners. For each position of the beam on the sample, the PA signal is digitised, and an A-scan is generated using a Hilbert transform. An intensity graph is produced by plotting the PA amplitudes extracted from each A-scan recorded as a function of X and Y position to form a PAM image, an. As mentioned earlier, a complete 3D volumetric image of size 410 × 410 × 410 pixels is acquired in 3.2 s. To improve the SNR; however, as conventionally done in PAM, data acquisition is repeated for 16 times, and signals averaged (averaging over 16 A-scans) before generating a B-scan. Therefore, the PAM images demonstrated in Fig. 3, require 51.2 s. This technique enhances the contrast in the image.

Fig. 3 shows an optical image and MS-PAM images of *ex vivo* adipose tissue that are z-projected *en-face* images at six different excitation bands. The images are normalised to their respective pulse energy in the excitation band used.

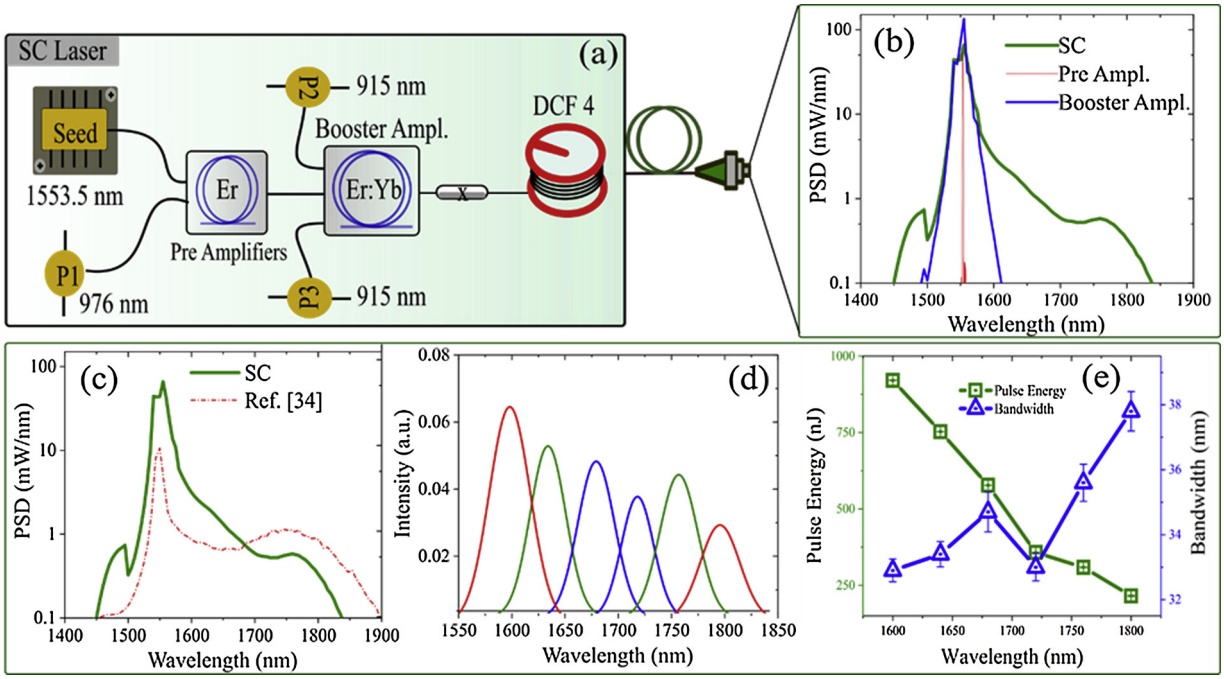


**Fig. 2.** (a) Schematic of the SC laser configuration. DCF4: dispersion-shifted fibre. (b): PSD of preamplifier, booster amplifier and the SC spectrum generated by pumping a 4.5 m non-zero DSF. (c): SC output spectrum (solid line) in comparison with the SC reported in our previous work (dashed line). (d): SC Excitation bands filtered using the LVF. (e): Pulse energy and bandwidth of filtered excitation bands from the SC laser.

The *ex vivo* adipose tissue images reveal a peak in the PA amplitude at 1720 nm, which is consistent with the PA spectrum measurements reported in our previous report [34]. PA spectra of the tissue acquired from two different regions are plotted in Fig. 4(a), both regions confirmed a stronger PA absorption at 1720 nm, which can be attributed to the stronger absorption of lipids at 1720 nm due to the first overtone transition of C–H bonds, [21,25,28,34]. The SNR (ratio of the measured PA signal to the overall noise at each A-scan) of MS-PAM images at all six excitation bands is calculated and plotted in Fig. 4(b). As expected, the SNR is higher at 1720 nm (18.1 dB) when compared to other excitation bands as the lipid absorption is higher at 1720 nm.

### 3.3. *In vivo* MS-PAM imaging of the *Xenopus laevis* tadpole

*Xenopus laevis* tadpoles were raised in water to stage 37–38, about 53 h post-fertilisation. Tadpoles were chosen at this early stage of development for MS-PAM imaging because they allow easy access to the yolk sac, a well-defined area (Fig. 5) with a high concentration of lipids [44]. Moreover, the skin covering the yolk sac lacks pigmentation, which permits unobstructed laser penetration in the intact animal. Laser radiation in the excitation bands throughout the experiment is well within the maximum permissible exposure (MPE) level. The MPE for tissue is 1 J/cm$^2$ for ns pulses and for the SC excitation band with maximum PED (914 nJ in the 1600 nm excitation band), the exposure level is about 0.88 J/cm$^2$.

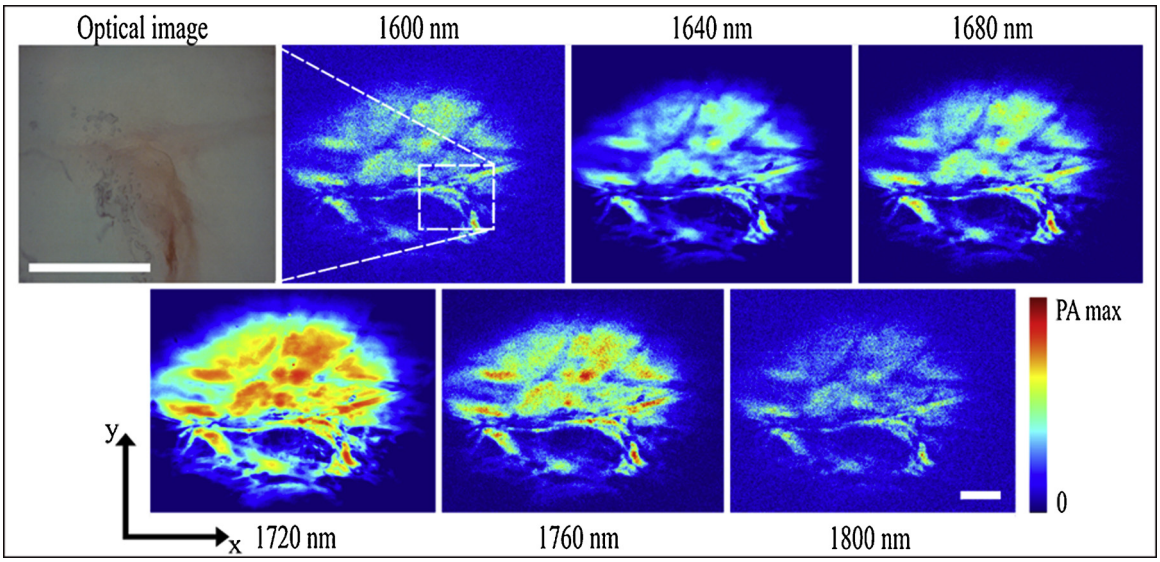


**Fig. 3.** Optical image and MS-PAM images of *ex vivo* adipose tissue. Six z-projected *en-face* MS-PAM images are acquired from 1600 nm to 1800 nm in steps of 40 nm. The white bar in the optical image and the last MS-PAM image at 1800 nm represents the scale bar of 1 mm.

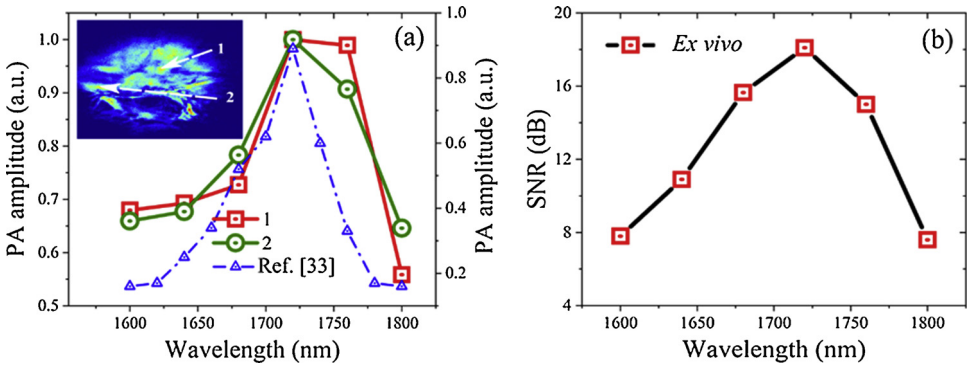


**Fig. 4.** (a) Normalized PA amplitudes at two different regions (labelled 1 and 2 in the inset) for the six excitation bands with corresponding PA amplitudes for adipose tissue measurements reported in our previous study [33]. The area of each region is 0.087 $mm^2$. (b) Measured spectral variation of the SNR of ex *vivo* adipose tissue measured in MS-PAM images.

Fig. 5 shows a photo of the tadpole together with z-projected *en-face* MS-PAM images of the whole body at the six different excitation bands. The MS-PAM images are averaged over 16 A-scans and normalised to the respective pulse energies in the excitation bands. Again, a strong signal is observed at 1720 nm excitation due to the high concentration of lipids, and the contrast decreases at all other excitation wavelengths. As it can be seen from the MS-PAM images of the tadpole, the yolk sack section of the tadpole shows PA signals, which are distributed throughout the section all along its anterior-posterior and the ventral-dorsal axis. The strong PA signals from the yolk sac can be attributed to the presence of vast reserves of lipid molecules [44], which have strong optical absorption due to the first overtone transition of the C–H bond. This agrees with the known abundance of the lipoprotein Vitellogenin in the Xenopus laevis yolk sac [44].

Fig. 6(a) shows the PA spectra of three different regions (Size of 0.087 $mm^2$ each) in the tadpole MS-PAM images measured at the 6 excitation bands as above. The PA signals demonstrate consistent results showing the expected maximum at 1720 nm. The SNR of the *in vivo* images at the six excitation bands is calculated and displayed in Fig. 6(b).

Again, the SNR is higher at 1720 nm when compared to other excitation bands. SNR for *in vivo* MS-PAM images are higher when compared to the SNR for *ex vivo* MS-PAM images as the image scan area used for *in vivo* experiments is smaller than in case of the *ex vivo* experiments.

## 4. Conclusions

A high-pulse energy all-fibre SC source based on standard telecom range optical components for MS-PAM imaging of lipids is demonstrated. The filtered optical pulses from the SC source have sufficient pulse energy density for MS-PAM studies on lipids over the first overtone transition of C–H vibration bonds (1650–1850). By employing the SC laser in conjunction with an LVF, we demonstrated the applicability of such a laser source by performing MS-PAM imaging of lipids in *ex vivo* adipose tissue and *in vivo* using *Xenopus laevis* tadpole. Our study has shown that the MS-PAM system can visualise lipids in both *ex vivo* and *in vivo* tissues, which makes it applicable for a wide range of applications. We believe the proposed high pulse energy SC laser paves a new direction towards more compact sources for label-free imaging of lipids in both developmental biology and medical imaging. In future, we would like to scale the PED of the SC laser by using large mode area fibres in the MOPA configuration so as to perform the MS-PAM with higher SNR. Moreover, the higher PED of the laser will allow the use of narrow bandpass filters (like AOTFs) which thereby enable high-resolution MS-PAM of multiple endogenous biological molecules (lipids, glucose, water and collagen) which reveal dominant absorption features in the emission wavelength (1540 − 1840 nm) of the developed source.

## Declaration of Competing Interest

The authors declare that there are no conflicts of interest

## Acknowledgements

The research project leading to this work has received funding from the European Union's Horizon 2020 research and innovation programme under the Marie Skłodowska-Curie grant agreement No 722380. C.M. acknowledges financial support from the Multi-BRAIN project funded by the Lundbeck Foundation (R276-2018-869) and Independent Research Fund Denmark (8022-00091B). C.M., C.R.P., and O.B. acknowledge financial support from the Innovation Fund Denmark (4107-00011A). The authors thank Kyei Kwarkye, Abubakar I. Adamu

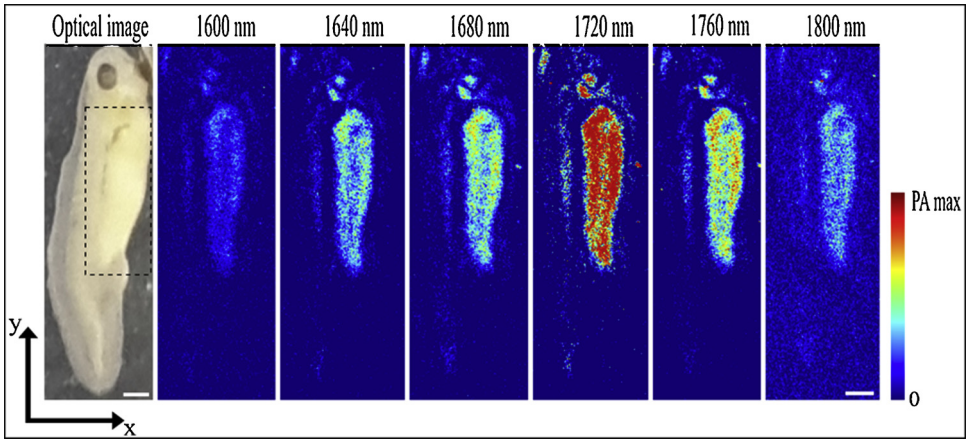


**Fig. 5.** Optical image and 6 *in vivo* z-projected *en-face* MS-PAM images of a *Xenopus laevis* tadpole acquired from 1600 nm to 1800 nm in steps of 40 nm. The highlighted region in the optical image shows the yolk sac. The scale bar represents 1 mm.

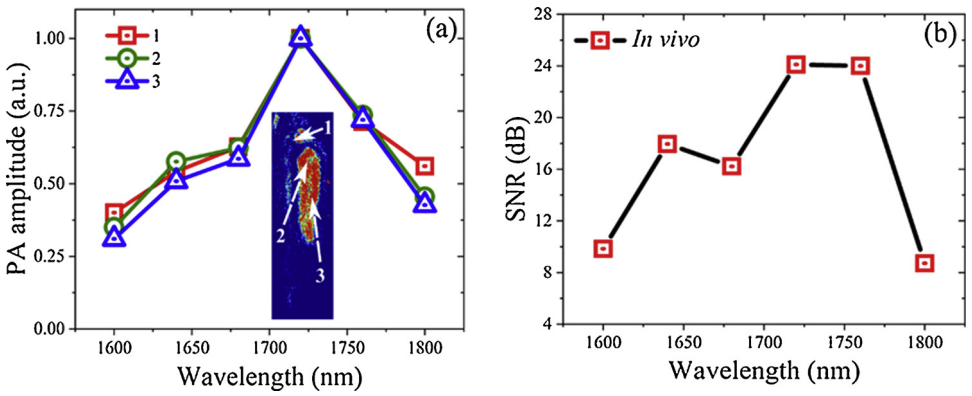


**Fig. 6.** (a) Normalized PA amplitudes of a small region (about 0.087 $mm^2$) in the MS-PAM images of a tadpole at three different places (labelled 1, 2, and 3) for the six excitation bands. (b) Measured SNR of tadpole MS-PAM images at all the six excitation bands.

and Getinet Woyessa for their help with the laser system, and Niels Møller Israelsen, Antonia Longo and Mikkel Jensen for their suggestions about imaging. G.N. acknowledges the University of Kent for financial support. A.B. and A.P. acknowledge EPSRC (RE-BOT grant, EP/N019229/1). A.P. also acknowledges NIHR Biomed. Research Centre at Moorfields Eye Hospital NHS Foundation Trust, the UCL Institute of Ophthalmology, University College London, and the Royal SocietyWolfson research merit award.

## References

[1] Y. Junjie, L.V. Wang, Photoacoustic microscopy, Laser Photonics Rev. 7 (5) (2013) 758–778.
[2] E.M. Strohm, M.J. Moore, M.C. Kolios, Single cell photoacoustic microscopy: a review, Ieee J. Sel. Top. Quantum Electron. 22 (3) (2015) 137–151.
[3] H.F. Zhang, K. Maslov, M. Sivaramakrishnan, G. Stoica, L.V. Wang, Imaging of hemoglobin oxygen saturation variations in single vessels in vivo using photoacoustic microscopy, Appl. Phys. Lett. 90 (5) (2007) 053901.
[4] J.T. Oh, M.L. Li, H.F. Zhang, K. Maslov, L.V. Wang, Three-dimensional imaging of skin melanoma in vivo by dual-wavelength photoacoustic microscopy, J. Biomed. Opt. 11 (3) (2006) 034032.
[5] S. Jeon, J. Kim, D. Lee, B.J. Woo, C. Kim, Review on practical photoacoustic microscopy, Photoacoustics (2019) 100141.
[6] Jr. Farese, V. Robert, T.C. Walther, Lipid droplets finally get a little RESPECT, Cell 139 (5) (2009) 855–860.
[7] S. Zhang, R. Trimble, F. Guo, H. Mak, Lipid droplets as ubiquitous fat storage organelles in C. Elegans, BMC Cell Biol. 11 (2010) 96.
[8] A. Folick, W. Min, M.C. Wang, Label-free imaging of lipid dynamics using Coherent Anti-stokes Raman Scattering (CARS) and Stimulated Raman Scattering (SRS) microscopy, Curr. Opin. Genet. Dev. 21 (5) (2011) 585–590.
[9] J. Chi, Z. Wu, C.H.J. Choi, L. Nguyen, S. Tegegne, S.E. Ackerman, A. Crane, F. Marchildon, M.T. Lavigne, P. Cohen, Three-dimensional adipose tissue imaging reveals regional variation in beige fat biogenesis and PRDM16-dependent sympathetic neurite density, Cell Metab. 27 (1) (2018) 226–236.
[10] T.B. Huff, J.-X. Cheng, In vivo coherent anti-Stokes Raman scattering imaging of sciatic nerve tissue, J. Microsc. 225 (2) (2007) 175–182.
[11] C.-R. Hu, D. Zhang, M.N. Slipchenko, J.-X. Cheng, B. Hu, Label-free real-time imaging of myelination in the Xenopus laevis tadpole by in vivo stimulated Raman scattering microscopy, J. Biomed. Opt. 19 (8) (2014) 086005.
[12] M.J. den Broeder, M.J.B. Moester, J.H. Kamstra, P.H. Cenijn, V. Davidoiu, L.M. Kamminga, F. Ariese, J.F. de Boer, J. Legler, Altered adipogenesis in zebrafish larvae following high fat diet and chemical exposure is visualized by stimulated Raman scattering microscopy, Int. J. Mol. Sci. 18 (4) (2017) 894.
[13] C.H. Chien, W.-W. Chen, J.-T. Wu, T.-C. Chang, Label-free imaging of Drosophila in vivo by coherent anti-Stokes Raman scattering and two-photon excitation autofluorescence microscopy, J. Biomed. Opt. 16 (1) (2011) 016012.
[14] P.C. Beard, T.N. Mills, Characterization of post mortem arterial tissue using time-resolved photoacoustic spectroscopy at 436, 461 and 532 nm, Phys. Med. Biol. 42 (1) (1997) 177–198.
[15] S. Sethuraman, J.H. Amirian, S.H. Litovsky, R.W. Smalling, S.Y. Emelianov, Spectroscopic intravascular photoacoustic imaging to differentiate atherosclerotic plaques, Opt. Express 16 (5) (2007) 3362–3367.
[16] H.W. Wang, N. Chai, P. Wang, S. Hu, W. Dou, D. Umulis, L.V. Wang, M. Sturek, R. Lucht, J.X. Cheng, Label-free bond-selective imaging by listening to vibrationally excited molecules, Phys. Rev. Lett. 106 (23) (2011) 238106.
[17] T.J. Allen, A. Hall, A.P. Dhillon, J.S. Owen, P.C. Beard, Spectroscopic photoacoustic imaging of lipidrich plaques in the human aorta in the 740 to 1400 nm wavelength range, J. Biomed. Opt. 17 (6) (2012) 061209.
[18] P. Wang, P. Wang, H.W. Wang, J.X. Cheng, Mapping lipid and collagen by multispectral photoacoustic imaging of chemical bond vibration, J. Biomed. Opt. 17 (9) (2012) 096010.
[19] K. Jansen, A.F.W. van der Steen, M. Wu, H.M.M. van Beusekom, G. Springeling, X. Li, Q. Zhou, K.K. Shung, D.P.V. de Kleijn, G. van Soest, Spectroscopic intravascular photoacoustic imaging of lipids in atherosclerosis, J. Biomed. Opt. 19 (2) (2014) 026006.
[20] W. Wu, P. Wang, J.X. Cheng, X.M. Xu, Assessment of white matter loss using bond-selective photoacoustic imaging in a rat model of contusive spinal cord injury, J. Neurotrauma 31 (24) (2014) 1998–2002.
[21] K. Jansen, M. Wu, A.F.W. van der Steen, G. van Soest, Photoacoustic imaging of human coronary atherosclerosis in two spectral bands, Photoacoustics 2 (1) (2014) 12–20.
[22] T. Buma, B.C. Wilkinson, T.C. Sheehan, Near-infrared spectroscopic photoacoustic microscopy using a multi-color fiber laser source, Biomed. Opt. Express 6 (8) (2015) 2819–2829.
[23] J. Hui, Q. Yu, T. Ma, P. Wang, Y. Cao, R.S. Bruning, Y. Qu, Z. Chen, Q. Zhou, M. Sturek, J.X. Cheng, High-speed intravascular photoacoustic imaging at 1.7 μm with a KTP-based OPO, Biomed. Opt. Express 6 (11) (2015) 4557–4566.
[24] Z. Piao, T. Ma, J. Li, M.T. Wiedmann, S. Huang, M. Yu, K. Kirk Shung, Q. Zhou, C.S. Kim, Z. Chen, High speed intravascular photoacoustic imaging with fast optical parametric oscillator laser at 1.7μm, Appl. Phys. Lett. 107 (8) (2015) 083701.
[25] M. Wu, K. Jansen, A.F.W. van der Steen, G. van Soest, Specific imaging of atherosclerotic plaque lipids with two-wavelength intravascular photoacoustics, Biomed. Opt. Express 6 (9) (2015) 3276–3286.
[26] J. Hui, R. Li, E.H. Phillips, C.J. Goergen, M. Sturek, J.X. Cheng, Bond-selective photoacoustic imaging by converting molecular vibration into acoustic waves, Photoacoustics 4 (1) (2016) 11–21.
[27] T. Buma, J.L. Farland, M.R. Ferrari, Near-infrared multispectral photoacoustic microscopy using a graded-index fiber amplifier, Photoacoustics 4 (3) (2016) 83–90.
[28] T. Buma, N.C. Conley, S.W. Choi, Multispectral photoacoustic microscopy of lipids using a pulsed supercontinuum laser, Biomed. Opt. Express 9 (1) (2018) 276–288.
[29] J.M. Dudley, G. Genty, S. Coen, Supercontinuum generation in photonic crystal fiber, Rev. Mod. Phys. 78 (4) (2006) 1135–1184.
[30] C. Markos, J.C. Travers, A. Abdolvand, B.J. Eggleton, O. Bang, Hybrid photonic-crystal fiber, Rev.Mod. Phys. 89 (4) (2017) 045003.
[31] A. Boucon, A. Fotiadi, P. Mégret, H. Maillotte, T. Sylvestre, Low-threshold all-fiber 1000 nm supercontinuum source based on highly non-linear fiber, Opt. Commun. 281 (15–16) (2008) 4095–4098.
[32] M. Bondu, C. Brooks, C. Jakobsen, K. Oakes, P.M. Moselund, L. Leick, O. Bang, A. Podoleanu, High energy supercontinuum sources using tapered photonic crystal fibers for multispectral photoacoustic microscopy, J. Biomed. Opt. 21 (6) (2016) 061005.
[33] E. Aytac-Kipergil, A. Demirkiran, N. Uluc, S. Yavas, T. Kayikcioglu, S. Salman, S.G. Karamuk, F.O. Ilday, M.B. Unlu, Development of a Fiber laser with independently adjustable properties for optical resolution photoacoustic microscopy, Sci. Rep. 6 (1) (2016) 38674.
[34] M.K. Dasa, C. Markos, M. Maria, C.R. Petersen, P.M. Moselund, O. Bang, High-pulse energy supercontinuum laser for high-resolution spectroscopic photoacoustic imaging of lipids in the 1650-1850 nm region, Biomed. Opt. Express 9 (4) (2018) 1762–1770.
[35] M.K. Dasa, C. Markos, J. Janting, O. Bang, Multispectral photoacoustic sensing for accurate glucose monitoring using a supercontinuum laser, JOSA B 36 (2) (2019) A61–A65.
[36] N.M. Israelsen, C.R. Petersen, A. Bahr, D. Jain, M. Jensen, G. Hannesschläger, P. Tidemand-Lichtenberg, C. Pedersen, A. Podoleanu, O. Bang, Real-time high-resolution mid-infrared optical coherence tomography, Light Sci. Appl. 8 (2019) 11.
[37] C.R. Petersen, P.M. Moselund, L. Huot, L. Hooper, O. Bang, Towards a table-top synchrotron based on supercontinuum generation, Infrared Phys. Technol. 91 (2018) 182–186.
[38] C.R. Petersen, N. Prtljaga, M. Farries, J. Ward, B. Napier, G.R. Lloyd, J. Nallala, N. Stone, O. Bang, Mid-infrared multispectral tissue imaging using a chalcogenide fiber supercontinuum source, Opt. Lett. 43 (5) (2018) 999–1002.
[39] C. Lee, M. Jeon, M.Y. Jeon, J. Kim, C. Kim, In vitro photoacoustic measurement of hemoglobin oxygen saturation using a single pulsed broadband supercontinuum

laser source, Appl. Opt. 53 (2014) 3884–3889.
[40] Y.N. Billeh, M. Liu, T. Buma, Spectroscopic photoacoustic microscopy using a photonic crystal fiber supercontinuum source, Opt. Express 18 (2010) 18519–18524.
[41] C. Lee, S. Han, S. Kim, M. Jeon, M.Y. Jeon, C. Kim, J. Kim, Combined photoacoustic and optical coherence tomography using a single near-infrared supercontinuum laser source, Appl. Opt. 52 (2013) 1824–1828.
[42] X. Shu, M. Bondu, B. Dong, A. Podoleanu, L. Leick, H.F. Zhang, Single all-fiber-based nanosecond-pulsed supercontinuum source for multispectral photoacoustic microscopy and optical coherence tomography, Opt. Lett. 41 (2016) 2743–2746.
[43] P.D. Nieuwkoop, J. Faber, Normal Table of Xenopus laevis (daudin): a Systematical and Chronologica Survey of the Development From the Fertilized Egg Till the End of Metamorphosis, (1956) North-Holland, Amsterdam.
[44] P. Jorgensen, A.J. Steen, H. Steen, M.W. Kirschner, The mechanism and pattern of yolk consumption provide insight into embryonic nutrition in Xenopus, Development 136 (9) (2009) 1539–1548.

**Manoj Kumar Dasa** received his M. Sc. in Electrical Communications Engineering with a specialisation in Optoelectronics from University of Kassel, Germany in April 2016. In February 2017, he joined the Technical University of Denmark as a Marie Curie pH.D. fellow at the Department of Photonics Engineering. His pH.D. focuses on developing high-pulse energy supercontinuum sources for multispectral photoacoustic microscopy applications in the extended near-infrared region.

**Ole Bang** is a professor at the Technical University of Denmark and Fellow of OSA. He heads the Fiber Sensors & Supercontinuum Group, who develops photonic crystal fibres for sensing and supercontinuum lasers and use them for applications in imaging and spectroscopy. He has published 232 journal papers with 11,083 ISI citations and ISI h-index 57. He holds several patents within supercontinuum lasers and polymer optical fibre sensors and is a co-founder of SHUTE Sensing Technologies and NORBLIS IVS.

scientific reports

Check for updates

OPEN

# Two octaves spanning photoacoustic microscopy

Gianni Nteroli[1,5]✉, Manoj K. Dasa[2,4,5], Giulia Messa[3], Stella Koutsikou[3], Magalie Bondu[4], Peter M. Moselund[4], Christos Markos[2], Ole Bang[2], Adrian Podoleanu[1] & Adrian Bradu[1]

**In this study, for the first time, a Photoacoustic Microscopy instrument driven by a single optical source operating over a wide spectral range (475–2400 nm), covering slightly more than two octaves is demonstrated. *Xenopus laevis* tadpoles were imaged in vivo using the whole spectral range of 2000 nm of a supercontinuum optical source, and a novel technique of mapping absorbers is also demonstrated, based on the supposition that only one chromophore contributes to the photoacoustic signal of each individual voxel in the 3D photoacoustic image. By using a narrow spectral window (of 25 nm bandwidth) within the broad spectrum of the supercontinuum source at a time, in vivo hyper-spectral Photoacoustic images of tadpoles are obtained. By post-processing pairs of images obtained using different spectral windows, maps of five endogenous contrast agents (hemoglobin, melanin, collagen, glucose and lipids) are produced.**

Photoacoustic Microscopy (PAM) is a rapidly emerging, non-ionizing, cross-sectional imaging technique, which provides structural and functional volumetric information with micrometre resolution. Most importantly, it allows non invasive detection of chromophores, paving the road for applications in medical diagnosis and oncology, as well as in biology and neuroscience[1–8].

Currently, PAM instruments operate over narrow spectral ranges where a small number of chromophores can be identified, hence their limited spectral capabilities. Such PAM instruments were developed for example either in the 532 nm[9,10], 900 nm spectral bands[11,12], or above 1440 nm[13].

Producing simultaneously PAM maps of several biological chromophores, such as Hb, melanin, collagen, glucose, and lipids is a challenging task for the available instrumentation. Several research groups have already demonstrated PAM's capability to produce oxygen saturation maps. For example, Liu et al measured simultaneously Hb concentration, oxygen saturation and blood flow speed via PAM, using 3 laser lines. For example, Liu et al. measured simultaneously Hb concentration, oxygen saturation and blood flow speed via PAM, using 3 laser lines[10]. This was achieved thanks to a single nanosecond pulsed laser operating at 532 nm and two stimulated Raman shifted pulses at 545 and 558 nm. By using a high numerical aperture acoustic lens, Li et al.[14] performed in vivo oxygen saturation imaging with only 10 nJ per pulse, at 532 nm without the need of data averaging. Galanzha et al.[15] employed in vivo PAM flow cytometry for label-free detection of melanin-bearing circulating tumor cells in patients with melanoma, using a pulsed laser operating at 1060 nm. On the other hand, supercontinuum (SC) optical sources provide a wide spectral range (typically 500–2400 nm), enabling multi-spectral PA imaging and spectroscopic PA sensing, despite exhibiting challenging low pulse energies. Shu et al.[16] demonstrated a single SC source powered OCT/PAM instrument capable of multi-spectral microscopy (MS-PAM) in the visible (500–800 nm). Also, Buma et al.[17] and Dasa et al.[13] developed in-house SC sources to map lipids in the near infra-red (NIR). Table 1, presents a review of the instrumentation of PAM systems employed to target absorbers in biological tissues. This shows that, currently, the imaging instrument needs to be tailored to match the spectral characteristics of the chromophore of interest.

Several research groups have attempted to develop low-cost PAM imaging instruments. To this goal, pulsed laser diodes (PLD) operating in the visible and NIR region were employed. However, PLD based PAM instruments exhibit a low pulse repetition rate (PRR). The low PRR results in slow imaging rate and low pulse energies leads to higher averaging of the detected signals by hundreds of times[11–13,18,25–27]. Other approaches include frequency-domain (FD) systems. For example Kellnberger et al.[21] used a CW laser emitting at 488 and 808 nm, whilst Tserevelakis et al.[28] employed a CW laser (at 488 nm) with an acousto-optic modulator at 10 MHz. In contrast to PLD based PAMs and FD CW laser based systems, a more costly instrument, was reported by Allen et al.[9]. They set up an ultra-fast PAM system with a PRR of 2 MHz using a master oscillator power amplifier

[1]Applied Optics Group, University of Kent, Canterbury, UK. [2]DTU Fotonik, Technical University of Denmark, 2800 Kgs. Lyngby, Denmark. [3]Medway School of Pharmacy, University of Kent, Chatham, UK. [4]NKT Photonics A/S, Blokken 84, 3460 Birkerød, Denmark. [5]These authors contributed equally: Gianni Nteroli and Manoj K. Dasa. ✉email: G.Nteroli@kent.ac.uk

configuration, frequency-doubled to 532 nm. So far, optical parametric oscillators (OPO) are popular optical sources employed for PAM. Although they are widely tunable in wavelength, they are characterized by a low PRR[22]. Recently, mapping of lipids using a low cost customised SC source to deliver sufficiently high energy per pulse (EPP) in the NIR was reported by Dasa et al.

To our knowledge, an optical source which,

(i) has the ability to cover both VIS and NIR ranges
(ii) can deliver sufficient EPP to enable PAM imaging
(iii) provides sufficiently high PRR for fast imaging
(iv) is cost effective

has not been reported yet. A source that addresses all criteria (i) to (iv) listed above is a commercial low-cost SC source employed for this study, whose wide emission spectrum enables to target several endogenous chromophores, with absorption peaks spread over a spectral region of almost 2000 nm (from 475 to 2400 nm).

Using such a source, for the first time, a two Octaves Spanning Photoacoustic Microscopy (OS-PAM) instrument is demonstrated. The instrument is capable of identifying chromophores over a spectral range of nearly 2000 nm across the electromagnetic spectrum, and can produce 3D PAM maps of various chromophores (melanin, hemoglobin (Hb), collagen, glucose and lipids) in real-time. In addition, we created an advanced multimodal imaging instrument (OS-PAM/OCT) by integrating a high-resolution Optical Coherence Tomography (OCT) imaging channel. The wide bandwidth covered and the multimodality demonstrated recommend such instruments for future studies of early stage cancer detection.

## Theoretical background/distinguishing different contrast agents

The absorption coefficient of the most common endogenous contrast agents in biological tissue as a function of wavelength is presented in Fig. 1. Water is also present in the biological tissue; however, it was not taken into consideration in our procedure as its absorption coefficient, especially in the VIS range, is extremely low, therefore will produce a negligible PAM signal. The spectrum of hemoglobin is presented in Fig. 1 only over the range 450–1000 nm where both HbO2 and Hb are strongly absorbing light and therefore produce a significant PAM signal. The strength of the PAM signal when the sample is illuminated by an optical source operating at a wavelength $\lambda_i$ is proportional to the photoacoustic initial pressure amplitude, which can quantitatively be determined using[29]:

$$p(\lambda_i) = \Gamma \times \mu_j \times \Phi(\lambda_i) \tag{1}$$

Here, $\Gamma$ represents the Grüneisen coefficient, $\mu_j$ the optical absorption coefficient of a specific contrast agent, and $\Phi$ is the laser's irradiance. As, $\Gamma$ exhibits only low variations within the biological media[30], it is reasonable to consider it as a constant. If a total number of $N$ contrast agents are present in the sample, the optical energy is absorbed by all of them, and Eq. (1) can be re-written as,

$$p(\lambda_i) = \Gamma \times \sum_{j=1}^{N} \mu_j \times \Phi(\lambda_i) \tag{2}$$

As it can be observed (Fig. 1), for any wavelength across the spectral range, typically only 2–3 chromophores contribute significantly towards the photoacoustic signal: melanin and hemoglobin in the visible, water, collagen, lipids in the 1200 nm spectral region, glucose, lipids and water in the 1550–2000 nm region.

For simplicity, let us consider that the sample is illuminated with a wavelength $\lambda_1$ then by one of wavelength $\lambda_2$ and that only two chromophores $a$ and $b$ of absorption coefficients, $\mu_a$ and $\mu_b$, respectively contribute towards the final photoacoustic signal. If we calculate the difference between the initial pressures created by the two chromophores at $\lambda_1$ and $\lambda_2$ ($\delta p$), by using Eq. (2), the initial pressures created by the radiation at each wavelength can be calculated as,

$$\begin{cases} p(\lambda_1, a) &= \frac{\delta p}{\zeta} \\ p(\lambda_1, b) &= m_1 \frac{\delta p}{\zeta} \\ p(\lambda_2, a) &= \alpha_a \frac{\delta p}{\zeta} \\ p(\lambda_2, b) &= m_2 \alpha_a \frac{\delta p}{\zeta} \end{cases} \tag{3}$$

In Eq. (3),

$$\begin{cases} m_1 = \frac{\mu_b(\lambda_1)}{\mu_a(\lambda_1)}, \quad m_2 = \frac{\mu_b(\lambda_2)}{\mu_a(\lambda_2)} \\ \alpha_a = \frac{\mu_a(\lambda_2)}{\mu_a(\lambda_1)} \frac{\Phi(\lambda_2)}{\Phi(\lambda_1)}, \quad \alpha_b = \frac{\mu_b(\lambda_2)}{\mu_b(\lambda_1)} \frac{\Phi(\lambda_2)}{\Phi(\lambda_1)} \\ \zeta = 1 + m_1 - \alpha_a - \alpha_a m_2 \end{cases}$$

The wavelengths $\lambda_1$ and $\lambda_2$ can be selected in such a way that the initial pressure due to chromophore $a$ is higher at $\lambda_1$, than at $\lambda_2$ and the initial pressure due to chromophore $b$ is lower at $\lambda_1$ than at $\lambda_2$. Supposing that

only one chromophore contributes to the brightness of a pixel in the image, we compute the difference between images generated at different wavelengths to figure out which of the chromophores is present at each location in the image. If for a given pixel, the difference is positive, the chromophore contributing to the signal is *a*. On the contrary, if the difference is negative, the contributing chromophore is b. Chromophore *a* can for example be Hb and chromophore *b* melanin, $\lambda_1 = 550$ nm (zone Z1 in Fig. 1) and $\lambda_2 = 650$ nm (zone Z2 in Fig. 1). Using the absorption coefficients of the two chromophores at their respective wavelengths, and the values of the optical powers on the sample experimentally measured (0.36 mW at 550 nm and 1.1 mW at 650 nm), we have $m_1 = 1.83$, $m_2 = 14.14$, $\alpha_a = 0.22$ and $\alpha_b = 1.72$. If we take for example $\frac{\delta p}{\zeta} = 1$ arbitrary unit, we obtain,

$$\begin{cases} p(\lambda_1, a) &= 1 \\ p(\lambda_1, b) &= 1.83 \\ p(\lambda_2, a) &= 0.22 \\ p(\lambda_2, b) &= 3.17 \end{cases}$$

So, if in a point of the PAM image we have contributions from both, melanin, and Hb, when switching from 550 to 650 nm we do expect an increase of the initial pressure due to the melanin and a decrease of the initial pressure due to the Hb. Now, if we suppose that from a single point, we have either signal from Hb or melanin then, $\delta p > 0$ indicates the presence of the Hb whereas $\delta p < 0$ that of the melanin.

By carefully selecting the operation wavelength of the instrument, various chromophores can be mapped in the en face (transverse) PAM image. To map Hb and melanin, we used the spectral windows Z1 and Z2, around 550 and 650 nm, respectively. To map glucose, collagen and lipids, three zones were selected (Z3 around 1200 nm, Z4 around 1600 and Z5 above 1700 nm, respectively). Because water is a major absorber at long wavelengths, zones Z3-Z5 were selected in such a way that, when performing the difference between images, one of the targeted chromophores increase (or decrease) its initial pressure from one zone to the other, whereas water and the other chromophore decrease (or increase) their initial pressure. An extensive description of the technique presented in this section is provided in the Supplementary Material.

## Results

**System characterization and OS-PAM/OCT imaging.** The OS-PAM system was rigorously characterized and the results are presented in Fig. 2. The EPP was measured on the sample for each wavelength and was found to range from 20 to 110 nJ (Fig. 2a). The FOV was estimated imaging a carbon fibre tape demonstrating high photoacoustic signal amplitude over 8 mm (Fig. 2b). As the lateral resolution varies with the wavelength and the beam diameter it is necessary to be measured for each wavelength. Thus, for each wavelength, a sharp edge of a USAF target (a letter on the USAF target) was imaged. Images of $500 \times 400$ $pixels^2$ were produced, of size $500 \times 400$ $\mu m^2$ therefore, each pixel in the image spans over 1 µm. The edge spread function (ESF) and the line spread function (LSF) were measured and the FWHM of the Gaussian fit to the LSF determined the lateral resolution. The measured lateral resolution, presented in Fig. 2c, was found to vary from 4.9 to 7.1 µm over a spectral range spanning from 475 to 1650 nm. This range of variation in the lateral resolution is expected due to the variation of the beam diameter at the output of the optical source as a function of wavelength (as detailed in the "Methods" part of the manuscript), the beam diameter at the output of the optical source is a function of wavelength. Therefore, if we define the lateral resolution of the instrument as given by 1/2 of the size of the Airy disk[34,35] and consider the 2× magnification of the beam expander BE, theoretical lateral resolutions of 5.8 µm at 500 nm (beam diameter 2 mm) and of 6.95 µm at 1500 nm (beam diameter 5 mm) are obtained. These values match the experimental values and ensure that the achromat lens employed did not introduce optical aberrations. The theoretical axial resolution of the OS-PAM system is 38 µm. However, outside the acoustic focal point, the SNR is weaker, and the axial resolution degrades. Furthermore, the transducer has a maximum detectable bandwidth when it is oriented orthogonal to the direction of propagation of the incident acoustic waves. Any small deviation of the incidence angle from 90 degrees, due to the angle directivity dependence, determines a reduction in the detectable signal bandwidth[36]. Hence, the measured axial resolution using the carbon fibre tubes (Fig. 2d) results as 50 µm. The ratio between the max signal amplitude (Fig. 2) and the standard deviation of the noise determines the SNR of the OS-PAM system, found to be 43.8 dB.

The method presented in section "Theoretical background/distinguishing different contrast agents" was experimentally confirmed by producing PAM images showing the spatial distribution of the melanin, hemoglobin, gelatine, glucose, and lipids present in various samples.

To map the spatial distribution of melanin, three human hairs were placed in the 3D sample holder S (please see Fig. 7), on the optical window, and illuminated from below using the instrument presented in section "OS-PAM/OCT system". To guide the imaging operation, and hold the hairs in place, a carbon fibre tape partially covered the hairs, as shown in the 2D schematic diagram of the sample presented in Fig. 3a. The three hairs are labelled as 1, 2 and 3, whereas the carbon fibre tape as 4.

Optical source OS1 is used to sequentially illuminate the sample with light at 550 nm and then at 650 nm to generate PAM maps of the chromophores producing acoustic waves when excited by light at these two wavelengths. Subsequently, by using the procedure introduced in section "Theoretical background/distinguishing different contrast agents", PAM spatial distribution maps of the melanin were produced. In addition, after producing the maps of melanin, the optical source OS2, operating at a central wavelength of 1300 nm, was used to illuminate the sample to generate OCT images.

OCT and PAM images hence obtained are presented in Fig. 3b–e. In Fig. 3b,d, en face OCT and PAM images are shown, whereas in Fig. 3c,e, examples of B-scan OCT and PAM images respectively. The images are presented in 8-bit format, therefore, as illustrated in their corresponding colormap bars, the brightness 0 of a pixel in the image corresponds to an OCT or PAM signal equal to zero, whereas a brightness of 255 to its maximum value.

The en face images were produced by using the maximum intensity projection algorithm. As expected, the carbon fibre tape is visible in both OCT and PAM images (areas 4) and very important, all three hairs are clearly identifiable in both images, which proves that the procedure suggested here to map the melanin is effective. The B-scan views show, as expected, that the axial resolution in the OCT image is better than in the PAM one.

To validate the potential of the method proposed to be used to generate spatial distribution maps of hemoglobin, gelatine, glucose, and lipids, mixtures of these chromophores with water were created. The mixtures were placed in the sample holders S, and illuminated with light of various wavelengths, from below, as explained in section "OS-PAM/OCT system". For imaging guidance purposes, carbon fibre tapes have been placed in the holder, on the optical window (the liquid mixtures would cover the carbon tape). In Fig. 4a1,b1,c1,d1, 2D schematic diagrams of the four samples so created are presented showing the position of the carbon fibre tapes in each of the four cases.

(i) To validate the potential of the technique to map the spatial distribution of hemoglobin, a mixture of dry hemoglobin and water (concentration 150 g/l) was placed in the sample holder, and sequentially illuminated with light from OS1, first at 550 nm and then at 650 nm. The two PAM images so created were subsequently used to generate distribution maps of hemoglobin. An en face PAM distribution map of hemoglobin is presented in Fig. 4a2 whereas an example of a B-scan map in Fig. 4a3.

(ii) To map the spatial distribution of gelatine, a mixture of cooking gelatine and water (concentration 150 g/l) was created, placed in the sample holder, and sequentially illuminated with light from OS1 at 1200 nm and then at 1700 nm. The two PAM images so created were subsequently used to generate gelatine distribution maps. An en face PAM distribution map of the gelatine is presented in Fig. 4b2 whereas an example of a B-scan in Fig. 4b3.

(iii) To produce glucose spatial distribution maps, a mixture of glucose and water (concentration 150 g/l) was created, placed in the sample holder, and sequentially illuminated with light from OS1 operating at 1600 nm and then at 1700 nm. The two PAM images so created were subsequently used to generate PAM glucose distribution maps. An en face PAM map of the glucose is presented in Fig. 4c2 whereas an example of a B-scan map in Fig. 4c3.

(iv) To generate PAM spatial distribution maps of the lipids, a mixture of water and chicken adipose fat has been created, placed in the sample holder, and sequentially illuminated with light from OS1 at 1600 nm and then at 1700 nm. The two PAM images hence created were subsequently used to generate PAM lipids distribution maps. A PAM en face distribution map of the lipids is presented in Fig. 4d2 whereas an example of a B-scan map in Fig. 4d3.

In all cases, en face PAM images are created via a maximum projection algorithm. A summary of the content of the samples created and the wavelengths used in each case to produce PAM spatial distribution maps of the 5 chromophores targeted in our experiments is presented in Table 2.

For all imaged chromophores, the values of the signal-to-noise ratio (SNR), normalised over the optical fluence, presented in the inset of Fig. 1 are consistent with the values of their absorption coefficients reported in the literature. To compute the SNR, we used a standard procedure[13,17] consisting in calculating the SNR as,

$$SNR = 20\log_{10}\left[\frac{\text{MAX(area 5)}}{\text{STD(area 6)}}\right] \tag{4}$$

In Eq. (4), MAX(area 5) and STD(area 6) are the maximum value of the PAM signal computed in area 5 and the standard deviation of the signals calculated over region 6 respectively. Regions 5 and 6 are all depicted using dotted yellow circles on the en face PAM images shown in Figs. 3 and 4 .

**In vivo whole SC range OS-PAM imaging of Tadpoles.** During the OS-PAM imaging, animals were anaesthetized (n = 4, as described in the "Methods" section) and positioned on a 3D printed sample holder. The sample holder was designed to keep the animal submerged in MS-222 solution, while the laser beam scanned the animal through a thin (0.22 mm) glass optical window from below (inset in Fig. 7). For OS-PAM imaging at different spectral bands, 12 hard coated band-pass filters, each of them of 25 nm bandwidth, were employed, enabling imaging from 475 nm up to 1600 nm. At 1600 nm the only commercially available filter to us had 50 nm bandwidth, whereas a long-pass filter with a cut off at 1650 nm was employed for imaging at longer wavelengths. In both OCT and PAM channels, B-scan images of 500 × 400 pixels were acquired and displayed in real-time at a frame rate of 20 Hz, hence a 500×400×400 3D volume was generated in 20 s (10 s to capture data and 10 s to process). To enhance the Signal to Noise Ratio (SNR) in the PAM images, 32 A-scans were averaged, increasing the acquisition time to 10.7 min. In Fig. 5, en face z-projected OS-PAM images over the whole SC range are presented, along with a structural en face OCT image clearly showing tadpole's anatomy.

Due to the unavailability of commercial band-pass filters of 25 nm bandwidth at wavelengths over 1650 nm, a long-pass filter with a cut-off at 1650 nm was employed, hence the notation > 1650 nm. This means that the spectral range used here is from 1650 to 2400 nm, allowing for absorption of chromophores with absorption over a much wider spectral range. Thus, brighter images at for the Z5 zone were obtained. The lateral resolution of 5–7 μm refers to the capabilities of the system when the distance between two consecutive points (pixels) in the image is smaller than the lateral resolution of the system. However, in Figs. 3, 4, 5, 6 we show very large size areas (5–8 mm) while keeping a quite low number of lateral points (500 pixels). Therefore, the lateral resolution was digitally degraded in these images to 10–16 μm respectively.

**Mapping of five endogenous contrast agents with OS-PAM/OCT.** Utilising the capabilities of the OS-PAM/OCT instrument in combination with the technique described in section "Theoretical background/distinguishing different contrast agents", five endogenous contrast agents: melanin, Hb, collagen, glucose and lipids were mapped on four tadpoles at developmental stage 37/38[37].

The tadpole OS-PAM images were overlaid on the corresponding structural OCT images and presented in Fig. 6. Maps of melanin are produced using filters operating at 550 and 650 nm. On the tadpole, at developmental stage 37/38, pigmentation (due to pigment cells) is present in the eye, on the head and on the dorsal side of the yolk sac (Fig. 5). Moreover, melanophores appear on the tail which is shown by the less intense melanin signal in Fig. 5. Maps of Hb are produced using filters operating at 550 and 650 nm. Hb appears at the level of the cardiac ventricle, as well as, along the developing vascular system which spans the yolk sac and travels along the side of the tail (Figs. 5 and 6). Maps of collagen are obtained by changing to filters operating 1200 and 1700 nm. Collagen has been detected on several areas of the tadpole's body and can be detected on the developing cranial structures and at the levels of the yolk sac and trunk muscles (Fig. 6). To map glucose, images were produced at 1600 and 1700 nm. High levels of glucose are present within the yolk sac area (Fig. 6) overlapping with the high concentration of lipoproteins in this region[38]. Finally, we used filters at 1200 and 1600 nm to map lipids. Our results show that lipids are highly concentrated in the yolk sac (Fig. 6), which is consistent with previous studies performing multi-spectral PAM imaging on zebrafish and tadpoles[13,17]. A more detailed visual illustration on how the technique was implemented to obtain the overlayed images is presented in Fig. S1 (Supplementary Material).

## Discussion and conclusion

A PAM imaging instrument operating at wavelengths over the entire spectral range of a commercial SC source, from 475 to 2400 nm, is demonstrated. This is employed on mapping five endogenous contrast agents in living tadpoles, namely melanin, hemoglobin, collagen, glucose, and lipids. Based on the supposition that only one chromophore contributes to the photo-acoustic signal of each individual voxel in the 3D PAM image, a novel technique of mapping absorbers is demonstrated. A sequentially operating ultrahigh resolution OCT imaging channel aids the investigation.

To compensate for the limited optical power delivered by the SC source employed here, losses and optical aberrations were minimized by a careful selection of the optical components used to convey light from the source, to the sample. As a result, the experimentally measured EPP on the sample ranged from 17 to 110 nJ, over the whole spectral range, hence sufficiently strong photo-acoustic signal could be generated. The main advantage of the PAM imaging method demonstrated here is its versatility in performing spectral measurements in the range of interest without resorting to multiple optical sources or changes in its optical design.

Our OS-PAM instrument, in its current stage of development, is not capable of performing spectroscopic PAM, therefore the results obtained are not directly comparable to conventional spectral unmixing techniques. By using the suggested procedure, the concentration of the targeted chromophores cannot be extracted quantitatively but only their spatial mapping distribution evaluated. Adequate experimental assessments require quantitative concentration measurements. Therefore, this was not the goal of the research presented here. Instead, the focus was on using a unique approach for the spatial distribution of the chromophore. In doing so, two milestones were targeted: (i) PAM imaging over an unprecedented spectral range using an ultra-broadband source and (ii) utilizing PAM imaging to map chromophores of bio-medical interest in vivo, in several spectral regions. These two milestones were targeted despite facing the issues of a low energy per pulse and intrinsic high noise challenges of a supercontinuum source. However, such sources are commercially available and utilisation of a single source for OCT and PAM as illustrated may represent a cost-effective solution. Although the technique proposed here cannot be used currently to produce quantitative absorption coefficient data, it shows great promise in detecting the presence of a plethora of chromophores, without limitations due to the restricted operational spectral range of the conventional sources employed in PAM.

The technique presented here has been successfully employed to detect the presence of chromophores using a particular Supercontinuum optical source and a particular design of the optical setup. Therefore, what it is important when detecting a specific chromophore, is not the absorption coefficient of a certain chromophore at a certain wavelength alone but also the fluence and the spectral density variation of the source. Therefore, the two interrogation wavelengths must be selected very carefully. The spectral region from 700 to 1100 nm, although of interest for biomedical applications, is not targetable by PAM due to the very low absorption of the chromophores, for which reason we did not perform any measurements over this range. By avoiding this, we also kept the project cost effective. As the diameter of the optical beam is a function of wavelength (intrinsic characteristic of the optical source), the lateral resolution of the system does not increase linearly with the wavelength. Consequently, although, the lateral resolution should deteriorate as we move to longer wavelengths, the size of the beam diameter expands, increasing the numerical aperture, and therefore improving the lateral resolution (Fig. 2c).

Although more sophisticated systems are capable of obtaining accurate absorption coefficient data, they are either limited to two chromophores due to lack of spectral coverage, or they cannot perform in vivo imaging due to lack of imaging speed (Table 1). We acknowledge that the rate at which images are produced in this study is comparable to that of the OPOs instrument. However, as our implementation is based on fast acquisition of cross-sectional slices, it is better suited for in vivo imaging.

A low-cost PAM imaging instrument could be devised with potential in various medical screening programs. Future work includes increasing the acquisition sensitivity of the OS-PAM instrument for faster acquisition by replacing the ultrasound transducer (UT) with a higher sensitivity focused transducer, applying lower noise amplification methods, implementing software noise reduction techniques, and replacing the band-pass filter wheel with and automated one, synced with the acquisition. For this proof of concept study, a transmission mode PAM was considered in order to minimize imaging artefacts and provide maximum achievable SNR. As the next

| Reference | OS Tech. | CWL (nm) | PRR | Cost | Target | EPP (μJ) |
|---|---|---|---|---|---|---|
| [18] | PLD | 405 | 1 kHz | Low | A | 0.052 |
| [11] | PLD | 905 | 1 kHz | Low | A | 3 |
| [9] | YFL | 532 | 2 MHz | High | A | 0.1–5 |
| [10] | YFL | 532 | 4 kHz | High | A | 0.8 |
| [19] | Dye Laser | 532 | 10 kHz | High | A | 5 |
| [20] | PLD | 780, 1560 | 5–20 kHz | N/A | C | 2–4 |
| [21] | CW | 488, 808 | N/A | Low | A,B | N/A |
| [15] | N/A | 1060 | 10 kHz | N/A | B | 240 |
| [22] | OPO | 270–1400 | 1 kHz | High | A, E | N/A |
| [23] | SC | 450–840 | 20 kHz | Low | A, B | N/A |
| [16] | Custom SC | 500–900 | 5 kHz | Low | A, B | N/A |
| [17] | Custom SC | 1210–1720 | 2 kHz | High | E | 1–6 |
| [13] | Custom SC | 1440–1870 | 100 kHz | Low | E | 0.197 |
| [24] | Custom SC | 1500–1900 | 30 kHz | Low | D | 1 |
| OS-PAM | SC | 475–2400 | 20 kHz | Low | A, B, C, D, E | 0.017–0.11 |

**Table 1.** Review of the instrumentation used for PAM imaging of hemoglobin (A), melanin (B), collagen (C), glucose (D) and lipids (E). *OS* optical source employed, *CWL* central wavelength of OS, *PRR* pulse repetition rate, *PLD* pulsed laser diode, *OPO* optical parametric oscillator, *SC* supercontinuum source, *YFL* Ytterbium fibre laser, *EPP* energy per pulse.

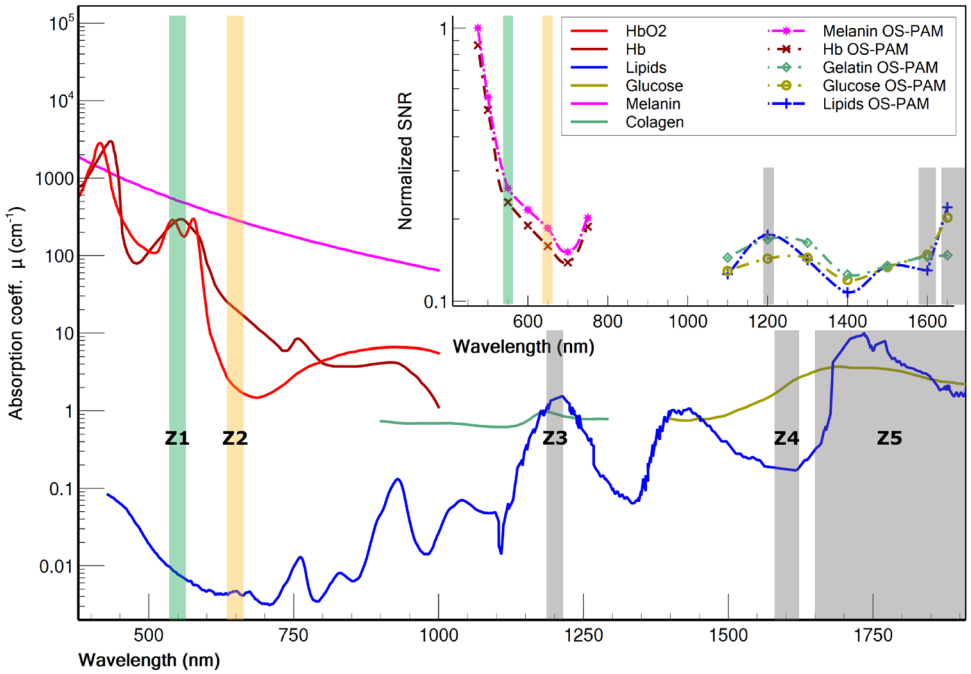


**Figure 1.** Graphs of the absorption coefficient for the most common endogenous contrast agents in tissue. Data for HBO2, Hb and Melanin were compiled from[31], data for Collagen from[32], data for Glucose from[24], whereas data for lipids from[33]. The spectral windows used for OS-PAM imaging are highlighted in colours. Z1–Z5 represent the spectral zones used for mapping the contrast agents. Inset data is obtained performing in vitro OS-PAM imaging.

step of these studies is to image BCC and melanoma in vitro, with the ultimate goal to monitor these notorious skin lesions in patients (clinical applications), the probe would require to be redesigned for reflection mode. We are confident that our system has the potential to tackle several challenges of skin cancer diagnosis. In melanoma for instance, the progression of melanocytes to subsequent pathological growth phases[1] can be monitored by mapping melanin in the epidermis. D'Alessandro et al.[2] demonstrated that multi-spectral imaging can be used to quantify saturated Hemoglobin ($HbO_2$), which is a major indicator for the early detection of melanomas whereas Fang et al.[3] showed how collagen can inhibit and promote tumor progression. Long et al.[4] showed that

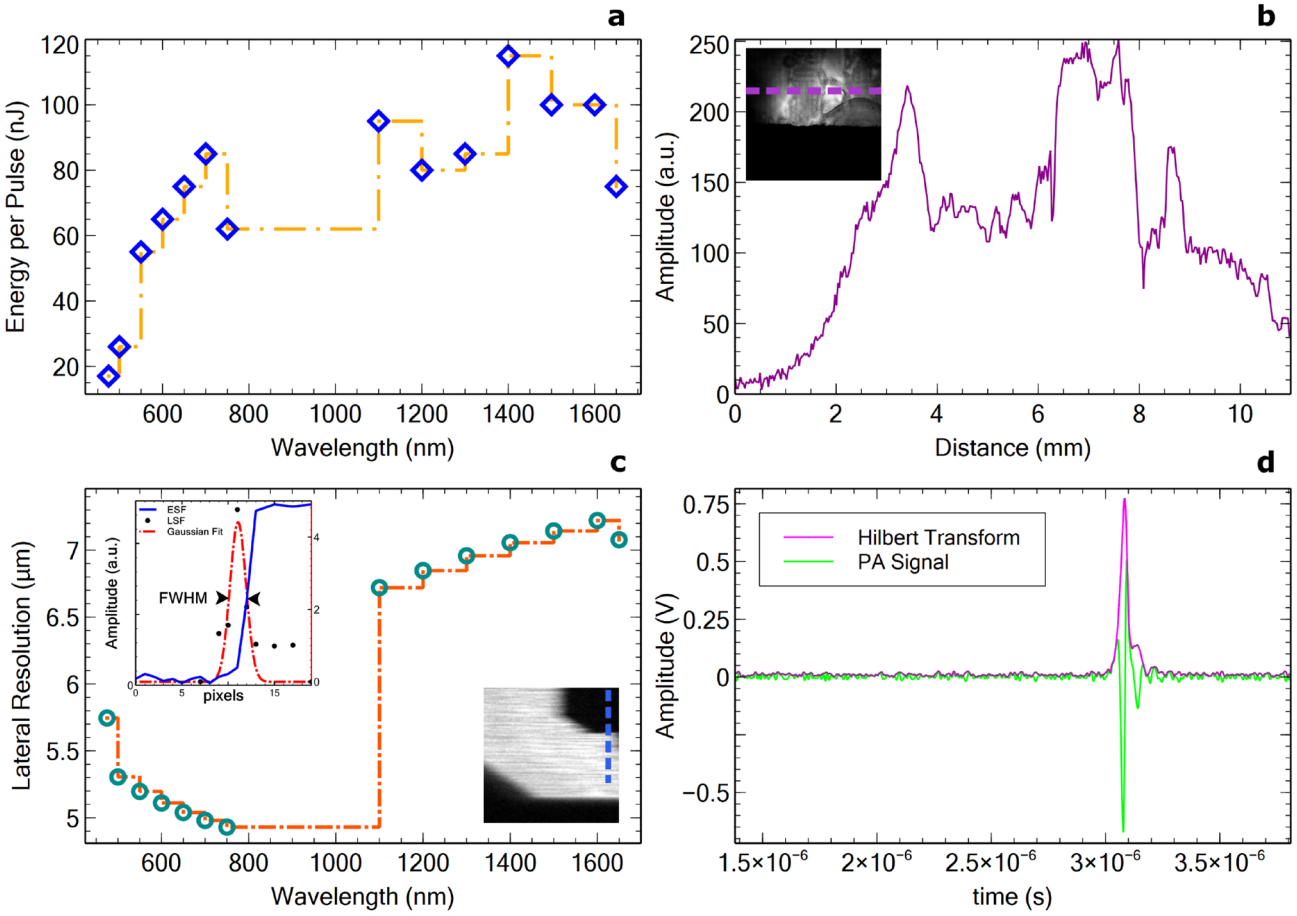


**Figure 2.** OS-PAM System characterization; (**a**) EPP graph over the whole imaging spectral range measured on the sample; (**b**) Characterisation of the lateral field of view (FOV) of the instrument. PAM signal collected whilst imaging a carbon fibre tape is plotted for each lateral position in the image. The plot corresponds to the amplitudes of the signal at the positions showed by the purple dashed line in the inset image. The size of the image 10 × 10 mm; (**c**) Lateral resolution per wavelength measured by imaging a sharp edge (letter) on a USAF target, extracting the ESF and calculating the LSF. The size of the image is 0.5 × 0.5 mm; (**d**) Axial resolution measured imaging carbon fibre tubes. The Axial resolution is defined by the FWHM of the Hilbert transform (Signal envelope).

energy metabolism, especially lipid metabolism, is significantly elevated during carcinogenesis. Furthermore, various studies also demonstrated that cell metabolism is highly dysregulated in cancer, as lipids and glucose become sources for tumor progression via multiple signaling pathways[5–8]. Although the localization in real-time of multiple endogenous chromophores in tissue seems to be of paramount importance, the available technology does not allow simultaneous detection of all the physiological changes listed above.

## Methods

**Ethical approval.** Animals and Ethical Approval In vivo imaging was performed on four *Xenopus laevis* tadpoles at developmental stage 37/38, based on Nieuwkoop and Faber 1956. All experimental procedures were approved by the University of Kent Animal Welfare and Ethical Review Body (AWERB; Institutional Ethics Reference Number: 0037-SK-17). Reporting of all in vivo experimental work conforms with the ARRIVE guidelines.

*Xenopus laevis* embryos were supplied by the European Xenopus Resource Center (EXRC; Portsmouth UK). The Xenopus embryos were kept in water at 20 C until they reached the developmental stage 37/38[37]. Prior to OS-PAM imaging, animals were anesthetized in 0.1% MS-222 solution (ethyl 3-aminobenzoate methane sulfonate, Sigma-Aldrich UK[39]. Animals remained anesthetised in MS-222 solution for the entire duration of the imaging procedure (4.2 min). All methods employed were performed in accordance with guidelines and regulations as described in the research protocol approved by the University of Kent Animal Welfare and Ethical Review Body.

**OS-PAM/OCT system.** The schematic diagram of the multi-modal OS-PAM/OCT imaging instrument is presented in Fig. 6. In the OS-PAM channel, a SC source (SuperK COMPACT, NKT Photonics) delivering pulses of 2 ns duration at 20 kHz PRR (maximum) is employed (OS1). To improve imaging lateral resolution, the size of the beam diameter was doubled by using a reflective beam expander BE (BEO2R/M, Thorlabs), as the spot size

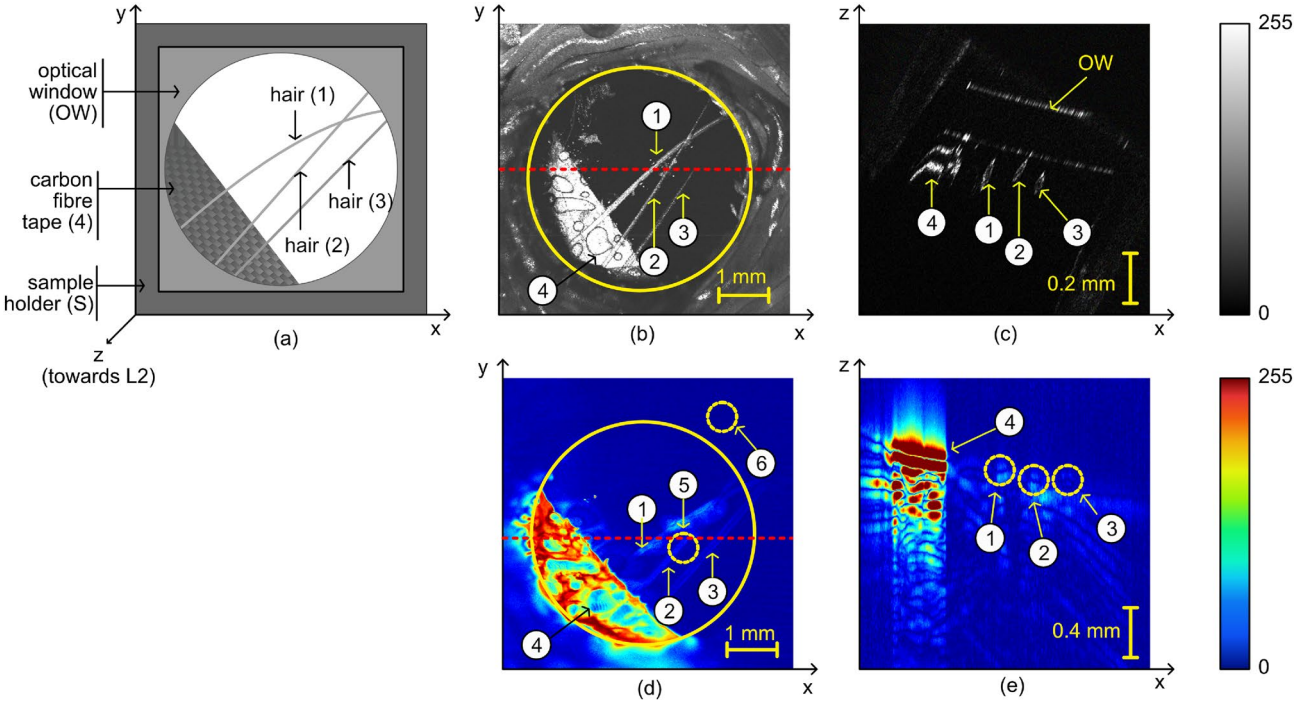


**Figure 3.** (**a**) Schematic diagram of the sample designed to produce images of the human hair: 1, 2, 3 are the three imaged hairs, placed on an optical window (OW); the ends of the hairs are covered by a carbon fibre tape (4); incident light from OS1 and OS2 travels towards the sample in the *z*-direction. (**b**) En face OCT image of the sample showing both the carbon fibre tape (4) and the three hairs. (**c**) Example of a B-scan OCT image showing the carbon fibre tape, the hairs as well as the optical window. The hairs look elongated as they are not placed orthogonal to the *xz*-plane. (**d**) En face PAM image showing the carbon fibre tape and the hairs. Regions 5 and 6 are used to calculate the signal-to-noise ratio using the procedure described within the manuscript. (**e**) Example of a B-scan PAM image. The optical window is not visible in the PAM image. The red horizontal dashed lines shown on the en face images indicate the y-position where the B-scans are originating from.

is proportional to the focal length and inversely proportional to the beam diameter. Sequentially, a smaller spot size means higher fluence (same energy over a smaller area), resulting in an improvement of SNR.

The lateral resolution per wavelength is presented in Fig. 2c. This is important especially at shorter wavelengths, as the output beam diameter delivered by the COMPACT source varies from 1 mm in the visible up to 3 mm in the near-infrared region. As the numerical aperture is determined by the diameter of the beam, whose size is determined by the wavelength employed, measurements of the lateral resolution of the OS-PAM system are presented for each operational wavelength (Fig. 2c). Doubling the beam diameter, means smaller spot size, thus the optical energy is delivered in a smaller area which is crucial for obtaining good quality PAM images when using a laser with low EPP (Fig. 2) such as the COMPACT.

To optimize the optical power on the sample, optical components were carefully selected in such a way that the beam wave-front is not disturbed by chromatic aberrations. To this aim, the only optical components in the beam's path are a reflective beam expander, a flipping silver coated mirror (FM, used to switch between the PAM and the OCT imaging modes), the 25 nm bandwidth hard coated band-pass filters (87-776, Edmund Optics), a pair of orthogonal galvo-scanners (6220H, Cambridge Technology) and a 19 mm focal length achromatic doublet (AC127-019-AB) as objective lens. When using achromatic doublets, due to the fact that the anti-reflection coating is effective only over a limited spectral range, losses can potentially be significant. However, the EPP presented in Fig. 2a was measured on the sample which includes the losses coming from the lens. In addition, the experimental lateral resolution measured did not change dramatically along the spectral range, therefore no, or very little aberrations were observed, which is evident from the images presented in Fig. 4. All these components attenuate the optical power by 13%. Switching between filters takes about 2–5 s, however this procedure can be faster by using PC controlled filters.

The sample is submerged in water to facilitate acoustic coupling. The acoustic waves are detected with a high frequency customized unfocused needle ultrasonic transducer (40.3 MHz center frequency, 90 % bandwidth at 6 dB, 0.4 mm diameter active element, University of Southern California) which provides an axial resolution of 50 μm (Fig. 2d). This is placed in contact with water. At the bottom of the 3D printed sample (S in Fig. 7) a circular optical window (OW) of 0.22 mm thickness is placed. The sample is sitting on the optical window, being illuminated from below. The OW does not absorb optical energy, therefore is invisible in all OS-PAM images. The electrical signal generated is then amplified by two low noise wide-band amplifiers (ZFL-500LN+, Mini Circuits) and then digitized using a 12-bit fast acquisition board operating at a sampling rate of 200 MS/s (PCI-5124, National Instruments).

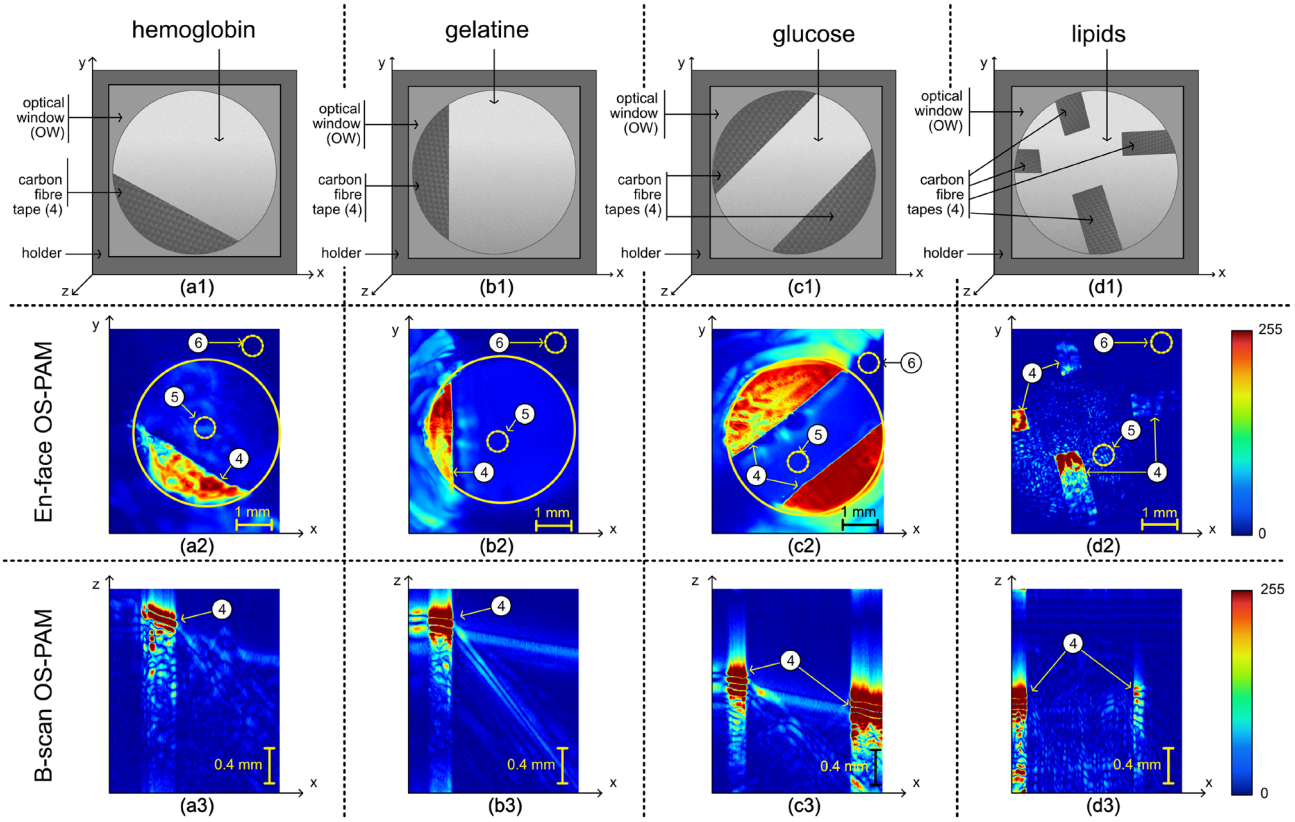


**Figure 4.** (**a1**), (**b1**), (**c1**) and (**d1**) Schematic diagrams of the samples designed to produce PAM spatial distribution maps of: hemoglobin, gelatine, glucose, and lipids respectively. In all cases, carbon fibre tapes (4) are placed on the optical window (OW) and covered by the liquid mixture created. (**a2**), (**b2**), (**c2**) and (**d2**) En face PAM maps showing the presence of hemoglobin, gelatine, glucose, and lipids respectively. Regions 5 and 6 are used to calculate the signal-to-noise ratio using the procedure described within the manuscript. (**a3**), (**b3**), (**c3**) and (**d3**) Examples of B-scan PAM images of hemoglobin, gelatine, glucose, and lipids respectively. All images show the carbon fibre tapes (4).

| Chromophore targeted | Content sample | $\lambda_1$ (nm) | $\lambda_2$ (nm) |
|---|---|---|---|
| Melanin | Human hair | 550 | 650 |
| Hemoglobin | Water and dry hemoglobin (150 g/l) | 550 | 650 |
| Gelatine | Water and gelatine (150 g/l) | 1200 | 1700 |
| Glucose | Water and glucose (150 g/l) | 1600 | 1700 |
| Lipids | Water and chicken adipose fat | 1200 | 1600 |

**Table 2.** Samples created to validate the proposed technique and the wavelengths at which they were sequentially illuminated using OS1 to generate PAM images and subsequently map the chromophores.

The COMPACT (OS1) could potentially be used as a light source for the OCT channel as well, as demonstrated in[23,40]. As the goal of this paper is to demonstrate OS-PAM system's capabilities, the OCT subsystem was implemented only to guide the OS-PAM imaging and to provide structural information. The need for multimodality imaging instruments has been emphasised in several studies[41,42]. Thus for the OCT channel, a second low noise supercontinuum laser (SuperK EXTREME EXR9, NKT Photonics) (OS2) was employed. OS2 is coupled into a tunable filter (SuperK Gauss, NKT Photonics), using its IR channel (central wavelength 1310 nm and spectral bandwidth 180 nm). The state-of-the-art ultrahigh resolution OCT instrument is used sequentially with the OS-PAM. Light from OS2 is directed towards the galvanometer scanner head (GM), then conveyed through the objective to the sample. Light back-scattered by the sample returns into the 50/50 directional coupler (DC) being directed towards the spectrometer. The spectrometer consists of a custom made collimator, a transmission diffraction grating (Wasatch Photonics), a doublet pair as a focusing lens and a line camera (LC, SU1014-LDHI, Goodrich,) with 1024 pixels and 25 µm pitch, 47 kHz max reading rate, here operated at 20 kHz. Data is digitized using a camera link board (National Instruments, model IMAQ 1429).

The display of B-scan OCT and PAM images is performed in real-time. The generation of the PAM A-scans does not involve complex mathematical operations (a Hilbert transform is applied to each acquired temporal

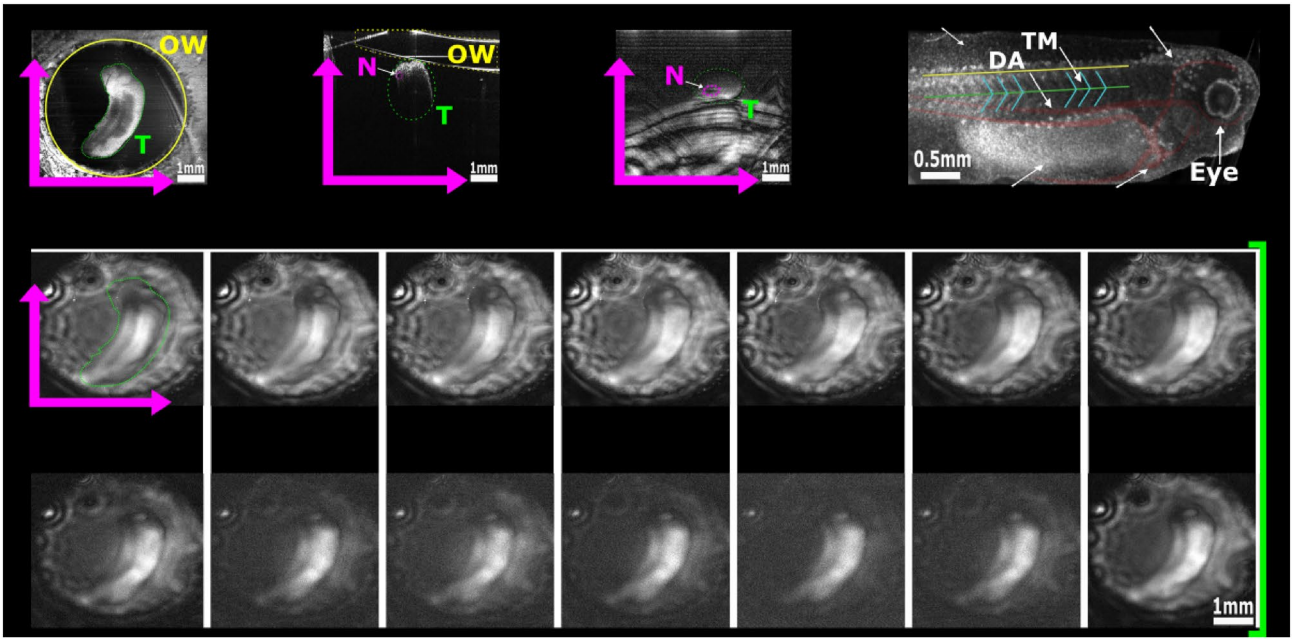


**Figure 5.** Representative in vivo OS-PAM en face images of one tadpole (T) generated at various wavelengths across the whole emission spectrum of the OS1. High noise levels can be observed above 1200 nm as water absorption increases. The OCT image has a wider field of view providing an overview of the optical window (OW) and the positioning of the tadpole; Top right: Structural en face OCT image displaying tadpole anatomy with highlighted main veins and aortas (red) as well as, the trunk muscles (blue). The green line indicates the position of the notochord (N) while the yellow line the position of the spinal cord. *DF* dorsal fin, *YS* yolk sack, *V* ventricle. This procedure was repeated on four animals (n = 4).

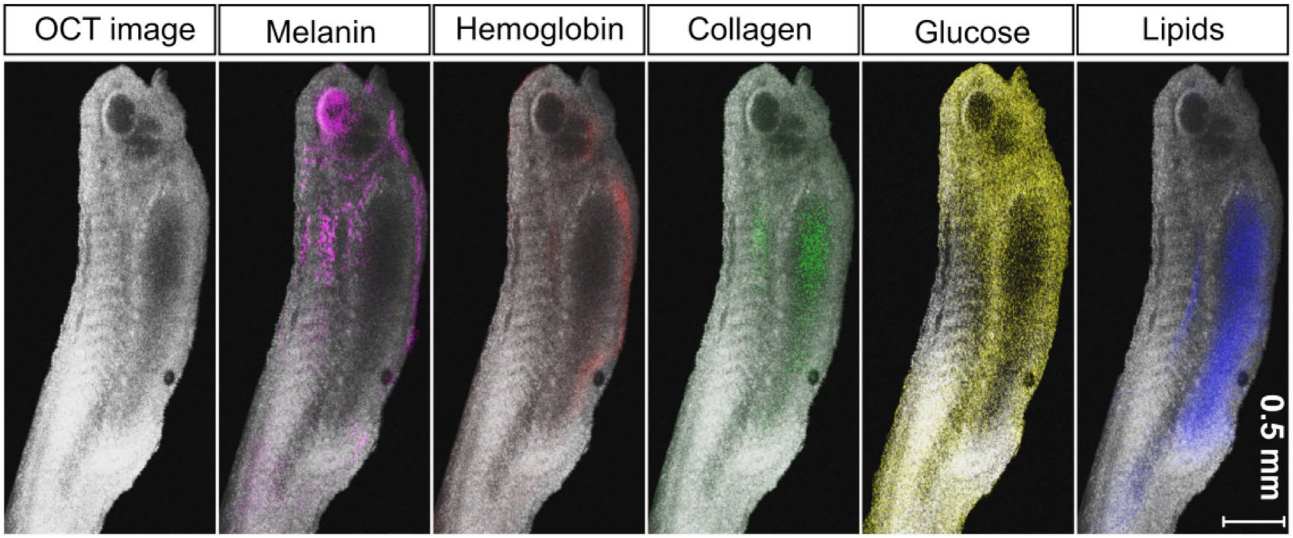


**Figure 6.** Qualitative illustrations of the superposition of the spatial mapping distribution of melanin (in pink), hemoglobin (magenta), collagen (green), glucose (yellow) and lipids (blue) within a tadpole obtained using the technique proposed, over a structural OCT image of the same tadpole. Similar in vivo images were obtained when imaging other four tadpoles. The image on the left shows the bare OCT image of the tadpole over which the maps of the chromophores were overlaid.

signal), hence the real-time display of the images is straightforward. The OCT channel is powered by the Master-Slave procedure, which allows for generation of direct en face views and of A-scans, with no need for resampling/linearisation of data[43,44].

An in-house LabVIEW software was developed to drive the acquisition and the analysis procedure. Thus, the PCI 5124 digitizer was employed to digitize the electrical signal generated by the ultrasound transducer in synchronism with the pulses generated by OS1. A-scans from the signals generated by both PAM and the OCT channels are produced for each position of the scanned beam during the lateral scanning of the sample.

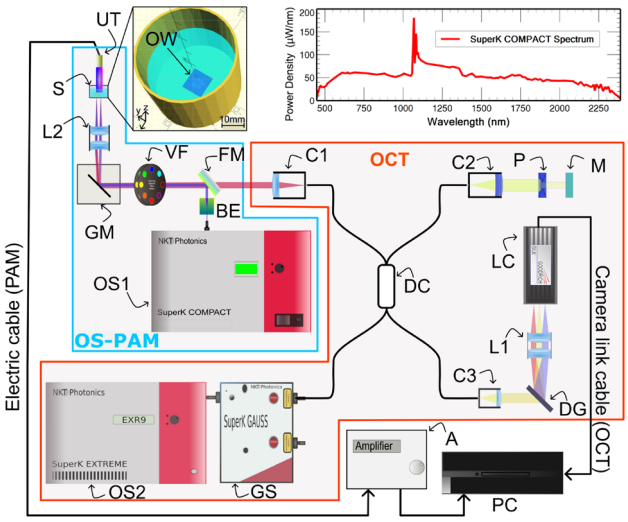


**Figure 7.** Schematic diagram of the OS-PAM/OCT system. *OS1* OS-PAM excitation optical source (SuperK COMPACT, NKT Photonics), *OS2* OCT optical source (SuperK EXTREME EXR9, NKT Photonics), *GS* Variable filter (SuperK GAUSS, NKT Photonics), *VF* Bandpass filter wheel, *BE* Beam expander, *FM* Flipping mirror, *GM* X–Y galvanometer mirrors, *LC* Line camera, *DG* Diffraction grating, *DC* 50/50 directional coupler, *UT* Ultrasound transducer, *S* Sample, *C1–C3* Collimators, *L1–L2* Lenses, *M* Flat mirror, *P* Pinhole, *A* Amplifier, *OW* Optical window of the 3D printed sample-holder; Drawing produced using Incscape 1.0.1 (https://inkscape.org/).

## Data availability

All data generated or analysed during this study are included in this published article (and its Supplementary Information files).

Received: 20 January 2022; Accepted: 14 June 2022
Published online: 22 June 2022

## References

1. Gray-Schopfer, V., Wellbrock, C. & Marais, R. Melanoma biology and new targeted therapy. *Nature* **445**, 851–857. https://doi.org/10.1038/nature05661 (2007).
2. D'Alessandro, B. & Dhawan, A. P. Transillumination imaging for blood oxygen saturation estimation of skin lesions. *IEEE Trans. Biomed. Eng.* **59**, 2660–2667. https://doi.org/10.1109/TBME.2012.2209647 (2012).
3. Fang, M., Yuan, J., Peng, C. & Li, Y. Collagen as a double-edged sword in tumor progression. *Tumour Biol.* **35**, 2871–2882. https://doi.org/10.1007/s13277-013-1511-7 (2014).
4. Long, J. *et al.* Lipid metabolism and carcinogenesis, cancer development. *Am. J. Cancer Res.* **8**, 778–791 (2018).
5. Filipp, F. V. *et al.* Glutamine-fueled mitochondrial metabolism is decoupled from glycolysis in melanoma. *Pigment Cell Melanoma Res.* **25**, 732–739. https://doi.org/10.1111/pcmr.12000 (2000).
6. Kluza, J. *et al.* Inactivation of the hif-1α/pdk3 signaling axis drives melanoma toward mitochondrial oxidative metabolism and potentiates the therapeutic activity of pro-oxidants. *Cancer Res.* **72**, 5035–5047. https://doi.org/10.1158/0008-5472.CAN-12-0979 (2012).
7. Parmenter, T. J. *et al.* Response of braf-mutant melanoma to braf inhibition is mediated by a network of transcriptional regulators of glycolysis. *Cancer Discov.* **4**, 423–433. https://doi.org/10.1158/2159-8290.CD-13-0440 (2014).
8. Scott, D. *et al.* Comparative metabolic flux profiling of melanoma cell lines: Beyond the Warburg effect. *J. Biol. Chem.* **286**, 42626–34. https://doi.org/10.1074/jbc.M111.282046 (2011).
9. Allen, T. *et al.* Ultrafast laser-scanning optical resolution photoacoustic microscopy at up to 2 million A-lines per second. *J. Biomed. Opt.*https://doi.org/10.1117/1.JBO.23.12.126502 *(2018).*
10. Liu, C., Liang, Y. & Wang, L. Single-shot photoacoustic microscopy of hemoglobin concentration, oxygen saturation, and blood flow in sub-microseconds. *Photoacoustics* **17**, 100156. https://doi.org/10.1016/j.pacs.2019.100156 (2020).
11. Wang, T., Nandy, S., Salehi, H. S., Kumavor, P. D. & Zhu, Q. A low-cost photoacoustic microscopy system with a laser diode excitation. *Biomed. Opt. Express* **5**, 3053–3058. https://doi.org/10.1364/BOE.5.003053 (2014).
12. Erfanzadeh, M., Salehi, H. S., Kumavor, P. & Zhu, Q. Improvement and evaluation of a low-cost laser diode photoacoustic microscopy system for ovarian tissue imaging. In *Photons Plus Ultrasound: Imaging and Sensing 2016*, vol. 9708, 97083I. https://doi.org/10.1117/12.2208943 (International Society for Optics and Photonics, 2016).
13. Dasa, M. K. *et al.* All-fibre supercontinuum laser for in vivo multispectral photoacoustic microscopy of lipids in the extended near-infrared region. *Photoacoustics* **18**, 100163. https://doi.org/10.1016/j.pacs.2020.100163 (2020).
14. Li, M., Chen, J. & Wang, L. High acoustic numerical aperture photoacoustic microscopy with improved sensitivity. *Opt. Lett.* **45**, 628–631. https://doi.org/10.1364/OL.384691 (2020).
15. Galanzha, E. I. *et al.* In vivo liquid biopsy using Cytophone platform for photoacoustic detection of circulating tumor cells in patients with melanoma. *Sci. Transl. Med.* **11**, eaat5857. https://doi.org/10.1126/scitranslmed.aat5857 (2019).
16. Shu, X. *et al.* Single all-fiber-based nanosecond-pulsed supercontinuum source for multispectral photoacoustic microscopy and optical coherence tomography. *Opt. Lett.* **41**, 2743–2746. https://doi.org/10.1364/OL.41.002743 (2016).
17. Buma, T., Conley, N. C. & Choi, S. W. Multispectral photoacoustic microscopy of lipids using a pulsed supercontinuum laser. *Biomed. Opt. Express* **9**, 276. https://doi.org/10.1364/BOE.9.000276 (2018).

18. Zeng, L., Piao, Z., Huang, S., Jia, W. & Chen, Z. Label-free optical-resolution photoacoustic microscopy of superficial microvasculature using a compact visible laser diode excitation. *Opt. Express* **23**, 31026–31033. https://doi.org/10.1364/OE.23.031026 (2015).
19. Haindl, R. *et al.* Functional optical coherence tomography and photoacoustic microscopy imaging for zebrafish larvae. *Biomed. Opt. Express* **11**, 2137–2151. https://doi.org/10.1364/BOE.390410 (2020).
20. Lee, H. D., Shin, J. G., Hyun, H., Yu, B.-A. & Eom, T. J. Label-free photoacoustic microscopy for in-vivo tendon imaging using a fiber-based pulse laser. *Sci. Rep.* **8**, 1–9. https://doi.org/10.1038/s41598-018-23113-y (2018).
21. Kellnberger, S. *et al.* Optoacoustic microscopy at multiple discrete frequencies. *Light Sci. Appl.* **7**, 109. https://doi.org/10.1038/s41377-018-0101-2 (2018).
22. Cao, R. *et al.* Multispectral photoacoustic microscopy based on an optical-acoustic objective. *Photoacoustics* **3**, 55–59. https://doi.org/10.1016/j.pacs.2014.12.004 (2015).
23. Bondu, M. *et al.* Multispectral photoacoustic microscopy and optical coherence tomography using a single supercontinuum source. *Photoacoustics* **9**, 21–30. https://doi.org/10.1016/j.pacs.2017.11.002 (2018).
24. Dasa, M. K., Markos, C., Janting, J. & Bang, O. Multispectral photoacoustic sensing for accurate glucose monitoring using a supercontinuum laser. *JOSA B* **36**, A61–A65. https://doi.org/10.1364/JOSAB.36.000A61 (2019).
25. Li, M.-L. & Wang, P.-H. Optical resolution photoacoustic microscopy using a Blu-ray DVD pickup head. In *Photons Plus Ultrasound: Imaging and Sensing 2014*, vol. 8943, 894315. https://doi.org/10.1117/12.2037146 (International Society for Optics and Photonics, 2014).
26. Zeng, L., Liu, G., Yang, D. & Ji, X. 3D-visual laser-diode-based photoacoustic imaging. *Opt. Express* **20**, 1237–1246 (2012).
27. Hariri, A. *et al.* Development of low-cost photoacoustic imaging systems using very low-energy pulsed laser diodes. *J. Biomed. Opt.* **22**, 075001. https://doi.org/10.1117/1.JBO.22.7.075001 (2017).
28. Tserevelakis, G. J., Mavrakis, K. G., Kakakios, N. & Zacharakis, G. Full image reconstruction in frequency-domain photoacoustic microscopy by means of a low-cost I/Q demodulator. *Opt. Lett.* **46**, 4718–4721. https://doi.org/10.1364/OL.435146 (2021).
29. Nguyen, V. P., Kim, J., Ha, K.-L., Oh, J. & Kang, H. W. Feasibility study on photoacoustic guidance for high-intensity focused ultrasound-induced hemostasis. *J. Biomed. Opt.* **19**, 105010. https://doi.org/10.1117/1.JBO.19.10.105010 (2014).
30. Yao, D.-K., Zhang, C., Maslov, K. & Wang, L. V. Photoacoustic measurement of the Grüneisen parameter of tissue. *J. Biomed. Opt.* **19**, 017007. https://doi.org/10.1117/1.JBO.19.1.017007 (2014).
31. Assorted Spectra. https://omlc.org/spectra/
32. Tsai, C.-L., Chen, W.-J. & Wang, J.-C. Near-infrared absorption property of biological soft tissue constituents. *J. Med. Biol. Eng.* **21**, 7 (2001).
33. Hui, J. *et al.* Bond-selective photoacoustic imaging by converting molecular vibration into acoustic waves. *Photoacoustics* **4**, 11–21. https://doi.org/10.1016/j.pacs.2016.01.002 (2016).
34. Hecht, E. *Optics* (Pearson, 2002).
35. Greivenkamp, J. E. *Field Guide to Geometrical Optics* (SPIE, 2004).
36. Zhang, C., Maslov, K. I., Yao, J. & Wang, L. V. In vivo photoacoustic microscopy with 7.6-μm axial resolution using a commercial 125-MHz ultrasonic transducer. *J. Biomed. Opt.* **17**, 1. https://doi.org/10.1117/1.jbo.17.11.116016 (2012).
37. Pshennikova, E. & Voronina, A. Expression of the transcription factor Xvent-2 in *Xenopus laevis* embryogenesis. *Am. J. Mol. Biol.* **2**, 124–131. https://doi.org/10.4236/ajmb.2012.22014 (2016).
38. Jorgensen, P., Steen, J. A. J., Steen, H. & Kirschner, M. W. The mechanism and pattern of yolk consumption provide insight into embryonic nutrition in *Xenopus*. *Development* **136**, 1539–1548. https://doi.org/10.1242/dev.032425 (2009).
39. Koutsikou, S. *et al.* A simple decision to move in response to touch reveals basic sensory memory and mechanisms for variable response times. *J. Physiol.* **596**, 6219–6233. https://doi.org/10.1113/JP276356 (2018).
40. Maria, M. *et al.* Q-switch-pumped supercontinuum for ultra-high resolution optical coherence tomography. *Opt. Lett.* **42**, 4744. https://doi.org/10.1364/OL.42.004744 (2017).
41. Park, J. *et al.* Quadruple ultrasound, photoacoustic, optical coherence, and fluorescence fusion imaging with a transparent ultrasound transducer. *Proc. Natl. Acad. Sci. U.S.A.* **118**, e1920879118. https://doi.org/10.1073/pnas.1920879118 (2021).
42. Lee, D. *et al.* In vivo near infrared virtual intraoperative surgical photoacoustic optical coherence tomography. *Sci. Rep.* **6**, 35176. https://doi.org/10.1038/srep35176 (2016).
43. Bradu, A. *et al.* Recovering distance information in spectral domain interferometry. *Sci. Rep.* **8**, 15445. https://doi.org/10.1038/s41598-018-33821-0 (2018).
44. Podoleanu, A. G. & Bradu, A. Master-slave interferometry for parallel spectral domain interferometry sensing and versatile 3D optical coherence tomography. *Opt. Express* **21**, 19324–19338. https://doi.org/10.1364/OE.21.019324 (2013).


## Acknowledgements

GN and GM would like to thank the support of the University of Kent. AP and AB acknowledge the support of Biological Sciences Research Council (BBSRC), "5DHiResE" project, BB/S016643/1; AP also acknowledges the European Union's Horizon 2020 research and innovation programme under the Marie Sklodowska-Curie grant NETLAS (agreement No 860807) and the National Institute for Health Research Biomedical Research Centre at Moorfields Eye Hospital NHS Foundation Trust (NIHR), the UCL Institute of Ophthalmology, University College London (AP) and the Royal Society Wolfson research merit award. SK acknowledges the support from The Physiological Society UK (Research Grant 2019). CM acknowledges financial support from the Multi-BRAIN project funded by the Lundbeck Foundation (R276-2018-869) and Villum Fonden (36063). MKD and OB acknowledge support from the Innovation Fund Denmark (4107-00011A) and European Union's Horizon 2020 research and innovation programme under the Marie Sklodowska-Curie grant (agreement No 722380). AB acknowledge the support of the Royal Society, project PARSOCT, RGS/R1/221324 and the support of the Academy of Medical Sciences/the Wellcome Trust/the Government Department of Business, Energy and Industrial Strategy/the British Heart Foundation/Diabetes UKSpringboard Award SBF007\100162.

## Author contributions

G.N. and M.D. contributed equally as first authors. G.N. and M.D. conceived the idea and obtained preliminary results. G.N. redesigned and conducted the experiments, analysed the results and structured the manuscript. M.D., G.M. , S.K. and A.B. contributed to the manuscript writing. G.M. and S.K. provided and prepared the animals. M.B. and P.M. provided SC expert support. A.B. supervised the experiments. C.M., O.B., S.K., A.P. and A.B. supervised the studies, with AP and AB equal contribution as last authors. All authors reviewed the manuscript.

## Competing interests

The authors declare no competing interests.

## Additional information

**Supplementary Information** The online version contains supplementary material available at https://doi.org/10.1038/s41598-022-14869-5.

**Correspondence** and requests for materials should be addressed to G.N.

**Reprints and permissions information** is available at www.nature.com/reprints.

**Publisher's note** Springer Nature remains neutral with regard to jurisdictional claims in published maps and institutional affiliations.

LETTER

# Enhanced resolution optoacoustic microscopy using a picosecond high repetition rate Q-switched microchip laser

Gianni Nteroli,[a] Giulia Messa,[b] Manoj K. Dasa,[c] Antti Penttinen,[d] Antti Härkönen,[d] Mircea Guina,[d] Adrian Gh. Podoleanu,[a] Stella Koutsikou,[b] and Adrian Bradu[a,*]

[a]University of Kent, Applied Optics Group, Canterbury, United Kingdom
[b]University of Kent, Medway School of Pharmacy, Chatham, United Kingdom
[c]Technical University of Denmark, DTU Fotonik, Lyngby, Denmark
[d]Tampere University, Optoelectronics Research Centre, Physics Unit, Faculty of Engineering and Natural Sciences, Tampere, Finland

**Abstract.** Conventional optoacoustic microscopy (OAM) instruments have at their core a nanosecond pulse duration laser. If lasers with a shorter pulse duration are used, broader, higher frequency ultrasound waves are expected to be generated and as a result, the axial resolution of the instrument is improved. Here, we exploit the advantage offered by a picosecond duration pulse laser to enhance the axial resolution of an OAM instrument. In comparison to an instrument equipped with a 2-ns pulse duration laser, an improvement in the axial resolution of 50% is experimentally demonstrated by using excitation pulses of only 85 ps. To illustrate the capability of the instrument to generate high-quality optoacoustic images, *en-face*, *in-vivo* images of the brain of *Xenopus laevis* tadpole are presented with a lateral resolution of 3.8 $\mu$m throughout the entire axial imaging range.  [DOI: 10.1117/1.JBO.27.11.110501]

**Keywords:** optoacoustic; Q-switched lasers; axial resolution enhancement.

Paper 220125LRR received Jun. 13, 2022; accepted for publication Nov. 4, 2022; published online Nov. 29, 2022.

## 1 Introduction

Optical imaging techniques used in modern biology, such as confocal, multi-photon, or light-sheet microscopy[1] require either the use of exogenous probes or genetic manipulations[2] to achieve the desired optical contrast. Optoacoustic microscopy (OAM) is a hybrid imaging technique employing the absorption of light by intrinsic components of the sample to achieve the desired optical contrast. Exhaustive literature is already available on the use of OAM to image complex biological samples.[3,4]

In most reports on OAM,[5,6] the excitation optical source is a laser delivering pulses of a typical duration of several nanoseconds, used in conjunction with a single-element ultrasound transducer (UT). The values of the pulse energy and duration provided by the source, and the acoustic bandwidth of the transducer, are of paramount importance for achieving high-quality OAM images in terms of signal-to-noise ratio (SNR) and axial resolution. When a very large bandwidth transducer is employed, the axial resolution is limited by the bandwidth of the generated acoustic waves.[7] So far, the techniques used to enhance the axial resolution have involved either the use of numerical methods requiring long post-processing times or high-frequency UTs.[8,9] The number of reports demonstrating improvement in the axial resolution by manipulating the bandwidth of the acoustic waves is limited and typically restricted to situations where the bandwidth is enhanced by reducing the duration of the pulses from hundreds to several nanoseconds.[5,6] Using numerical simulations, it has been demonstrated that a 3-ps pulse duration laser is more efficient in generating high-frequency acoustic signals than a 3-ns pulse duration laser, however, no improvement in axial resolution was reported.[10] To our knowledge, enhancement in axial resolution by reducing the pulse duration below several nanoseconds has not been

*Address all correspondence to Adrian Bradu, a.bradu@kent.ac.uk

experimentally demonstrated yet. Here, we show that an OAM imaging instrument, equipped with a Q-switched microchip laser, delivering short pulses of 85 ps at 532 nm, can provide a better axial resolution than when equipped with a supercontinuum optical source delivering excitation pulses of 2 ns, and operating at the same wavelength as the ps laser. The capability of the OAM instrument equipped with the ps-based Q-switched microchip laser to produce high-resolution OAM images is illustrated by images of the brain of the *Xenopus laevis* tadpole.

## 2 Methods and Materials

*In-vivo* imaging was performed on four *Xenopus laevis* tadpoles at developmental stage 37/38 (Nieuwkoop and Faber 1956). *Xenopus laevis* fertilized eggs were purchased from EXRC (Portsmouth, UK) and raised in tap water treated with a commercially available aquarium water conditioner at 20°C. The tadpoles were immobilized in $\alpha$-bungarotoxin (Invitrogen), placed in saline solution during imaging experiments and remained immobilized during imaging acquisition. All experimental procedures on living tadpoles were approved by the University of Kent Animal Welfare and Ethical Review Body, reference: 0037-SK-17.

The schematic diagram of the OAM instrument used in this work is shown in Fig. 1. The optical source (OS1) is a frequency-doubled Q-switched microchip laser emitting at 532 nm (Picophotonics Ltd, Tampere, Finland) capable to generate optical pulses of typically 85 ps and variable output power. OS1 was operated at 60 nJ per pulse and a pulse repetition rate of 50 kHz. The average optical power on the sample was 3 mW. OS2 is a supercontinuum optical source (SuperK Compact, NKT Photonics, Denmark) delivering pulses of 2 ns duration with a repetition rate of 20 kHz. Both OS1 and OS2 delivered the energy per pulse.

The TTL signals (TTL1/2) are used to trigger the digitization of the electrical signal at the output of the low noise amplifiers (LNA) (ZFL-500LN+, Mini Circuits), by a 12-bit data acquisition board, DAQ1 (National Instruments, Model PCI-5124). DAQ1 was operated at a sampling rate of 200 MS/s. The lasers were used sequentially by switching the position of the flipping mirror (FM). The samples were submerged in water to facilitate acoustic coupling. The sample holder (SH) is mounted on a high-resolution 3D translation stage (TS) to position the sample accurately.

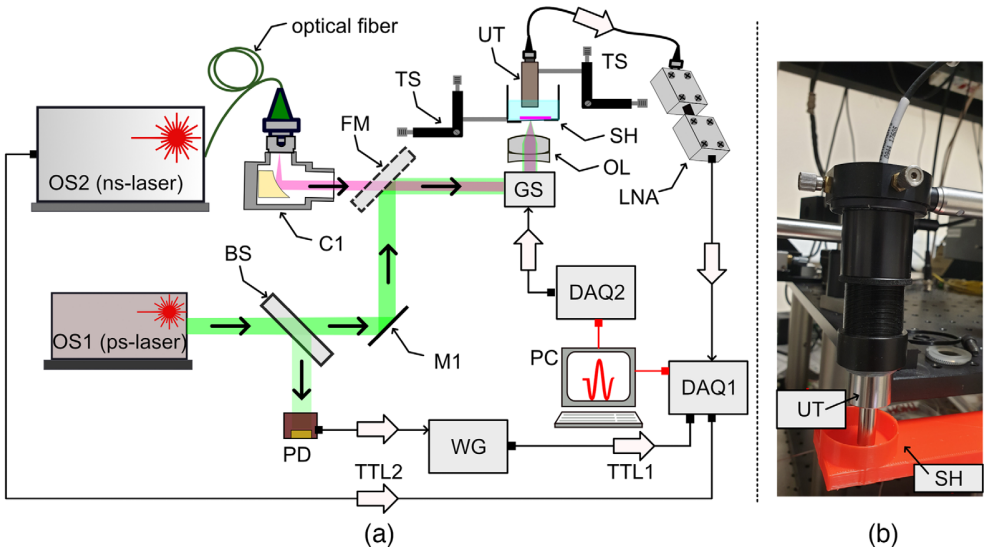


**Fig. 1** (a) Schematic diagram. OS1: picosecond laser; OS2: supercontinuum optical source; C1: reflective collimator; SH: sample holder; FM: flipping mirror; PD: photodetector; GS: orthogonal galvo-scanners; DAQ1,2: data acquisition cards; LNA: low noise amplifiers; UT: ultrasound transducer; OL: objective lens. TS: translation stage; TTL1,2: TTL signals synchronized with the emission of the pulses. (b) Picture showing the UT and SH.

The acoustic waves are detected by a high-frequency Polyvinylidene Fluoride ultrasonic transducer (50-MHz central frequency, 53% bandwidth at 6 dB, Model PA1199, Precision Acoustics) placed in contact with the water. The sample lies on an optical window of 0.22-mm thickness, whereas the excitation beam illuminates the sample from below. The electrical signal generated by the transducer is amplified by the two LNAs, before digitization by DAQ1.

As a relatively low central frequency transducer and optical focusing were used to achieve high lateral resolution, our instrument operates in an optical resolution (OR-) OAM regime.

To illustrate the capability of the instrument to produce high-quality images in terms of SNR and spatial resolution, in the picosecond regime, we imaged the brain of *Xenopus laevis* tadpole. The energy per pulse we operated at was 60 nJ, so within ANSI safety standards, which limits the pulse energy to maximum of 1 $\mu$J for OR-OAM instruments.[11] During imaging, the tadpoles were immobilized and positioned in the SH, (SH in Fig. 1). B-scan images, in the $XZ$ plane, of $400 \times 500$ pixels$^2$ were produced and displayed in real-time at a frame rate of 62.5 Hz (8 ms to capture data and 8 ms to process it). Therefore, $XYZ$ volumes of $400 \times 400 \times 500$ pixels$^3$ were generated in 6.4 s. To preserve the lateral resolution throughout the entire axial imaging range, volumetric data were collected for various focusing axial positions of the optical beam inside the tadpole by shifting the SH (in increments of 50 $\mu$m) with respect to the objective lens (OL in Fig. 1).

## 3 Results and Discussion

Several experiments were conducted to evaluate the capabilities of our OAM instrument. To evaluate the lateral resolution, a sharp edge of a positive USAF target was imaged. Using the image produced, the edge spread function [magenta curve in Fig. 2(a)], and the line spread function [green line in Fig. 2(a)] were calculated. The lateral resolution, defined as the full-width-at-half-maximum (FWHM) of the line spread function, was found to be 3.8 $\mu$m, close to the expected theoretical value (3.1 $\mu$m using Rayleigh's criterion[12]). In Figs. 2(b) and 2(c), we show the capability of the instrument in terms of its axial depth of field (DOF), and lateral field of view (FOV), respectively. The axial DOF showed in Fig. 2(b) has been provided by the manufacturer of the transducer, whereas the lateral FOV [Fig. 2(c)] was measured by imaging a carbon fiber tape with OS1. As shown in Fig 2(b), when the OAM signal drops by 3 dB, the axial range is around $z_{\max} = 1.5$ mm, which represents a sufficiently long axial imaging range to cover a large variety of biological samples, including the *Xenopus laevis* tadpole, which is <1 mm in thickness. As a focused ultrasonic transducer was employed, the OA signal recorded at various lateral positions on the sample shows a maximum in the middle of the image. The lateral FOV, estimated from Fig. 2(c) was $1 \times 1$ mm$^2$.

To experimentally measure the axial resolution, a carbon fiber tape was imaged using both the microchip ps laser, OS1 and the supercontinuum ns source, OS2. Both sources operate at the same central wavelength of 532 nm, however, over different spectral ranges. The ps laser, with an intrinsic bandwidth of a couple of nanometers, delivers sufficient energy per pulse to obtain

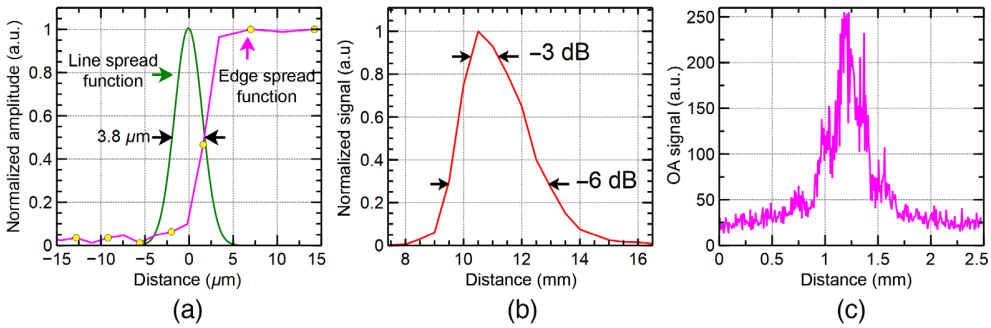


**Fig. 2** (a) Experimentally measured edge (magenta) and line (green) spread functions. (b) Detected acoustic signal versus axial position (data provided by the manufacturer of the transducer). (c) Lateral FOV, measured by imaging a carbon fiber tape.

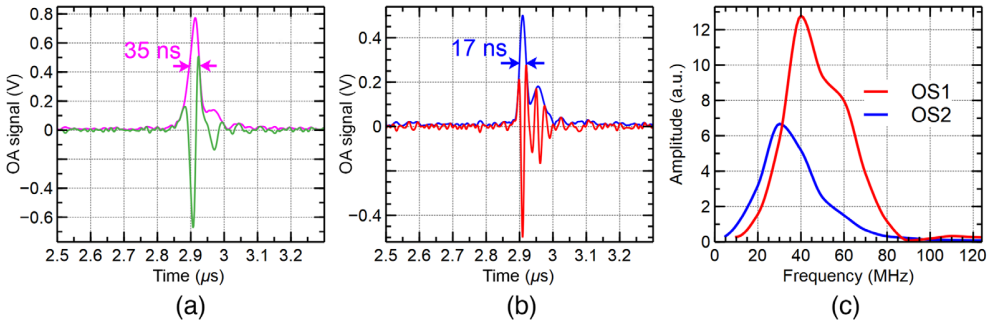


**Fig. 3** Typical OA signals generated by exciting a carbon fiber with a 2-ns pulse duration [green curve in (a)] and 85-ps pulse duration laser [red curve in (b)]. The envelopes of the two signals are presented in pink and blue, respectively. From the signals presented in (a) and (b), the acoustic spectra generated by using OS1 and OS2 were calculated in (c). By measuring the FWHM of the two spectra, we could infer axial resolutions of 25 and 51 $\mu$m, respectively. The fact that the two spectra are not identical in terms of central frequency and bandwidth shows that, the axial resolution is not determined by the bandwidth of the transducer alone.

high-quality images in terms of SNR. To obtain images of similar quality, the light from the supercontinuum source was filtered by a bandpass filter of 25-nm bandwidth. As shown in Fig. 3(a), when pulses of 2-ns duration were employed, the FWHM of the acoustic signal was found to be 35 ns, which, given the speed of sound in soft tissues of ~1480 m/s, corresponds to an axial resolution of 51 $\mu$m. Differently, for an 85-ps pulse duration, the FWHM of the acoustic signal was found to be 17 ns, therefore, an axial resolution of 25 $\mu$m [Fig. 3(b)]. This shows that when the bandwidth of the transducer employed is sufficiently wide, the axial resolution can be adjusted by tunning the duration of the pulses. These results were consistent with those obtained in subsequent measurements by imaging different regions of the sample. In Figs. 3(a) and 3(b), only one typical result is presented.

Both picosecond and nanosecond pulse duration optical sources allowed for similar optoacoustic SNRs of 42.9 and 43.8 dB, respectively. In terms of the axial resolution achievable with the two lasers, a 50% enhancement is obtained when using the picosecond pulses in comparison to the nanosecond pulses, when higher frequency acoustic waves are generated as illustrated in Fig. 3(c). The ps-induced optoacoustic signal shows a central frequency at around 41 MHz [Fig. 3(c), red curve], whereas the nanosecond-induced optoacoustic signal shows a central frequency at around 30 MHz [Fig. 3(c), blue curve]. To perform these measurements, the same ultrasonic transducer and sample were employed.

Figure 3(c) shows that the spectrum of the acoustic waves collected using OS1 (red) is larger than the spectrum collected using the OS2 (blue). As a further manifestation of different spectra generated, the centers of the two spectra do not coincide, more acoustic energy is generated by the OS1 closer to the central frequency of the transducer of 50 MHz than when using OS2.

In Fig. 4, *en-face*, high-resolution optoacoustic images at different axial positions inside the tadpole are presented, along with an optical microscopy *en-face* image [Fig. 4(a)]. The *en-face* OAM images were produced by using the maximum intensity projection algorithm. Images obtained at different focusing positions of the optical beam were color-coded (i.e., colors correspond to different focusing positions) and then combined into a composite image such as that depicted in Fig. 4(b). In Figs. 4(c)–4(e), three *en-face* images are presented, which are spaced by 200$\mu$m from each other's axial position. In Fig. 4(c), the focus of the beam is inside the eye, therefore, sharp images of the tadpole's eye and part of the otic capsule are visible. As a high concentration of melanin is localized in the eye, a high amplitude optoacoustic signal is expected to be generated by the ocular tissue. When the focal plane of the OL is shifted inside the tadpole by 200 $\mu$m, the blurred shapes of the midbrain and the forebrain appear [Fig. 4(d)], whereas a sharp image of the eye is not resolved in this focal plane. Moving another 200-$\mu$m inward, the hindbrain is displayed, as shown in Fig. 4(e). A flowchart illustrating the procedure employed to record the images and the post-processing steps needed to produce the overlayed images is presented at the top of Fig. 4 (part A).

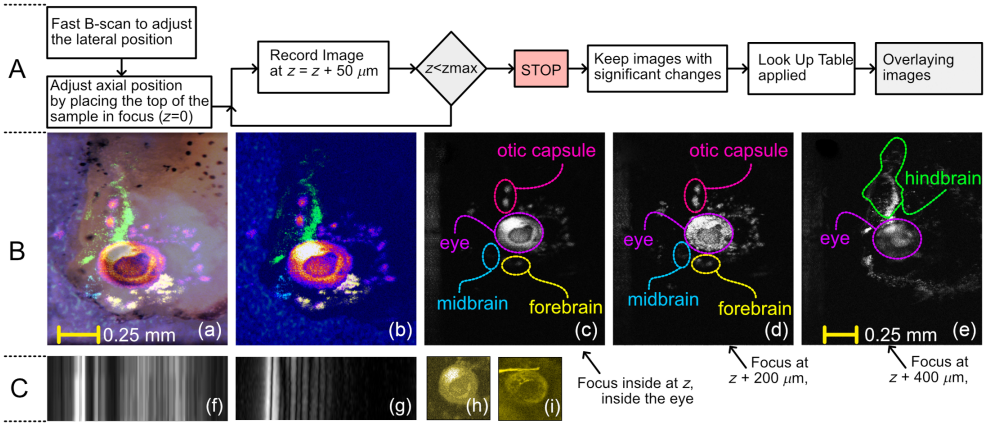


**Fig. 4** Part A: flowchart describing the imaging protocol and the post-processing steps. Part B: (a) microscope image of the tadpole's head over which the OAM image showed in (b) is overlapped. (b) Composite *en-face* image obtained by merging images collected at 24 axial positions separated by 50 $\mu$m. (c)–(e) Single-plane images showing significant examples of defined brain structures that appear as the focal plane is shifted deeper into the tadpole. The axial separation between (c) and (d), and (d) and (e) is 200 $\mu$m. It is noteworthy that (a) has the same lateral size as (b) and (c) has the same lateral size as (d) and (e). Part C: (f) and (g) B-scan images of the carbon tape produced using the ps and the ns lasers, respectively. Axial size (along the horizontal direction): 1.6 mm. Lateral size (vertical direction): 50 $\mu$m. (h) and (i), typical *en-face* images of the tadpole's eye produced using the ps and the ns lasers, respectively. In both cases, the light is focused inside the eye. The artifact in (i) is due to a structural defect of the optical window.

In Figs. 4(f) and 4(g), we demonstrate B-scan images of the carbon fiber tape produced using the ps and the ns lasers respectively. The axial resolution in Fig. 4(f) is better than in Fig. 4(g). The apparent better depth penetration observable in Fig. 4(f) is possibly due to, (i) the fact that the two images were collected in different experimental conditions (light focused deeper when using the ps laser) and, (ii) not all the wavelengths emitted by the ns laser are probably absorbed by the sample, and therefore, do not contribute to the OAM signal to the extent that the spectrum content of the ps laser is absorbed.

To the best of our knowledge, this level of detail of the tadpole's brain shown in Fig. 4 has not been demonstrated yet by any other research group using an OAM instrument equipped with a ps pulse duration laser.

## 4 Conclusion

In this letter, we demonstrated that the axial resolution of any OAM instrument can be improved by narrowing the pulse duration of the excitation laser, therefore high-axial resolution images can be produced. More precisely, we experimentally proved that by using a Q-switched microchip laser delivering 85-ps pulses, the axial resolution is 50% better than when employing a 2-ns pulse duration laser. It is expected that by using narrower laser pulses, the axial resolution to be improved even further. By simulation, a 3-ps pulse duration laser has been shown[10] to generate frequencies well above 270 MHz. In principle, if the conditions to produce the photo-acoustic effect are fulfilled, extremely low pulse duration lasers can be used to develop high-axial resolution instruments. Extreme short pulses however for similar energies, may exhibit such high peak pulse power that nonlinear optical effects may limit further reduction of the pulse duration. Compared to other types of optical sources used in OAM, such as frequency-converted ns Q-switched lasers[13,14] or supercontinuum, fiber systems[15,16] the microchip laser employed, although at the moment is only capable to operate at a single wavelength, offers other advantageous features, such as a higher pulse repetition rate than standard Q-switched systems, and/or higher pulse energy compared to mode-locked systems. Moreover, the laser has a small footprint ($15 \times 15 \times 12$ cm$^3$), a rather simple architecture, and low cost, which makes it advantageous also compared to solutions based on amplified gain-switched lasers. Although the ps laser employed

here only operates at 532 nm, we must point out that 532 nm is a very popular wavelength used for opto-acoustic imaging as light at this wavelength is absorbed by a plethora of chromophores present in biological samples. Finally, a quite high repetition rate suggests that the chip laser employed here can be a highly sought-after optical source for OAM. To take full advantage of the enhancement in axial resolution, further investigations are needed as soon as faster OA transducers become available, and more shorter laser pulse technologies are developed. As of now, we need to mention two limitations of the instrument we developed due to the repetitive nature of the experiments conducted. First, to achieve constant high lateral resolution along the axial direction, and therefore be able to differentiate the anatomical brain structures of the tadpole, repetitive imaging at 50 $\mu$m increments was required and second, although the B-scan images were produced in real-time, the combined image shown in Fig. 4 required post-processing. To overcome these limitations, higher pulse repetition rates must be used in an instrument equipped with a fast-focusing capability (such as the use of a liquid lens, instead of the manual adjustment we performed) and harness the computing power of the graphics cards to improve the post-processing time.

## Disclosures

The author(s) declare no competing interests.

## Acknowledgments

GN and GM thank the support of the University of Kent. AGhP and AB acknowledge the support of BBSRC, "5DHiResE" project, BB/S016643/1; AGhP and MG acknowledge the European Union's Horizon 2020 research and innovation programme (Marie Sklodowska-Curie grant NETLAS 860807). AGhP further acknowledges the NIHR Biomedical Research Centre at Moorfields Eye Hospital NHS Foundation Trust, UCL Institute of Ophthalmology, and the Royal Society Wolfson research merit award. SK acknowledges the support from The Physiological Society UK (Research Grant 2019). MKD acknowledge support from Union's Horizon 2020 research and innovation programme (Marie Sklodowska-Curie grant, 722380). AGhP, AH, and MG acknowledge Business Finland (TEMPO, 168/31/2020). AB also acknowledges the support of the Royal Society, project PARSOCT, RGS/R1/221324 and the support of the Academy of Medical Sciences/the Welcome Trust/the Government Department of Business, Energy and Industrial Strategy/the British Heart Foundation/Diabetes UK Spring-board Award SBF007\100162.

## References

1. J. Ripoll, B. Koberstein-Schwarz, and V. Ntziachristos, "Unleashing optics and optoacoustics for Developmental Biology," *Trends Biotechnol.* **33**, 679–691 (2015).
2. T. Peresse and A. Gautier, "Next-generation fluorogen-based reporters and biosensors for advanced bioimaging," *Int. J. Mol. Sci.* **20**, 6142 (2019).
3. S. Jeon et al., "Review on practical photoacoustic microscopy," *Photoacoustics* **15**, 100141 (2019).
4. M. K. Dasa et al., "Multispectral photoacoustic sensing for accurate glucose monitoring using a supercontinuum laser," *Opt. Soc. Am. J. B: Opt. Phys.* **36**, A61–A65 (2019).
5. K. Irisawa et al., "Influence of laser pulse width to the photoacoustic temporal waveform and the image resolution with a solid-state excitation laser," *Proc. SPIE* **8223**, 79 (2012).
6. T. Agano et al., "Effect of light pulse width on frequency characteristics of photoacoustic signal – an experimental study using a pulse-width tunable LED-based photoacoustic imaging system," *Int. J. Eng. Technol.* **7**, 4300–4303 (2018).
7. L. V. Wang and S. Hu, "Photoacoustic tomography: *in-vivo* imaging from organelles to organs," *Science* **335**, 1458–1462 (2012).
8. P. Burgholzer, J. Bauer-Marschallinger, and M. Haltmeier, "Breaking the resolution limit in photoacoustic imaging using non-negativity and sparsity," *Photoacoustics* **19**, 100191 (2020).

9. E. M. Strohm, M. J. Moore, and M. C. Kolios, "High-resolution ultrasound and photoacoustic imaging of single cells," *Photoacoustics* **4**, 36–42 (2016).
10. J. Yao et al., "High-speed label-free functional photoacoustic microscopy of mouse brain in action," *Nat. Methods* **12**, 407–410 (2015).
11. W. Liu and J. Yao, "Photoacoustic microscopy: principles and biomedical applications," *Biomed. Eng. Lett.* **8**, 203–213 (2018).
12. E. Hecht, *Optics*, 4th ed., Pearson International Edition (2002).
13. S.-W. Cho et al., "High-speed photoacoustic microscopy: a review dedicated on light sources," *Photoacoustics* **24**, 100291 (2021).
14. G. Hu et al., "Tunable multidimensional multiplexed Q-switched pulse outputs from a linear fiber laser with a bidirectional loop," *Opt. Laser Technol.* **141**, 107138 (2021).
15. M. K. Dasa et al., "All-fibre supercontinuum laser for *in vivo* multispectral photoacoustic microscopy of lipids in the extended near infrared region," *Photoacoustics* **18**, 100163 (2020).
16. M. Bondu et al, "Multispectral photoacoustic microscopy and optical coherence tomography using a single supercontinuum source," *Photoacoustics* **9**, 21–30 (2018).

# Combining photoacoustic and optical coherence tomography imaging for nondestructive testing applications

Gianni Nteroli, Adrian Podoleanu, Adrian Bradu

Gianni Nteroli, Adrian Podoleanu, Adrian Bradu, "Combining photoacoustic and optical coherence tomography imaging for nondestructive testing applications," Proc. SPIE 12170, Advances in 3OM: Opto-Mechatronics, Opto-Mechanics, and Optical Metrology, 121700P (5 May 2022); doi: 10.1117/12.2626041

SPIE.

Event: Advances in 3OM: Opto-Mechatronics, Opto-Mechanics, and Optical Metrology, 2021, Timisoara, Romania

Keynote Paper

# Combining Photoacoustic and Optical Coherence Tomography Imaging for Non-Destructive Applications

Gianni Nteroli[a], Adrian Podoleanu[a], and Adrian Bradu[a*]
[a]Applied Optics Group, University of Kent, CT2 7NH Canterbury, United Kingdom
*a.bradu@kent.ac.uk

## ABSTRACT

Robust, non-destructive testing imaging instruments, capable to provide valuable information from within the body of materials is important for both quality control and the development of new materials, for industrial and medical applications. Conventional non-destructive testing (NDT) methods, such as radiographic or ultrasound-based techniques, allow for deep axial range imaging, however, they are either using non-safe radiation or/and exhibit low imaging resolutions. The speed at which the standard NDT methods deliver images is also limited. The development of photoacoustic (PA) and optical coherence tomography (OCT) applications in the field of NDT have grown exponentially over the past years, offering faster, higher resolution images. Both techniques, PA and OCT bring a plethora of benefits to the current methods. However, a multitude of challenges still needs to be addressed to truly make either of them the technique of choice for NDT applications. In this manuscript, a short overview of the challenges that these two imaging techniques are facing when used for NDT applications is presented. Illustrative high-resolution images, produced by a dual PA/OCT imaging instrument developed within the Applied Optics Group at the University of Kent are presented. These images demonstrate unique capabilities for NDT applications.

**Keywords:** Photoacoustic Imaging, Optical coherence tomography, non-destructive testing

## 1. CHALLENGES IN PA AND OCT

### 1.1 Limited lateral resolution

The beauty of both PA and OCT technologies is that their axial resolution is decoupled from the lateral one. The axial resolution in PA imaging is basically determined by the electrical bandwidth of the ultrasound transducer (UT) and the speed of the acoustic wave within the material investigated whereas the bandwidth of the optical source employed determines the axial resolution in OCT. The transversal resolution depends on the interface optics, mainly on the numerical aperture of the microscope objective employed to focus light on the sample. Optical sources with a sufficient broad optical spectrum ensure an excellent axial resolution for OCT, whereas large bandwidth ultrasound transducers that of the PA. To improve the lateral resolution, a high numerical aperture microscope objective must be used. The immediate drawback of this approach is a limited axial image restricted to the extension of the confocal gate. A solution suitable for high numerical aperture interface optics can be the Gabor method [1], currently used with OCT, which potentially can be extended to PA instrumentation. Using the Gabor technique, data acquisition is repeated for several focus positions, corresponding to various shifts of the confocal gating profile through the sample. The images obtained are then fused to form a final larger image covering an extended axial range. As the data acquisition must be performed multiple times the real-time operation of the instrument is limited. The axial resolution in PA depends on the imaging depth. The axial resolution decreases from shallow depths, reachable by ballistic photons, to deeper depths due to acoustic attenuation. As the higher acoustic frequencies are stronger attenuated than the lower frequencies, a deterioration of the resolution at large depths occurs. Several numerical and hardware-based techniques [2,3] have been proposed so far to tackle this problem.

In PA instruments, the axial imaging range is limited by the depth at which photons, ballistic or multi-scattered ones can penetrate the sample and the attenuation of the acoustic waves and the bandwidth of the ultrasonic transducer. However, typically PA axial range is larger than that of OCT. Considering the two waves, incident and returned waves, simply in OCT, both waves are optical, while in PA one is optical while the other is a sound wave. Both implementations of spectral-domain OCT, respectively spectrometer based (CB) and swept-source (SS), can be used to produce images with high speed and high sensitivity. The SS-OCT technology seems to be the method of choice over CB-OCT when a long axial range is required. Due to the finite coherence length of the lasers used, the axial imaging range in SS-OCT is still limited, an

Advances in 3OM: Opto-Mechatronics, Opto-Mechanics, and Optical Metrology, edited by Virgil-Florin Duma, Jannick P. Rolland, Adrian G. H. Podoleanu, Proc. of SPIE Vol. 12170, 121700P
© 2022 SPIE · 0277-786X · doi: 10.1117/12.2626041

exception from this being the tunable vertical-cavity surface-emitting lasers (VCSEL) and akinetic light sources, which can provide long axial ranges, exceeding centimeters but are costlier than the microelectromechanical swept sources conventionally used.

As the operation of OCT is based on detecting ballistic photons, the axial imaging capability of OCT is certainly also limited by the characteristics of the sample to be imaged. PA can break the optical diffusion limit as multi-scattered photons can also generate acoustic waves, leading to a better penetration depth than that provided by the OCT instrumentation.

### 1.2 Real-time imaging capability

The production of real-time images in OCT is very often limited by the complex mathematical operations required to process acquired data. In OCT, to produce a cross-sectional image, interferometric spectra acquired while scanning the probing beam over the sample is subject to a fast Fourier transform (FFT). Before the FFT, several preparatory signal processing steps are needed to achieve high axial resolution and sensitivity. Some of the preparatory operations are extremely time-consuming as can only be sequentially executed, therefore the production of the OCT images in real-time is limited. So far, several techniques involving both hardware and software solutions have been demonstrated to successfully eliminate or diminish the execution time of the preparatory steps.

The most demanding preparatory steps in terms of computation time are data resampling and compensation for dispersion mismatch between the arms of the interferometer. To eliminate the resampling step, in CB-OCT, hardware solutions were proposed. However, this requires careful adjustment of the hardware components and the use of extra optical components in the interferometer or in the spectrometer [4] introduces losses. In SS-OCT, the swept sources are often equipped with a supplementary k-clock that adds to the cost of the source [5]. Other techniques such as using an additional light source that produces several spectral lines in the region of interest of the spectrometer, parametric iteration methods, phase linearization techniques, and automatic calibrations have been also proposed. All these methods are normally computationally expensive and limit the real-time operation of OCT systems.

As the computational requirements for high-speed image processing usually exceed the capabilities of most personal computers, the display rates of OCT images rarely match the acquisition rates. After the preparatory steps, most image generation, analysis, and diagnosis become a post-processing operation. A true, real-time display of processed cross-sectional, and *en-face* images could benefit NDT applications that require instant feedback of image information.

In contrast to OCT, in PA, there is no need for an interferometer, therefore no need for a complex mathematical procedure to decode the information needed from the raw data. A simple Hilbert transform of the detected acoustic signal suffices to generate an A-scan, so fast generation in real-time of the cross-sectional images is possible.

### 1.3 Contact-less imaging

OCT is well known for its capability of producing images without any need of contact between the microscope objective and the sample investigated, however, PA does require either direct contact between the ultrasonic transducer and the sample or involves the use of ultrasonic gels, which may not be ideal for some industrial applications. There are a plethora of reports demonstrating the use of Fabry-Perot interferometric sensors [6] instead of the ultrasonic transducers not requiring contact with the sample, however, they add complexity to the instrument or do not provide sufficient quality of the images.

## 2. SOLUTION: COMBINING PA AND OCT

To tackle the limitations of the current PA or OCT instruments, we develop imaging instruments combining these two technologies [7-10]. The PA channel provides better axial penetration and offers excellent spectral capabilities due to the PA signal being dependent on spectral absorption. If the optical source for PA uses a supercontinuum optical source, then the large spectrum of such optical sources allows a wideband spectroscopic analysis. At the same time, a broadband optical source enables high axial resolution OCT imaging. A broadband source demands enhanced signal processing when using a Fourier Transform, which is considerably simplified employing the Master/Slave (MS) technique [11,12] developed by our research group. These combined instruments can meet the demands of various NDT applications such as high lateral and axial resolution, long axial range, and real-time operation. They are also offering flexibility as the MS approach allows for easy, quick adjustments of the OCT channel in the combined instrument if required by a specific application, as well as robustness, and spectral capabilities of the PA imaging channel.

The benefits of the MS method originate from the fact that the method does not use FFTs to generate images [12]. Instead, there is no need for any of the preparatory steps, and as the method is only based on the multiplication of digital signals, is highly parallelizable [13]. As no sequential mathematical operations are needed, the MS method can operate in true real-time. The MS method compares, raw, unprocessed spectra which incorporate all the information about nonlinearities and unbalanced dispersion. As a result, there is no need for data resampling or procedures to compensate for unbalanced dispersion. An enhanced MS-OCT instrument is an instrument free of non-linearities and perfectly compensated for dispersion. The PA imaging instruments do not require any calibration procedures. With no need to decode the raw signals, only a Hilbert transform is needed to generate a PA axial reflectivity profile.

Various MS enhanced PA/OCT imaging instruments were developed in our group and used for different NDT applications, operating at various spectral ranges, and allowing quite long axial ranges [7-10]. In Fig. 1, we present a basic diagram describing how our combined instruments are developed by using the same optical source for both imaging channels. The optical source (OS) is a supercontinuum laser capable to emit pulsed light with a repetition rate of a few tens of kHz, and several ns pulse duration. When combining PA and OCT, each pulse must contain a wide spectral bandwidth to enable good axial OCT resolution, but sufficiently narrow to allow for spectral measurements in the PA channel. PD on the sketch presented in Fig. 1 is a spectrometer devised for the spectral range targeted. The speed at which the two channels are operating is the same, given by the repetition rate of the pulses emitted by the optical source, therefore, like no other multimodality imaging instrument, high-resolution cross-sectional images can be obtained in both channels, eventually simultaneously.

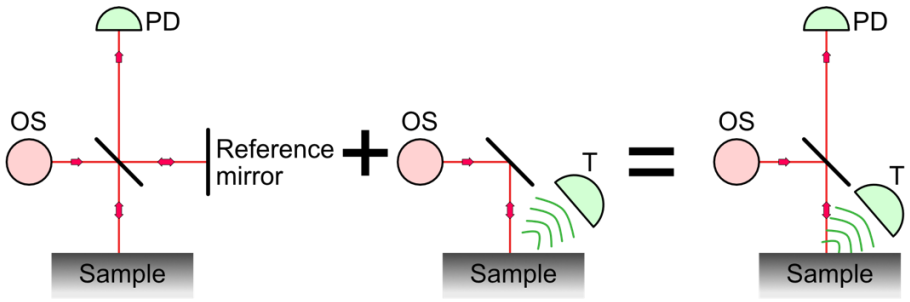


Figure 1. Combining an OCT and a PA instrument within a multimodality imaging tool using a single optical source (OS). PD is a spectrometer operating over the spectral range needed, whereas OS delivers pulses of a duration of a few ns with a repetition rate of tens of kHz. The combined instruments share a single OS, but not the same detection paths.

A more detailed diagram of a combined PA/OCT instrument currently in use in our labs is illustrated in Fig. 2 where light is emitted by a supercontinuum optical source over a spectral range from 450 to 1,800 nm. When the two flipping mirrors FM are in the UP position (i.e. FM1 deflects the optical beam towards the flat mirror M and FM2 towards the galvos), the whole optical power delivered by the source is conveyed towards the sample. The optical bandpass filter F placed between the flat mirror M and the flipping mirror F can be employed to select the spectral range needed to target the chromophores present within the material of the sample under investigation. A transducer T collects the acoustic waves, and an electronic amplifier A amplifies the transducer output electric signal that is directed towards an analogue-to-digital converter ADC1. When the two flipping mirrors are in the DOWN position, the whole optical power is used by the OCT channel. An optical bandpass filter F1 placed between the flipping mirror FM1 and the achromatic lens L selects the spectral range utilized by the OCT channel. Although the operation of such an instrument is sequential, it has the advantage of employing the whole available optical power delivered by OS in each mode of operation. Depending on the requirements of the application, the instrument can be interfaced with optics ensuring a very high lateral resolution.

Using an instrument as that depicted in Fig. 2, images as those presented in Fig. 3 can be produced. To generate such images, a supercontinuum optical source (SuperK Compact, NKT Photonics) is employed. This OS delivers pulses at 20 kHz of 2 ns duration and a sufficient energy per pulse to produce good quality PA images. The OCT channel operates in the 1300 nm spectral range (160 nm spectral bandwidth) with an axial resolution of 5 µm (measured in air). As, at the same time, the instrument is equipped with a high numerical aperture microscope objective, high lateral resolution images can be generated. Typically, the lateral resolution in both channels is 5-7 µm across the entire spectral range, therefore isotropic resolution volumes can be generated in the OCT channel. The axial resolution in the PA channel, measured experimentally, is around 38 µm, value limited by the duration of the pulse, the attenuation of the high-frequency acoustic waves by the

sample and the bandwidth of the ultrasonic transducer employed. The lateral field of view of our instruments can extend over several millimeters making them ideal for several NDT applications.

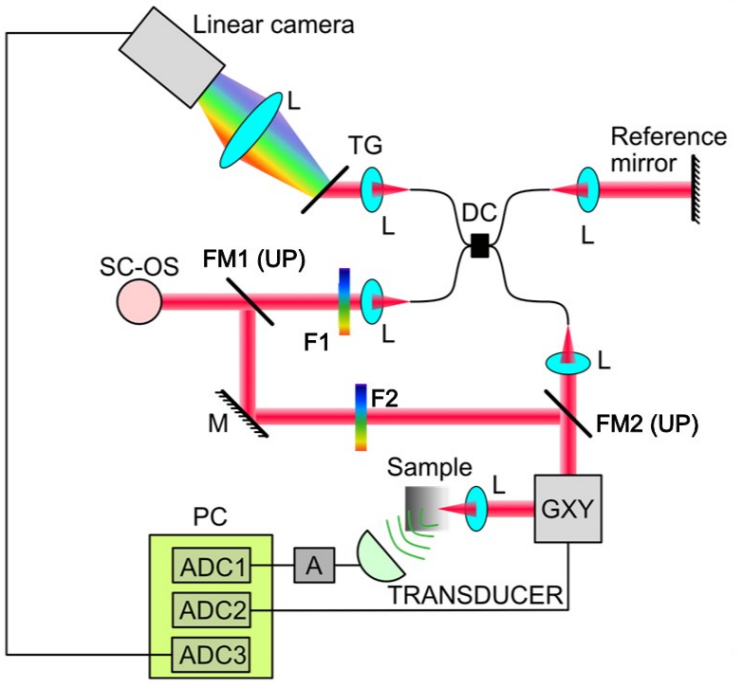


Figure 2. Schematic diagram of a combined sequential PA/OCT imaging instrument. ADC1-3: digitizers or signal generators; A: amplifier; L: achromatic lenses, GXY: galvos-scanners; FM1,2: flipping mirrors (both in the UP position)); F1,2: optical bandpass filters; M: flat mirror; DC: directional coupler, TG: transmission diffraction grating; SC-OS: supercontinuum optical source.

All the instruments developed so far employ the MS technology in the OCT channel, useful for a variety of NDT applications. The *en-face* images shown in Fig. 3 present 400 lateral pixels. Data to produce each volumetric image was collected in 8 s. Taking advantage of the MS method and of the simplicity of the mathematical operations needed in the PA channel, the instrument delivers cross-sectional images in both channels at a rate of 50 Hz, in real-time.

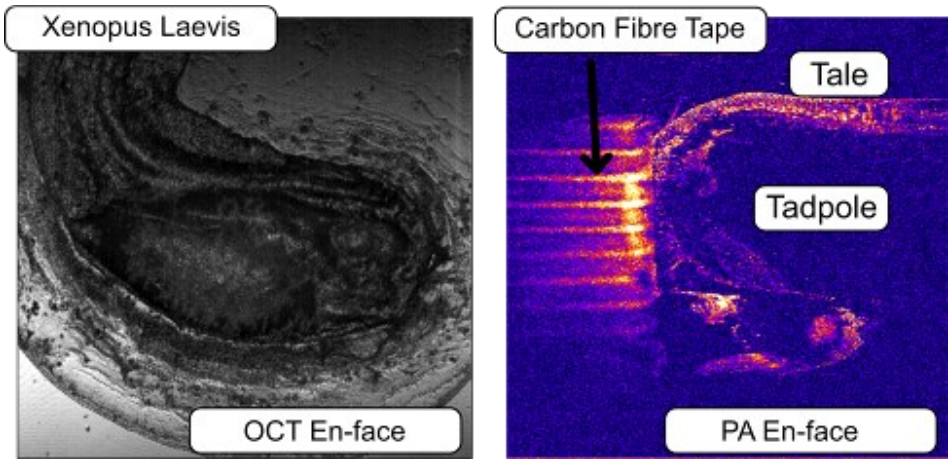


In Fig. 3 (left) an *en-face* OCT image of the Xenopus Laevis tadpole, of isotropic resolution of 5 µm is shown, whereas, on the right, an *en-face* PA image of the same tadpole is presented. Here, a carbon fiber tape was placed in the focal plane of the microscope objective, next to the tadpole, which is also placed approximately in the focal plane of the objective. The amplitude of the PA signal from within the tadpole is sufficiently high to generate a high-quality image, amplitude

depending on the optical energy within each pulse. In our case, we managed to obtain an energy per pulse of over 50 nJ over the whole spectral range of the supercontinuum source when a bandpass filter of 25 nm was employed. As a result, it is expected that high sensitivity PA images of the biological samples are possible with sufficient spectral resolution. In NDT applications, the typical amplitude of the PA signals would normally be much stronger than that obtained from biological tissue. This is illustrated on Fig. 3 (right) where the carbon fiber tape is brighter than the body of the tadpole.

## 3. DISCUSSIONS AND CONCLUSIONS

In this manuscript, a short review of some limitations of the current PA and/or OCT technologies was presented. To overcome them, the use of the Master/Slave approach was proposed in the OCT channel and a combined PA/OCT instrument using a single optical source. Some illustrative images produced using PA/OCT enhanced instruments developed in our group suitable to be used for NDT applications were demonstrated. The advantages of such an enhanced multimodality instrument recommend such technology for NDT applications.

The combined instrument offers great advantages, such as excellent resolution, uses two contrast methods (optical absorption and optical scattering), offers great spectral capabilities (especially in the PA channel), ability to perform widefield scans, uses non-ionizing, safe radiation, does not require heavy computational resources, etc.

The multimodal instrument is ideally suited to measurement of the shape of the surfaces (OCT), detection of micro-cracks in ceramic materials (PA+OCT), stress measurements (OCT), ablation-depth monitoring (PA+OCT), characterization of the multi-layered structures (PA+OCT), tablet coating monitoring (PA+OCT) [14], Li metal batteries imaging (PA) [15], monitoring structural changes such as corrosion (PA+OCT) [16], metal contaminations (PA+OCT) [17], defects, porosity, damage in composite materials (PA+OCT) [18], defects and damage in silicon (PA+OCT), coatings and underdrawings (OCT), analysis of microstructure in various materials (OCT), etc.

In terms of real-time production of the cross-sectional images, current CPUs are capable of data processing as required by the MS approach and by PA data processing with no need to resort to FPGA or GPUs. As our enhanced PA/OCT instruments can produce sequentially or simultaneously cross-sectional, *en-face* and volumetric images in real-time, such combined instruments are appropriate to industrial settings where swift imaging of the samples is required as for example for fast quality control along a production line.

Extra research is needed to overcome limitations of the two imaging technologies presented here, including developments on,

- the size of the transducer and its bandwidth
- non-uniform light fluence effects in the PA channel,
- acoustic attenuation
- sample heterogeneities,
- the need for contact with the sample (not ideal for some industrial applications, but when the OCT channel can be employed
- a limited penetration depth (PA may be used for some applications rather than OCT)
- high cost of the optical source (which is reduced when it is shared by both techniques), etc.

## ACKNOWLEDGEMENTS

GN thanks the support of the University of Kent. AP and AB acknowledge the support of Biological Sciences Research Council (BBSRC), “5DHiResE” project, BB/S016643/1; AP also acknowledges the European Union’s Horizon 2020 research and innovation program under the Marie Sklodowska-Curie grant NETLAS (agreement No 860807) and the National Institute for Health Research Biomedical Research Centre at Moorfields Eye Hospital NHS Foundation Trust (NIHR), the UCL Institute of Ophthalmology, University College London (AP) and the Royal Society Wolfson research merit award.

## REFERENCES


[1] Rolland, J. P., Meemon, P., Murali, S., Thompson, K. P., and Lee, K., "Gabor-based fusion technique for Optical Coherence Microscopy," Optics Express 18, 3632–3642 2010.

[2] Burgholzer, P., Bauer-Marschallinger, J., and Haltmeier, M., "Breaking the resolution limit in photoacoustic imaging using non-negativity and sparsity," Photoacoustics 19, 100191 2020.

[3] Strohm, E., Moore, M., and Kolios, M., "High resolution ultrasound and photoacoustic imaging of single cells," Photoacoustics 4, 36–42 2016.

[4] Hu, Z., and Rollins, A., "Fourier domain optical coherence tomography with a linear-in-wavenumber spectrometer," Opt. Lett. 32, 3525-3527 2007.

[5] Leitgeb, R., Drexler, W., Unterhuber, A., Hermann, B., Bajraszewski, T., Le, T., Stingl, A., and Fercher, A., "Ultrahigh resolution Fourier domain optical coherence tomography," Opt. Express 12, 2156-2165 (2004).

[6] Zhang, E., Laufer, J., and Beard, P., "Backward-mode multiwavelength photoacoustic scanner using a planar Fabry-Perot polymer film ultrasound sensor for high-resolution three-dimensional imaging of biological tissues," Appl. Opt. 47, 561-577 2008.

[7] Dasaa, M., Nteroli, G., Bowen, P., Messa, G., Feng, Y., Petersen, C., Koutsikou, S., Bondu, M., Moselund, P., Podoleanu, A., Bradu, A., Markos C., and Bang, O., "All-fibre supercontinuum laser for in vivo multispectral photoacoustic microscopy of lipids in the extended near-infrared region," Photoacoustics 100163 2020.

[8] Nteroli, G., Koutsikou, S., Moselund, P., Podoleanu, A., and Bradu, A., "Real-time multimodal high resolution biomedical imaging instrument using supercontinuum optical sources," in Frontiers in Optics + Laser Science APS/DLS, The Optical Society, paper JTu3A.99 2019.

[9] Nteroli, G., Bondu, M., Moselund, P, Podoleanu, A, and Bradu, A., "Developments on using supercontinuum sources for high resolution multi-imaging instruments for biomedical applications," Proc. SPIE 11077, Opto-Acoustic Methods and Applications in Biophotonics IV, 110770N 2019.

[10] Bondu, M, Marques, M., Moselund, P., Lall, G., Bradu, A., and Podoleanu, A., "Multispectral photoacoustic microscopy and OCT using a single supercontinuum source," Photoacoustics 9, 21-30 2018.

[11] Podoleanu, A., and Bradu, A., "Master–slave interferometry for parallel spectral domain interferometry sensing and versatile 3D optical coherence tomography," Opt. Express 21, 19324-19338 2013.

[12] Rivet, S., Maria, M., Bradu, A., Feuchter, T., Leick, L., and Podoleanu, A., "Complex master slave interferometry," Opt. Express 24, 2885-2904 2016.

[13] Bradu, A., Kapinchev, K., Barnes, F., and Podoleanu, A., "On the possibility of producing true real-time retinal cross-sectional images using a graphics processing unit enhanced master-slave optical coherence tomography system," J. Biomed. Opt., 20, 076008 2015.

[14] Markl, D., Hannesschläger, G., Sacher, S., Leitner, M., Khinast, J., "Optical coherence tomography as a novel tool for in-line monitoring of a pharmaceutical film-coating process,", European J. Pharmaceutical Sciences, 55, 58-67 2014.

[15] Liu, H., Zhao, Y., Zhou, J., Li, P., Bo S., Chen, S., "Photoacoustic imaging of lithium metal batteries," ACS Appl Energy Mater 3, 1260–1264 2020.

[16] Swapna, S., Nampoori V., Sankararaman, S., "Photoacoustics: a nondestructive evaluation technique for thermal and optical characterisation of metal mirrors," J Opt 47, 405–411 2018.

[17] Liu, L., Huan, H., Zhang, M., Shao, X., Zhao, B., Cui X, Zhu, L., "Photoacoustic spectrometric evaluation of soil heavy metal contaminants," IEEE Photonics J 11, 3900507 2019.

[18] Karabutov, A., Murashov, V., Podymova, N., "Evaluation of layered composites by laser optoacoustic transducers. Mech Compos Mater 35, 89-94 1999.

# Methods of dental shade determination

Christa Serban, Gianni Nteroli, Emanuela Craciunescu, Meda L. Negrutiu, Helmine Serban, et al.

Christa Serban, Gianni Nteroli, Emanuela L. Craciunescu, Meda L. Negrutiu, Helmine Serban, Virgil F. Duma, Adrian Bradu, Adrian Podoleanu, Cosmin Sinescu, "Methods of dental shade determination," Proc. SPIE 11942, Lasers in Dentistry XXVIII, 1194206 (4 March 2022); doi: 10.1117/12.2606721

SPIE.

Event: SPIE BiOS, 2022, San Francisco, California, United States

# Methods for dental shade determination

Christa Serban*[a†], Gianni Nteroli[b], Emanuela L. Craciunescu[a], Meda L. Negrutiu[a], Helmine Serban[c], Virgil F. Duma[d,e], Adrian Bradu[b†], Adrian Podoleanu[b], Cosmin Sinescu[a]
[a]Victor Babeș University of Medicine and Pharmacy Timișoara, Piața Eftimie Murgu 2, Timișoara, Timiș, Romania 300041; [b]University of Kent, Giles Ln., Canterbury, Kent, UK CT2 7NZ; [c]Simon Fraser University, 13450 102 Ave Unit 1100, Surrey, B.C., Canada V3T 0A3; [d]Aurel Vlaicu University of Arad, Bulevardul Revoluției 77, Arad, Arad, Romania 310032; [e]Polytechnic University of Timisoara, Piața Victoriei 2, Timișoara, Timiș, Romania 300006
[†]These two authors had equal contributions.

## ABSTRACT

Dental shade determination and seamless integration of restorative work in the oral cavity are challenging and important tasks in the everyday clinical dental practice. The aim of this *in-vitro* study is to create an easy-to-use color analysis solution in which images of teeth captured by a high-resolution smartphone camera are used to build color maps that enable objective shade determination. Furthermore, the shade determinations yielded using this method were evaluated comparatively with spectrophotometric and conventional visual dental shade determination methods. Visual shade determination of the incisal, middle, and cervical thirds of ten extracted human teeth was performed using the Vita Classical and Vita 3D Master shade guides. Shade determination of the thirds of each tooth was also performed using the Vita Easyshade spectrophotometer. Subsequently, photographs of each tooth were captured using a smartphone camera. Color charts were produced using an in-house image processing technique, and the tooth color captured by smartphone photography was interpolated to shade guide tabs. The results show that the camera-based method had better agreement with the spectrophotometric and visual methods when the Vita Classical shade guide was employed. Software-based color analysis of smartphone photography should be further explored for its use as an affordable potential tool for increasing objectivity and accuracy in dental shade determination.

**Keywords:** tooth color, shade selection, mobile phone photography, color maps, spectrophotometer, restorative dentistry, image processing

## 1. INTRODUCTION

Accurate dental color determination and communication is essential to enable esthetic integration of dental restorative work and to ensure patient satisfaction [1, 2]. Dental shade management is considered to be one of the most difficult challenges of restorative dentistry [2, 3]. Dental clinicians and technicians must be able to closely match natural teeth and create a lifelike imitation of tooth structure using restorative materials[3, 4]. This is challenging because natural teeth have great variation in color and many factors influence shade management in esthetic dentistry including light source, translucency, opacity, light scattering, and fluorescence [5]. In addition, color perception varies among clinicians [2]. Dentist-laboratory communication of subjective qualities in shade selection may lead to unwanted errors and subsequent remakes [3]. Despite advancements in protocols and technologies, shade matching in the anterior region remains a challenging task that often results in an unpredictable outcome. To minimize errors, reliable and objective shade determination and communication methodologies are needed [1, 3].

Traditionally, tooth shade matching can be approached through visual techniques using stock shade guides [5, 6]. The most widespread and popular shade guides in dental practice are the Vita Classical System (Vita Zahnfabrik) [7] and Vita 3D Master (Vita Zahnfabrik) [7]. The Vita 3D Master guide is arranged more systematically in the color space and studies have reported that the Vita 3D Master guide allows for superior shade matching [3, 6, 8]. Nonetheless, results of visual techniques using shade guides can be influenced by the examiner's experience and the environmental viewing conditions [8].

Lasers in Dentistry XXVIII, edited by Peter Rechmann, Daniel Fried, Proc. of SPIE
Vol. 11942, 1194206 · © 2022 SPIE · 1605-7422 · doi: 10.1117/12.2606721

Instruments for tooth shade determination include spectrophotometers and colorimeters [8, 9]. Computerized colorimeters and spectrophotometers have been developed in attempt to overcome the shortcomings associated with the subjectivity of visual techniques using shade guides [9]. Vita Easyshade (Vita Zahnfabrik) is a popular instrument for spectrophotometric shade determination and has been found to be more accurate than colorimeters [10]. Previous studies have found that these instruments produce consistent results but are not associated with higher accuracy than conventional visual methods using stock shade guides [1, 9, 11].

New techniques and technologies are emerging to enable more effective shade management [12, 13]. Recently, intraoral scanners have been implemented for shade management [13-15]. Digital shade management is a topic of interest that is continuously developing [1, 3, 13, 16]. The eLAB system has developed a standardized protocol for dental shade determination using digital camera photography [1, 3]. In this modern era of technology smartphones have become advanced devices that can produce high quality images. With further investigations, smartphone photography could become an affordable and easy to use potential tool for increasing objectivity and accuracy in dental shade determination [13].

The aim of this *in-vitro* study is to create an easy-to-use color analysis solution in which images of teeth captured by a high-resolution smartphone camera are used to build color maps that allow for objective shade determination. Furthermore, the shade determinations yielded using this method were evaluated comparatively with spectrophotometric and conventional visual dental shade determination methods.

## 2. MATERIALS AND METHODS

Ten extracted human teeth were obtained and stored in physiological serum. Each tooth was cleaned using running water and was evaluated visually using the Vita Classical (VC) and Vita 3D Master (V3DM) shade guide. Visual shade selection was conducted near a window using natural light and shade selection was performed for each tooth on the incisal, middle and cervical third. Then, each tooth was evaluated with the VITA Easyshade dental spectrophotometer. The spectrophotometer was used to identify the color of each tooth in the cervical, middle, and incisal thirds using the Vita Classical (VESC) and Vita 3D Master (VES3DM) shade scale settings. The identification of the colors has been performed (using all the techniques above) a number of five times for every individual tooth and area of interest.

High-resolution images of the teeth were captured using a mobile phone camera by placing them at an approximative distance of 10 cm from the camera's lens. The mobile phone camera was equipped with a single 12.2 MP standard array 1/2.55-inch sensor with 1.4µm pixels. For all situations, a flashlight was used to uniformly illuminate the samples, however no other filters (such as polarizing filters) were used. Color charts of the regions of interest were produced using an in-house image processing technique. To generate the color charts, the following steps were used:

1. The original RGB (Red, Green, Blue) [17] image was converted into an enhanced grayscale image (image 2 in Fig. 1).
2. An in-house developed fast edge detection technique was employed to isolate the object of interest (the tooth). Once the tooth is isolated, it was displayed on a black background with all noise removed (image 3 in Fig. 1).
3. The RGB image was converted into CIELAB [18] which is a color space established by the International Commission on Illumination (abbreviated as CIE) . The three parameters of this color model (**L***, **a*** and **b***) shown as examples in Fig. 1 (5, 6, 7) can be closely examined.
4. Based on the L*-values, an image was mapped into a specific color-space (copper), that allows mapping to the color chart (image 8 in Fig. 1).


**Figure 1.** Procedure employed to build the colormaps of the teeth. 1: original image; 2: enhanced, gray-scaled image; 3: edge detection; 4: tooth extracted from the image; 5: L-map of the tooth; 6: a-map of the tooth; 7: b-map of the tooth; 8: color-mapped tooth (copper mapping) using the values of L.

## 3. RESULTS

Five images of each, the incisal, middle, and cervical areas of the ten teeth were taken and the technique described in the previous section was employed to generate the L*a*b* values. As no filter was employed, on some occasions, the specular reflection of light off the enamel lead to L*-values above those available in the shade guides, therefore they were displayed as 0-values in the L*-maps and show as black spots in the image (as for example in Fig. 1(8)). In addition, due to the shape of the teeth and the relative position of the camera with respect to the teeth, slight variations of the L*a*b* values from a pixel to another were obtained. As a result, averages of the L*a*b* values were calculated across several regions of interest for each incisal, middle, and cervical areas of the tooth. The computations were done in such a way that the regions of interest considered avoided the areas where large values of L* were produced. Data obtained for all ten teeth are summarised in Fig. 2.

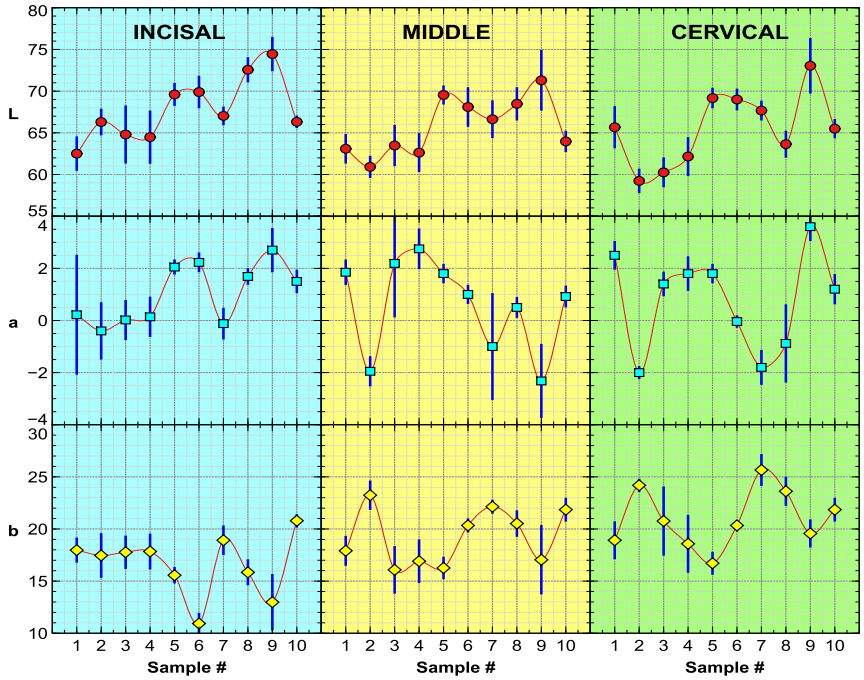


Figure 2. L, a, and b values for each of the 10 teeth for the incisal, middle, and cervical areas. The blue vertical bars represent the standard deviations for each measurement set.

As illustrated in Fig. 2, as most of the numerical values of L*, a*, and b* fall within the range of the values employed by the Vita classical and Vita 3D Master shade guides, we used them to generate the corresponding shades based on our techniques [19] and compared to the results obtained from the visual and spectrophotometric methods. The Vita Classical shade tabs A1-D4 are grouped alphabetically (A, B, C, D) by hue and then further narrowed down numerically (ie. A1, A2, A3, A3.5, A4) in terms of chroma and value [18]. The Vita 3D Master categorizes the tooth color space in six lightness groups (0, 1, 2, 3, 4, 5). Each group has variations in hue (L, M, R) and value (1, 2, 3) [18].

In Figs. 3, 4, and 5 we present the shades determined by:

1. Spectrophotometric measurements employing the Vita Easyshade spectrophotometer using the Vita Classic (VESC) and Vita 3D Master (VES3DM) shade scale settings.
2. Visual shades determinations, using VC (Vita Classic shade guide) and V3DM (Vita 3D Master shade guide)
3. Shade determinations using the procedure employing the camera of a mobile phone: CAM (Vita Classic shade guide) and CAM3D (Vita 3D Master shade guide).

| Incisal | VESC | VC | CAM | VES3DM | V3DM | CAM3D |
|---|---|---|---|---|---|---|
| 1 | A3.5 | A3.5 | A3.5 | 4.5M3 | 3R2.5 | 3R2.5 |
| 2 | A3.5 | A3 | A3 | 4M3 | 3M3 | 2R2.5 |
| 3 | A3.5 | A3 | A3.5 | 5M3 | 3R2.5 | 3R2.5 |
| 4 | A3.5 | A2 | A2 | 5M3 | 3M2 | 3R2.5 |
| 5 | A2 | A2 | A2 | 1.5M2.5 | 1M2 | 1M2 |
| 6 | A2 | A2 | A2 | 2M3 | 2M1 | 2M1 |
| 7 | A3.5 | A3.5 | A3 | 3.5M3 | 4M3 | 3M1 |
| 8 | B3 | B4 | A1 | 3L2 | 3L1.5 | 1M1 |
| 9 | A3 | B1 | A1 | 3M3 | 2M2 | 1M1 |
| 10 | A3.5 | A3.5 | A3.5 | 4M3 | 4M3 | 3M3 |

Figure 3. Shade determination using the Vita Classic and Vita 3D Master shade guides of the incisal area for each of the 10 teeth using three methods: spectrophotometric (VESC and VES3DM), visual (VC and V3DM) and camera-based one (CAM and CAM3).

| Middle | VESC | VC | CAM | VES3DM | V3DM | CAM3D |
|---|---|---|---|---|---|---|
| 1 | A3.5 | A3.5 | A3.5 | 5M3 | 3R2.5 | 3R2.5 |
| 2 | A3.5 | A3.5 | A3.5 | 4.5M3 | 4M3 | 4M3 |
| 3 | A3.5 | A3.5 | A3.5 | 5M3 | 4M3 | 3R2.5 |
| 4 | A3.5 | A2 | A3.5 | 5M3 | 3M3 | 3R2.5 |
| 5 | A2 | B2 | A2 | 1.5M2.5 | 1M2 | 2M1 |
| 6 | A3 | A2 | A3 | 2.5M3 | 2M3 | 2M3 |
| 7 | A3.5 | A3.5 | A3 | 4M3 | 4M3 | 3M3 |
| 8 | B3 | C2 | B3 | 3.5L2 | 3L2.5 | 2M3 |
| 9 | A3 | B1 | A1 | 2.5M3 | 2M2 | 2M2 |
| 10 | A3.5 | A3.5 | A3.5 | 4M3 | 4M3 | 3R2.5 |

Figure 4. Shade determination using the Vita Classic and Vita 3D Master shade guides of the middle area for each of the 10 teeth using three methods: spectrophotometric (VESC and VES3DM), visual (VC and V3DM) and camera-based one (CAM and CAM3).

| Cervical | VESC | VC | CAM | VES3DM | V3DM | CAM3D |
|---|---|---|---|---|---|---|
| **1** | A3.5 | A3.5 | A3.5 | 5M3 | 3R2.5 | 3M3 |
| **2** | A3.5 | A4 | C4 | 5M3 | 4M3 | 4M3 |
| **3** | A3.5 | A3.5 | A4 | 5M3 | 4M3 | 4M3 |
| **4** | A3.5 | A2 | A3.5 | 5M3 | 3M3 | 4M2 |
| **5** | B2 | B2 | B3 | 1.5M2.5 | 1M2 | 2M2 |
| **6** | A3 | A3 | A3 | 3M3 | 2M3 | 2M3 |
| **7** | A3.5 | A3.5 | A3.5 | 4M3 | 4M3 | 3M3 |
| **8** | A4 | C3 | A4 | C3 | 3L2.5 | 3R2.5 |
| **9** | B3 | B1 | A1 | 2.5M3 | 2M2 | 1M2 |
| **10** | A3.5 | A3.5 | A3.5 | 4M3 | 4M3 | 3M3 |

Figure 5. Shade determination using the Vita Classic and Vita 3D Master shade guides of the cervical area for each of the 10 teeth using three methods: spectrophotometric (VESC and VES3DM), visual (VC and V3DM) and camera-based one (CAM and CAM3).

All shades presented in tables on Figs. 4-6 are based on the average values generated by each individual technique. The cells with a green background shows agreement between cells across all three techniques, the blue cells show agreement on the shade between the camera-based method and either the spectrophotometric or visual techniques, whereas the red cells show situations in which there is no matching between the camera technique and the other two conventional methods. From these tables, it appears that the camera method produces shades closer to those obtained using the Vita Classical guide. 60-80% of the shades predicted by the camera technique matches at least one of shades determined by spectrophotometer and visual methods when the Vita Classical guide is employed, whereas when the Vita 3D Master shade guide is employed, only 30-50% of the shades matches the spectrophotometric/visual techniques.

## 4. DISCUSSION

The camera-based method had better agreement with the spectrophotometric and visual methods when the Vita Classical shade guide was employed. The camera-based method had moderate agreement with the spectrophotometric and visual methods when the Vita Classical shade guide was employed and low agreement when the Vita 3D Master was employed. A reduced agreement and consistency between the three methods could have resulted from the fact that shade tabs were used to report and compare colors and the degree of closeness of the shade tabs given by the three methods was not measured.

When using the camera-based method, the L* parameter or brightness generated the most uncertainty. Since no filter was used, the specular reflection of light off the enamel sometimes lead to L*-values above those available in the shade guides. In these areas of the color maps, they are displayed as 0-values and appear as black spots (as for example in Fig. 1(8)). As a result, since the main distinguishing factor in the Vita 3D Master shade guide is the L*-value or the brightness, this may explain why the agreement was lower with this shade guide compared to the Vita Classical guide. The use of polarizing filters for the smartphone camera should be considered as a potential option to overcome this limitation. In addition, due to the shape of the teeth and the relative position of the camera with respect to the teeth, slight variations of the L*a*b* values from a pixel to another were obtained. As a result, averages of the L*a*b* values were calculated across several regions of interest for each incisal, middle, and cervical areas of the tooth. The computations were done in such a way that the regions of interest considered avoided the areas where large values of L* were produced. The calibration of the smartphone camera would be a needed step in future studies. The software program requires input images of consistent spatial resolution and bit-depth. Calibration through the use of a test image can be used to solve this issue.

Currently, smartphones are efficient and have the ability to produce high quality images. The future development of a smartphone application with a built-in camera for dental shade determination could serve as an easy-to-use tool for dental shade management and an affordable alternative to subjective visual method and costly spectrophotometers and digital camera photography protocols. Future studies using color analysis of mobile phone photography are needed to explore different color models, phone cameras, and effect of external conditions. Software-based color analysis of smartphone photography should be further explored in order to enable increased accuracy and objectivity in dental shade determination.

## ACKNOWLEDGEMENTS

This research was supported by the Romanian Ministry of Research, Innovation and Digitization, CNCS/CCCDI–UEFISCDI, project PN-III-P4-ID-PCE-2020-2600, within PNCDI III. GN thanks the support of the University of Kent. AP and AB acknowledge the support of Biological Sciences Research Council (BBSRC), "5DHiResE" project, BB/S016643/1; AP also acknowledges the European Union's Horizon 2020 research and innovation program under the Marie Sklodowska-Curie grant NETLAS (agreement No 860807) and the National Institute for Health Research Biomedical Research Centre at Moorfields Eye Hospital NHS Foundation Trust (NIHR), the UCL Institute of Ophthalmology, University College London (AP) and the Royal Society Wolfson research merit award.

## REFERENCES

[1] S. Hein, J. Tapia, and P. Bazos, "eLABor_aid: a new approach to digital shade management," Int J Esthet Dent, 12(2), 186-202 (2017).
[2] J. Fondriest, "Shade matching a single maxillary central incisor," Quintessence Dental Technology, 28, 215-225 (2005).
[3] S. Hein, D. Modrić, S. Westland *et al.*, "Objective shade matching, communication, and reproduction by combining dental photography and numeric shade quantification," J Esthet Restor Dent, 33(1), 107-117 (2021).
[4] J. Fondriest, "Shade matching in restorative dentistry: The science and strategies," The International journal of periodontics & restorative dentistry, 23, 467-79 (2003).
[5] M. Ginzburg, and I. Gilboa, "[Tooth color matching systems and communication with dental laboratory in indirect restorations: 2011 update]," Refu'at ha-peh veha-shinayim (1993), 29(1), 28-34, 64 (2012).
[6] A. J. Hassel, A. Zenthöfer, N. Corcodel *et al.*, "Determination of VITA Classical shades with the 3D-Master shade guide," Acta Odontologica Scandinavica, 71(3-4), 721-726 (2013).
[7] A. Hassel, U. Koke, M. Schmitter *et al.*, "Clinical effect of different shade guide systems on the tooth shades of ceramic-veneered restorations," The International journal of prosthodontics, 18, 422-6 (2006).
[8] A. Caglar, K. Yamanel, K. Gulsahi *et al.*, "Could digital imaging be an alternative for digital colorimeters?," Clinical Oral Investigations, 14(6), 713-718 (2010).
[9] S. Kim-Pusateri, J. D. Brewer, E. L. Davis *et al.*, "Reliability and accuracy of four dental shade-matching devices," J Prosthet Dent, 101(3), 193-9 (2009).
[10] N. Alghazali, G. Burnside, R. Smith *et al.*, "Performance assessment of Vita Easy Shade spectrophotometer on colour measurement of aesthetic dental materials," The European journal of prosthodontics and restorative dentistry, 19, 168-74 (2011).
[11] C. Igiel, K. M. Lehmann, R. Ghinea *et al.*, "Reliability of visual and instrumental color matching," J Esthet Restor Dent, 29(5), 303-308 (2017).
[12] F. D. Jarad, M. D. Russell, and B. W. Moss, "The use of digital imaging for colour matching and communication in restorative dentistry," British Dental Journal, 199(1), 43-49 (2005).
[13] N. Sirintawat, T. Leelaratrungruang, P. Poovarodom *et al.*, "The Accuracy and Reliability of Tooth Shade Selection Using Different Instrumental Techniques: An In Vitro Study," Sensors, 21(22), 7490 (2021).
[14] M. Fattouh, "Repeatability Of Visual, Spectrophotometer And Intraoral Scanner Methods In Shade Matching: A Comparative In-Vivo Study," International Journal of Dentistry and Oral Science, 2439-2445 (2021).
[15] J. Reyes, P. Acosta, and D. Ventura, "Repeatability of the human eye compared to an intraoral scanner in dental shade matching," Heliyon, 5(7), e02100 (2019).
[16] F. Tabatabaian, E. Beyabanaki, P. Alirezaei *et al.*, "Visual and digital tooth shade selection methods, related effective factors and conditions, and their accuracy and precision: A literature review," Journal of Esthetic and Restorative Dentistry, 33(8), 1084-1104 (2021).
[17] R. Hirsch, [Exploring colour photography : a complete guide] Laurence King, London(2004).
[18] C. L. Novak, S. A. Shafer, and R. G. Willson, [Obtaining accurate color images for machine vision research] Jones and Bartlett Publishers, Inc., (1992).
[19] A. Wee, [Description of color science, color replication progress and esthetics], (2006).

European Conferences on Biomedical Optics 2021 (ECBO) © OSA-SPIE 2021

# Chasing sub-micrometer axial resolution in Visible Optical Coherence Tomography

Gianni Nteroli*, Adrian Bradu and Adrian Podoleanu

*Applied Optics Group, School of Physical Sciences, University of Kent, Canterbury, UK*
*E-mail: gn86@kent.ac.uk

**Abstract:** Optical Coherence Tomography instruments can provide images of ultrahigh, depth dependent axial resolution. Here we demonstrate an instrument employing visible light, enhanced by the Master-Slave technique, which deliver nearly constant axial resolution over the whole imaging range.

**Keywords**: visible light, optical coherence tomography, imaging, ultrahigh resolution

## 1. Introduction

Visible Optical Coherence Tomography (VIS-OCT) is an emerging imaging technique that can provide ultrahigh axial resolution of biological tissues. By using lower wavelengths than the conventional OCT imaging instruments and employing broadband optical sources such as supercontinuum lasers, resolutions of typical 1-3 μm in tissue were demonstrated [1-2]. The reported axial resolutions are however referring to measurements performed for very shallow depths (optical path differences (OPDs) between the arms of the interferometer, close to zero. As mentioned in various reports [1-2] the value of the axial resolution is depth dependent. Typically, in NIR/IR OCT, a deterioration of the axial resolution of 1-2 μm over an imaging range of 1 mm does not have a tremendous effect on the sharpness of the image however, in VIS-OCT, doubling the axial resolution can affect the outcomes of the measurements greatly. Although noticed in various research papers, no rigorous study on mitigating the deterioration of the axial resolution with depth has been reported so far. In this paper, we demonstrate a VIS-OCT imaging instrument enhanced by the Complex Master-Slave technique [3-4] showing a nearly constant axial resolution of around 2.1 μm in air (1.5 μm in tissue) along the entire axial imaging range of the instrument.

## 2. Methodology, Results and Discussion

Light from a supercontinuum broadband light source (SuperK Extreme EXR-20, NKT Photonics), providing a broad spectrum of nearly 250 nm with a central wavelength at 600 nm, was directed towards the sample and reference arm of an interferometer using a directional coupler (30/70). In the sample arm, light was conveyed towards the object to be imaged using a pair of orthogonal galvo-scanners (6220H, Cambridge Technology) and an achromatic in-house developed scan lens. The optical power emitted by the source was altered in such a way that, only 120 μW reached the sample. Light back-scattered by the sample and reflected by a reference mirror interfered at the directional fibre coupler and was conveyed towards an in-house devised spectrometer. At the core of the spectrometer, a Basler Sprint SPL4096-140KM line camera was employed. To produce the plots/images shown in this abstract, all 4096 pixels of the camera were utilised and vertically binned, hence the size of each individual pixel was 10×20 μm, whereas camera was operated at 20 kHz. The axial range which can be targeted with our instrument, determined by the coherence length of waves after diffraction on the grating (532 nm CWL, 1800 l/mm, Wasatch Photonics) combined with the spectral capability of the camera in sampling the spectrum was 1.6 mm (in air). The sensitivity drop-off was measured by using a flat mirror as object and using the procedure described in [5].

European Conferences on Biomedical Optics 2021 (ECBO) © OSA-SPIE 2021

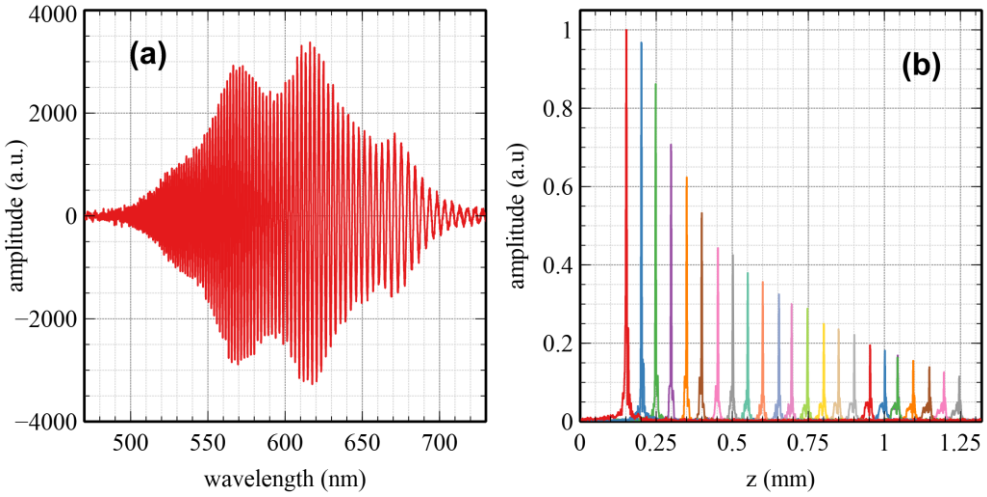


**Figure 1** (a) Example of a channelled spectrum collected by the camera (to better observe the modulation, the channelled spectrum was high pass filtered before plotting). (b) Sensitivity drop-off of the instrument. All A-scans were normalised with respect of the maximum value of the A-scan produced when placing the sample mirror at z = 150 µm away from OPD = 0. The measured sensitivity of the instrument for z = 150 µm and 125 µWon the sample was 78 dB.

As it can be seen in Fig. 1(b), the sensitivity drops by around 10 dB over an axial range of 1 mm, which is slightly better than the values reported in literature (14-15 dB). The full-width-at-half-maximum axial resolution of each A-scan peak shown in Fig. 1(b) was measured. In Fig. 2(a1-a3), for clarity, A-scans corresponding to various OPDs are shown (no data apodization) whereas their equivalent A-scans when a Hamming window was applied to the spectra are demonstrated in Figs. 2(b1-b3). As it can be seen for the 3 A-scans presented, the axial range is around 2.1 µm, however a little worsening of the resolution with depth could be observed (increase by ~ 5% at z = 1.2 mm with respect to z = 150 µm). This increase of the axial resolution is expected, being due to the limited number of pixels utilised. A large bandwidth per each camera pixel translates into a reduction of the dynamic coherence length of the interfering waves. A poor sampling of the channelled spectrum with a low number of camera pixels leads to an interpolation failure in conventional Fourier transform based OCT [6]. By using no interpolation, and perfectly compensating for unbalanced dispersion in the interferometer, our CMS based instrument performs better at depth than the conventional ones.

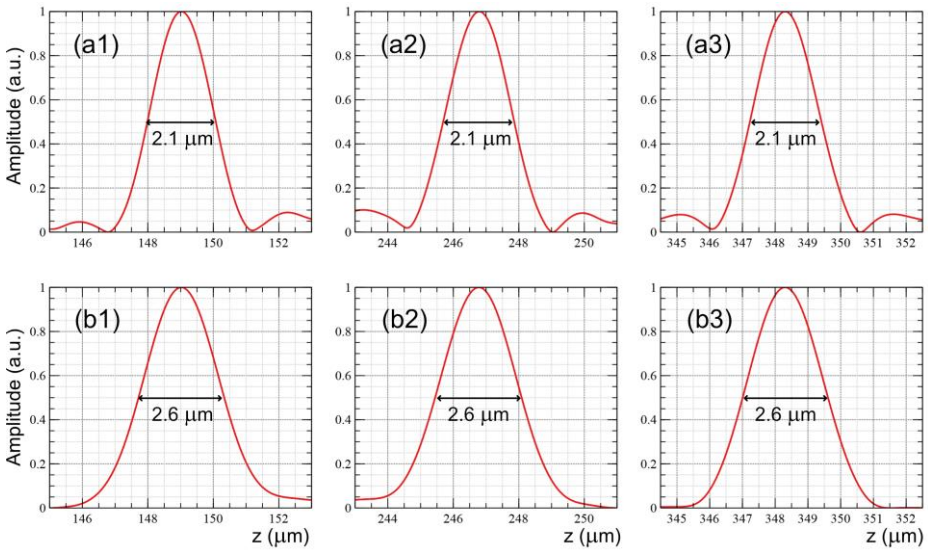


**Figure 2** Examples of A-scans for various OPDs in the interferometer with no apodization of the spectra (a1-a3) and when a Hamming window was applied to the spectra (b1-b3).

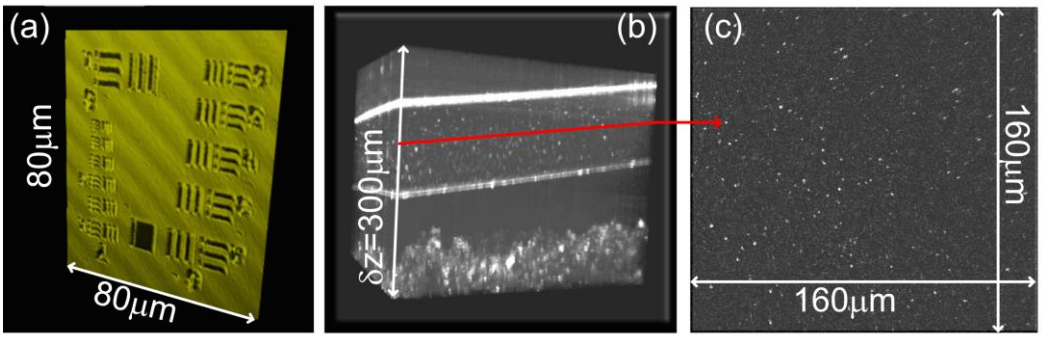


**Figure 3 (a)** 3D image of an USAF target showing that smallest future (group 7 element 6) is visible. **(b)** 3D image o fan IR card. **(c)** *En-face* view of the infrared card at the axial position shown by the red line.

In Fig. 3(a), a 3D image of an USAF target is demonstrated. As the smallest futures of this card are visible (group 7, element 6) are visible, the lateral resolution of our instrument is better than 2.19 μm (the theoretical value is 1.8 μm). In Fig. 3(b) a 3D image of an IR card is shown. The phosphor sensor area (bottom image) is below the coating layer. The fine borderline between the coating and the sensor is clearly visible. In Fig. 3(c) fine structures in the *en-face* view of the coating layer are shown. Additional details on the hardware employed, and the theoretical approach behind the VIS-OCT instrument we developed will be presented at the conference.

## Acknowledgments

AP and AB acknowledge the support of BBSRC (BB/S016643/1) and GN and AP the support of the NIHR Biomedical Research Centre at the UCL Institute of Ophthalmology and Moorfields Eye Hospital.

## References

[1] X. Shu, L. Beckhmann, and H. Zhang, "VIS OCT: a review", J. Biomed. Opt, **22**, p.121707 (2017).
[2] T. Zhang, et al, "Improving VIS OCT of the human retina with rapid spectral shaping and axial tracking", Biomed. Opt. Express **6**, p. 2918-2931 (2019).
[3] S. Rivet, et. al, "Complex master slave interferometry", Opt. Express 24, 2885-2904 (2016).
[4] A. Bradu et al, "Recovering distance information in spectral domain interferometry", Sci. Rep. **8**, p.15445 (2018).
[5] A. Bradu and A. Podoleanu, "Attenuation of mirror image and enhancement of the signal-to-noise ratio in a Talbot bands OCT system," J. Biomed. Opt. 16, 076010 (2011).
[6] Yun et al, "High-speed spectral-domain OCT at 1.3 μm wavelength," Opt. Express **11**, p.3598–3604 (2003).

# Real-time multimodal high resolution biomedical imaging instrument using supercontinuum optical sources

**Gianni Nteroli[a], Stella Koutsikou[b], Peter Moselund[c], Adrian Podoleanu[a], Adrian Bradu[a]**

[a]*Applied Optics Group, School of Physical Sciences, University of Kent, Canterbury, CT2 7NH, UK,* [b] *Medway School of Pharmacy, University of Kent, UK,* [c]*Photonics A/S, Blokken 84, Birkeroed, Denmark, 3460*

*G.Nteroli@kent.ac.uk*

**Abstract:** We present progress towards developing a multimodality imaging instrument, optical coherence tomography (OCT)/ photo-acoustic microscopy (PAM). By utilizing supercontinuum optical sources, that deliver wide spectral bandwidths and high energy densities, we devised a real-time imaging instrument which can be employed to image biological tissues. The OCT channel was devised to operate around 1300 nm. A custom built spectrometer ensures a constant axial resolution of 6 $\mu$m over an axial range of up to 1.5 mm. The PAM operates within the therapeutic window providing an axial resolution of 30 $\mu$m. The lateral resolution in both channels is 6 $\mu$m.

**OCIS codes:** 170.4500, 110.5120, 070.1060.

Keywords: optical coherence tomography, photo-acoustics, high-resolution, imaging, multimodal-imaging.

## 1. Introduction

Multi-modality imaging instruments can provide diverse contrast and supplementary, structural and functional information about the biological tissues. Optical coherence tomography (OCT) relies on the scattering properties of the tissues while Photo-acoustic microscopy (PAM) relies on the absorption of the optical energy from specific tissue chromophores, such as haemoglobin, lipids, melanin, water, etc

Optical Coherence Tomography is a high acquisition speed, non invasive, high resolution imaging modality, capable of producing cross-sectional and also volumetric high sensitivity images of biological tissues [1]. Optical Coherence Tomography instruments are capable to deliver axial resolutions down to 2 microns and depth penetration of a few millimeters in the biological tissue. Thus, during the past decade, OCT systems have been employed in various biomedical applications for *in-vivo*, and *ex-vivo* imaging. On the other hand, PAM is an emerging imaging technique able to provide both high resolution, high optical absorption contrast, high depth penetration and functional information such as oxygen saturation, blood flow and melanin concentration [2], vital information for cancer angiogenesis and monitoring cancer treatment response [3]. Here we report the capabilities of an OCT-PAM hybrid multimodal imaging instrument powered by supercontinuum sources.

## 2. Experimental setup

The dual imaging instrument is presented in Fig.1. In the PAM channel, a commercially available, supercontinuum laser (SuperK Compact, NKT Photonics) delivering pulses of 2 ns bandwidth. To make use of the VIS/NIR channel (400-800 nm) light is coupled into a filter (SuperK VARIA, NKT Photonics) which provide a flexible way to swiftly change the central wavelength and the spectral bandwidth. For the OCT channel, to ensure a better sensitivity of the images, a second supercontinuum laser (SuperK EXTREME EXR9, NKT Photonics), coupled into another tunable filter (SuperK Gauss, NKT Photonics) is employed. This uses the IR channel (1310 nm). The VIS and the IR beam are combined by a dichroic mirror and directed towards the galvanometric scanner head (GXY) (6220H, Cambridge Technology), then conveyed through a custom made objective to the sample. IR light back-scattered by the sample returns into the 50/50 directional coupler DC being directioned towards the spectrometer. The spectrometer consists of a custom made collimator, a transmission diffraction grating (Wasatch Photonics), a doublet pair as a focusing lens and a line camera (LC, Goodrich, model SU1014-LDHI) equipped with 1024 pixels with a 25 $\mu$m pitch. Camera is typically operated at 20 kHz but in principle can be operate at reading speeds of up to 47 kHz. Data is digitised using a camera link board (National Instruments, model IMAQ 1429).

The PA waves are detected by a PMN-PT needle transducer (NT) of 60 MHz bandwidth. The electrical signal hence produced is then amplified and digitized. The digitization is performed in sync with the pulse repetition rate

of the SuperK Compact which is around 20 kHz by using a fast digitizer (National Instruments, model PCI 5124). The display of B-scan OCT and PAM images is done in real-time. The generation of the PAM A-scans does not involve complex mathematical operations (only a Hilbert transform is applied to each acquired temporal signal) hence the real-time display of the images is straightforward. The OCT channel is powered by the Master-Slave method which allows for fast generation of B-scans without need of calibration and dispersion compensation procedures [4, 5].

## 3. Results and Discussion

The spectrometer is designed in such a way that a very wide spectral bandwidth of the optical source is employed. In addition, the spectrometer was designed to use the less noisy spectral range so a very high sensitivity was achieved, whilst mitigating the optical aberrations and obtaining a sufficiently small spot size on the linear camera. Thus, a spatially constant, isometric resolution of 6 $\mu$m is achieved in the OCT channel over an axial range of 1.5 mm (resolutions measured in air). The acquisition synchronization architecture makes possible for a B-scan of 500 A-scans to be obtained and displayed, in both channels a frame rate of 20 Hz. For both OCT and PAM, both volumetric, cross-sectional and *en-face* images can easily be produced. As an illustration, some images produced by our instrument are presented in Fig. 1(top). Further details and data about the capabilities of the instrument will be presented at the conference.

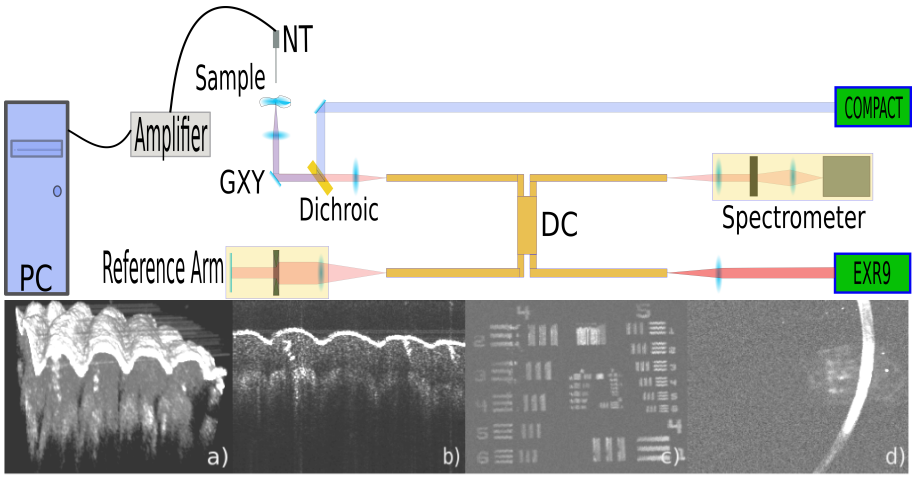


Fig. 1. Schematic of working principle of the OCT/PAM system and images obtained : (a) 3D OCT image of a fingertip. (b) OCT B-scan of the fingertip, (c) *En-face* PAM image of a USAF target, (d) PAM z-projection of a human hair.

## 4. Acknowledgments

G.N. acknowledges the University of Kent for the financial support. A.B. and A.P. acknowledge EPSRC (REBOT grant, EP/N019229/1). A.P. also acknowledges NIHR Biomed. Research Centre at Moorfields Eye Hospital NHS Foundation Trust, the UCL Institute of Ophthalmology, University College London, and the Royal Society Wolfson research merit award.

## References

1. Huang, D., Swanson, E. A., Lin, C. P., Schuman, J. S., Stinson, W. G., Chang, W., Hee, M. R., et al, Optical coherence tomography, Science 254, 1178–1181 (1991).
2. Song, W.; Wei, Q.; Liu, W.; Liu, T.; Yi, J.; Sheibani, N.; Fawzi, A.A.; Linsenmeier, R.A.; Jiao, S.; Zhang, H.F., "A combined method to quantify the retinal metabolic rate of oxygen using PA ophthalmoscopy and OCT." Sci. Rep. 2014, 4, 6525.
3. Weidner, N., Semple, J. P., Welch, W. R., and Folkman, J., Tumor angiogenesis and metastasis–correlation in invasive breast carcinoma, N. Engl. J. Med. 324(1), 18 (1991).
4. Bradu, A., Israelsen, N.M., Maria, M., Marques, M.J., Rivet, S., Feuchter, T., Bang, O., and Podoleanu, A., "Recovering distance information in spectral domain interferometry," Scientific Reports 8, 15445 (2018).
5. Bradu, A., Maria, M., and Podoleanu, A., "Demonstration of tolerance to dispersion of Master/Slave Interferometry," Opt. Express, 23(11) 14148-14161 (2015).

# Developments on using supercontinuum sources for high resolution multi-imaging instruments for biomedical applications

Gianni Nteroli[a], Magalie Bondu[b], Peter M. Moselund[b], Adrian Podoleanu[a] and Adrian Bradu[a]
[a]Applied Optics Group, School of Physical Sciences, University of Kent, Canterbury, UK
[b]NKT Photonics A/S, Blokken 84, Birkeroed, Denmark, 3460

## ABSTRACT

We report on further progress made on enhancing the capabilities of a multi-imaging modality instrument capable of producing high resolution images of biological tissues. At the core of the instrument is a supercontinuum (SC) source. Two SC sources commercialized by NKT Photonics were employed for our experiments: SuperK COMPACT and SuperK Extreme (EXR9). Using these two sources, we assembled an instrument capable to simultaneously provide in real-time cross-section high-resolution Optical Coherence Tomography (OCT) and Photo-acoustic (PA) images in various spectral ranges. Currently, the OCT channel is operating in the IR range around 1300 nm to allow better penetration into the tissue using either the COMPACT or the EXR9. The measured optical power on the sample is in both cases above 9.5 mW. An *in-house* spectrometer equipped with a sensitive InGaAs camera capable of operating at 47 kHz and sampling data over a spectral range from 1205 to 1395 nm was developed. A constant axial resolution provided by the instrument in the OCT channel over a range of 1.5 mm was experimentally measured (4.96 μm), matching the theoretical prediction. The spectral range 500-800 nm was used for PA channel. The COMPACT, used in the PA channel, can select the central wavelength and the spectral bandwidth of operations. Typically, the optical energy per pulse on the sample is superior to 60 nJ when a bandwidth superior to 50 nm is employed. This make the instrument usable for PA imaging of tissues.

**Keywords:** optical coherence tomography, photo-acoustics, high-resolution, multi-spectral imaging, multi-imaging.

## 1. INTRODUCTION

Optical Coherence Tomography is a high-resolution imaging technique able to measure backscattered light wave-fronts generated from a low-coherence light source illuminating the sample [1]. The axial resolution of OCT ranges typically from one micron to tens of microns and an axial range in tissue limited to only 1-1.5 mm, depending on various parameters such the central wavelength, the spectral bandwidth, optical power on the sample, etc. So far, OCT systems have been used to image a variety of tissues *in-vivo* or *ex-vivo* that can be accessed either directly or via endoscopes or catheters, including the eye. To further extend the limited axial resolution provided by the OCT instruments, PA imaging was proposed as an emerging biomedical imaging technique capable of providing optical absorption contrast at an acceptable axial resolution [2]. An ultrasonic transducer is employed to measure the ultrasonic waves generated through the photoacoustic effect, which generates a transient temperature rise due to the short pulse light absorption in the biological tissue. The produced ultrasonic waves are used to reconstruct the light absorption distribution which directly can be related for example to the vasculature of tumors [3]. Then, using multispectral PA techniques, the PA signals can be used to look at cell oxygenation, so indicators of tumor metabolism and therapeutic response become available.

Multimodal imaging modalities show great promise, providing complementary information and diverse contrast of biological tissues. In all the previous reports, each imaging modality benefited from its own optical source. This indicates a high cost of the instrument as well as restrictions in the operation of the instrument to spectral ranges determined by the optical source employed. In a recent report, we demonstrated that by using a single SC (SuperK COMPACT) decent quality images in terms of signal-to-noise ratio can be obtained in both channels, OCT and PA [4]. Here, we report further development on this research activity, especially on enhancing the axial resolution and the sensitivity in the OCT channel by designing a new spectrometer and on taking different approach on illuminating the sample to enhance the energy per pulse and thus the signal-to-noise ratio in the PA channel.

## 2. EXPERIMENTAL SET-UP

**Set-up 1 (a single supercontinuum source for both imaging modalities).** The multi-imaging modality experimental setup is depicted on the right side of Fig. 1. Light from the SuperK COMPACT is conveyed towards the dual band filter (Varia, NKT Photonics A/S) which splits the spectrum into two spectral bands: a short wavelength, covering all the VIS

range, ranging between 450 and 850 nm, and a longer wavelength band in the IR, around 1300 nm. The short wavelength band is used for PA. At a later stage, this band will also be used to deliver light for a VIS OCT instrument. Currently only the IR OCT channel is operational. In the IR OCT channel light from Varia is split by the 50/50 broadband directional fiber coupler towards a reference arm and a sample arm. Light from both outputs of the filter are multiplexed using a dichroic filter D and conveyed towards the sample to be investigated via a galvo-scanner head GXY and a microscope objective (Mitutoyo MPlan NIR 10). To maximize the power on the sample for PA, we did not convey light via optical fibers. A transducer needle TN based on a PMN-PT crystal is immersed into the aqueous close to the sample. The TN converts the US wave into an electric signal which is amplified before digitization. The digitization is performed in synchronism with the pulse repetition frequency of the SC which is around 20 kHz.

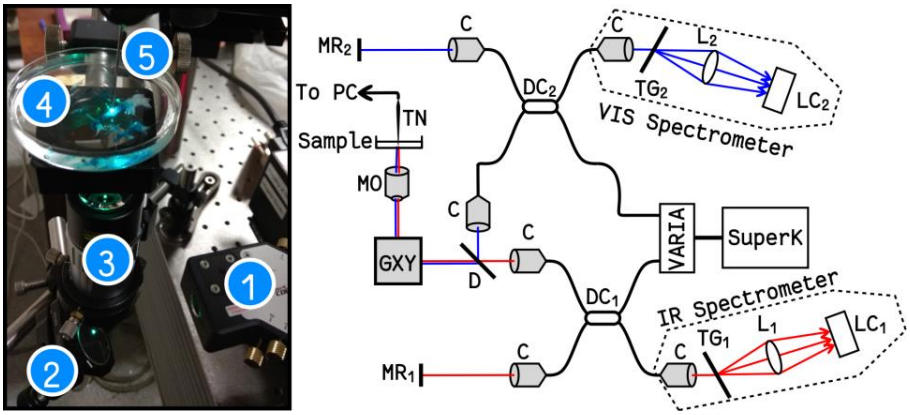


Figure 1: Schematic diagram of the instrument (left) and a picture showing the arrangements in the sample arm (right). C: parabolic collimators; $L_{1,2}$: achromatic lenses; $LC_{1,2}$: linear cameras; $TG_{1,2}$: transmission diffraction gratings; $DC_{1,2}$: directional couples; MO: microscope objective; GXY: orthogonal galvo-scanners; $MR_{1,2}$: flat mirrors; TN: needle transducer. In the left image, 1: Varia's VIS output; 2: flat mirror; 3: microscope objective; 4: sample; 5: transducer.

IR light backscattered by the sample interferes with light originating from the reference arm (back-reflected by MR1), at $DC_1$. To detect the channel spectra, the IR Spectrometer whose sketch is presented in Fig. 1 was devised. It incorporates a transmission diffraction grating $TG_1$ (Wasatch Photonics, model HP 1145 l/mm blazed @ 1310 nm) an achromatic doublet pair lens $L_1$ (Thorlabs, AC508-150-C). A linear camera (LC1, Goodrich, model SU1014-LDHI.7RT-0500/L) equipped with 1024 pixels is used to read the channeled spectra synchronous with the repetition rate of SuperK. At a later stage, a VIS spectrometer will be ensembled. For this one we are intending to use a linear camera $LC_2$ (Basler, spL4096-140km), whose reading will also be synchronized with the SC source.

**Set-up 2 (two supercontinuum sources employed).** The schematic diagram of this instrument is depicted in Fig. 2. The PA channel still uses the SuperK Compact, however the OCT channel uses the EXR9. The spectrometer used was identical to the one presented in Fig. 1. Now, the synchronization between the camera reading and the optical pulses generated by EXR9 is not possible anymore. This allows in principle to take advantage of the full speed of the camera employed (47 kHz) to produce B-scan OCT images faster by at least a factor of 2 than the PA B-scan images.

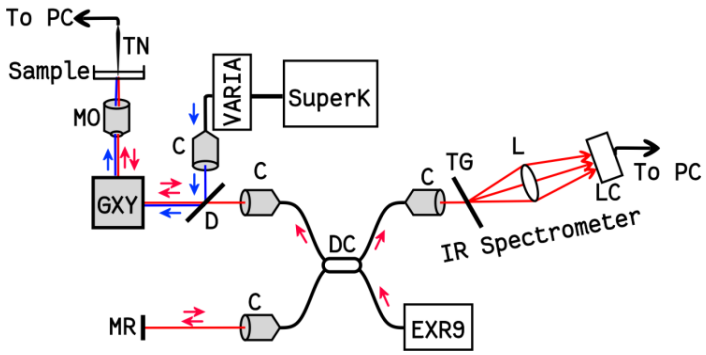


Figure 2: Schematic diagram of the instrument 2 employing two SCs). C: parabolic collimators; $L_{1,2}$: achromatic lenses; LC: linear cameras; TG: transmission diffraction gratings; DC: directional couples; MO: microscope objective; GXY: orthogonal galvo-scanners; MR: flat mirrors; TN: needle transducer.

## 3. RESULTS AND DISCUSSION

The IR spectrometer was designed in such a way that a spectral bandwidth as wide as possible is accommodated by the 1024 pixels of the linear camera. As illustrated in Fig. 3(a), a quite good contrast was achieved over all the pixels the camera is equipped with (range of wavelengths from 1205 nm to 1395 nm (190 nm bandwidth) around a central wavelength of 1300 nm). Given that the shape of the spectrum as read by the camera is approximately Gaussian, with a full width at half maximum of around 150 nm, we can expect a theoretical axial resolution as good as 4.96 µm.

To correct for non-linearities, compensate for the dispersion left uncompensated in the interferometer which can be significant when using wide spectral bandwidths, and produce the sensitivity drop-off, we employed the Master-Slave technique [5-7]. By using it, we matched the theoretical values of the axial resolution over a quite large axial range (1.5 mm) as illustrated in Fig. 2(b). When spectra are subject to apodization, the axial resolution deteriorates to around 6.1 µm. The same axial resolutions were found for both supercontinuum sources, however EXR9 provides a sensitivity of at least 15 dB superior to that obtained with the COMPACT, for the same optical power on the sample, and the same reading speed of the camera (20 kHz).

The axial reflectivity profiles at various axial positions depicted in Fig. 3(b) were produced by windowing the theoretically inferred spectra using a Hamming filter. The apparent axial shift of maximum of sensitivity is an artifact due to high pass filtering of the channeled spectra employed to remove noisy low frequency components. Over the axial range of 1.5 mm, the sensitivity drops by around 8 dB. The sensitivity drop-off depicted in Fig. 3 was obtained using the COMPACT, however a similar one was achieved with the EXR9.

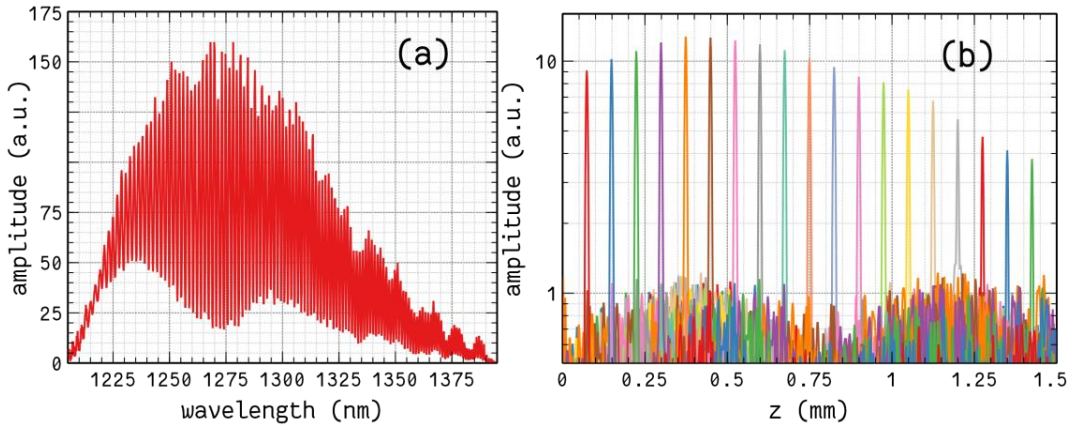


Figure 3: (a) Example of experimental channeled spectrum (z=0.5 mm) by $LC_1$ showing modulation over 190 nm. (b) Sensitivity roll-off of the OCT signal over 1.5 mm. Over this range the axial resolution exhibits quite low fluctuations. Data presented in this figure were generated using the COMPACT supercontinuum optical source. Similar plots could be generated using the EXR9, however the sensitivity of the instrument with EXR9 is better than that obtained when using the COMPACT by at least 15 dB for a given optical power on the sample.

To characterize the PA channel, we used a black duct tape immersed in water. We experimentally noticed that, for a given absorption of this sample, the response of the transducer TN scales linearly with the optical power on the sample. As illustrated in Fig. 4(d) the power on the sample increases with wavelength, however the amplitude of the PA signals decreases with wavelength for this particular sample. By doubling the spectral bandwidth, the power on the sample increases by a factor of 2. There is also a factor of 2 between the PA signals collected using the two spectral ranges.

To produce strong PA signals in biological tissues, the sources employed should provide an energy per pulse of over 50 nJ. The high repetition rate of the SC employed here (20 kHz), higher than those of the Q-switched lasers used for PA applications (typically tens of Hz) enables a greater number of pulses to be acquired and the signal to be averaged over a certain time. This offers the prospect of increasing the signal-to-noise ratio of the detected PA signal. Also, as we have the flexibility of manipulating the wavelength of the SC laser, we can adjust its operation to avoid undesirable absorption by various chromophores (as for example water absorption). For the experimental data presented in Fig. 4, at 500 nm, and a bandwidth of 50 nm, the average power measured on the sample was 1.2 mW, corresponding to an energy per pulse of 60 nJ which is enough for imaging biological tissues.

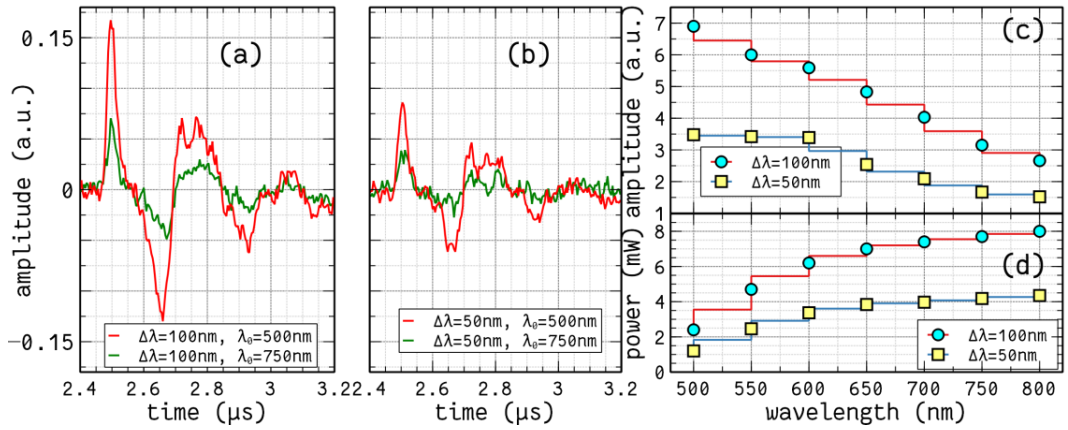


Figure 4: (a) and (b): typical PA signals for different wavelengths and bandwidths. (c) PA signals for several central wavelengths, computed by integrating signals as those depicted in (a) and (b). (d) Average power on the sample.

Using the instrument described above, OCT and PA images of various samples were produced. In Fig. 5(a-c), 3D OCT reconstructions of various samples are presented (thumb, tooth, finger). The measured axial resolution in these images is around 5 µm. Each volume has a size of 500×500×400 pixels$^3$. Each B-scan used for 3D-reconstruction was produced and displayed in real-time, every 50 ms. The whole 3D data set was acquired in 2.5 s and a volumetric image immediately displayed. The images were obtained using EXR9.

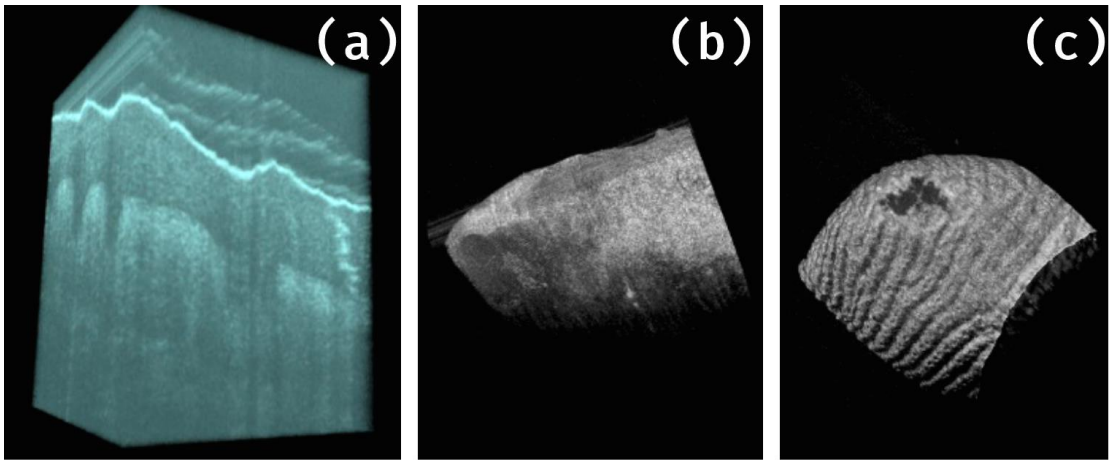


Figure 5: Examples of OCT volumetric images obtained using the EXR9 SC (a) human thumb; (b) human tooth; (c) human finger. All B-scan images were displayed in real-time. Some artifacts due to involuntary movements are visible in each of the 3 images.

In Fig. 6(a) an *en-face* PA image of an USAF target is presented. The smallest elements which c an be separated on this target belong to group 6, element 2. This corresponds to a lateral resolution in the PA channel of 6 µm. Due to the illumination/signal collection geometry, the VIS photons from the COMPACT can eventually hit the transducer itself, so it is very likely that the transducer itself appears in the *en-face* images. This is quite clearly observed in both, Fig. 6(a) and 6(b). To produce the images of the USAF target and human hair, a spectral range of 50 nm around the central wavelength 550 nm was employed.

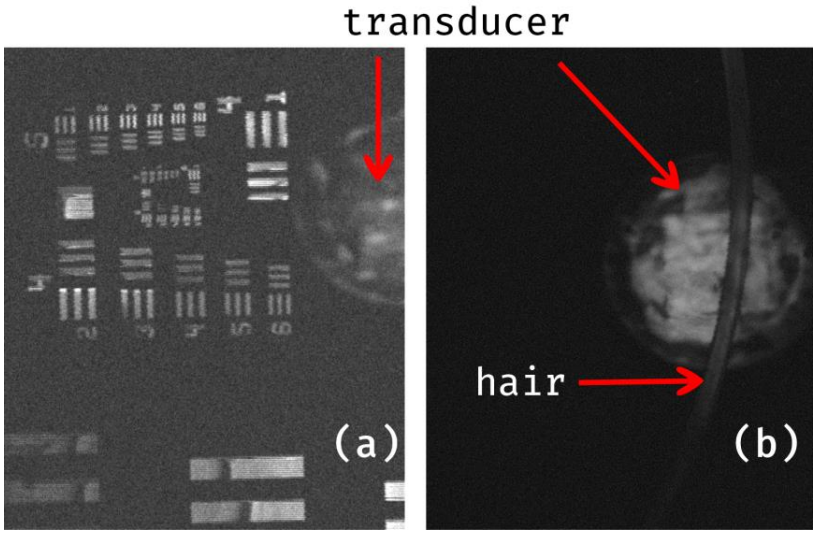


Figure 6: Illustration of the capability of the instrument to produce high resolution PA images. (a) *en-face* PA image of a positive USAF target showing that a lateral resolution as good as 6 µm can be achieved; (b) *en-face* view of the human hair. Due to the illumination geometry the transducer itself can produce ultrasonic waves, hence it appears in the images.

## 4. ACKNOWLEDGMENTS

G.N. acknowledges the University of Kent for the financial support. A.B. and A.P. acknowledge EPSRC (REBOT grant, EP/N019229/1). A.P. also acknowledges NIHR Biomed. Research Centre at Moorfields Eye Hospital NHS Foundation Trust, the UCL Institute of Ophthalmology, University College London, and the Royal Society Wolfson research merit award.

## REFERENCES

[1] Huang, D., Swanson, E. A., Lin, C. P., Schuman, J. S., Stinson, W. G., Chang, W., Hee, M. R., Flotte, T., Gregory, K., Puliafito, C. A., and Fujimoto, J. G., "Optical coherence tomography," Science 254, 1178–1181 (1991).

[2] Andreev, V. G., Karabutov, A. A., Solomatin, S. V., Savateeva, E. V., Aleinikov, Zhulina, et al., "Optoacoustic tomography of breast cancer with arc-array transducer," Proc. SPIE 3916, 36–47 (2000).

[3] Weidner, N., Semple, J. P., Welch, W. R., and Folkman, J., "Tumor angiogenesis and metastasis--correlation in invasive breast carcinoma," N. Engl. J. Med. 324(1), 1–8 (1991).

[4] Bondu, M., Marques, M., Moselund, P. Lall, G., Bradu, A., and A. Podoleanu, "Multispectral photoacoustic microscopy and OCT using a single supercontinuum source," Photoacoustics 9, 21-30 (2018).

[5] Bradu, A. Israelsen, N., Maria, M., Marques, M., Rivet, S., Feuchter, T., Bang, O. and Podoleanu, A., "Recovering distance information in spectral domain interferometry," Scientific Reports 8, 15445 (2018).

[6] Rivet, S., Maria, M., Bradu, A., Feuchter, T., Leick, L., and Podoleanu, A., "Complex master slave interferometry," Opt. Express 24, 2885-2904 (2016).

# PRECISION ACOUSTICS LTD

Hampton Farm Business Park
Dorchester, DT2 8QH
UNITED KINGDOM

## TRANSDUCER TEST CERTIFICATE

This certificate provides traceability of measurement to recognised national standards and to units of measurement realised at the National Physical Laboratory or other recognised national standards laboratories. Precision Acoustics Ltd is certified to the ISO 9001 standard.

**Device Identification**

| | |
|---|---|
| Transducer S/N | PA1199 |
| Transducer Type | PVDF - Focussed |
| Transducer Diameter | 6.0 mm |
| Nominal Centre Frequency | 50.00 MHz |

**Calibration Conditions**

| | |
|---|---|
| Calibration date | 14/06/2019 |
| Water temperature | 22.0 °C |
| Water treatment | De-gassed, De-ionised, filtered |
| Acoustic path length | 10 mm |
| Source signal type | Impulse |
| Pulser Settings | Energy 2, Damping 2, PRF 500 Hz, LP filter Full BW, HP filter out |
| Peak to peak source signal amplitude | 120 V |
| Electrical impedance | 50 Ohms |
| Cable type, length | RG58, 1.5 m |
| Measurement type | Hydrophone measurement |

**Test Equipment used**

| | |
|---|---|
| Signal Generator | Olympus 5073PR |
| Signal Amplifier | N/A |
| DAQ Device / Analyser | Agilent Technologies DSO-X 3024A |

| Calibrated by; | Checked by; |
|---|---|
| 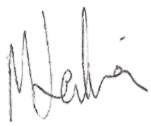 |  |
| ---------- | ---------- |
| Megan Jenkinson | Thomas Kelley |

PRECISION ACOUSTICS

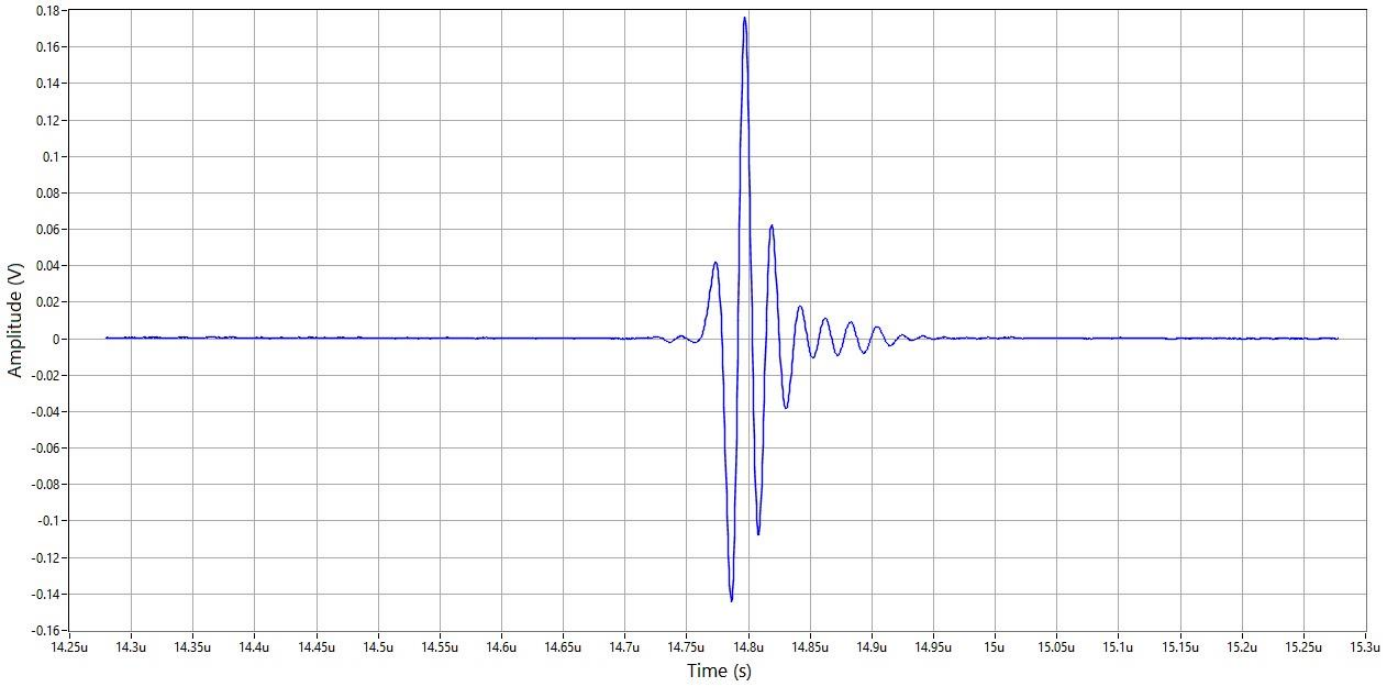


**Impulse (time domain) response for PA1199**

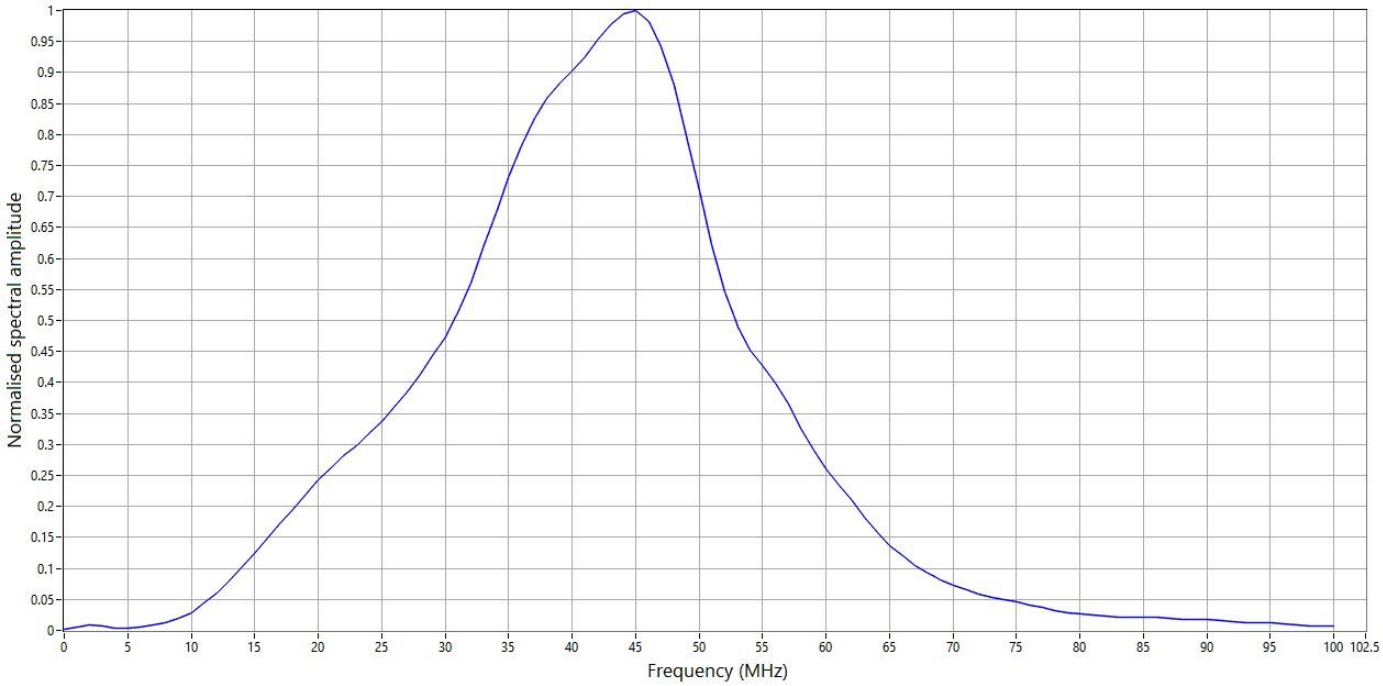


**Frequency spectrum of time domain response for PA1199**

| **Peak Frequency (MHz): 45.02** | **-3.0 dB** | **-6.0 dB** | **-12.0 dB** | **-20.0 dB** |
|---|---|---|---|---|
| **Lower limit (MHz)** | 34.61 | 30.70 | 20.37 | 13.91 |
| **Centre frequency (MHz)** | 42.33 | 41.77 | 40.39 | 40.65 |
| **Upper limit (MHz)** | 50.05 | 52.84 | 60.42 | 67.39 |
| **Bandwidth (MHz)** | 15.44 | 22.15 | 40.05 | 53.48 |
| **Bandwidth (%)** | 36.48 | 53.02 | 99.15 | 131.55 |

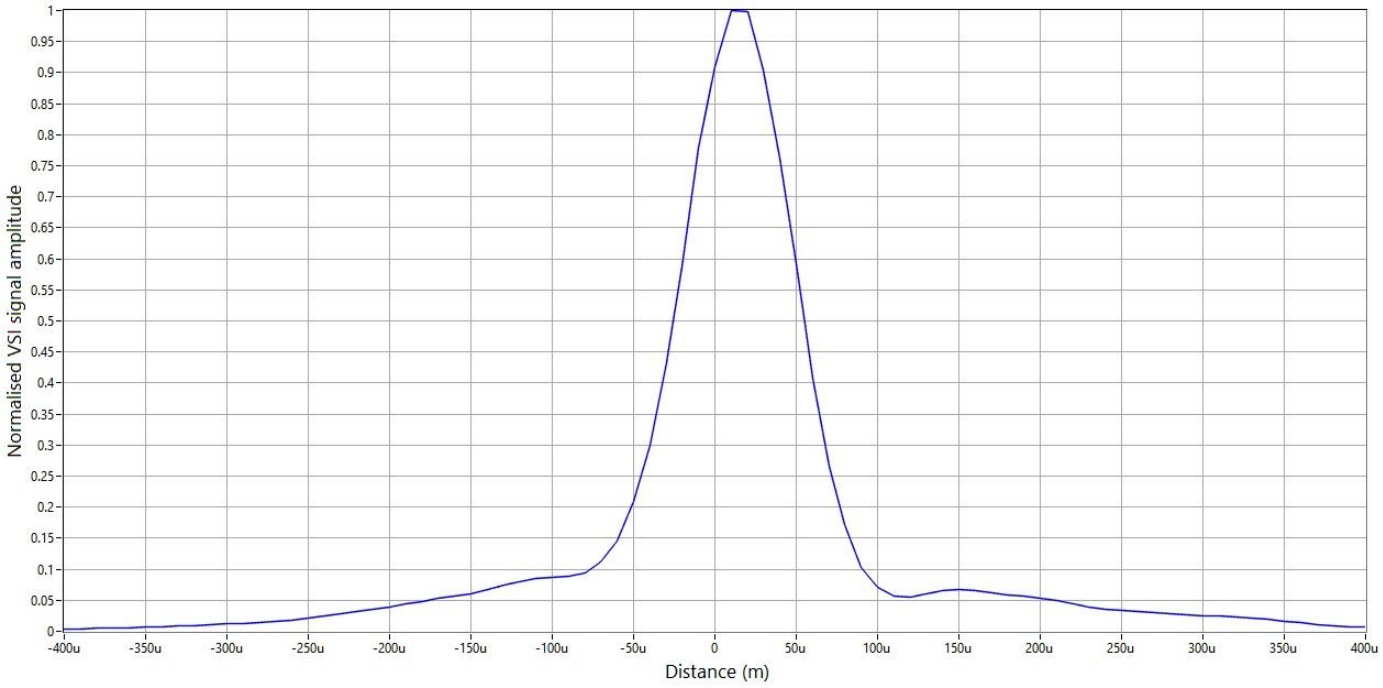


**Transverse X Profile for PA1199**

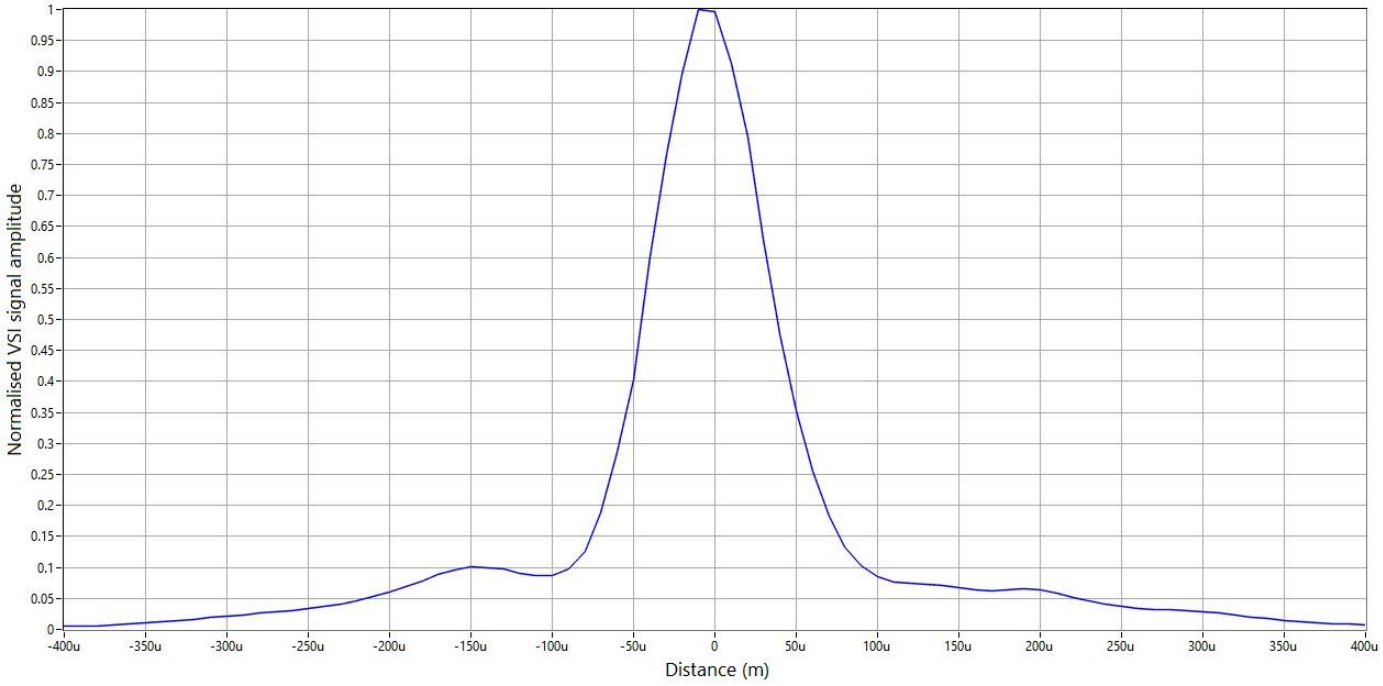


**Transverse Y Profile for PA1199**

| | **-3.0 dB** | **-6.0 dB** | **-12.0 dB** | **-20.0 dB** |
|---|---|---|---|---|
| **X-profile beamwidth (mm)** | 0.08 | 0.12 | 0.25 | 0.69 |
| **Y-profile beamwidth (mm)** | 0.08 | 0.12 | 0.40 | 0.72 |

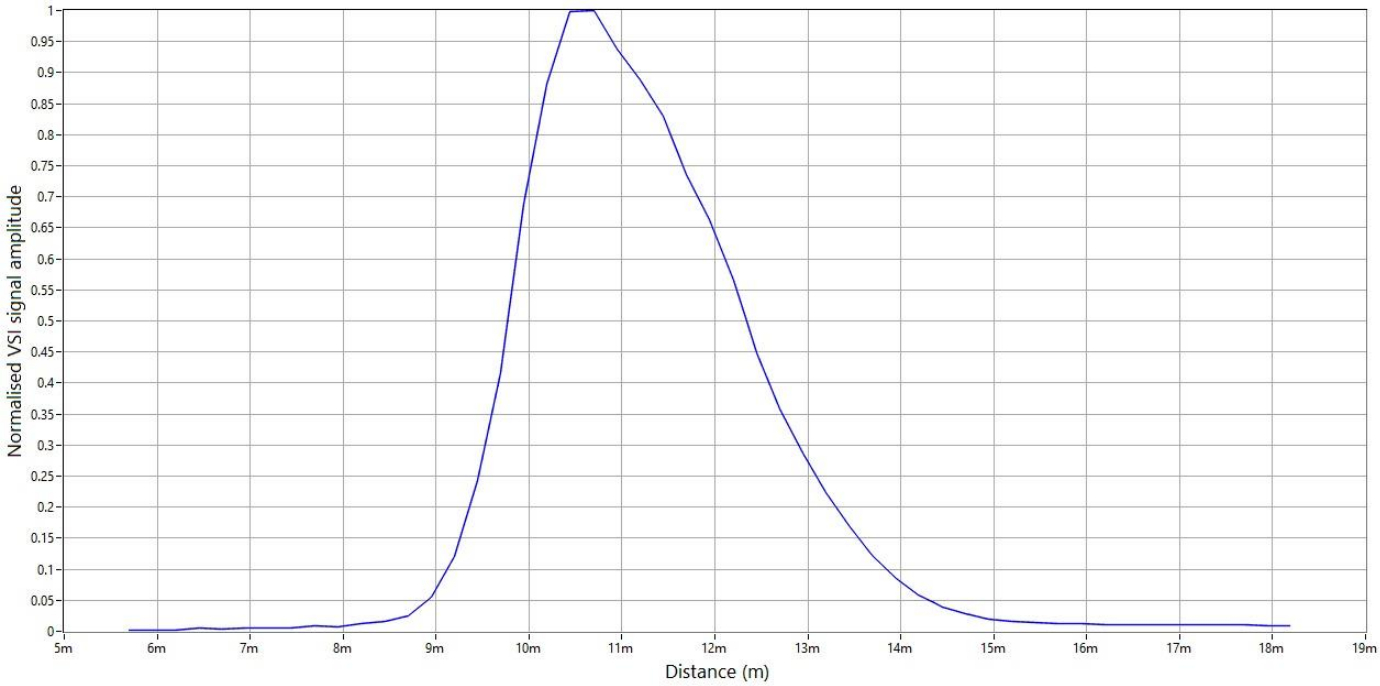


**Axial Z Profile for PA1199**

| **Focal Peak (mm): 10.70** | **-3.0 dB** | **-6.0 dB** | **-12.0 dB** | **-20.0 dB** |
|---|---|---|---|---|
| **Axial profile beamwidth (mm)** | 2.57 | 3.64 | 5.18 | 9.56 |

# 0.4 mm × 0.4 mm aperture size PMN-PT needle transducer performance

06/23/2016
Ruimin Chen

Length of the Cable
(100cm – 50 Ohms)

**Pulse Echo Test Conditions**
**Panametrics 5900PR**

| | |
|---|---|
| Attenuation | 26.0 dB |
| Gain | 26.0 dB |
| PRF | 200 Hz |
| Energy | 1 μJ |
| Damping | 50 ohm |
| HP filt | 10 MHz |
| LP filt | 100 MHz |

| sample# | Receive $V_{pp}$ [mV] | $F_{center}$[MHz] | -6 dB BW [%] | Natural Focus (mm) | F1 (MHz) | F2 (MHz) |
|---|---|---|---|---|---|---|
| 2 | 691 | 40.3 | 89.2 | 2.10 | 22.3 | 58.2 |

**PMN-PT transducer Pulse-Echo, 100 cm 50 Ohms cable, Panametrics 5900, 1 μJ energy, 26 dB attenuation, 26 dB gain, aperture size 0.4 mm × 0.4 mm, and natural focus 2.10 mm**

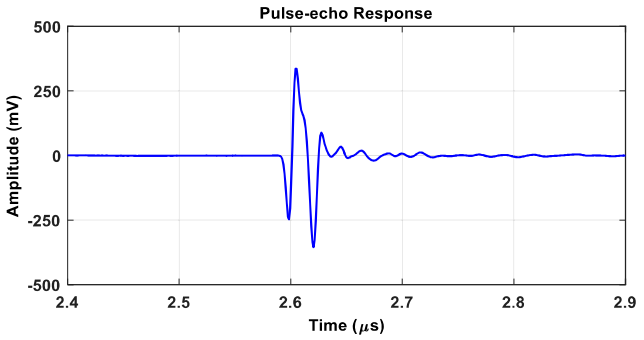


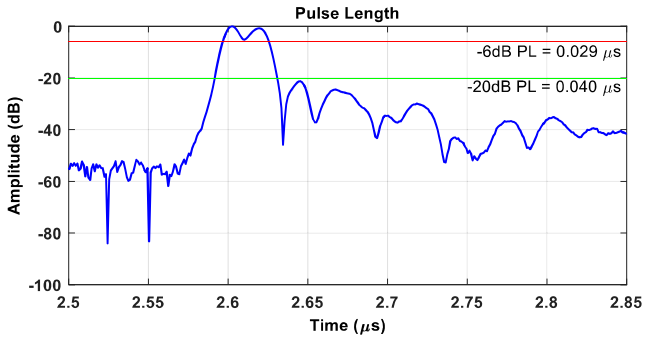


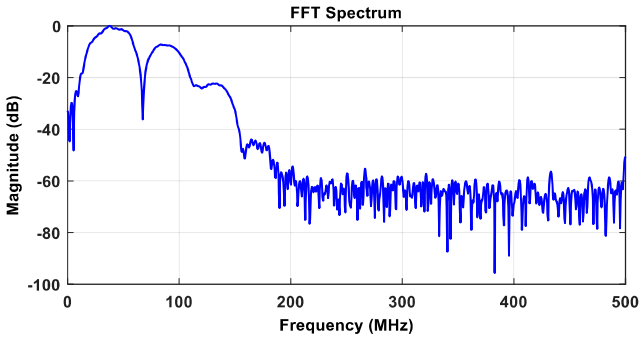


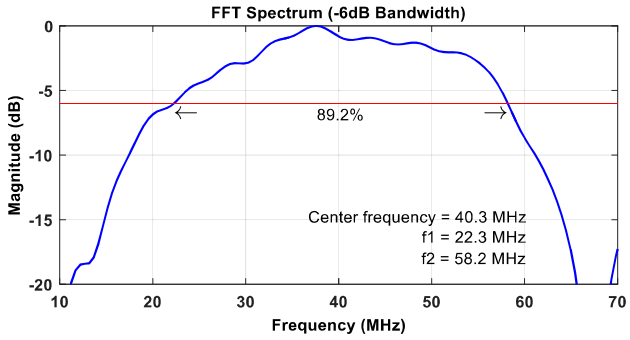

# SuperK COMPACT

## Compact single mode white light laser


## BROADBAND AND ULTRA-BRIGHT

### Ideal for SLED and ASE replacement

The SuperK COMPACT is a cost-efficient turn-key supercontinuum white light source with a wide output spectrum covering the entire 450-2400 nm region - from visible to infrared.

Its single mode output has a brightness many orders of magnitude larger than other white light sources, such as incandescent lamps - and it has far more bandwidth than ASE sources and SLEDs.

### Applications

- Spectroscopy
- CWDM/DWDM component test
- Optical Coherence Tomography
- Fiber and grating characterization
- Superluminescent diode (SLED) source alternative
- Amplified spontaneous emission (ASE) source alternative

# SUPERK COMPACT

## Covers the spectrum from visible to infrared

The SuperK COMPACT is a cost-efficient turn-key supercontinuum white light source with a wide output spectrum covering the entire 450-2400 nm region.

## Broad output and ultra-bright

Its single mode output has a brightness many orders of magnitude larger than other white light sources, such as incandescent lamps - and it has far more bandwidth than ASE sources and SLEDs.

## External trigger and low jitter

The SuperK COMPACT can be triggered externally and synced - with low jitter - up to 20 kHz. The trigger signal can be provided to a standard coax input or to the industrial trigger input which is galvanically isolated.

## Graphical user interface and lots of accessories

The SuperK COMPACT is easily operated via our CONTROL software. It is compatible with all SuperK filters and accessories, such as the SuperK SPLIT and SuperK CONNECT fiber delivery accessory range, for easy delivery and filtering/splitting of the light.

## Thousands of hours maintenance-free use

The all-fiber architecture ensures a stable 24/7 operation and a maintenance-free lifetime of thousands of hours backed by our 2-year warranty.

## Very versatile

The SuperK COMPACT can be found in laboratories around the world where it is the daily driver for many users within applications like component characterization, test & measurement, spectroscopy and OCT or simply as a general purpose laboratory white light source.

## Features

- Cost-efficient broadband source
- High brightness and long lifetime
- Visible to infrared in one module
- Input pulse trigger
- Variable repetition rate
- Flexible accessory range
- Single mode fiber termination
- Alternative to ASE sources, lamps, and SLEDs
- Simple and intuitive user interface via NKT Photonics CONTROL
- Plug and Play with all SuperK accessories
- Robust and compact industrial design
- Maintenance-free 24/7 operation

# SPECIFICATIONS

## Optical

| | |
|---|---|
| Repetition rate [Hz] | Variable 1 Hz to min. 20 kHz |
| Spectral coverage [nm] | 450-2400 |
| Total power [mW] [2)] | > 110 |
| Total visible power (450-850 nm) [mW] [2)] | > 20 |
| Total power stability [%] [1)] | < ± 1.0 |
| Output pulse width [ns] | < 2 |
| Pulse-pulse jitter (standard dev.) [µs] [2)] | < 2 |
| Polarization | Unpolarized |
| Beam quality, $TEM_{00}$ | $M^2$ < 1.1 |
| Beam diameter, collimated [mm] | 1 @ 530 nm<br>2 @ 1100 nm<br>3 @ 2000 nm |

1) Contact us for ± 0.5 %.
2) Repetition rate dependent.

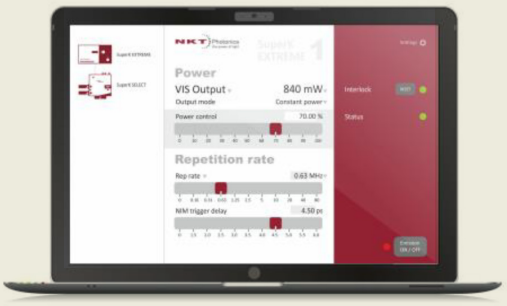


### Software — NKT Photonics CONTROL

Like other NKT Photonics lasers, the SuperK COMPACT can be controlled by our intuitive CONTROL software that gives easy access to all laser functions.

The software automatically detects all units attached to the computer. You can control the source and any filtering accessories from CONTROL. It is easy to use and supports touch input as well as traditional mouse+keybord control.

## Typical output spectrum

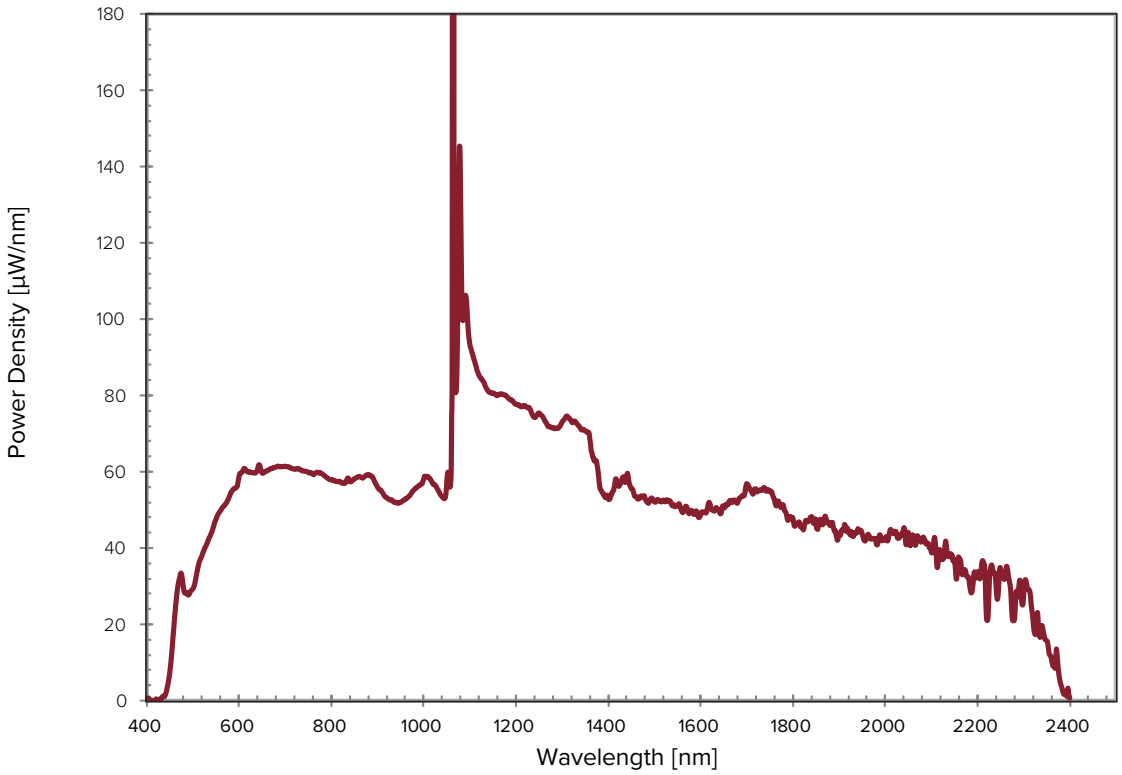

# SPECIFICATIONS

## Mechanical/Electrical/Environmental

| | |
|---|---|
| Laser output | Gaussian, single mode |
| Output termination [1] | Collimator, FC/PC or FC/APC |
| Computer interface | USB |
| Power supply requirements [VAC, Hz] | 100-240 V, 50-60 Hz |
| Power consumption [W] [2] | Up to 40 |
| Pulse signal output | Analog and digital |
| Trigger input | Standard industrial, galvanically isolated |
| Door interlock connector | 2-pin LEMO 0B |
| External bus interface | 15-pin D-sub |
| Operation temperature [°C] | 18 – 30 |
| Storage temperature (non-condensing) [°C] | 5 – 50 |
| Humidity [% RH] | 20 – 80 |
| System cooling | Air |
| Dimensions (WxHxL) [mm³] | 220.5 x 93 x 367 |
| Weight [kg] | 3.8 |

1) Contact us for standard single mode output fiber.

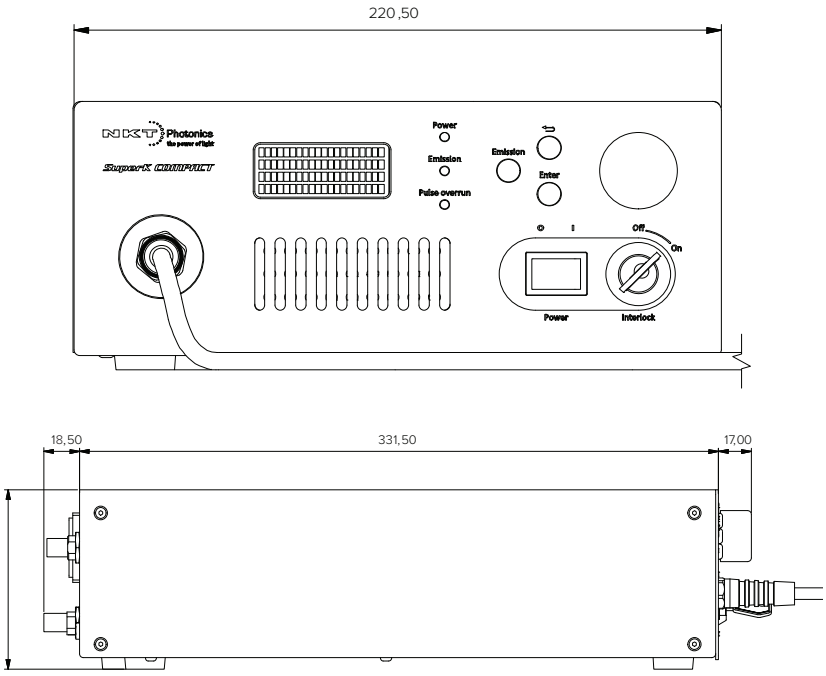


## Support and warranty

**SuperK warranty**
All SuperK COMPACT products comes with industry leading reliability and are backed by our standard 2 year warranty.

**Lifetime and service**
Before shipping, all our SuperK lasers undergo an extensive burn-in to ensure performance and conformity to specifications.

Our systems boast over 10,000 hours of continuous lifetime and underlines the high reliability of our NKT Photonics Crystal Fibre technology.

**Maintenance-free in the entire lifetime**
A SuperK laser is completely maintenance-free in the entire lifetime.

Should your laser be damaged, the modular platform ensures fast turnaround on service and repairs. Typically, it takes four weeks or less to get your laser back.

All NKT Photonics products are produced under our quality management system certified i accordance with the ISO 9001:2015 standard.

FORCE Certification
Systemcertificering
DS/EN ISO 9001 - Kvalitet

# SuperK EXTREME

## High Power Supercontinuum fiber laser series

- 400-2400nm single mode spectrum
- Unsurpassed reliability and lifetime
- On-the-fly variable repetition rate
- Plug'n'Play filter accessories
- Flexible trigger and power locking functions
- Operation at the press of a button
- Instant on with light on-demand
- NIM trigger output approved for FLIM


SuperK supercontinuum sources delivers a wide spectral output covering hundreds of nanometers while keeping the high brightness and mode quality known from single line lasers. Our lasers are fully fiber monolithic ensuring excellent reliability — completely alignment and maintenance free.

The SuperK EXTREME series is based on NKT Photonics world renowned Crystal Fibre technology that has reliably delivered supercontinuum to all fields for over 10 years. The SuperK platform is fully modular, allowing easy operation and service where accessory modules can be added without configuration—all plug&play. Operation is simple and functions can be changed on-the-fly without powering down the system. The SuperK EXTREME series provides high power and exceptional lifetime together with the highest of safety standards.

The SuperKontrol graphic user interface ensures that users from any discipline finds the SuperK EXTREME an easy tool to use.

## Applications

- Microscopy
- Fluorescence Lifetime Imaging
- Optical Coherence Tomography
- Spectroscopy
- White light interferometry
- Plasmonics & meta materials

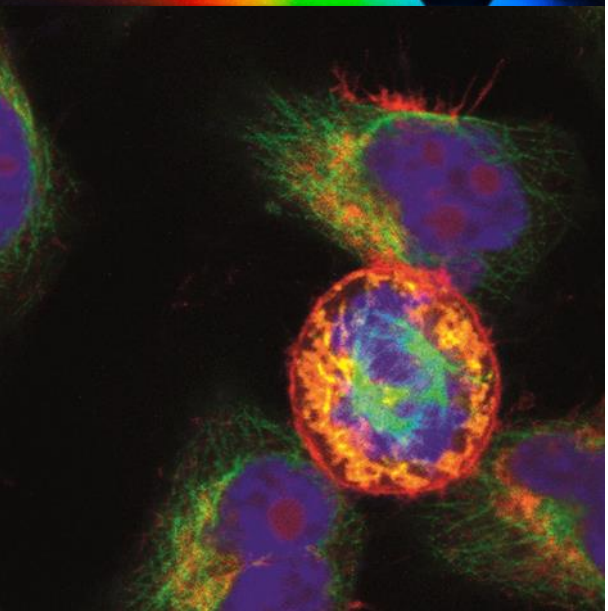

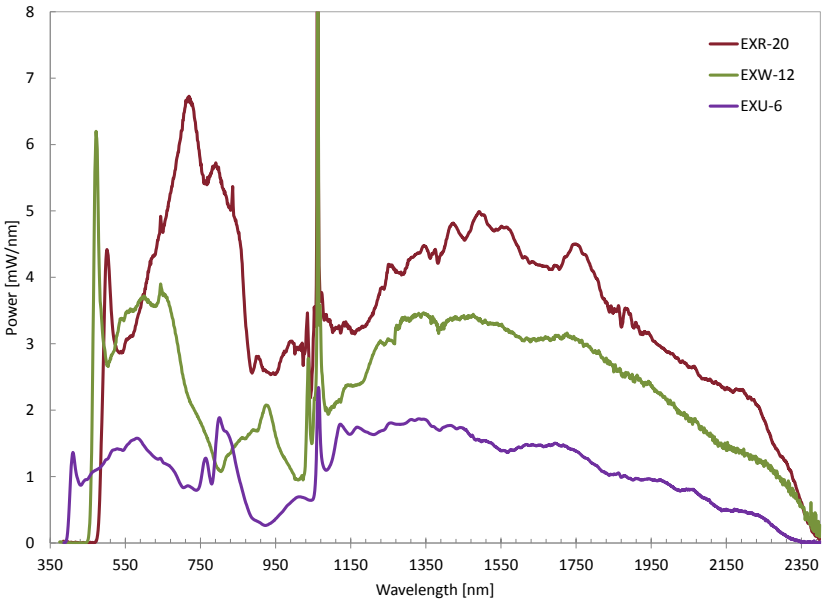


Violet (EXU), Blue (EXB), White (EXW) and Red (EXR) systems provide users with a comprehensive coverage of the supercontinuum spectrum in the 400-2400 nm range.

| EXU series | EXW series | EXR series | Visible power* (350-850nm) |
|---|---|---|---|
| | | EXR-4 | 400 mW |
| EXU-6 | EXW-6 | - | 600 mW |
| | EXW-12 | - | 1200 mW |
| | - | EXR-15 | 1500 mW |
| | | EXR-20 | 2000 mW |
| | | Custom | 3500 mW |

* SuperK EXTREME is the industry's most efficient supercontinuum lasers with the highest visible to total power ratio. High efficiency means better reliability and less unwanted recidual pump power at the output. For a thorough description of optical power measurement, see our application note on www.nktphotonics.com/superk_extreme_support.

## Support and Warranty

### SuperK CARE support/warranty

All SuperK EXTREME products comes with industry leading reliability and are backed by our standard 2 year warranty. Should you need the extra security of an extended warranty and remote diagnostics support this is available in our SuperK CARE support and warranty extension package. Please contact your sales representative for more information.

### Lifetime and Service

Before shipping, all our SuperK lasers undergo a 96 hours burn-in to ensure performance and conformity to specifications. Systems exhibiting over 10,000 hours of continuous lifetime underlines the high reliability of NKT Photonics Crystal Fibre technology.

A SuperK laser is completely maintenance-free in the entire lifetime, and should your laser be damaged, the modular platform ensures fast turnaround on service and repairs. Typically, four weeks or less after a repair is ordered.

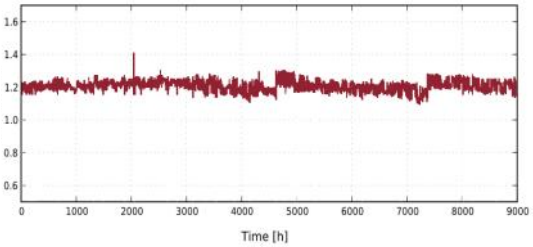


## Spectral coverage

The SuperK EXTREME is available in three different variants:

- Violet EXU series
- White EXW series
- Red EXR series

Choose the EXU series if you need short blue/violet wavelengths. The EXW series is a great all-around source providing good coverage of the visible spectrum while offering higher power than the blue EXU series. The red EXR series are for those who need serious power or applications where the shortest wavelengths are not important. The EXR series is our most popular model for high resolution OCT.

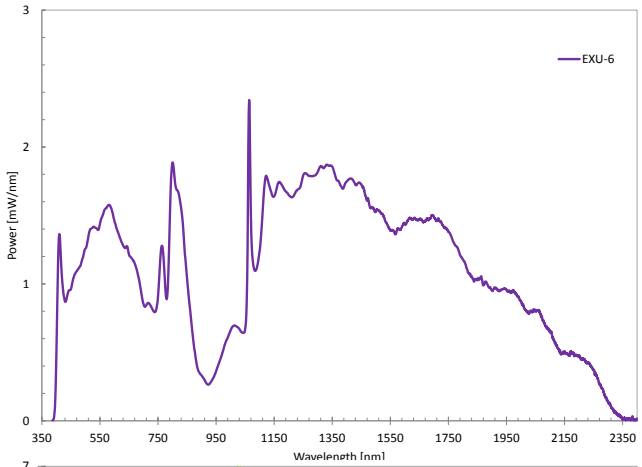



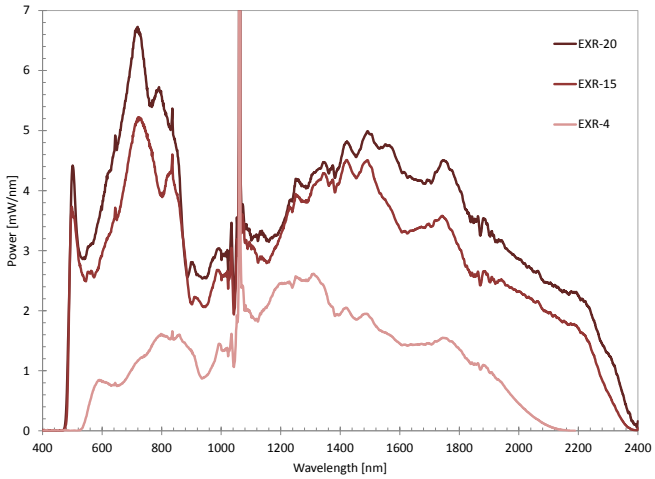

## Options

- Violet (EXU), Blue (EXB), White (EXW) or Red (EXR) spectrum
- 100 mW—2 W visible power
- Master repetition rate 40 MHz or 78 MHz
- On-the-fly variable repetition rate (pulse picker)
- Software Development Kit (SDK)
- 12 and 24 months warranty extension packages
- Power Lock external power locking functionality

| | |
|---|---|
| Typical power stability* | < ± 0.5 % |
| Modulation input voltage | 0 – 10 V |
| Current mode | |
| Modulation bandwidth, 3dB | 70 Hz (typ) |
| Rise- and falltime | <5 ms (typ) |
| Power mode | |
| Modulation bandwidth, 3dB | 40 Hz (typ) |
| Rise- and falltime | <10 ms (typ) |
| Feedback input voltage | 0 – 4 V |
| Feedback bandwidth | <100 Hz |
| Feedback sample rate | 200 Hz |

*Depending on setup and wavelength range

## Software

### NKT Photonics CONTROL

Like other NKT Photonics lasers, the SuperK EXTREME can be controlled by our unified CONTROL software that gives easy access to all the functions in the source.
The software automatically detects all units attached to the computer and you can control both the source and any filtering accessories from the same software. CONTROL is easy to use and supports touch input as well as traditional mouse+keybord control. Download the latest version at www.nktphotonics.com/software

### Software Development Kit (SDK)

The free SuperK EXTREME software development kit (SDK) enables control of the SuperK laser using third party software and hardware. The SDK contains a full description of the communication protocols as well as LabView drivers and C++/C# source code.

# Features and Options

## Power Lock (external power locking)

The Power Lock option enables you to lock the power at any place in a set-up. Simply place a photo detector at the desired location and connect the detector to the External Feedback BNC connector of the SuperK. Activate locking from the control panel and the SuperK will now lock the power level at the position of the photo detector—automatically compensating for any drift or variation in external components in the setup up to 100 Hz.

Most of our SuperK accessories are also available with a build-in Power Lock monitor for ultra stable output (typically < ± 0.5 %). See more in our application note at www.nktphotonics.com/superk_extreme_support.

## Variable repetition rate (pulse picker)

The pulse picker option allows the repetition rate of the SuperK EXTREME to be easily changed on-the-fly while the system is running at full output. Repetition rates of 1-40 MHz or 2-78 MHz are available as standard (down to 150 kHz on custom request), giving the user ultimate choice for lifetime measurement applications such as FLIM.

For more information on how to use the SuperK EXTREME for FLIM se e.g. Leica Microsystems SP8X confocal microscope.

- Ideal for FLIM, FRET and diffuse optical tomography
- 1-78 MHz on-the-fly variable repetition rate with 23 steps
- > 1:10,000 Pulse Suppression ratio
- NIM standard trigger output (directly usable for FLIM)
- Timing delay generator

| | |
|---|---|
| Master Seed Repetition Rate | 78 (standard) or 40 MHz |
| Repetition Rate Reduction | 78 – 2 MHz (23 steps) |
| | 40 – 1 MHz (23 steps) |
| Pulse Suppression Ratio | > 1:10,000 |
| Operation Mode | Constant Pulse Energy |
| Changing Repetition Rate [1)] | < 1 s |
| Timing Trigger Output Jitter | < 20 ps |
| NIM Trigger Output (BNC) | 0.1 – 1 V peak |
| Monitor Trigger Output (BNC) | 0 – 1 V |
| Adjustable Trigger Delay Timing [2)] | up to 9.2 ns |
| Adjustable Trigger Delay Resolution [2)] | 15 ps |

1) The system does not need to be electrically shut down.
2) The electrical output trigger signal can be delayed up to 9.2 ns in steps of 15 ps. This enables trigger delay optimization without the need for a expensive delay box. Adjustable from front panel.

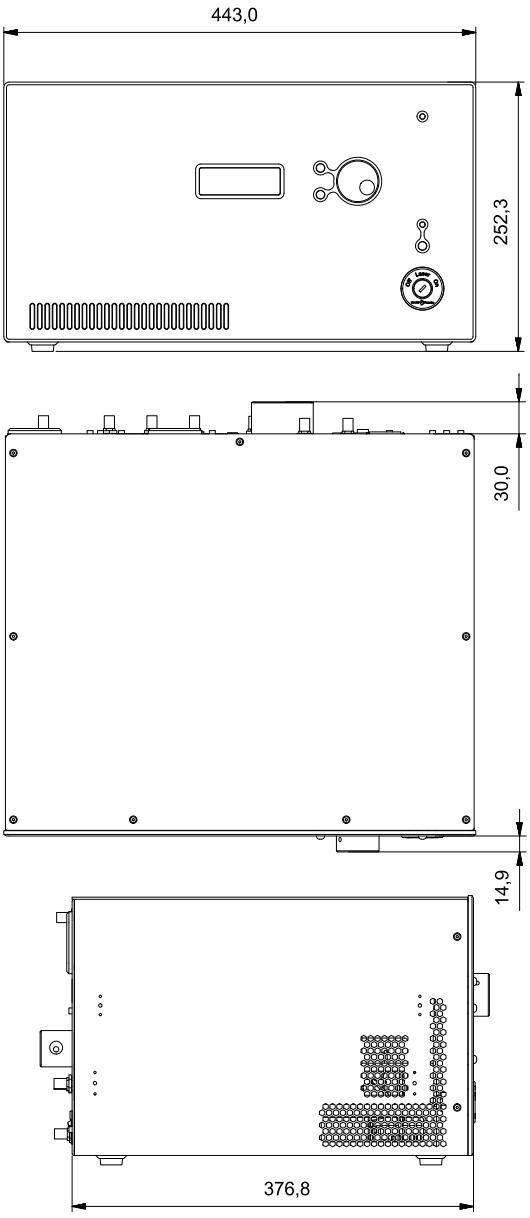


All dimensions in mm

# Specifications

## Optical

| | |
|---|---|
| Master Rep Rate | 40 MHz or 78 MHz |
| Master seed laser pulse | ~5 ps |
| Total visible power stability | +/-1.5 % (without Power Lock)<br>< ± 0.5 % (typical with Power Lock) |
| Polarization | Unpolarized |
| Beam output | Gaussian, single mode |
| $M^2$ | < 1.1 |
| Output options | Collimated (standard)<br>Divergent (on request) |
| Length of output fiber | 1.5 m |
| Beam diameter | ~1 mm at 530 nm<br>~2 mm at 1100 nm<br>~3 mm at 2000 nm |
| Beam Divergence (half angle) | < 5 mrad |
| Beam Pointing Accuracy[1)] | < 1 mrad |
| Beam Pointing Stability | < 50 µrad |
| Typical single mode fiber coupling efficiency | >70 % |

## Mechanical/Electrical

| | |
|---|---|
| Computer Interface | USB 2.0 |
| Operation Voltage | 100-240 VAC 50/60 Hz |
| Power Consumption | <100 W (<120W with pulse picker) |
| Door Interlock Connector [2)] | 2-pin LEMO |
| External Bus interface [3)] | 16-pin sub-D |
| System Cooling | Air Cooled |
| Operation Temperature | +18° to +30°C |
| Storage Temperature | -10° to +60°C |
| Dimensions (WxHXL) | 440x243x380 $mm^3$ |
| Weight | 18 kg (19 kg with pulse picker) |

1) Measured relative to the mechanical axis running through the center of the collimator
2) The SuperK Extreme is a Class 4 laser and is required to be connected to a door interlock/circuit
3) External communication and power supply port for accessories

**NKT Photonics A/S (Headquarters)**
Blokken 84, 3460 Birkerød, Denmark
Phone: +45 4348 3900
Fax: +45 4348 3901

**NKT Photonics GmbH**
Schanzenstrasse 39, Bldg D9-D13
51063 Cologne, Germany
Phone: +49 221 99511-0
Fax: +49 221 99511-650

**NKT Photonics Inc.**
1400 Campus Drive West
Morganville NJ 07751, USA
Phone: +1 732 972 9937
Fax: +1 732 414 4094

All NKT Photonics products are produced under our quality management system certified in accordance with the ISO 9001:2008 standard.

VISIBLE AND INVISIBLE LASER RADIATION
AVOID EYE OR SKIN EXPOSURE TO DIRECT OR SCATTERED RADIATION
CLASS 4 LASER PRODUCT

# Light Manipulation Accessories

## SuperK VARIA

SuperK VARIA is a cost effective and flexible alternative to a monochromator, effectively turning the SuperK into a powerful single-line laser with a 440 nm tuning range and variable bandwidth. The center wavelength of the pass band can be tuned between 400 and 840 nm and the bandwidth is variable between 10 and 100 nm, making the VARIA the most flexible filter solution on the market. Increasing the bandwidth of the filter increases power throughput and reduces speckle in imaging applications. Moreover, a high out-of-band suppression of 50dB makes the SuperK VARIA ideal for FLIM and other applications using high sensitivity detectors.

## SuperK EXTEND-UV

SuperK EXTEND-UV is a deep-UV spectral extension unit for our SuperK EXTREME supercontinuum lasers. Get tunable UV light from a robust fiber laser source with 270-480 nm range and 2-80 µW output power. The collimated output enables tight focusing and the fast pulses, down to 20 ps in length, make it ideal for studying ultrafast photochemical processes. The performance and output characteristics of the system depends on the Supercontinuum source used.

## SuperK SELECT

SuperK SELECT is a tunable wavelength filter based on acusto-optic tunable filter technology (AOTF). AOTFs tune over one octave of optical frequency and the SuperK SELECT allows the integration of two AOTF crystals to provide wide spectral coverage. Together with a range of unique features, the SuperK SELECT provides an easy to use, flexible and accurate tuning accessory to access any wavelength in the SuperK spectrum.

## SuperK SPLIT

SuperK SPLIT allows the SuperK spectrum to be divided into two spectral outputs. In its standard form, the SuperK SPLIT provides two outputs: Visible and nIR. However, the choice of the split in the spectrum can be user-defined to be anywhere in the SuperK spectrum. Additionally, standard mounts within the SPLIT allow the insertion of narrow band filters, polarisers or attenuators at each output exit for further flexibility.

## SuperK CONNECT

SuperK CONNECT is a high performance fiber delivery system complete with broadband fibers and a range of termination options such as FC/PC connectors or collimators. Interfacing is handled by the CONNECT fiber coupling unit that ensure easy and stable single-mode coupling that can be disconnected and reconnected without alignment.

**Table A.5 – Maximum permissible exposure (MPE) of the skin to laser radiation [a, b]**

<table>
<tr><th rowspan="2">Wavelength<br>$\lambda$<br>nm</th><th colspan="6">Exposure time $t$<br>s</th></tr>
<tr><th>$<10^{-9}$</th><th>$10^{-9}$ to $10^{-7}$</th><th>$10^{-7}$ to $10^{-3}$</th><th>$10^{-3}$ to 10</th><th>10 to $10^{3}$</th><th>$10^{3}$ to $3\times10^{4}$</th></tr>
<tr><td>180 to 302,5</td><td rowspan="3">$3 \times 10^{10}$ W·m$^{-2}$</td><td colspan="5">30 J·m$^{-2}$</td></tr>
<tr><td>302,5 to 315</td><td colspan="3">$C_1$ J·m$^{-2}$ ($t \le T_1$)<br>$C_2$ J·m$^{-2}$ ($t > T_1$)</td><td colspan="2">$C_2$ J·m$^{-2}$</td></tr>
<tr><td>315 to 400</td><td colspan="3">$C_1$ J·m$^{-2}$</td><td>$10^{4}$ J·m$^{-2}$</td><td>10 W·m$^{-2}$</td></tr>
<tr><td>400 to 700</td><td>$2 \times 10^{11}$ W·m$^{-2}$</td><td>200 J·m$^{-2}$</td><td colspan="2">$1{,}1 \times 10^{4}\ t^{0,25}$ J·m$^{-2}$</td><td colspan="2">2 000 W·m$^{-2}$</td></tr>
<tr><td>700 to 1 400</td><td>$2 \times 10^{11}\ C_4$ W·m$^{-2}$</td><td>200 $C_4$ J·m$^{-2}$</td><td colspan="2">$1{,}1 \times 10^{4}\ C_4\ t^{0,25}$ J·m$^{-2}$</td><td colspan="2">2 000 $C_4$ W·m$^{-2}$</td></tr>
<tr><td>1 400 to 1 500</td><td>$10^{12}$ W·m$^{-2}$</td><td colspan="2">$10^{3}$ J·m$^{-2}$</td><td>5 600 $t^{0,25}$ J·m$^{-2}$</td><td colspan="2" rowspan="4">1 000 W·m$^{-2}$ [c]</td></tr>
<tr><td>1 500 to 1 800</td><td>$10^{13}$ W·m$^{-2}$</td><td colspan="3">$10^{4}$ J·m$^{-2}$</td></tr>
<tr><td>1 800 to 2 600</td><td>$10^{12}$ W·m$^{-2}$</td><td colspan="2">$10^{3}$ J·m$^{-2}$</td><td>5 600 $t^{0,25}$ J·m$^{-2}$</td></tr>
<tr><td>2 600 to $10^{6}$</td><td>$10^{11}$ W·m$^{-2}$</td><td>100 J·m$^{-2}$</td><td colspan="3">5 600 $t^{0,25}$ J·m$^{-2}$</td></tr>
</table>

[a] For correction factors and units, see Table 9.

[b] There is only limited evidence about effects for exposures of less than $10^{-9}$ s. The MPEs for these exposure durations have been derived by maintaining the irradiance applying at $10^{-9}$ s.

[c] For exposed skin areas greater than 0,1 m$^2$, the MPE is reduced to 100 W·m$^{-2}$.
Between 0,01 m$^2$ and 0,1 m$^2$, the MPE varies inversely proportional to the irradiated skin area.

## A.2 Limiting apertures

An appropriate aperture should be used for all measurements and calculations of exposure values. This is the limiting aperture and is defined in terms of the diameter of a circular area over which the irradiance or radiant exposure is to be averaged. Values for the limiting apertures are shown in Table A.6. When the MPE values for the retinal hazard region expressed as power or energy are used (Table A.3 or Table A.4) the exposure value is to be expressed as power or energy and determined as power or energy passing through an aperture with a diameter of 7 mm.

For repetitively pulsed laser exposures within the spectral range between 1 400 nm and $10^5$ nm, the 1 mm aperture is used for evaluating the hazard from an individual pulse; whereas the 3,5 mm aperture is applied for evaluating the MPE applicable for exposures greater than 10 s.

The values of ocular exposures in the wavelength range 400 nm to 1 400 nm are measured over a 7 mm diameter aperture (pupil). The MPE shall not be adjusted to take into account smaller pupil diameters.

**Table A.6 – Aperture diameters for measuring laser irradiance and radiant exposure**

| Spectral region nm | Aperture diameter for mm | |
|---|---|---|
| | Eye | Skin |
| 180 to 400 | 1 | 3,5 |
| ≥ 400 to 1 400 | 7 | 3,5 |
| ≥ 1 400 to $10^5$ | 1 for $t \leq 0{,}35$ s<br>$1{,}5\ t^{3/8}$ for 0,35 s < $t$ < 10 s<br>3,5 for $t \geq 10$ s | 3,5 |
| ≥ $10^5$ to $10^6$ | 11 | 11 |
| NOTE For multiple pulse exposures, refer to Clause A.3. | | |

## A.3 Repetitively pulsed or modulated lasers

The following methods should be used to determine the MPE to be applied to exposures to repetitively pulsed radiation.

The exposure from any group of pulses (or sub-group of pulses in a train) delivered in any given time should not exceed the MPE for that time.

The MPE for ocular exposure for wavelengths less than 400 nm and longer than 1400 nm, as well as the MPE for skin exposure is limited by the most restrictive of requirements a) and b).

The MPE for ocular exposure for wavelengths from 400 nm to 1 400 nm is determined by using the most restrictive of requirements a), b) and c). Requirement c) applies only to the retinal thermal limits and not to the retinal photochemical limits.

a) The exposure from any single pulse within a pulse train does not exceed the MPE for a single pulse.

b) The average exposure for a pulse train of exposure duration $T$ does not exceed the MPE given in Tables A.1, A.2 and A.3 for a single pulse of exposure duration $T$. For irregular pulse patterns (including varying pulse energies), $T$ has to be varied between $T_i$ and the maximum assumed exposure duration. For regular pulse patterns it is sufficient to average over the assumed maximum exposure duration.

c) The exposure per pulse does not exceed the MPE for a single pulse multiplied by the correction factor $C_5$. $C_5$ is only applicable to individual pulse durations shorter than 0,25 s.

$$MPE_{s.p.train} = MPE_{single} \times C_5$$

where

$MPE_{single}$ is the MPE for a single pulse;

$MPE_{s.p.train}$ is the MPE for any single pulse in the pulse train.

If pulse duration $t \leq T_i$, then:

For maximum anticipated exposure duration less than or equal to 0,25 s

$C_5 = 1{,}0$

For maximum anticipated exposure duration larger than 0,25 s

If $N \leq 600$ $C_5 = 1{,}0$

If $N > 600$ $C_5 = 5 \cdot N^{-0{,}25}$ with a minimum value of $C_5 = 0{,}4$